Electron Scattering From Polyatomic Molecules

by

Wyndham Michael Johnstone

A thesis submitted in partial fulfilment

of the requirement for the degree of

Doctor of Philosophy

University of London

1990

ProQuest Number: 10608932

All rights reserved

INFORMATION TO ALL USERS
The quality of this reproduction is dependent upon the quality of the copy submitted.

In the unlikely event that the author did not send a complete manuscript
and there are missing pages, these will be noted. Also, if material had to be removed,
a note will indicate the deletion.

ProQuest 10608932

Published by ProQuest LLC (2017). Copyright of the Dissertation is held by the Author.

All rights reserved.
This work is protected against unauthorized copying under Title 17, United States Code
Microform Edition © ProQuest LLC.

ProQuest LLC.
789 East Eisenhower Parkway
P.O. Box 1346
Ann Arbor, MI 48106 – 1346

Dedication

To my dear and loving parents

Abstract

The design and use of a high resolution electron spectrometer to measure absolute elastic collision cross sections for electron scattering from molecular targets is described. The spectrometer was constructed around two 180° hemispherical energy selectors which were employed to define the energy spread of the incident electron beam and to analyse the energy of the scattered electrons. Electrons emitted from a thoriated tungsten hairpin filament were transported to and from the selectors using several two and three element cylinder lenses. The total resolution of the spectrometer was variable between 28meV for an incident beam current of 2nA and 100meV for currents in excess of 60nA. The range of incident energies and scattering angles at which electron scattering could be measured with the spectrometer was 2–100eV and 10°–120°, respectively.

Three polyatomic molecules have been studied, SF_6, H_2O and N_2O and absolute differential cross sections for electron scattering from these molecules have been measured for incident energies between 5eV and 80eV. By extrapolation of the differential cross sections to 0° and 180°, integral and momentum transfer cross sections were also obtained. A two stage process was employed in the determination of the absolute differential cross sections. The relative differential cross section (normalised to 90°) was first measured for scattering angles between 10° and 120° using the subtraction technique. In this method problems arising from the overlap geometry of the gas and electron beam plus background effects were accounted for. The relative differential cross sections were then normalised to an absolute scale using the absolute differential cross section at 90° obtained using the relative flow technique. The errors associated with the absolute differential cross sections obtained using this approach were ≈14%.

Contents

List Of Tables

List Of Figures

Acknowledgements

To Dr. Roy Newell for his supervision and encouragement during the course of this work.

To Dr. Nigel Mason for many interesting discussions and advice on the preparation of this thesis.

To Ivan Rangué and Ted Oldfield for their invaluable assistance in the construction of the apparatus.

To Dr. Tony Smith, Dr. Bella Mapstone, Joe Sanderson, Sarah Barnet and Joan Furlong-my fellow colleagues in the atomic physics group.

To Geoff Parsons and Vishal Nayar for their encouragement and support.

To the Physics and Astronomy department for financial support.

To Nicholas James for his help, patience and understanding.

To Dr. Nazrene Zafar for many helpful comments and discussions during the course of this work and her motivation and friendship at all times.

To my parents and sister for their support and help at all times.

To Benjamin Palatine for many stimulating discussions.

You've got to accentuate the positive
Eliminate the negative
Latch onto the affirmative
And don't mess with Mr. Inbetween.

from a song "Ac–cent–tchu–ate The Positive"
sung by Bing Crosby and The Andrews Sisters.
(Arlene, Mercer/E.H. Morris) Pre 1957 MCA Records Inc.

Chapter 1

Review of Electron Scattering Experiments and Theory

1.1 Introduction

Since the first experimental and theoretical studies of electron-molecule collisions were performed in the early 1900s, the field of electron-molecule collision physics has expanded into a vast area of research. The results of this research have not only provided a basic knowledge on the properties of molecules, the dynamics of electronic structure and the molecular interaction, but has led to a better understanding of many processes where electron-molecule interactions are important. The underlying physical principles of the scattering process were first identified in the early days of quantum mechanics (Born, 1926; Oppenheimer, 1928; Massey and Mohr, 1932) and have been summarised by Massey and Burhop (1969) and Massey (1969). But, as a result of the considerable complexities of the problem it is only in the last twenty years, with the availability of high speed supercomputers, that it has become possible to perform realistic calculations which provide accurate cross sections for electron-molecule collisions at low and intermediate energies. The experimental methods employed to measure electron-molecule collision cross sections have also undergone rapid development in the last twenty years, partly in response to the demand for collision cross sections for laser development, atmospheric modelling, various plasma and fusion schemes and for comparison with theory.

In this work, electron scattering from three polyatomic molecules, SF_6, H_2O and N_2O, has been studied and this thesis describes the experimental techniques employed and results obtained. In the remaining sections of this chapter, a brief description of the various experimental techniques used to measure electron collision cross sections relevant to this work are given. This is followed by a discussion of the theoretical aspects of the electron-molecule process. This is by no means a review of

the field and only those methods pertinent to the results obtained in the present work are discussed.

1.2 Definitions Of Electron Collision Cross Sections

Electrons scattering from a molecular target may undergo one of two collision processes: those in which the electrons lose a portion of their kinetic energy to the excitation of internal degrees of freedom of the molecule (inelastic collisions) or those in which no energy is transferred to the internal motion of the molecule (elastic collisions). The number of electrons (N_s) scattered from an incident beam of N electrons per second by a molecular beam of density N_m into a solid angle $d\Omega$, defined by the polar angles θ and ϕ, is

$$N_s = N_m N \times [d\sigma/d\Omega\ (E_o,\theta,\phi)]\ d\Omega \qquad 1.1$$

where E_o is the kinetic energy of incident electrons, x is the length of the overlap of the electron and molecular beam and $d\Omega=\sin\theta d\theta d\phi$. The quantity $d\sigma/d\Omega(E_o,\theta,\phi)$ is defined as the differential cross section for the particular elastic or inelastic scattering process. As the molecules in a gaseous target are free to rotate, the differential cross section is independent of the azimuthal polar angle ϕ.

In most experiments, the resolution is insufficient to directly observe rotational and some vibrational excitations therefore, the cross section measured is generally an average of a number of indistinguishable processes. Thus, to enable a comparison with theoretically derived cross sections it may be necessary to average the state to state theoretical cross sections over the experimentally unresolved initial (i) and final (f) states

$$d\sigma/d\Omega(E_o,\theta) = \sum_i N_i \sum_f d\sigma^{i\rightarrow f}/d\Omega(E_o,\theta) \qquad 1.2$$

where N_i is the fractional population in the ith state.

The total number of electrons elastically scattered by the target is obtained by integrating the differential cross section (as defined in 1.1 and 1.2) over all polar angles

(θ). This integration yields the integral cross section, which is defined by

$$\sigma_t = 2\pi \int_o^\pi d\sigma/d\Omega(E_o,\theta)\sin\theta d\theta \qquad 1.3$$

The momentum transfer cross section provides a measure of the amount of energy transferred in each collision due to the change in momentum and is defined by

$$\sigma_m = 2\pi \int_o^\pi d\sigma/d\Omega(E_o,\theta)[1-(k_f/k_i)\cos\theta]\sin\theta d\theta \qquad 1.4$$

where k_i and k_f are the initial and final momenta of the electron, respectively. The total cross section, σ_T, represents the sum of the integral cross sections associated with all process and includes contributions from elastic scattering, vibrational and rotational excitation, electronic excitation, ionisation and dissociation. In most cases the total cross section is dominated by elastic scattering, ionisation and excitation processes and can given by

$$\sigma_T = \sigma_t + \sigma_{exe} + \sigma_{ion} \qquad 1.5$$

where σ_{exe} is the integral cross section associated with excitation of the molecule and σ_{ion} is the ionisation cross section.

1.3 Experimental Techniques Used To Measure Electron Collision Cross Sections

1.3.1 Total Cross Section Measurements

The first quantitative total cross section measurements were made by Ramsauer in 1921. While the methods he employed are still in use today (Zecca *et al*, 1987) most total cross section measurements are now made using the experimental arrangement illustrated in figure 1.1. In this arrangement an electron beam enters a scattering chamber containing the gaseous species under investigation through an aperture S1. Any electrons scattered by the gas in the chamber are collected on the

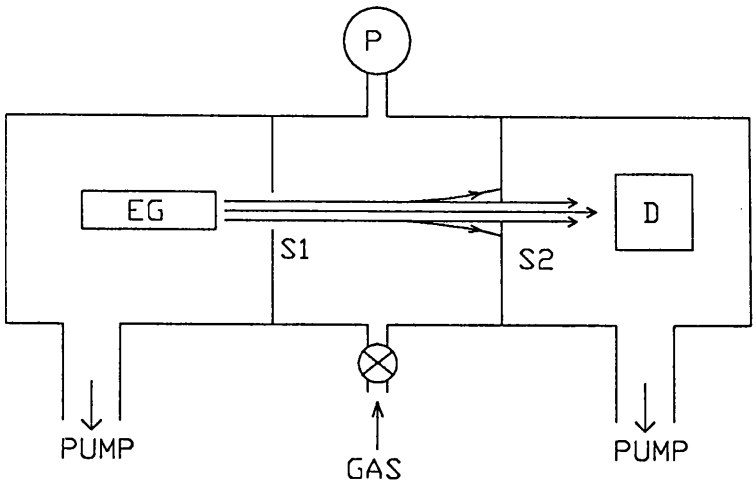

Figure 1.1 Schematic diagram of the transmission method for determining total cross sections. EG, P, D, S1 and S2 denote the electron gun, pressure gauge, electron detector and entrance and exit slits, respectively (Trajmar and Register, 1984).

chamber walls, while the unscattered beam passes through the exit aperture S2 and its intensity subsequently measured by the detector D. Measurement of the electron current scattered in the chamber and that reaching the detector together with a knowledge of the gas density in the chamber and the path length between S1 and S2, allows the total cross section to be determined (Bederson and Kieffer, 1971). There are several problems associated with this method, namely:–

1) discrimination against small angle scattering (elastic and inelastic) of electrons into the view cone of the detector,

2) electrons which undergo multiple collisions and are scattered back into the view cone of the detector,

3) space charge spreading of the beam within the chamber.

Nevertheless provided these points can be accounted for, cross sections accurate to a few percent may be obtained.

Some of the problems outlined above can be overcome using the time of flight (TOF) technique (Kennerly and Bonham, 1978; Ferch *et al*, 1985). In this method, a pulsed electron beam is passed through the target chamber. From a measurement of

the time taken for the electrons to pass through the chamber, it is possible to differentiate between elastically and inelastically scattered electrons. The energy resolution of the apparatus is then dependent on the energy of the electrons and the timing resolution. For example, Ferch *et al* (1985) quote resolutions of 0.003eV to 2.9eV for incident energies corresponding to 0.08eV and 20eV. Using the TOF technique also eliminates the problems associated with space charge as it is usual to have only one electron in the chamber at any one time.

1.3.2 Momentum Transfer Cross Section Measurements

Momentum transfer cross sections at low incident electron energies are most commonly determined using the electron swarm technique. In this technique, electrons are allowed to enter a gas filled chamber where they are accelerated by a uniform electric field E. As the electrons drift through the chamber they collide with the gas molecules and will eventually attain a steady state drift velocity as the accelerations in the field direction *between* collisions are balanced by the decelerations that occur *during* the collisions. By measuring the drift velocity as a function of E/N (N is the number density of the gas in the chamber) it is possible to determine the momentum transfer cross section (Huxley and Crompton, 1974). This method is generally only used for low energy scattering (0 to a few eV) as it is difficult to account for effects associated with inelastic scattering which becomes significant at higher energies. Therefore for energies greater than 1eV or 2eV, the momentum transfer cross sections are obtained by extrapolation of differential cross section data (see chapters 5, 6 and 7).

1.3.3 Differential Cross Section Measurements

Differential cross sections as a function of energy and angle have been measured since the 1930s (Ramsauer and Kollath, (1932), but it is was only with the advent of significant improvements in the production and detection of electron beams of high resolution and small angular spread, that it has been possible to measure accurate differential cross sections. The three areas of development that have had the greatest impact on the measurement of differential cross sections are:–

1) the availability of extensive and accurate data on the focal properties of

several types of electrostatic lens (e.g. Harting and Read, 1976),

2) the development of a large variety of energy selectors capable of producing electron beams with energy spreads (full width half maximum) ≈10–20meV (e.g. Sevier, 1972),

3) the significant improvement in electron detection achieved with the introduction of channel electron multipliers (channeltrons or CEMs) and micro channel plates combined with advances made in digital electronics.

The design and use of the apparatus required for the measurement of differential cross sections is discussed in more detail in chapters 2 and 4.

1.4. Review Of Electron-Molecule Scattering Theory

Since the first electron-molecule scattering calculations were performed by Massey and co-workers in the 1930s, considerable progress has been made in this field with much of the work aided by the improvements in computing technology. The electron-molecule system poses special problems over and above those encountered in the electron-atom case. Calculating the contribution of the three terms in electron-molecule interaction, static potential, exchange and polarisation (see section 1.4.6), proves to be difficult as a result of the non-spherical nature of the target. Also the additional degrees of freedom introduced by the nuclear motion (rotation and vibration) adds further complications. In the following sections, a brief description is given of some of the approaches used in the formulation of the electron-molecule scattering calculation. This includes an introduction to the basic quantum mechanical problem, a brief description of some of the strategies employed to solve the problem, a description of the electron-molecule interaction and a short review of the theoretical approaches relevant to the experimental data in this work. A more detailed explanation of the theory of electron-molecule scattering can be found in the reviews of Lane (1980), Morrison (1983) and Gianturco and Jain (1986) and the references therein.

1.4.1 The Basic Theoretical Problem

In a quantum mechanical treatment of the electron-molecule scattering problem, the system is described by the Schrödinger equation which includes an interaction

Hamiltonian and a corresponding wave function of the total system

$$(H\text{-}E)\Psi_T(\mathbf{r},\mathbf{r}',\mathbf{R})=0 \qquad 1.6$$

where E is the total energy of the system and Ψ_T is the total wavefunction. H is the electron-molecule Hamiltonian and is given by

$$H = H_e(\mathbf{r}) + V_{int}(\mathbf{r},\mathbf{r}',\mathbf{R}) + H_m(\mathbf{r}',\mathbf{R}) \qquad 1.7$$

where H_e represents the kinetic energy of the scattered electron, H_m is the Hamiltonian of the isolated molecule and V_{int} represents the Coulomb interaction between the incident electron and the molecule. This last term is the sum of the two contributions

$$V_{int} = V_{elec\text{-}nucl} + V_{elec\text{-}mol\ elec} \qquad 1.8$$

where $V_{elec\text{-}nucl}$ is the interaction between the incident electron and the nuclei and $V_{elec\text{-}mol\ elec}$ is the interaction between the incident electron and the bound electrons in the molecule. The coordinates $\mathbf{r}$, $\mathbf{r}'$ and $\mathbf{R}$ represent the position of the scattered electron, bound electrons and the nuclei, respectively. The total wavefunction Ψ_T, describes both the scattered electron and the target molecule and satisfies the boundary condition

$$\Psi_T(\mathbf{r},\mathbf{r}',\mathbf{R}) \underset{r\to\infty}{\approx} \exp(i\mathbf{k}_i\cdot\mathbf{r})\phi_i(\mathbf{r}',\mathbf{R}) + r^{-1}\textstyle\sum_f \exp(i\mathbf{k}_f\cdot\mathbf{r})\phi_f(\mathbf{r}',\mathbf{R})f_n(\mathbf{k}_f\cdot\mathbf{k}_i) \qquad 1.9$$

The first term on the right hand side of equation 1.9 is the product of a plane wave, representing the incident electron ($\exp(i\mathbf{k}_i\cdot\mathbf{r})$), and the initial state of the molecule $\phi_i(\mathbf{r}'\mathbf{R})$. The second term is summed over the number of energetically accessible states of the molecule and is the product of the final state molecular wave function ($\phi_f(\mathbf{r}',\mathbf{R})$), an outgoing spherical wave $r^{-1}\exp(i\mathbf{k}_f\cdot\mathbf{r})$ (representing the scattered electron) and the scattering amplitude ($f_f(\mathbf{k}_f\cdot\mathbf{k}_i)$) for the transition $\phi_i(\mathbf{r}',\mathbf{R})\rightarrow\phi_f(\mathbf{r}',\mathbf{R})$. It is the magnitude

of this amplitude which is the focus of the theoretical calculations, as once determined the scattering cross section can be obtained.

The determination of the quantities that appear in an evaluation of the scattering amplitude, e.g. the wave functions of the bound electrons and the interaction forces between the molecule and the incident electron, is non-trivial due to the multicentred, non-spherical nature of the molecule. The complicated interplay between the motion of the nuclei with the bound and scattered electrons also adds to the problem. To reduce the complexity of the problem, eigenfunction methods are commonly used to obtain a tractable set of equations that depend only on the radial coordinate of the scattering electron. This is normally achieved by expanding the total wavefunction in terms of the molecular wavefunction ϕ, to give

$$\Psi_T(\mathbf{r},\mathbf{r}',\mathbf{R}) = A\sum_n F_n(\mathbf{r})\phi_n(\mathbf{r}',\mathbf{R}) \qquad 1.10$$

where A is the usual antisymmetriser and ensures that the Pauli principle is satisfied by Ψ_T. $F_n(\mathbf{r})$ is a one-particle scattering function describing the motion of the scattered electron in a molecular state n. The summation is over all the possible energy levels in the molecule, which should include continuum as well bound states. The one-particle scattering functions can then be expanded further in terms of angular functions $Y_l(\hat{\mathbf{r}})$ which contain the full dependence of $F_n(\mathbf{r})$ on the angular variables, where

$$F_n(\mathbf{r}) = \sum_l u_l(\mathbf{r})Y_l(\hat{\mathbf{r}}) \qquad 1.11$$

and $u_l(\mathbf{r})$ are the radial scattering functions and satisfy the same boundary conditions as the total wave function. Equation 1.11 is often called a partial wave expansion. Once values of $u_l(\mathbf{r})$ have been determined the scattering amplitude can be calculated

directly from the radial scattering functions in the asymptotic region. As a result of the small energy spacing between the rotational and vibrational states, a large number of nuclear states are energetically accessible even at low incident energies. Many, if not all of these states must be included in the expansion in equation 1.10 to obtain accurate cross sections. It may also be necessary to include some or all of the infinity of the electronic states, as they contribute to the polarisation of the molecule by the scattering electron. The introduction of terms to account for exchange and polarisation effects further complicates the situation. Additional difficulties arise from couplings between the individual radial scattering functions which dictate that the entire set of equations are solved simultaneously.

1.4.2 Close Coupling Theories

The inclusion of all the terms in the expansion of equation 1.10 is impossible, therefore it is truncated. The states retained in the expansion are those which are "close" (in energy) to the initial and final states of the molecule before and after the scattering event and this is the essential idea behind close coupling theories. In general, all the continuum and most of the bound states are left out of the expansion, but even though these states may be energetically inaccessible, they are still germane to the scattering process as they are responsible for polarisation effects. These effects are therefore included by other means which will be described further in section 1.4.5. As a result of the small energy spacing between rotational and vibrational states a large number of coupled equations are still generated in this approach, therefore a full ro-vibrational close coupling approach using a realistic representation of the electron-molecule interaction potential has only been applied to low energy e–H_2 scattering (Henry and Lane, 1969).

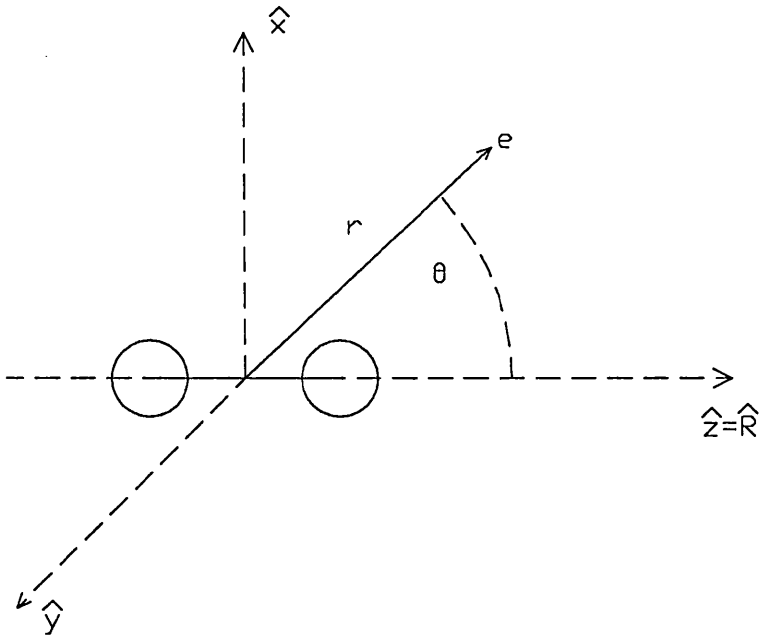

Figure 1.2 Schematic representation of the electron molecule system in the body-frame coordinate system, which is defined so that $\hat{z}=\hat{R}$ This coordinate system is used in the fixed nuclei model.

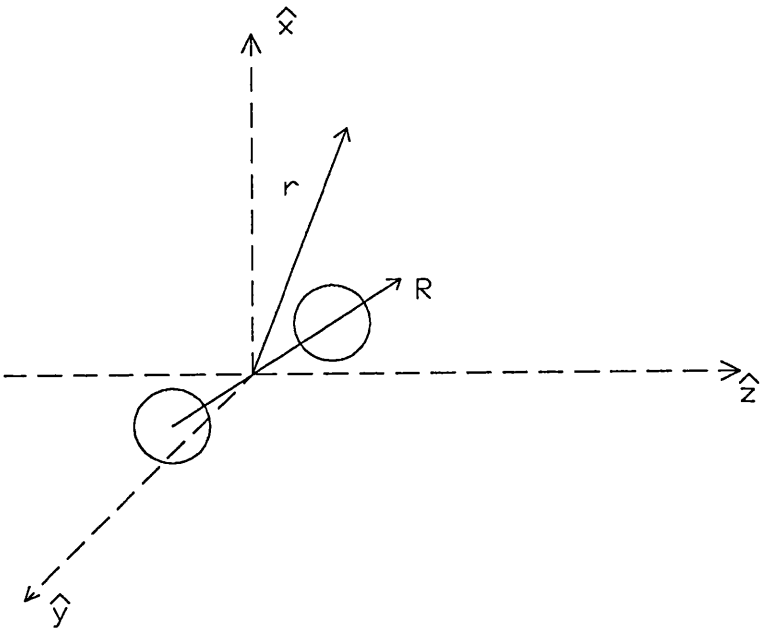

Figure 1.3 Schematic representation of an electron (with coordinate r) and a molecule (with internuclear axis R) in a space fixed (lab-frame) reference frame. This coordinate system is used in lab-frame close coupling theories.

1.4.3 The Fixed Nuclei Model And The Adiabatic Nuclei Approximation

In order to simplify the electron-molecule scattering problem, the fixed nuclei model is often used. In 1930 Massey introduced the concept of the fixed nuclei (FN) model in his work on elastic electron scattering from molecular hydrogen when he assumed that the direction of the molecular axis and the internuclear distance remained fixed during the scattering process. By also assuming that the molecule remained in the ground electronic state, the expansion in equation 1.10 was reduced to just one term. The calculations were performed in the "body-frame" coordinate system (see figure 1.2) which rotates with the molecule and where the internuclear axis lies along the polar z-axis. The resulting cross sections were then averaged over all orientations of the internuclear axis in the space fixed, laboratory frame ("lab-frame" see figure 1.3) to obtain cross sections for comparison with experiment. Using this approach within the framework of the Born approximation, Bullard and Massey (1931) and Massey and Mohr (1932) were able to obtain elastic differential cross sections for electron scattering from H_2 and N_2 at incident energies greater than 100eV and the results they obtained were found to be in good agreement with those obtained experimentally. Below these energies the agreement was poor as the effects of exchange and polarisation were not included.

Massey (1930) subsequently extended the fixed nuclei model to obtain rotational and vibrational excitation cross sections using a technique which has subsequently become known as the adiabatic nuclei (AN) approximation. In this approximation the scattering problem is solved in two steps. First, the scattering amplitude $f^{FN}(\theta)$, is calculated within the fixed nuclei model in the body frame. $f^{FN}(\theta)$ is then averaged over the nuclear coordinate **R** using the formula

$$f_{i\to f}^{AN}(\theta) = \int \chi_f^*(\mathbf{R}) f^{FN}(\theta) \chi_i(\mathbf{R}) d\mathbf{R} \qquad 1.12$$

where $\chi_i(\mathbf{R})$ and $\chi_f^*(\mathbf{R})$ are the initial and final state nuclear wave functions of the molecule before finally transforming into the lab frame. Altshuler (1957), using the general "adiabatic approximation" of Chase (1956) discussed the quantitative criteria for

the applicability of this approximation and stated that the adiabatic nuclei approximation was valid if:

1) the period of the molecular motions (rotation and vibration) were much larger than the time required for the electron to cross the region of interaction (i.e. collision time),

2) that the number of excited states of the target that contribute significantly to the total wave function was limited.

As the typical rotational and vibrational periods are $\approx 10^{-12}$s and $\approx 10^{-14}$s, respectively, and the collision time is $\approx 10^{-16}$s for a non-polar molecule, the adiabatic nuclei approximation is valid in most cases. The circumstances where this approximation is not valid are those where the electron remains within the "field" of the molecule for times comparable to or greater than those associated with the nuclear motion. Situations where is likely to occur are

1) close to the threshold of an excitation process where the scattered electron will move slowly away from the molecule,

2) in the vicinity of a resonance where the incident electron may become temporarily bound to the molecule for times comparable to the period of the nuclear motion

3) scattering from polar molecules where the "collision time" is large due to long range nature of the dipole potential.

When using the fixed nuclei model to calculate cross sections for electron scattering from polar molecules, the differential cross sections are found to diverge in the forward direction (Garrett, 1971). However, Collins and Norcross (1978) have shown that the adiabatic nuclei approximation and the fixed nuclei model can still be used to calculate the differential cross at scattering angles away from the forward direction i.e. $\theta > 30°$.

An important result discussed in detail by Lane (1980) is that

$$d^{FN}\sigma/d\Omega = \sum_{vJM} d^{AN}\sigma/d\Omega \qquad 1.13$$

where $d^{AN}\sigma/d\Omega$ is the differential cross section for the excitation of the vJM state (where v, J and M are the final state vibrational and rotational quantum numbers) calculated

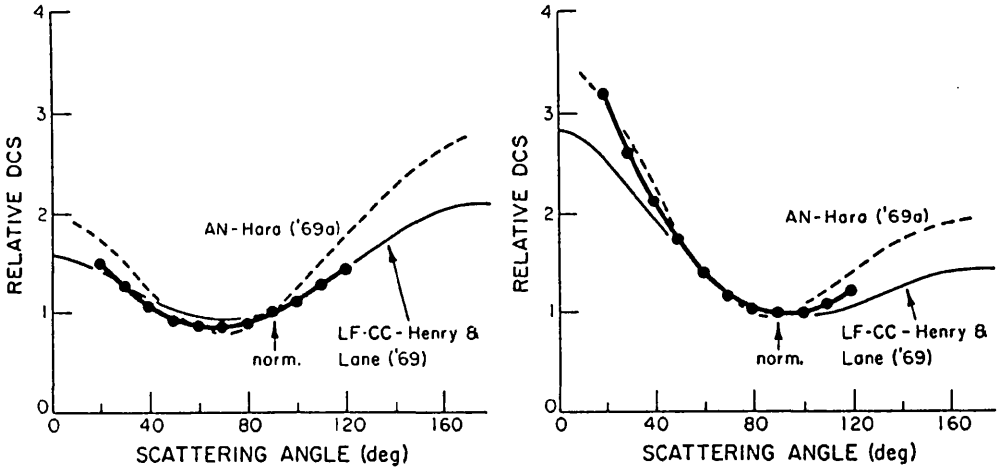

Figure 1.4 Comparison of the results obtained using the adiabatic nuclei approximation and close coupling methods. Relative differential cross sections for elastic scattering of: (a) 2.5eV incident energy electrons by H_2; (b) same as (a) except for 4.5eV incident energy. Experimental data: Linder and Schmidt (1971). Theory: —— Henry and Lane (1969) using a lab-frame close coupling approach;——Hara (1969) using the adiabatic nuclei approximation.

in the adiabatic nuclei approximation and $d^{FN}\sigma/d\Omega$ is the elastic differential cross section calculated in the fixed nuclei model. Therefore, when theoretical results are to be compared with experimentally obtained values, where the rotational and some vibrational states are often unresolved, the calculations can be performed within the fixed nuclei model thereby reducing the complexity of the calculations. Also, it has been observed that the results from the lab frame close coupling calculations and those obtained using the adiabatic nuclei approximation, where the same interaction potentials have been used, give very similar results. This is illustrated in figure 1.4 where the adiabatic nuclei results of Hara (1969) and the lab frame close coupling calculations of Henry and Lane (1969) are compared with the experimental results of Linder and Schmidt (1971). Thus where valid, the computationally less complex adiabatic nuclei approximation can be used to obtain electron scattering cross sections.

1.4.4 The Frame Transformation Theory

To combine the advantages of the close coupling methods with those of the fixed nuclei model, Fano (1970) and Chang and Fano (1972) formulated the frame

transformation theory. In this theory the scattering problem is divided into an inner and outer region. In the inner region, the incident electron is in or just outside the molecular charge cloud and as a result of strong Coulomb forces its velocity increases. As the velocity of the electron is much greater than that associated with the nuclear motion it essentially "sees" a fixed nuclei geometry. Thus for small values of **r**, the fixed nuclei model can be used within the body-frame coordinate system. In the outer region, a close-coupling calculation within the lab-frame coordinate system can be used in which full effect of the nuclear motion is included. The degree of coupling between the different nuclear states and within the radial scattering functions is weak, thus reducing the number of terms needed in the expansions. Also, the short range exchange and electron-correlation effects need not be included. The two regions are then matched at an arbitrarily chosen value of **r** where the frame transformation is implemented. Such an approach has been applied to electron scattering from CO by Chandra (1977).

A commonly used derivative of this approach is the R–matrix method which is a mathematical device for transforming the solutions of a given problem from one region to another. In the inner region the problem is treated as a molecule with N+1 electrons. Standard molecular structure codes can then be adopted and modified in order to evaluate the R–matrix at the boundary of the inner and outer regions, usually taken as the surface of the molecular charge cloud. Details of this method are given by Burke (1979) and Buckley *et al* (1984).

An alternative method, known as the angular frame transformation, has been proposed by Collins and Norcross (1978) principally for use in studying electron scattering from polar molecules. In this approach the problem is divided into different regions of orbital angular momentum space. If l refers to the electronic angular momentum quantum number, then for a range of angular momenta $l \leq l_t$ (where l_t is determined on physical grounds), the adiabatic nuclei approximation is used for any value of **r** and for $l > l_t$ a suitable lab-frame calculation is used for all r values. This technique has been successfully applied by Collins *et al* (1980) and Seigel *et al* (1981) and further details can be found in the review of Norcross and Collins (1982).

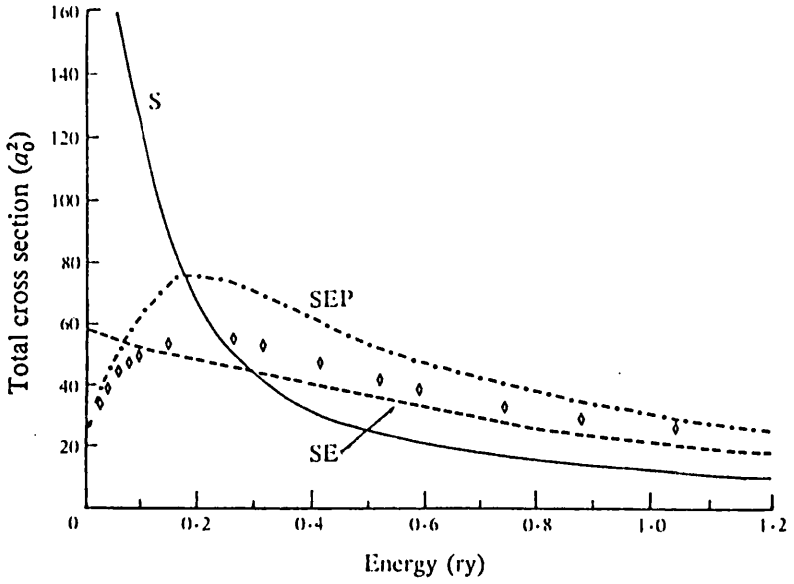

Figure 1.5 Total cross sections for e-H_2 collisions calculated using the fixed nuclei model employing three interaction potential: S, static only; SE static and exchange; SEP, static, exchange and polarisation. The diamonds are the experimental data of Golden et al (1966). The theoretical results shown here were calculated using rather crude model potentials and are designed to show qualitative behaviour only (Morrison, 1983).

1.4.5 The Electron-Molecule Interaction

Three physically distinct effects influence the scattering of electrons from atoms and molecules: the static potential, exchange and polarisation. The importance these effects have on the scattering process is illustrated in figure 1.5 which shows the measured total integral cross section for e-H_2 scattering and the results of three theoretical studies. The theoretical results differ only in their representation of the interaction potential; the first includes only the static potential, the second the static potential and exchange and in the third, all three effects are included. It can be seen that to achieve the best agreement with the experimental results all three contributions to the interaction potential must be included.

a) The Static Potential

The static potential arises from the pure Columbic forces between the scattering electron and the positively charged nuclei and the bound electrons in the molecule. It has a strong, attractive, non-spherical short range character and of the three

contributions to the electron-molecule interaction, it is the easiest to determine. The major difficulty in calculating the static potential is in handling the singularities resulting from the Coulomb interaction between the scattered electron and the nuclei. Multicentre expansion techniques (Burke and Noble, 1983 and references therein) can be used but require the solution of several multicentre integrals. Alternatively, single centre expansion techniques can be employed where all quantities such as bound and continuum orbitals are expanded about the centre of mass of the molecule. However, a major difficulty associated with this approach lies in the representation of the orbitals of the off centre nuclei, as they may require a large number of terms in the expansion to gain sufficient accuracy. This method has been successfully used by Gianturco and Thompson (1976) to calculate reliable static potentials for several molecules including H_2O, CH_4 and NH_3.

b) Exchange

Unlike the static and polarisation interactions, exchange has no classical analogue, as it is purely a quantum mechanical effect. When its effects are included in the scattering equations, usually by an "antisymmetriser" operator, integral terms are introduced into the coupled equations which contain the unknown radial scattering functions. In an attempt to solve this problem, two approaches have been employed. In the first, computation procedures have been developed in which the coupled integrodifferential equations can be solved numerically, allowing exchange effects to be included exactly (e.g. Lima *et al*, 1985). In the second approach, "model exchange potentials" have been devised which mimic the exchange effects but are computationally easier to handle.

Three types of model exchange potential are commonly employed the first of which is known as the semiclassical exchange (SCE) potential and is a function of the incident energy of the electron and the unperturbed charge density of the molecule (Gianturco and Scialla, 1987a). It is calculated using the following expression

$$V_{ex}(r,k^2) = 1/2[2k^2-V_{st}(r)]-1/2\{[2k^2-V_{st}(r)]+4\pi\rho_o(r)\}^{1/2} \qquad 1.14$$

where V_{st} is the static potential and $\rho_o(\mathbf{r})$ is the unperturbed charge density of the molecule. In deriving 1.14 it is assumed that the momentum of the bound electrons can be disregarded with respect to that of the impinging electron. Whilst this assumption is valid at large collision energies, it is unlikely to remain so at lower incident energies. To overcome this problem, Gianturco and Scialla (1987a) obtained a modified form of equation 1.14 known as the modified semiclassical exchange (MSCE) potential

$$V_{ex}(\mathbf{r},k^2) = 1/2\{2k^2-V_{st}+3/10[3\pi^2\rho(r)]^{2/3}\} \\ -1/2\{[k^2/2-V_{st}+3/10(3\pi^2\rho(r))^{2/3}]^2+4\pi\rho(r)\}^{1/2} \qquad 1.15$$

The second type of model exchange potential commonly employed treats the bound electrons as a free electron (Fermi) gas. Hara (1967) first introduced this treatment into electron-molecule scattering and it has since been used to model the exchange contribution for a large variety of molecular systems. The Hara free electron gas exchange (HFEGE) potential is given by

$$V_{ex}(\mathbf{r}) = (2/\pi)k_f(\mathbf{r})[1/2+(1-\eta^2)/4\eta\ln|1+\eta/1-\eta|] \qquad 1.16$$

where

$$k_f(\mathbf{r})=(3\pi^2\rho_o(\mathbf{r}))^{1/3} \qquad 1.17$$

and

$$\eta(\mathbf{r})=(k^2+2I+k_f^2)^{1/2}/k_f \qquad 1.18$$

k_f is the maximum momentum of the bound electrons at the surface of the Fermi sphere, $\eta(\mathbf{r})$ is the ratio of the magnitude of the local momentum of the continuum electron k to k_f and I is the ionisation potential. As $r\rightarrow\infty$, the numerator of η should approach k and not $(k^2+2I)^{1/2}$ as is implied in equation 1.18. This has led to an alternate form of the HFEGE potential where I is removed from equation 1.18 and this is known as the asymptotically adjusted free electron gas exchange (AAFEGE) potential. However, this can result in values of V_{ex} which are too large, especially at low energies.

Another form of the exchange potential commonly used combines the HFEGE potential with the orthogonality technique developed by Burke and Chandra (1972). This method is based on the requirement in the exact static-exchange theory of electron scattering from a closed shell molecule that the radial scattering functions are necessarily orthogonal to the bound orbitals of the target molecule (Morrison and Collins, 1981). In general, it has been found that combining the orthogonalisation procedure with a local exchange potential produces the best results (Morrison, 1983).

c) Polarisation

The static and exchange potentials described above are attractive short range effects and dominate the scattering process when the incident electron is close to the molecule. When the electron is outside the molecular charge cloud, forces resulting from the polarisation of the molecule become important due to the long range nature of the induced dipole moment. For an exact treatment of polarisation, Castillejo *et al* (1960) have shown from a complicated analysis of the Schrödinger equation, that all possible electronic target states should be included as they give rise to terms in the scattering equations which represent the induced polarisation effects. This makes an exact treatment of polarisation, even for electron atom scattering impossible. This problem has been most often circumvented by making use of the fact that in the asymptotic region, the response of the molecule to the electric field of the incident electron can be accurately described using a potential of the form (Morrison, 1983)

$$V_{pol}(\mathbf{r}) \underset{r\to\infty}{\longrightarrow} -\alpha(\hat{\mathbf{r}})/2r^4 \qquad 1.19$$

where $\alpha(\hat{\mathbf{r}})$ is the polarisability of the molecule. However, when the electron is closer to the molecule (in or just outside the charge cloud) its velocity will increase due to the short range attractive Columbic forces. The molecular charge cloud is not able to respond quickly enough to the changing position of the electron and the induced polarisation becomes dependent on the velocity of the electron in addition to its position. Therefore, equations of the form of 1.19 cannot be used as they overestimate

the size of the potential in this region. A simple solution has been to propagate the asymptotic potential modified with a cut-off function $C(r,r_c)$,

$$V_{pol}(r,r_c) = C(r,r_c)(-\alpha(\hat{r})/2r^4) \qquad 1.20$$

into the inner region where $C(r,r_c)$ usually takes the form $1-\exp[(-r/r_c)^6]$ and r_c is an adjustable parameter which can be "tuned" to bring the calculated cross sections into agreement with an experimentally determined feature (e.g. a shape resonance). Alternatively, r_c may be chosen to be coincident with the approximate radius of the molecular charge cloud. However, whilst some promising results (Lane, 1980) have been obtained with this model, potentials of this form are still found to be too attractive near the molecule.

A parameter free polarisation potential has recently been developed for use with polyatomic molecules (Gianturco *et al*, 1987) which appears to be able to overcome the problems of the short range correlation between the motion of the scattered electron and the bound electrons in the molecule. In this method, the total electron density is derived using the free electron gas model and the correlation energy is given by an analytic function of the molecular charge density in the high and low density limits and interpolated in the intermediate regions. However, the resultant potential does not show the correct behaviour for large values of r and so is simply matched to a potential of the type shown in equation 1.19 where their values coincide near the boundary of the molecular charge cloud.

Finally, it should be noted that when both exchange and polarisation model potentials are incorporated in the theoretical treatment, the polarisation term may unwittingly compensate for exchange effects and *vice versa* leading to some degree of "coupling" between the two potentials. Therefore, if the polarisation potential was

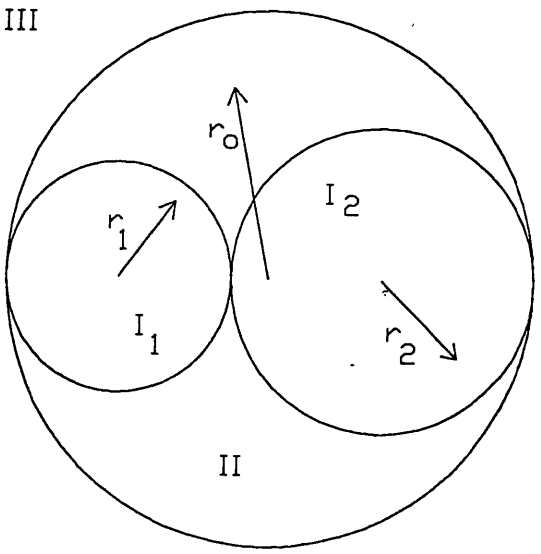

Figure 1.6 Partitioning of the molecular field for a heternuclear diatomic molecule used in the continuum multiple scattering method.

subsequently used with an exact static-exchange calculation, the results may prove unsatisfactory (Gianturco and Jain, 1986).

1.5 Computational Methods Used In Solving Scattering Equations

In the following sections, a brief outline will be given of three computational methods used to solve the electron-molecule scattering problem within the various approximations discussed in the previous sections. Only those methods relevant to the theoretical calculations compared with the results from the present work in chapters 5, 6 and 7 will be discussed.

1.5.1 The Continuum Multiple Scattering Method

The continuum multiple scattering (CMS) method is one of the simplest and most approximate methods which has been used to study electron scattering from a molecule. A detailed account of the CMS method can be found in the work of Dehmer and Dill (1979) and so only the important points will be outlined here. The essence of the CMS method lies in the division of the molecule into spherical regions as shown in figure 1.6. A sphere is constructed around each nucleus, the size of which is chosen to achieve the maximum packing density and reflect the atomic radii of each atom in

the molecule. A second sphere is then constructed, with its centre at the centre of mass of the molecule and its radius chosen such that it encloses all the individual atomic spheres. Thus the molecule is been divided into three regions:

region I, the volume enclosed by the atomic spheres,

region II, the interstitial volume between the atomic spheres,

region III, the volume outside the molecule.

The electron-molecule interaction potential is usually constructed such that in regions I and III it is spherically symmetric whilst in region II it has a constant value. The static potential is determined directly from self consistent field calculations of the ground state charge distribution of the molecule. A Hara exchange potential is commonly used to allow for exchange effects and polarisation is included by the addition of a potential of the form of equation 1.19 in region III.

1.5.2 Single Centre Expansion Methods

Single centre expansion methods involve expanding both the interaction potential and the scattered electron orbital in partial waves about the centre of mass of the molecule. When the incident electron is outside the charge cloud of the molecule, the electron-molecule scattering problem becomes similar that of the electron-atom problem and therefore similar methods can be employed. However, when the incident electron is near or within the molecular charge cloud the problem becomes multicentred in nature. To deal accurately with the singularities resulting from the attractive electron-nuclei interaction requires a large number of terms in the expansion. When the nuclear charge is large and not close to the expansion centre, the expansion may converge slowly. Several authors have used this method to obtain results for certain hydride molecules of the form XH_n. For example CH_4, Gianturco *et al* (1987); NH_3, Jain (1988); SiH_4, Jain (1987); H_2O see chapter 6.

1.5.3 The Schwinger Variational Method

The Schwinger variational method (SVM) is based on an adaptation of the L^2 methods used by quantum chemists to determine bound state molecular wavefunctions

(Takatsuka and McKoy, 1981 and 1984). In this approach the total wavefunction is expanded as

$$\Psi_T(\mathbf{r}',\mathbf{R}) = \sum_i c_i\phi(\mathbf{r}',\mathbf{R}) \qquad 1.21$$

where the incident electron is represented by a continuum orbital of the molecule. Both the bound state and continuum orbitals are expanded as a set of Gaussian like wavefunctions centred both on the nuclei and on the centre of mass of the molecule. The advantage of expanding the problem in terms of molecular orbitals is that full use can be made of the molecular structure codes, adapted to include the extra electron. The correct form of Ψ_T is normally determined using a variational approach in which a functional $I(\Psi_T)$ of the trial function Ψ_T is employed. One example is

$$I(\Psi_T) = \langle\Psi_T|H\text{-}E|\Psi_T\rangle \qquad 1.22$$

where the trial function usually satisfies the asymptotic boundary conditions. The functional has the properties that an exact solution of $I(\Psi_T)=0$ and for a small variation $\partial\Psi_T$ in the trial function, $\partial I=0$ (stationary solution). Using the Schwinger variational method has the advantage that the trial wavefunctions need not satisfy the asymptotic boundary conditions. The disadvantage in using the SVM are the large number of orbitals that are required in the expansion (equation 1.21). The SVM has been used to determine electron scattering cross sections from H_2 (Gibson *et al*, 1984), CH_4 (Lima *et al*, 1985) and H_2O (Brescansin *et al*, 1986).

1.6 Summary

In this chapter, a brief review of the various aspects of electron molecule scattering theory has been given, with particular emphasis payed to the methods which have been used to obtain results relevant to the present work. The complexity of the electron-molecule scattering problem means that so far, most of the theoretical effort has been concentrated on diatomic molecules and the smaller polyatomic molecules (e.g. CH_4, H_2O). In the future, it is expected that with the developments of such methods

such as the R–matrix technique and the availability of more powerful computers, that theoretical calculations for a wide range of polyatomic molecules will become available.

In the remainder of this thesis the experimental details and the results obtained in this work are given. In chapters two and three, experimental details of the electron spectrometer and the vacuum system used in this work are given. Chapter four contains details of the experimental procedures employed in measuring absolute cross sections and an analysis of the possible sources of errors. In chapters five, six and seven, the results of the measurements on SF_6, H_2O and N_2O in the form of differential, integral and momentum transfer cross sections are given and where possible compared with previously reported measurements. Finally, in chapter eight suggestions for future work are made. This includes proposals for further improvements to the apparatus and possible molecular targets for investigation.

CHAPTER 2

The Electron Spectrometer

2.1 Introduction

A typical electron spectrometer can be divided into two halves. The first half produces a beam of electrons with a small energy spread, typically 20-40meV, for use in collision experiments with a wide variety of targets e.g. a gas beam or surface. The second half of the spectrometer is used to measure the energy distribution of those electrons scattered or ejected from the target as a function of angle, usually with a resolution comparable to the energy spread of the incident electron beam. The availability of accurate data on the focusing properties of a large number of electron lens systems (Harting and Read, 1976), together with the development of several types of energy selectors, e.g. hemispherical monochromators and 127° cylindrical monochromators (Ballu, 1980), has enabled the construction of high resolution electron spectrometers capable of separating closely spaced (≈10meV) features, such as the rotational lines in molecular hydrogen (Wong and Schulz, 1974).

In this thesis, a conventional double hemispherical electrostatic spectrometer was employed and the following chapter describes the design criteria used in its construction and a description of the tests undertaken to determine its performance. The chapter begins with a brief guide to the terms and principles used in designing an electron optical system and is followed by a list of some common electron sources used in electron spectrometers. A description of the electron optics used in the present apparatus is then given, together with a discussion of their operational characteristics. In the second half of the chapter details are given of the monochromator which was used to produce an electron beam with a narrow energy spread and the analyser which was employed to measure the energy distribution of electrons scattered from a target. The equations used in calculating the performance of the monochromator and analyser

are given, the results of which are compared with those obtained from a number of experiments.

2.2 The Formation And Position Of An Image Formed By An Electron Beam

The focusing of an image formed by an electron beam is achieved by passing the beam from one region of constant potential to another. For example, if the electrons emitted from a source are passed between two regions at different potentials, the changing electrostatic field deflects the individual electrons in the beam and an image is formed of the original source. Figure 2.1 shows the path of a single electron moving through two cylinders held at potentials V_1 and V_2, respectively. The changing electrostatic field is illustrated by the equipotential contours traced in the adjacent ends of the two cylinders. There are several electrode arrangements which can provide the electrostatic fields necessary to focus a beam of electrons and the most widely used have been described by Harting and Read (1976). The two types of lenses employed in this work are shown in figure 2.2. Figure 2.2a shows a double element cylinder lens. The focusing properties of this lens are dependent on the voltage ratio V_2/V_1 and the ratio G/D where G is the gap between the two elements and D is the diameter of the lens. Figure 2.2b shows a triple element cylinder lens whose focusing properties depend on the two independent voltage ratios V_2/V_1 and V_3/V_1, in addition to G/D and A/D, where A is the distance separating the mid-points of the spaces between the two outer elements and the inner element.

Analogous to light optics, it is possible to predict the behaviour of the electron beam in the regions outside the focusing field of the lens if the positions of the cardinal points of an electrostatic lens are known. The cardinal points are shown in figure 2.3 and their positions are determined by the locations of the principal foci and the principal planes of the lens. The focusing field of an electrostatic lens extends for an appreciable distance on either side of the reference plane (defined as the plane through the geometric centre of the lens). Therefore the Newton thick lens equation,

$$(P-F_1)(Q-F_2)=f_1f_2 \qquad 2.1$$

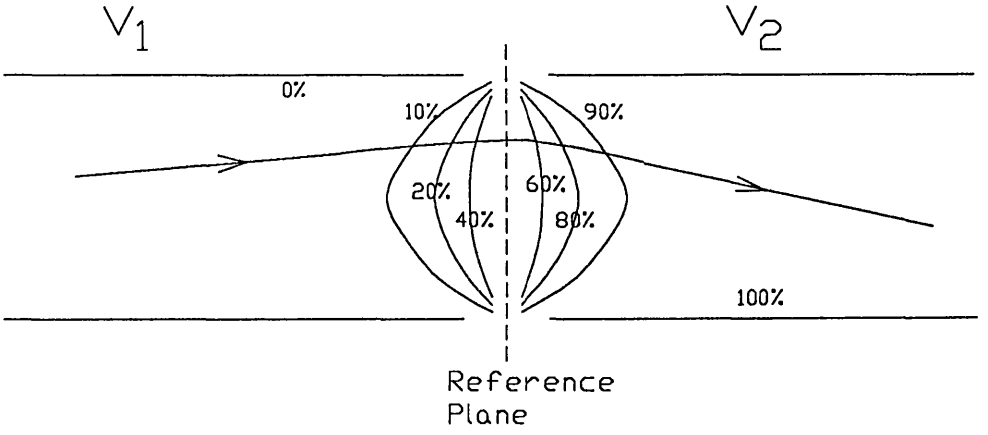

Figure 2.1 The electrostatic field distribution within a two element cylinder lens. The ray through the lens marks a typical trajectory of a single lens (Klemperer and Barnet, 1971).

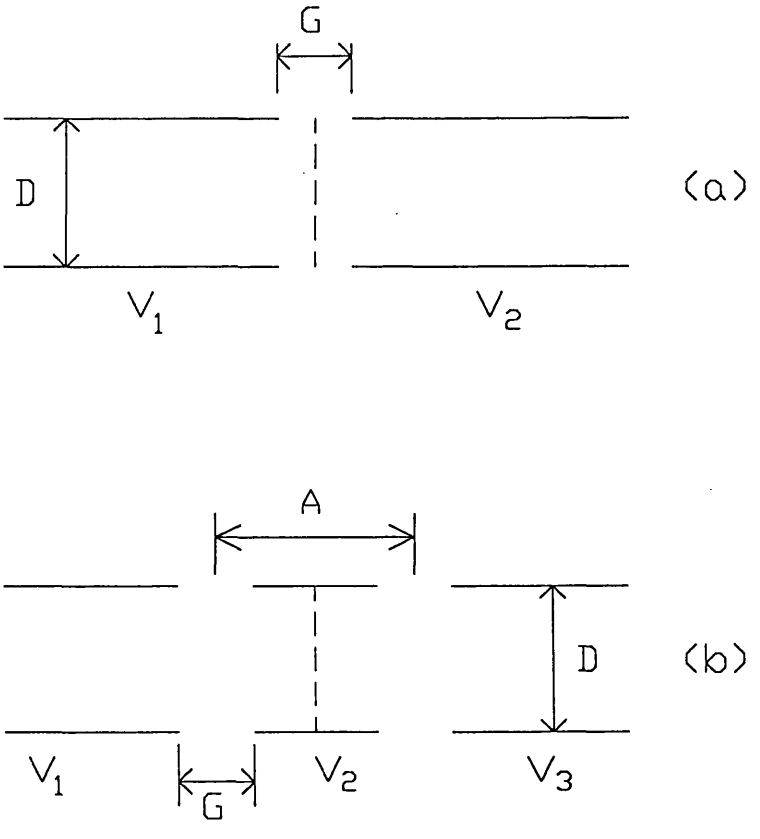

Figure 2.2a and 2.2b Two and three element cylinder lenses. The reference planes of each lens are shown as a dashed vertical line (Harting and Read, 1976).

is used to describe the relationship between the object and image distances (P and Q), where f_1 and f_2 are the focal lengths and F_1 and F_2 are the mid focal lengths shown in figure 2.3. The magnification of an image is defined as

$$M = -f_1/(P-F_1) = -(Q-F_2)/f_2 \qquad 2.2$$

For the cylindrical lenses used in this work, it is conventional to measure all lengths in terms of the lens diameter D and the values of P and Q are defined as the distances from the object or image position to the reference plane. The values of f_1, f_2, F_1 and F_2 have been calculated for the lenses shown in figure 2.2 by Harting and Read (1976) for a large range of voltage ratios and several values of G/D and A/D, thus simplifying the calculation of P, Q and M.

An important relationship which must hold if correct point to point imaging between conjugate planes is to occur is the Helmholtz-Lagrange law. It is usually expressed in the form

$$r_1 (V_1)^{1/2} \sin\theta_1 = r_2 (V_2)^{1/2} \sin\theta_2 \qquad 2.3$$

where r_1 and r_2 are the distances from the axis of the corresponding object and the image points respectively (see figure 2.4), θ_1 and θ_2 are the half angles of the bundles of rays at the object and image points respectively and V_1 and V_2 are the regions of constant potential in which the object and image are situated. An important consequence of this law is that as the size of an image is reduced the angular divergence of the rays at the image point increases.

2.3 Aberrations

Equation 2.1 and 2.2 only apply to paraxial electron trajectories, i.e. those trajectories which are close to the central axis. In practice, the object and image sizes in most electron optical systems are generally so large that paraxial electrons constitute only a small part of the observed image. This results in an image size that is different from that calculated using equations 2.1 and 2.2 and such a discrepancy is termed the

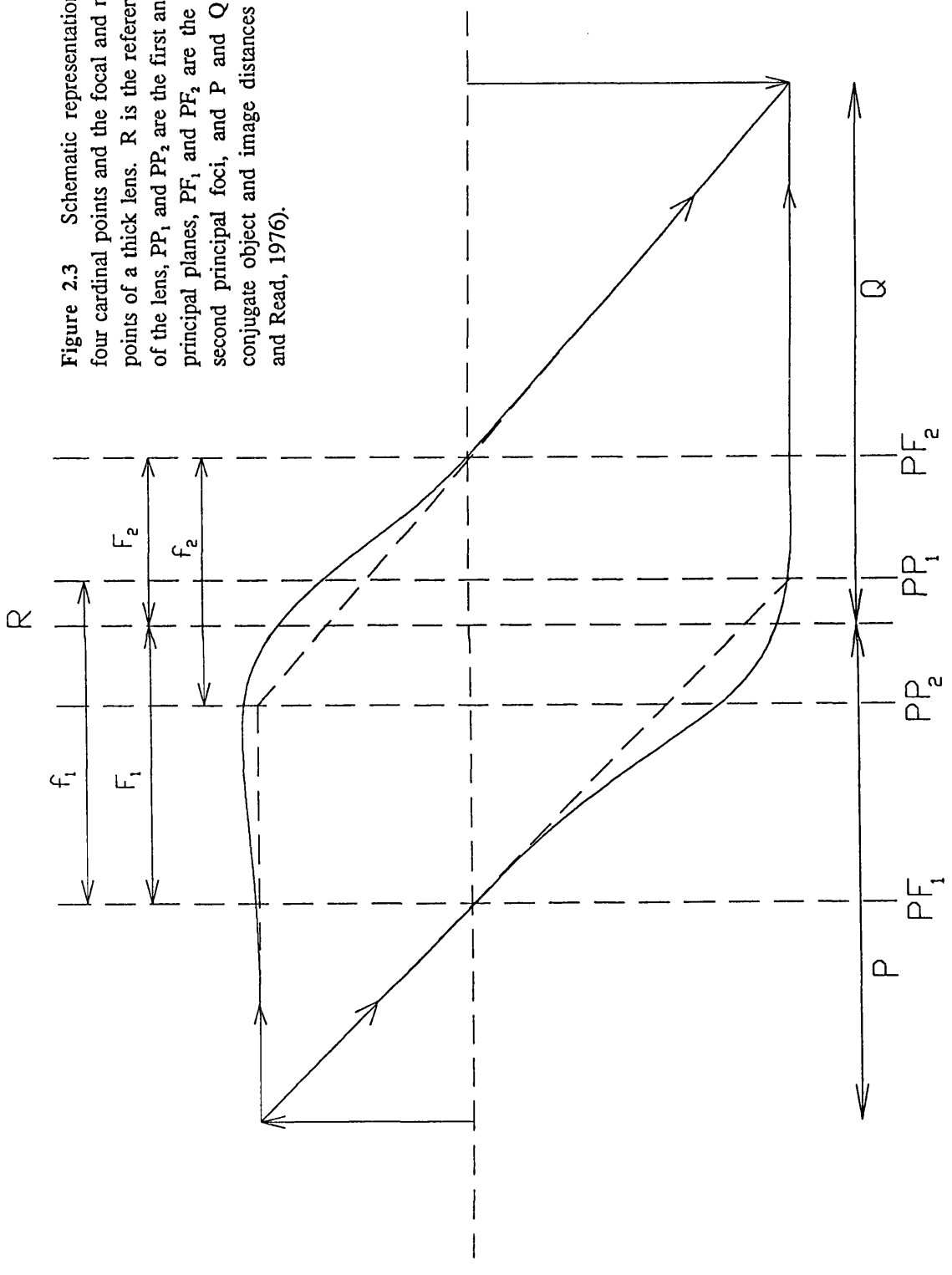

Figure 2.3 Schematic representation of the four cardinal points and the focal and mid-focal points of a thick lens. R is the reference plane of the lens, PP_1 and PP_2 are the first and second principal planes, PF_1 and PF_2 are the first and second principal foci, and P and Q are the conjugate object and image distances (Harting and Read, 1976).

aberration of the image. In any electron optical system, it is particularly important to calculate the magnitude of this effect as all electron lenses are extremely susceptible to large aberrations (Brunt and Read, 1975) which can result in increased image sizes of over 100%. The total aberration of an image is made up from the sum of several aberrations which fall into one of two categories: those due to geometric lens errors and those due to the properties of a charged particle beam.

2.3.1 Aberrations Due To Geometric Lens Errors

There are five geometric lens errors which affect the final aberration of an image; spherical aberration, coma, astigmatism, curvature of field and distortion. The last four lens errors are a result of the finite size of the image and are harder to quantify. Brunt and Read (1975) have shown that the contributions from these four aberrations is at most 30% of the spherical aberration. The effect of spherical aberration is illustrated for a point source in figure 2.5. Spherical aberrations arise due to paraxial and non-paraxial electrons from the same object point being focused at different positions on the central axis of the lens system. The increase in the radius of the image Δr due to spherical aberration, can be calculated using (Klemperer and Barnet, 1971)

$$\Delta r = M\, C_s\, \alpha^3 \qquad 2.4$$

where M is the linear magnification defined by equation 2.2, α is the maximum half angle of the electrons leaving the object and C_s is the spherical aberration coefficient which is a function of both the object and image distances.

A useful indication to the size of the aberrations at an image can be gained by calculating a quantity known as the filling factor, η. The value η, is calculated by extrapolating the trajectories of the incident electrons to the reference plane of the lens and taking the ratio of the maximum distance of the extrapolated rays from the central axis to the radius of the lens. In general, for values of η less than 50%, the magnitude of the aberrations (Δr) will be less than 3% of the lens diameter. If the filling factor of a lens rises above 50%, the magnitude of the aberrations and hence the total size of

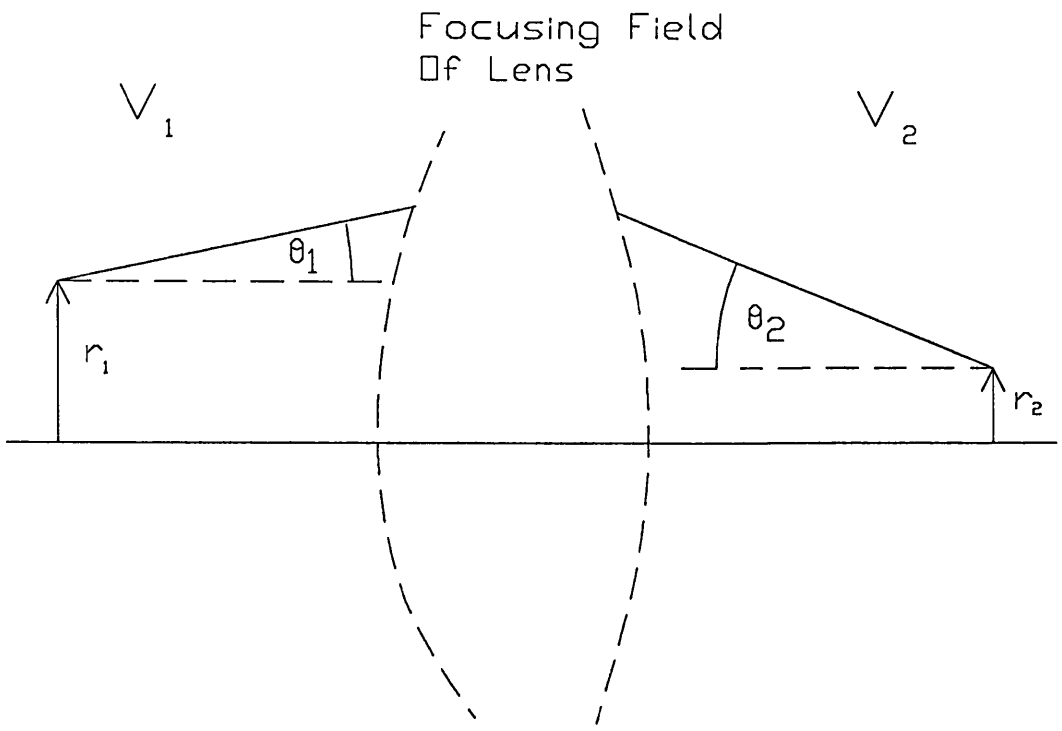

Figure 2.4 Illustration of the Helmholtz-Lagrange law.

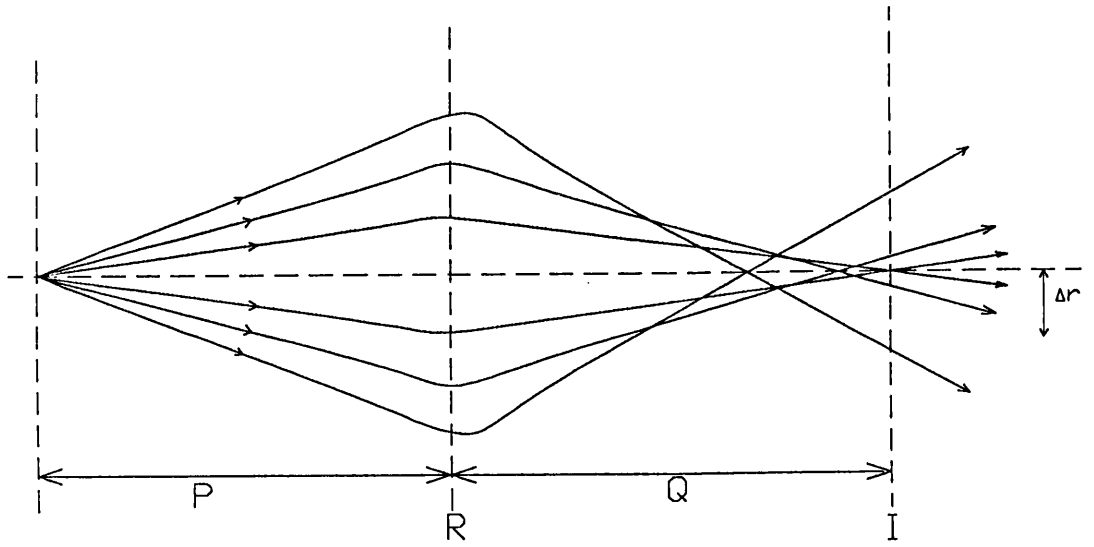

Figure 2.5 Schematic representation of the spherical aberration at an image of a point axial object O. R is the reference plane and I is the Gaussian image plane (Harting and Read, 1976).

the image, begins to rise rapidly and therefore the value of η should be kept below 50% wherever possible.

Finally from figure 2.5, it can be seen that the diameter of the beam forming the image is smallest not at the image plane, but at a point between the image and reference planes. The minimum diameter of the beam corresponds to the best possible focus and is called the "disc of least confusion". Thus, if circumstances permit, the lens should always be weakened slightly by reducing the ratio V_2/V_1 to achieve the minimum beam size in the desired position.

2.3.2 Aberrations Due To Properties Of The Electron Beam

In addition to the geometric lens errors discussed above, there are two other sources of aberration that can affect the size of the image. These are chromatic aberration and aberrations due to space charge. The magnitude of the chromatic aberration is dependent on the energy spread of the electron beam. Electrons are produced from a source (usually a heated filament) with a range of energies and thus when the electron beam is focused by the lens, the focal length of the lens is shorter for lower energy electrons than for those with higher energies. The resultant effect is similar to that caused by the spherical aberration (see figure 2.5). The lateral chromatic aberration is given by (Klemperer and Barnet, 1971)

$$\Delta r_{cr} = C_{cr}\alpha\,(\Delta E/E) \qquad 2.5$$

where C_{cr} is the chromatic aberration constant, ΔE is the energy spread of the electrons in the beam, E is the energy of the beam and α is the half angle of the angular divergence.

All aberrations discussed so far can all be found in conventional light optics. However, there is an additional aberration, the cause of which is unique to a charged particle beam. This effect, commonly referred to as space charge is due to the repulsive Coulomb forces between the particles in the beam and affect the electron beam in two ways. First, it sets a lower limit on the size of the beam for a given electron beam current. For example, consider an electron beam in a region of constant

potential V of initial radius r_1 and current I which is initially converging towards a point on the central axis. As the current density increases, the repulsive Coulomb forces will act to reduce the convergence and will ultimately be strong enough to cause the beam to diverge. Read *et al* (1974) have found that a useful approximation to the maximum current that can be focused through an image of radius r_2 over the range r_2/r_1=0.0035 to 0.27 is given by the expression

$$I_{max} \approx 38.5\text{x}10^{-6} \ln(r_1/2r_2)\ V^{3/2}\ (r_1/z)^2 \qquad 2.6$$

where Z is the distance between r_1 and r_2. An alternative approximation which can be used over the range r_2/r_1=0.01 to 1.0 is

$$I_{max} \approx 38.5\text{x}10^{-6}\ (0.3+3.7r_2/r_1)\ V^{3/2}\ (r_1/z)^2 \qquad 2.7$$

Both expressions are accurate to ±20% and all quantities are measured in S.I. units.

The repulsive forces within the beam can also result in an alteration of the energy distribution of the electrons in the beam. This effect was first seen by Boersch (1954) and is commonly known as the "Boersch effect". A number of theories have been proposed to quantify this effect and Jansen *et al* (1984) have compared these with their results from experiment and a Monte Carlo simulation. They found that for an electron beam focused to form an image of radius r with a half angle α_o, the best agreement between the Monte Carlo simulation and the experiment was obtained using the following expression (van Leeuwen and Jansen, 1983)

$$\Delta E = (m/8\varepsilon_o^2)^{1/4}\ (I/V^{3/2})^{1/2}\ F(r_o) \qquad 2.8$$

where $F(r_o)$ is given by

$$F(r_o) = (8/r_o\pi) \int_o^1 (1-t^2)/t\ \sinh^{-1}(r_o t/2)\ dt \qquad 2.9$$

and

$$r_o = (8\pi\varepsilon_o/e)\ \alpha_o^2\ V\ r \qquad 2.10$$

From equations 2.8, 2.9 and 2.10 it can be seen that ΔE will be largest when I is large and V, r and α_o are small. In an electron spectrometer, this condition is most likely to occur in the electron gun where the energy spread of the beam can be increased by up to 5%.

2.4 The Beam Angle And Pencil Angle

In order to minimise the filling factor of a lens, the angular divergence of the electron beam must be kept small. This can be achieved by placing two apertures in the path of the electron beam before the lens and these are known as the window and pupil. The pupil limits the size of an object which can be imaged by a lens while the window defines the magnitude of the beam angle. The beam angle, α_b, is a purely geometric quantity set by the size of the window and the pupil-window separation (see figure 2.6). It is possible to arrange for the beam angle to be zero by placing the window at the focal plane of a lens. This will result in the image of the window being projected to infinity and the beam angle, set by the pupil and window image positions, will then be zero.

There also exists another term which contributes to the angular divergence of an electron beam and this is commonly known as the pencil angle, α_p. The existence of the pencil angle is a consequence of the emission process at the electron source and is illustrated in figure 2.7. At a heated hairpin filament, electrons are emitted from the tip at all angles between 0° and 90° with respect to a normal at the surface. In figure 2.7, the ray marked (1) represents electrons emitted normally from the surface, while rays (2) and (3) represent the extreme case of electrons emitted tangentially from the surface. The anode is held at a positive voltage with respect to the filament such that the field between the anode and the filament tends to converge electrons following paths (2) and (3) towards the normal; the angle made by these rays make with ray (1) is the pencil angle α_p. The magnitude of the pencil angle is a function of the temperature, the material of the filament and the accelerating voltage between the anode the filament.

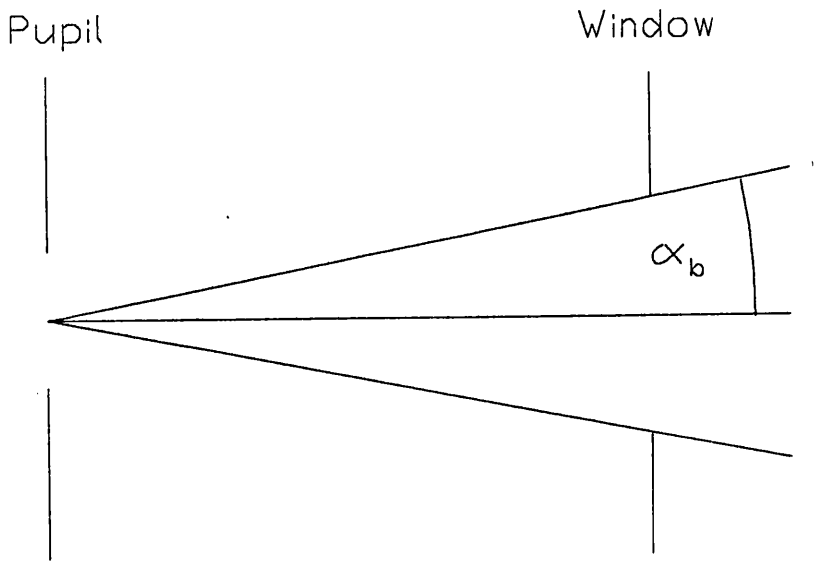

Figure 2.6 Illustration of the beam angle.

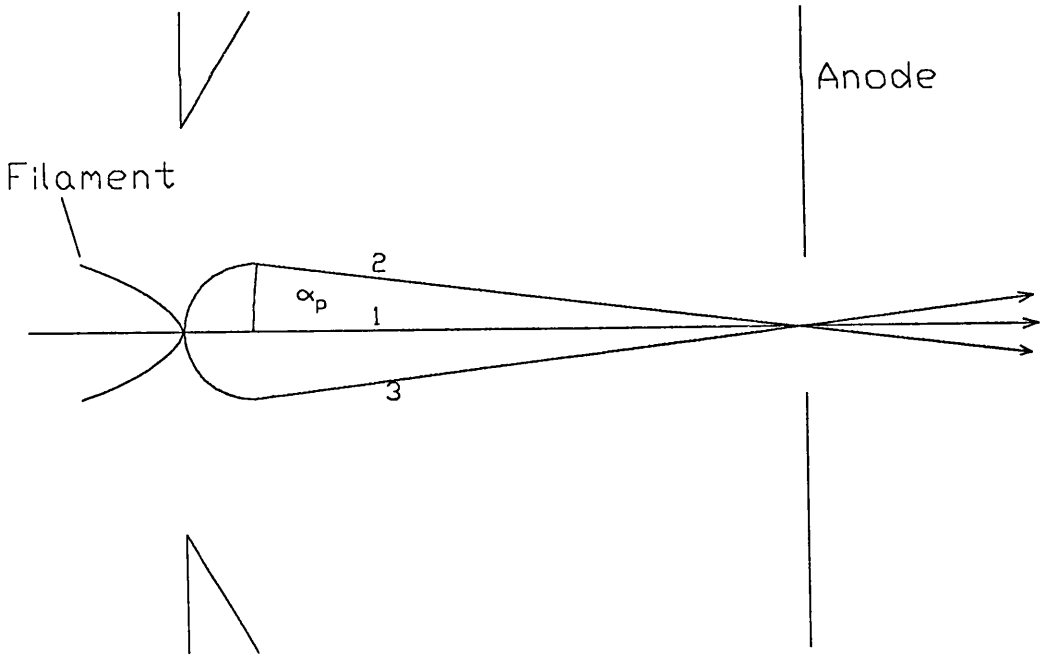

Figure 2.7 Pencil angle formation in the emission system.

The value of α_p (in radians) may be calculated using the equation (Kuyatt and Simpson, 1967)

$$\alpha_p = (eV_k/eV_a+eV_k)^{1/2} \qquad 2.11$$

where eV_k is the energy at which the greatest number of electrons are emitted from the filament and V_a is the anode voltage.

Unlike the beam angle, the pencil angle can never be zero and its subsequent value in an electron optical system is calculated using the Helmholtz-Lagrange equation (equation 2.3). The pencil angle at an image will depend on the initial value at the filament and the subsequent focusing properties of the electron lens. For small angles ($\sin\theta \approx \theta$) the magnification of the pencil angle M_p can be expressed as

$$M_p = (1/M)\ (V_1/V_2)^{1/2} \qquad 2.12$$

where M is the linear magnification.

2.5 The Emission System

The first half of any electron spectrometer is used to produce a beam of electrons of small energy spread (10-40meV) but with the highest possible current. The extent to which the spectrometer is able to simultaneously meet these two requirements is determined in part by the choice of the electron source and the emission system configuration. Electron sources generally fall into two categories: heated filament sources and photo-ionisation or photo-emission sources. A brief summary of these sources is given below, followed by a description of the emission system configuration adopted in the electron spectrometer used in this work.

2.5.1 Electron Sources

Three types of heated filaments are commonly used:

1) Pure metal filaments. Tungsten is the most commonly utilised material for directly heated pure metal filaments and is used because of its durability and long lifetime (1000s of hours). However, due its relatively high electron work function

(≈4.5eV), tungsten filaments have to be heated to temperatures in excess of 2900K. The electrons emitted from the filament possess a Maxwell-Boltzmann distribution of energies and for a temperature of 3000K, this distribution has a full width half maximum (FWHM) greater than 0.5eV.

2) Doped metal filaments. Thoriated tungsten (Th-W) filaments are the most widely used doped metal filament. These are made from tungsten wire containing a small amount of thorium oxide (2%). The filament is activated by flashing it at 2800K to drive the thorium oxide (ThO) to the surface and then held at 2200K for between one and two minutes in order to reduce the ThO to metallic thorium. The work function of this type of filament is ≈2.6eV, allowing it to be run at lower temperatures (1950K) than a pure tungsten filament. This results in a energy spread of ≈0.3eV, whilst achieving similar electron emission densities.

3) Metal oxide coated filaments. A metal oxide coated filament is manufactured by coating a metal base (usually nickel), with a solution containing equal quantities of barium and strontium carbonate plus a small amount of calcium carbonate. When the filament is heated the carbonates are reduced to oxides and the work function of the resultant surface is ≈1eV. Thus the filament can be operated at a temperature of ≈1100K and the energy spread of the emitted electrons is of the order of 0.1eV. Unfortunately the oxide surface is not very robust. It is easily poisoned and has a short life time due to evaporation and damage by positive ion bombardment.

Two other electron sources have utilised photo-ionisation of a gas or a photo-emission from a surface. The former method has been employed by Field *et al* (1988) who used a synchrotron source to photo-ionise Ar atoms, producing an electron beam with a energy spread as low as 3meV (FWHM) and a beam current of $1x10^{-12}$A. Kennerly *et al* (1981) achieved similar resolutions and currents by using a He–Cd ultraviolet laser to photo-ionise a beam of metastable barium atoms. However, it should be noted that the electron beam currents obtained in these experiments is at least six orders of magnitude less than that obtained using a heated filament source. In the last ten years, photo-emission sources using laser radiation have also been developed. Light from a GaAlAs laser is used to illuminate a GaAs surface activated with caesium and oxygen. These sources were originally developed as sources of polarised electrons

(Pierce *et al*, 1980) but it was found that high current electron beams with low energy spreads could be obtained. Recently, Zhou *et al* (1989) have reported energy spreads of the order of 40meV with emission currents of $1x10^{-4}$A. The disadvantage of using such a source is that the GaAs surface must be kept in a vacuum of at least 10^{-10} torr to avoid contamination of the surface and that the emission current and energy spread of the emitted electrons does not remain constant over a period of hours (Guo *et al*, 1990). Except in circumstances where the polarisation of the electron beam is important or very low energy spreads are required, it is impractical to use photo-emission or photo-ionisation electron sources.

The electron source used in this work was a directly heated filament. As it was intended to investigate electron scattering from a wide range of atoms and molecules, the use of oxide filaments was ruled out due to problems of poisoning. Of the two remaining materials available, a thoriated-tungsten filament was chosen due to its ability to produce electrons with a smaller energy spread.

2.5.2 The Emission System Configuration

To achieve the maximum available current density from a filament (cathode) surface, it is important to choose the correct anode-cathode configuration. If the extraction field at the emitting surface varies considerably, then the maximum emission density obtainable from any point on the surface is dependent on the field at that point and therefore the average emission density from the surface may be substantially below the maximum. Pierce (1940) found that if the filament was placed at the centre of an aperture in an electrode whose surface was at an angle of 67.5° to the central axis, there would be a homogeneous field at the cathode surface.

The emission system used in this work is based on the Pierce design and is shown in figure 2.8. A hairpin filament was used and the tip was located just behind the centre of the aperture (2mm diameter) in the grid electrode. The filament to anode separation, d, was 6mm and the anode aperture was 0.33±0.05mm in diameter. A hairpin filament was used as it has been reported that the pupil position could be taken to be at the tip of the filament itself, or from a point immediately in front of it (Klemperer and Klinger, 1951; Bernius *et al*, 1988). Haine and Einstein (1952) have

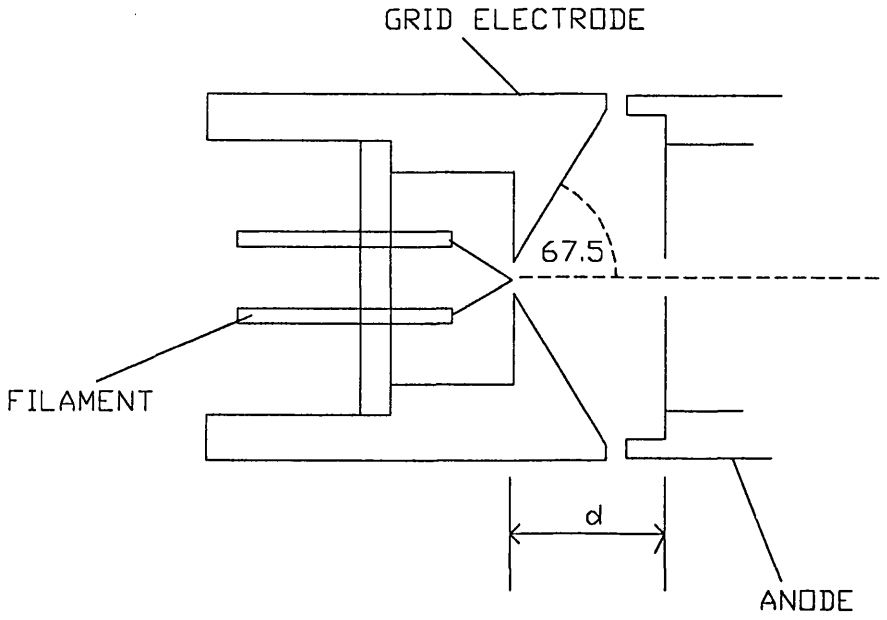

Figure 2.8 The emission system configuration.

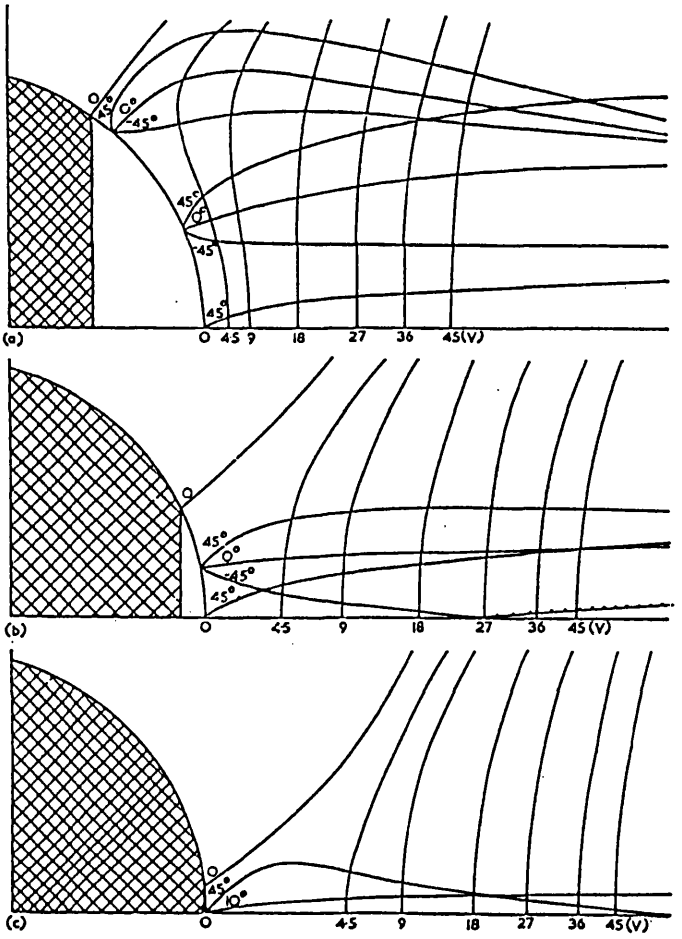

Figure 2.9 The potential field and electron trajectory plots near the tip of the hairpin filament. As the value of V_g is made progressively more negative, figures 2.9a, 2.9b and 2.9c show how the size of the emitting area of the filament is reduced (Haine and Einstein, 1952).

found that the size of the emitting area is dependent on the potential, V_g, applied to the grid electrode. They found that as the value of V_g was made progressively more negative (with respect to the filament), the position of the zero equipotential moved towards the tip of the filament cutting it in a ring (see figure 2.9). Behind this ring (the cross hatched area shown in figure 2.9), the surface field was found to be negative and no emission was possible from the filament in this region. As the value of V_g was increased further, the zero equipotential moved in front of the hairpin tip such that the whole filament was in a region of negative potential thus suppressing the electron emission. They also found that the intensity distribution across the resultant beam only became Gaussian for values of V_g slightly less than that required to totally suppress emission.

In the emission system shown in figure 2.8, the location of the window was taken as the anode aperture and the beam angle, α_b, was calculated to be 2.05°. The pencil angle, calculated using equation 2.11, was found to range from 2.88° for V_a=162V to 4.97° for V_a=54V. These values of V_a were the maximum and minimum potentials applied to the anode during the course of this work.

2.6 The Electron Optics

In the electron spectrometer used in this work, eight electrostatic lens systems were employed and these are shown in the schematic diagram of the spectrometer (figure 2.10). Lenses 1 and 2 make up the electron gun and these were designed to focus electrons emitted from the filament to the entrance of a hemispherical monochromator. Those electrons reaching the exit of the monochromator were then focused by lenses 3 and 4 (pre-interaction region optics) to the centre of an interaction region where they could intersect a gas beam produced from a capillary tube. Electrons which were scattered through an angle θ were focused to the entrance of a hemispherical analyser by lenses 5, 6 and 7 (post-interaction region optics). Finally, the electrons reaching the exit of the analyser were focused into a channel electron multiplier for detection. In the following sections, the design and operational characteristics of the lens systems will be described. Lens R in the reference detector

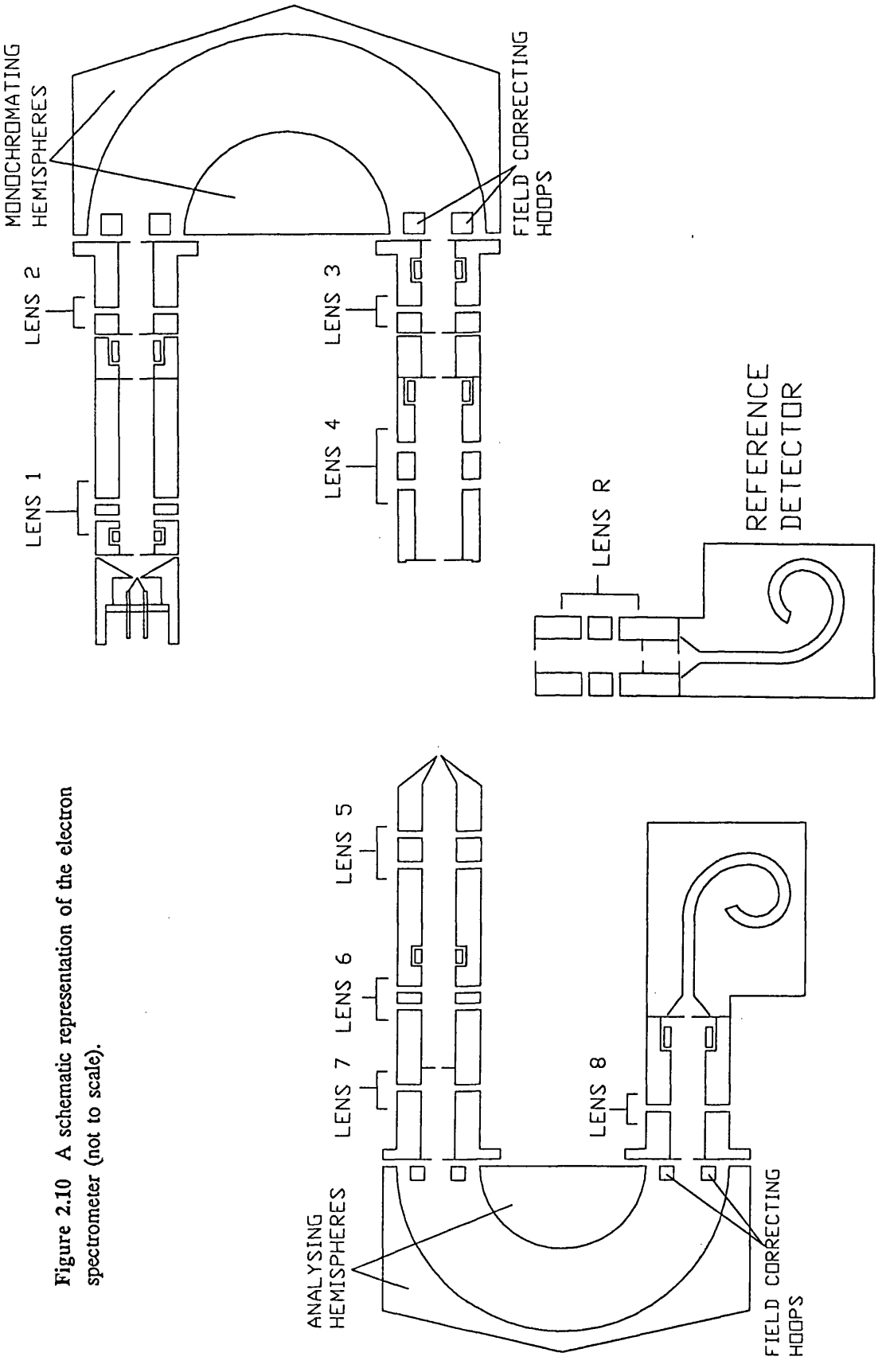

Figure 2.10 A schematic representation of the electron spectrometer (not to scale).

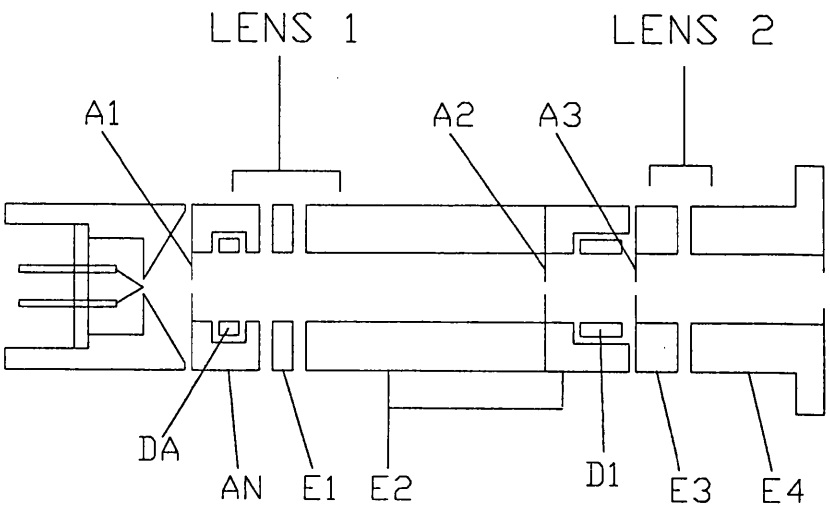

Figure 2.11 A schematic representation of lenses 1 and 2 in the electron gun (not to scale).

was used to discriminate between electrons of different energies rather than as an imaging device and so will be discussed later with the monochromator and analyser.

2.6.1 The Electron Gun (Lenses 1 and 2)

The purpose of the electron gun was to focus electrons emitted from the filament to the entrance of the monochromator. The operational characteristics of the monochromator (see section 2.7.1) dictated that the electron beam size, energy and the angular divergence should all be small at the monochromator entrance. There are many examples in the literature of such electron guns, for example, Chutjian (1979) and Mason and Newell (1986). However, these require three lenses to produce the desired image size and angular divergence. In the present experiment, space limitations allowed only two lenses to be used. The lens system adopted is shown in figure 2.11 and consisted of two decelerating cylinder lenses with an internal diameter, D, of 6mm. Lens 1 was a three element lens (AN, E1 and E2) with A/D=0.5 and A/G=0.1 and a fixed voltage ratio between the outer elements (AN:E2) of 3:1. Lens 2 was a two element lens with A/G=0.1 and a fixed voltage ratio between E3 and E4 of 9:1. Elements E2 and E3 were held at the same potential but were physically separated to allow the electron beam current to be measured individually on the apertures A2 and A3. Two sets of deflectors DA and D1 (each set consisting of four plates) were also

included to correct for any slight mechanical misalignment between the lens elements and any deviation of the electron beam caused by external fields. All the apertures were positioned at least 6mm (one lens diameter) from the reference plane of any lens to avoid distortion of the focusing field (Barton and Allison, 1988). A 2mm splatter aperture was placed at the end of the last element in the gun (E4) to prevent electrons with a large axial displacement from entering the monochromator.

The energy spread of the beam at the exit of the monochromator was dependent on the energy of the beam at its entrance (see section 2.7.1), which in turn was determined by the potential applied to E4. Once the desired energy spread had been decided, the potential applied to E4 was chosen accordingly and the voltages applied to AN and E2(=E3) were calculated from the voltage ratios given above. For example, for a beam energy at the monochromator entrance of 3eV (E4=3V), the voltages applied to the anode and the elements E2 and E3 were 81V and 27V, respectively. The voltage applied to E1 could then be adjusted to give the optimum current transmission through A2 and A3. It was originally intended that the image of the anode aperture would be focused at A2 by lens 1 and that lens 2 would then focus the image of A2 at the entrance plane of selector. Using the data of Harting and Read (1976) and equation 2.1, the voltage ratio between E1 and E2 required to focus the image of A1 at A2 was calculated to be 9:1. To optimise the voltage settings in the gun, the electron beam current striking the outer hemisphere of the monochromator was measured (without the deflecting fields present in the monochromator) and the voltage applied to E1 and the deflector plates adjusted. It was found that to achieve the maximum current on the outer hemisphere, the voltage ratio between the elements E1 and E2 was nearer 7:1 as opposed to the calculated ratio of 9:1. A recalculation of the image positions of lens 1 for this voltage ratio indicated that the image of the hairpin tip was now coincident with A2 and that the image of A1 was now placed beyond A3. This not only confirmed that the hairpin tip could be taken as the initial pupil position of the emission system, but indicated that its initial dimensions were smaller than that of the anode aperture. The narrowest part of the electron beam (highest current density) coincided with the image of the pupil and thus gave the highest current transmission through the apertures A2 and A3.

With the aid of the electrostatic lens data of Harting Read (1976), the electron focal properties of the lenses 1 and 2 were calculated for a final electron beam energy at the monochromator entrance of 3eV. Using equation 2.2, the magnification of the image of the hairpin tip at A2 was calculated to be 2.07 and using equation 2.13 the pencil angle was found to be 4.07°. The filling factor of lens 1 was calculated to be 95% which resulted in large aberrations and increased the image size at A2 from 0.24mm to 1.3mm (determined using equation 2.4). Lens 2 was calculated to have a filling factor of 65% and the final image size including abberations was calculated to be 1.22mm. The aperture A3 was placed at the focal plane of lens 2 which ensured that the angular divergence (beam angle) in the electron beam at the entrance would be zero. Thus the only contribution to the angular divergence was from the pencil angle which was 5.5°.

The magnitude of the current measured on the outer hemisphere was dependent on the beam energy set by E4. As the voltage on E4 was increased, so in turn was the voltage on the anode (AN:E4=27:1), resulting in a greater current drawn from the emission system. The value of the current reaching the outer hemisphere was found to range from 1.3×10^{-7}A to 4.2×10^{-7}A for beam energies between 2eV and 6eV. Using equation 2.7, these values were found to be at most 50% of the current where the effects of space charge spreading would have been important.

To verify these calculations on the beam size at the image plane of lens 2, a Faraday cup was placed at the end of the gun such that its entrance aperture was coincident with the image plane of lens 2. By measuring the current on the entrance aperture and that passing through to the cup, the size of the image could be estimated and was found to be between 1.14mm and 1.25mm thus confirming the calculations above.

Finally, it was noted that the magnitude of the beam current was dependent on the potential applied to the grid electrode (V_g). As in the work of Haine and Einstein (1952), it was found that a negative potential applied to the grid electrode gave the highest current, but the magnitude of V_g was found to be dependent on the anode voltage and the gas present in the system.

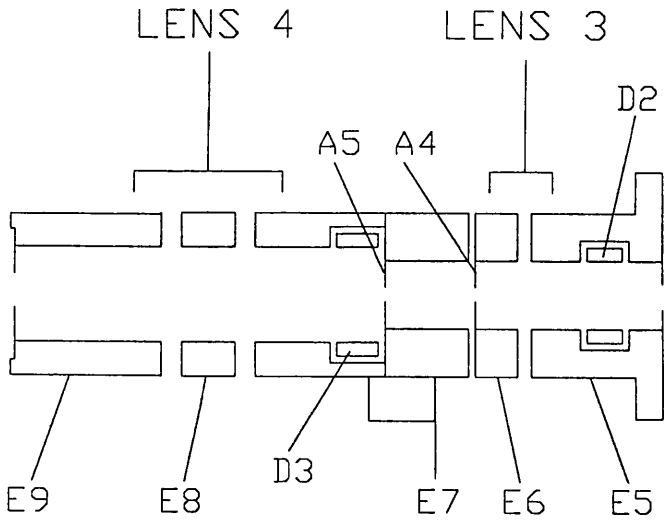

Figure 2.12 A schematic representation of lenses 3 and 4 (not to scale).

2.6.2 Pre-interaction Region Optics (Lenses 3 and 4)

On passing through the monochromator, the electron beam was dispersed across the monochromator exit plane. Lenses 3 and 4, shown in figure 2.12, were designed to focus electrons arriving at the centre of the exit plane to the centre of the interaction region where they could intersect a gas beam. Lens 3, which was identical to lens 2 in the electron gun, focused a central area of the monochromator exit plane, 0.92mm in diameter, through a 0.5mm aperture, A5. The image of A3, which was projected to infinity by lens 2, was brought to a focus at the aperture A4 (0.5mm in diameter) placed at the focal plane of lens 3. A set of deflectors, D2, were placed between the monochromator exit plane and A4. These were used to correct for any misalignment in the beam caused by stray magnetic fields or small errors in the positioning of the monochromator with respect to lenses 2 and 3.

Lens 4 was a three element cylinder lens (A/D=1, G/D=0.1 and D=8mm) designed to focus the image of A4 to the centre of the interaction region. The voltage ratios between elements E7 and E9 and elements E8 and E9 were variable to allow the electron beam energy to have a wide range of values at the interaction region while maintaining a constant beam size (0.75). The ratio E7:E9 varied between 1:0.1 to 1:5.5 and the ratio E8:E9 between 1:0.7 to 1:7.5. The position of the aperture A5, was chosen such that it was close to the focal plane of lens 4 for a large range of

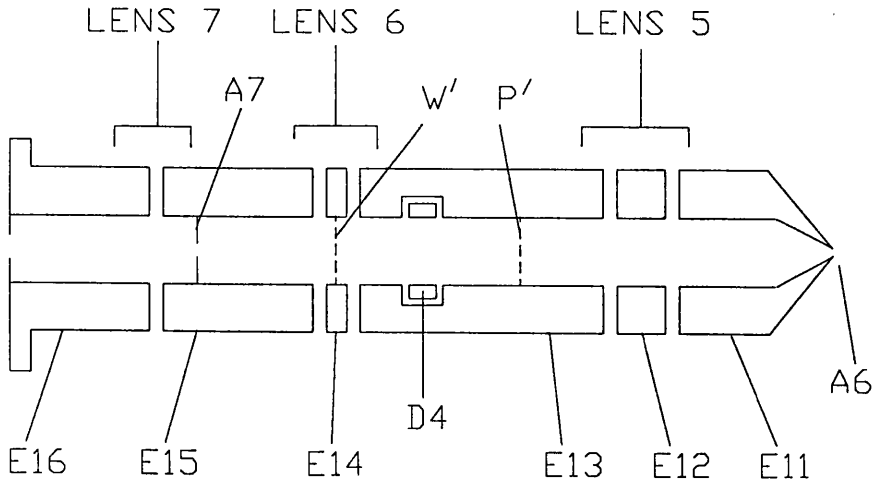

Figure 2.13 A schematic representation of lenses 5, 6 and 7 (not to scale).

values of E7:E9, thereby ensuring that its image distance would be large compared to the image distance of A4. This reduced the contribution of the beam angle to the angular spread of the beam as it crossed the interaction region. A set of deflectors D3, was placed immediately after A5 and were used to guide the electron beam through the centre of the gas beam.

2.6.3 Post-interaction Region Optics (Lenses 5, 6 and 7)

Lenses 5, 6 and 7, shown in figure 2.13, were designed to focus electrons scattered from the gas beam at the centre of the interaction region into a hemispherical analyser where their energy distribution could be determined. The source of electrons for the post-interaction region optics was defined as the overlap of the electron and gas beams in the interaction region with aperture A6, in element E11 acting as the initial window. Lens 5 was a three element cylinder lens (A/D=1 and G/D=0.1) and focused the image of the electron/gas beam overlap (an area with an approximate diameter of 1mm), to a position between the reference planes of lenses 5 and 6 marked as P′ on figure 2.13. The image of A6 was focused onto the reference plane of lens 6 marked as W′ in figure 2.13. Lens 6 was a three element cylinder lens (A/D=0.5 and G/D=0.1) and was operated as an einzel lens, i.e with the outer most elements maintained at the same potential. In general, the principal planes of such an einzel lens lie very close

together near its reference plane. Any object which is coincident with the first principal plane is focused with unit magnification onto the second principal plane. Hence, lens 6 had no effect on the image W′ placed at its centre. The pupil image P′ was focused by lens 6 onto a 0.7mm aperture A7 placed in lens element E15.

The final lens, lens 7, was a two element decelerating cylinder lens (G/D=0.1) operated at a fixed voltage ratio of 10:1. It focused the image W′ at the reference plane of lens 6 onto the entrance plane of the analyser with a diameter between 0.8 and 1.0mm (depending on the energy of the electrons leaving the interaction region). The aperture A7 was placed at the focal plane of lens 7 ensuring that the beam angle at the analyser entrance was zero. A set of deflectors D4, were used to guide the electron beam through A7. A 2mm splatter aperture was placed at the end of element E16 and prevented electrons with a large axial displacement from entering the analyser. The internal diameter, D, of lenses 5, 6 and 7 was 6mm.

2.6.4 The Operating Conditions Of Lenses 3 To 7

The correct focusing of lenses 3 to 7 was achieved by positioning the first half of the spectrometer in the zero scattering angle position and collecting the electron beam in the second half of the spectrometer. Lenses 5, 6 and 7 were then used to transport the beam to the analyser where it could be collected on the outer hemisphere. The potentials applied to the elements in lenses 3 to 7 were in part determined by the energy of the beam at the interaction region and the beam energy required at the entrance and exit of the analyser and the monochromator. For example, if the incident beam energy was 10eV and the monochromating and analysing energies chosen to be 3eV and 2eV, respectively, the resulting potentials applied to elements in lenses 3 to 7 were E5=3V, E6=E7=27V, E9=10V, E11=10V, E13=E15=20V and E16=2V. The voltages applied to the remaining elements E8, E12 and E14 were then initially set according to the voltage ratios calculated from the data of Harting and Read (1976). These voltages were then adjusted to maximise the current measured on the outer hemisphere of the analyser. It was found that the maximum current was registered when the voltages applied to E8, E12 and E14 were close (within 5%) of their calculated values.

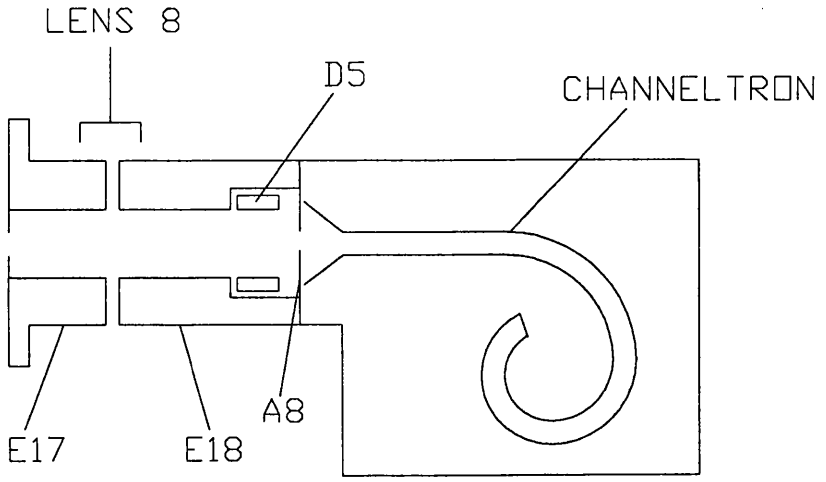

Figure 2.14 A schematic representation of lens 8 and channeltron (not to scale).

2.6.5 Lens 8

The final lens in the spectrometer (lens 8 shown in figure 2.14) focused those electrons arriving at the exit of the analyser through an aperture, A8, where they could be detected by a channeltron (Mullard X919BL). Lens 8 was a two element cylinder lens (G/D=0.1) operated at a fixed voltage ratio between elements E18 and E17 of 20:1. The aperture A8, was 0.7mm in diameter and was placed immediately in front of the channeltron. As the magnification of the lens was 0.7, only those electrons arriving in a central area of the analyser exit, 1mm in diameter, could reach the channeltron. A set of deflectors, D5, was used to guide the electrons through the aperture into the channeltron. Again a splatter aperture, 2mm in diameter, was placed at the end of E17 near the analyser exit to prevent those electrons outside the central area of the exit from entering the lens.

2.7 The Monochromator And Analyser

In performing electron scattering experiments, the target is generally either an atomic or molecular gas beam. If an atomic target is studied, it is relatively easy to differentiate between elastically and inelastically scattered electrons due to the large differences in the energy of the ground and first excited states of the atom. However, if a molecular target is studied, the problem of differentiating between elastically and

inelastically scattered electrons is more difficult. Most molecules have vibrational energy levels of the order of 100meV above the ground state and thus the incident electron beam must have an energy spread less than this spacing. As the energy spread of the electrons emitted from a typical heated filament source is ≥0.3eV, the electron beam must be passed through some form of filtering or monochromating process before it can be used. A similar process is required in the detection of the scattered electrons where they need to be passed through an analyser capable of differentiating between electrons with energies which differ by as little as 100meV.

There exist several types of monochromators and analysers using either electrostatic or magnetic fields and these have been reviewed by Sevier (1972) and Ballu (1980). In the following sections, the choice and the evaluation of the performance the monochromator and analyser used in this work are discussed. For clarity, the term "selector" will be used in place of monochromator and analyser as both devices work on the same principles.

2.7.1 The Selector Resolution

In the field of electron spectroscopy, electrostatic selectors are almost always used as the fields they employ are easy to generate and limit spatially. Three commonly used types are shown in figure 2.15. The selector which is used has to accept a beam of electrons of radius r_s which is diverging in two dimensions. The divergence is defined using angles α and β where α is the angle of the beam in the plane of the selector and β is the angle perpendicular to this plane. The range of electron energies, ΔE, transmitted by the selector can be defined using a basic equation of the form

$$(x_1-x_2)/D = \Delta E/E_o - W_t/D \qquad 2.13$$

where x_1 and x_2 are the displacements of the beam from the centre of the entrance and the exit apertures respectively and E_o is the energy of an electron which follows the central ray through the selector. The term W_t is the trace width and is the image size for a monoenergetic point source for a given range of incident angles α and β. The

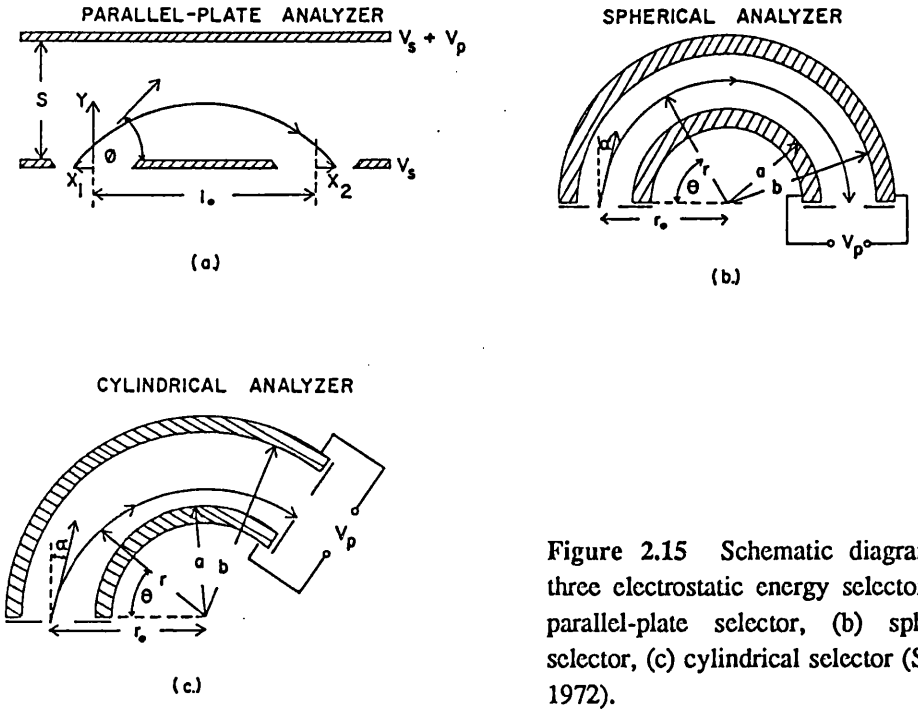

Figure 2.15 Schematic diagrams of three electrostatic energy selectors: (a) parallel-plate selector, (b) spherical selector, (c) cylindrical selector (Sevier, 1972).

term D is defined as the dispersion of a selector and represents the displacement of the image point for a unit fractional change in energy. From equation 2.13 it can be seen that to achieve the smallest energy spread from a selector, large values of D and small values of W_i are desirable. The form of D, W_i and the basic equation are given in table 2.1 for the three types of selector illustrated in figure 2.15. From inspection of table 2.1, it was decided to use a 180° hemispherical selector for both the monochromator and the analyser because for a given electron beam size and angular divergence at the entrance and exit, this type of selector gave the smallest energy spread. Purcell (1938) was the first to consider the focusing properties of a spherical electrostatic field and the maximum energy spread, ΔE_B, of the beam from this type of selector is given by

$$\Delta E_B/E_o = r_s/2R + \alpha_m^2 \qquad 2.14$$

where r_s is the radius of the electron beam, α is the half angle of the angular divergence at the entrance and exit and R is the mean radius of the selector.

Selector type	Dispersion	Trace width	Basic Equation
Parallel plate	l_o	$l_o(2\alpha^2+\beta^2)$	$(x_1+x_2)/l_o=\Delta E/E_o-2\alpha^2-\beta^2$
Cylindrical	R	$R(4\alpha^2/3+\beta^2)$	$(x_1+x_2)/R=\Delta E/E_o-4\alpha^2/3-\beta^2$
Hemispherical	2R	$2R\alpha^2$	$(x_1+x_2)/2R=\Delta E/E_o-\alpha^2$

Table 2.1 Summary of the basic properties of the parallel plate, cylindrical and hemispherical selectors.

In most published works on electron spectroscopy, it is the full width at half maximum (FWHM) of the electron beam which is quoted as a figure of merit when discussing the performance of a selector. It is also common to use the term resolution of a selector and this is defined as $\Delta E_{1/2}/E_o$. Read *et al* (1974) have computed the FWHM ($\Delta E_{1/2}$) for a hemispherical selector for a variety of conditions and have found that it can be calculated using

$$\Delta E_{1/2} = E_o\ (a_{1/2}\ r_s/2R + b_{1/2}\alpha_s^2) \qquad 2.15$$

The values of $a_{1/2}$ and $b_{1/2}$ were found to be functions of the type of defining aperture used at the entrance and exit (circular or slot) and the ratio $R\alpha^2/2r_s(=x)$. The relationship between x and $a_{1/2}$ and $b_{1/2}$ is shown in figure 2.16 for circular apertures and slots. It should be noted that the use of equations 2.14 and 2.15 assume that the field at the entrance and exit planes is radial.

The size of r_s can be defined in one of two ways: either by real apertures placed in the entrance and exit planes or by the image of an aperture focused at the entrance and exit planes by the lens systems immediately before and after the selector (virtual apertures). It was first recognised by Kuyatt and Simpson (1967) that there are a number of advantages in placing the beam defining apertures in a region of higher potential, away from the selector entrance and exit planes and transporting the electron beam to the selector by means of electrostatic lenses. One reason is that the electron reflection coefficient of a metal surface increases rapidly with decreasing impact energy.

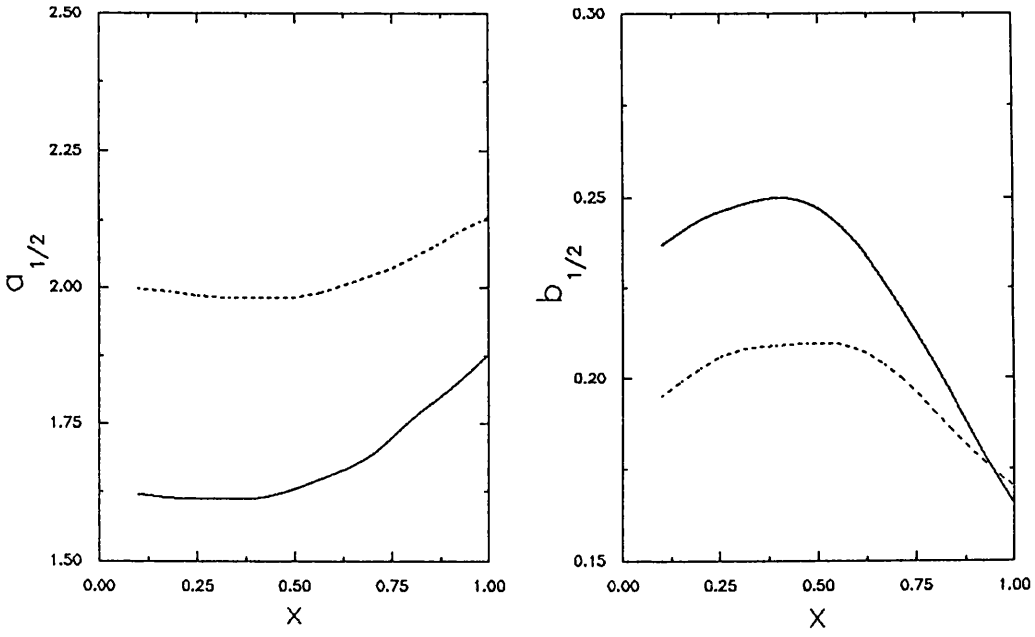

Figure 2.16 Graphs of the functions $a_{1/2}$ and $b_{1/2}$ for a hemispherical selector. The full curves apply to circular apertures and the broken curves apply to slot apertures (Read *et al*, 1974).

Therefore, electrons incident on the metal surface around an aperture can be reflected and may reduce the transmission of the beam through the aperture. It should be noted that if virtual apertures are used, great care should be taken with the adjustment of the lenses immediately before and after the selector as the size of the virtual apertures is defined by the focusing properties of these lenses.

2.7.2 Fringing Fields

In the previous section it was noted that equations 2.14 and 2.15 were only valid if the electrostatic field in the region of the entrance and exit apertures was radial. In practice, when using a hemispherical selector, the equipotential planes of the terminating lens elements are perpendicular to those of the adjacent radial field. This configuration inevitably causes severe distortions of the electron trajectories in the most critical regions of the spectrometer and can result in observed energy spreads much larger than those calculated using equations 2.14 and 2.15. Herzog (1935) suggested that by an appropriate choice of geometry for the lens elements immediately before

and after the entrance and exit of the selector, the disturbance in the field could be minimised to a first approximation. Whilst this method is compatible with the use of virtual apertures, the first order corrections provided by this technique prove to be inadequate if there is a large gap between the inner and outer hemispheres.

Jost (1979) suggested another arrangement which may be used when the entrance and exit apertures are defined by real apertures in the image plane. Two rings placed in the entrance and exit planes on either side of the entrance aperture are physically connected to the inner and outer hemispheres. By varying the distance between the inner edge of the rings and the centre of the aperture, Jost (1979) found that for a distance equal to a/3, (2a is the separation between the inner and outer hemispheres) a good approximation to the ideal radial field could be obtained. A similar method, compatible with the use of virtual apertures, was proposed by Brunt *et al* (1977a). In this work, four electrodes with empirically determined shapes were placed in the entrance and exit planes. By varying the potential on each electrode, they were able to reduce the fringing fields present in the central region of the entrance and exit planes to a minimum.

2.8 Monochromator And Analyser: Design And Performance

In deciding the diameters of the hemispheres used in both the monochromator and analyser, it was necessary to make a compromise between a number of conflicting requirements. The spacing between the inner and outer hemispheres needed to be large enough to avoid loss of electrons to the surfaces and to reduce the effects of manufacturing errors in the hemispherical surfaces. Also to obtain the smallest energy spread the mean radius of the hemispheres has to be large. Against these requirements was the limited space in the vacuum chamber and the need to measure the scattered electron intensity over a large angular range. The monochromator was chosen to have a mean radius of 37.5mm and a separation between the inner and outer hemispheres of 18mm. The mean radius of the analyser was 25mm with separation between the inner and outer hemispheres again equal to 18mm.

For the reasons discussed in the section above (section 2.7), virtual apertures were used in both the monochromator and analyser. To overcome the problem of

fringing fields, a pair of field correcting hoops were placed in the object and image planes of both the monochromator and analyser in the manner of Comer and Read (1971). This arrangement was chosen because of the large spacing between the inner and outer hemispheres compared to the mean radius and because of its mechanical simplicity. The voltage on each hoop was adjusted empirically to obtain the optimum resolution and transmitted current.

From a knowledge of the electron beam size and divergence at the entrance and exit of the monochromator and analyser, the resolution of the spectrometer may be calculated (using equation 2.15) and compared with experimentally obtained values. In the monochromator, for a mean pass energy set at 3eV, the angular divergence at the entrance and exit was calculated to be 5.5°. The radius of the virtual aperture at the entrance of the hemisphere, including the contribution from aberrations was 0.6mm and the radius of the exit aperture, which was the image of A5 projected onto the exit plane by lens 3, was 0.46mm. As the magnitude of the current transmitted by the monochromator was determined by the size of the exit aperture (and therefore its resolution), it's size was used in equation 2.15 to determine $\Delta E_{1/2}$. Using the values r_s=0.46mm and θ_s=5.5°, the values of $a_{1/2}$ and $b_{1/2}$ obtained from figure 2.16 were 1.6 and 0.24 respectively. Therefore, for E_o=3eV, $\Delta E_{1/2m}$ was calculated to be 33.5meV. Using the same procedure for the analyser, the exit aperture was defined by the size of the image of A8 formed at the exit plane by lens 8. This was calculated to be 1mm in diameter, therefore r_s=0.5mm. As the beam energy at the interaction region was changed the angular divergence at the entrance of the analyser changed slightly, so an average value of θ_s=5° was used. This gave $a_{1/2}$=1.6 and $b_{1/2}$=0.25. Therefore at an analysing energy of 2eV, $\Delta E_{1/2A}$ was calculated to be 35.8meV. The total resolution of the spectrometer was then found by adding the resolution of the monochromator and the analyser in quadrature

$$(\Delta E_{1/2T})^2 = (\Delta E_{1/2M})^2 + (\Delta E_{1/2A})^2 \qquad 2.16$$

and this gave the total resolution $\Delta E_{1/2T}$=49.0meV.

To determine the validity of these calculations, two experiments were performed. In the first experiment, the total resolution of the spectrometer ($\Delta E_{1/2T}$) was measured as a function of the analysing energy E_{oA}. The justification for the this method is seen by examination of equations 2.15 and 2.16. From equation 2.15, it can be seen that $\Delta E_{1/2A}=AE_{oA}$ where A is a constant. Equation 2.16 can be rewritten as

$$(\Delta E_{1/2T})^2 = (\Delta E_{1/2M})^2 + (AE_{oA})^2 \qquad 2.17$$

Therefore, a graph of $(\Delta E_{1/2T})^2$ plotted against $(E_{oA})^2$ should yield a straight line with a gradient equal to A^2 and an intercept equal to $(\Delta E_{1/2M})^2$. To measure $\Delta E_{1/2T}$, the spectrometer was tuned for a desired incident beam energy and a gas beam produced at the centre of the interaction region, by admitting helium to the system via the capillary tube. The first half of the spectrometer was then moved to a scattering angle of 20° and the scattered electron flux was measured as a function of scattered electron energy. The FWHM of the energy distribution was taken as $\Delta E_{1/2T}$. This procedure was repeated for several different values of E_{oA}. Figure 2.17 shows a graph of $(\Delta E_{1/2T})^2$ plotted against $(E_{oA})^2$ with E_{oM}=3eV. From the gradient of the graph, the value $\Delta E_{1/2A}$=37.7±1.1meV was obtained at E_{oA}=2eV and from the intercept, $\Delta E_{1/2M}$ was found to be 31.2±0.3meV.

In the second experiment, the width of the He resonance in the elastic scattering channel was measured and $\Delta E_{1/2M}$ was inferred from the increase in the observed width. The position and width of this resonance has been accurately measured by Brunt *et al* (1977b) and found to be E_{res}=19.366eV and Γ=9meV where Γ is the resonance width. The observed resonance profile in the present work, was the result of a convolution of the natural profile with that of the electron beam. Measurements of the resonance profile were made at a scattering angle of 90° using the reference detector described in section 2.9.

The electron beam profile was then determined by convoluting a trial gaussian profile with the theoretically calculated resonance shape until a good fit to the experimental data was obtained. Several experimentally measured profiles are illustrated in figure 2.18 together with calculated fits. Figure 2.19 shows the square of the

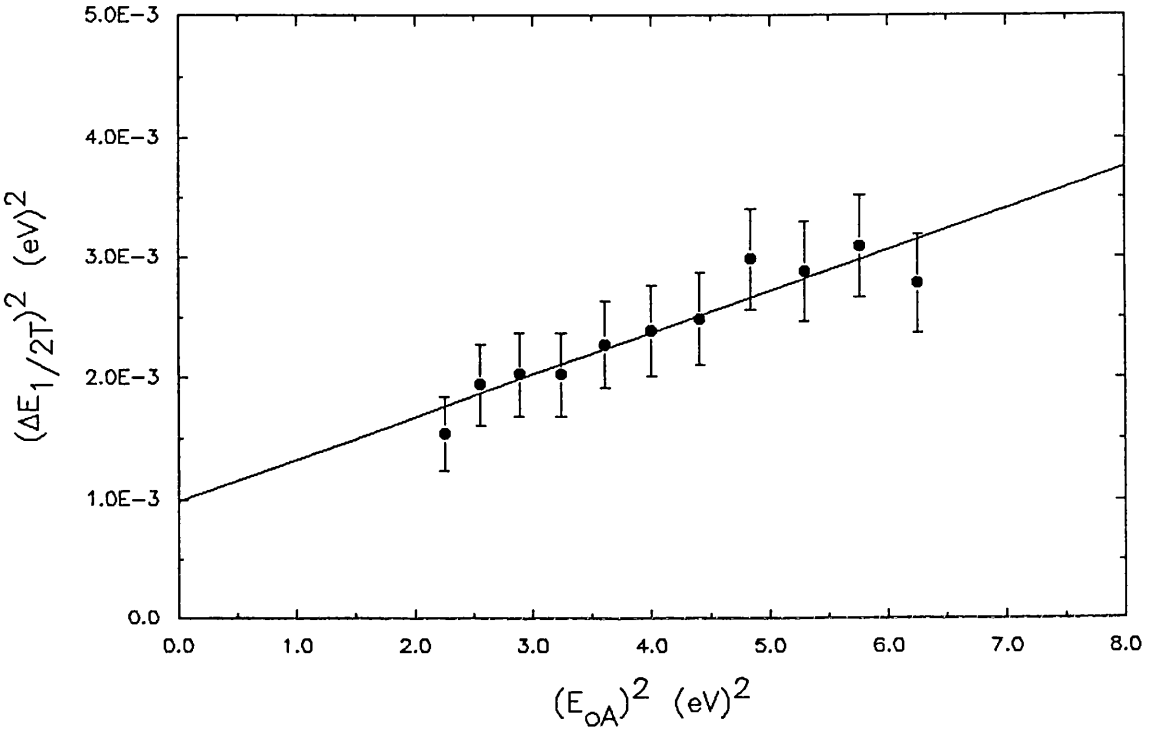

Figure 2.17 A graph of the total spectrometer resolution ($\Delta E_{1/2T}$) measured as function of the analysing (E_{oA}).

calculated FWHM plotted against $(E_{oM})^2$. The calculated FWHM does not represent the true width of the electron beam as it contains a contribution from the reference detector, hence the non zero intercept. The value of the intercept can be taken as $(\Delta E_{1/2RD})^2$ which gives $\Delta E_{1/2RD}$=15.1±8.05meV where $\Delta E_{1/2RD}$ is the contribution from the reference detector. From the gradient, the value of $\Delta E_{1/2M}$ was found to be 35.5±1.41meV for E_{oM}=3eV.

Table 2.2 compares the theoretically calculated values of $\Delta E_{1/2M}$ and $\Delta E_{1/2A}$ with those determined experimentally. It can be seen that the experimental values of $\Delta E_{1/2A}$ and $\Delta E_{1/2M}$ are consistently higher than those calculated using equation 2.15 but they agree within the limits of the experimental errors. A number of factors may affect the resolution obtained from both the monochromator and the analyser and these may explain the differences between the calculated values of $\Delta E_{1/2A}$ and those observed experimentally. The resolution was found to be highly dependent on the potentials applied to the field correcting hoops placed at the entrance and exit of the monochromator and analyser. Changes of the order of ±0.1eV were found to increase the value of $\Delta E_{1/2T}$ by 10s of meV. To determine the optimum voltages, the potential

E_{om} (V)	$\Delta E_{1/2m}$ (meV)[1]	$\Delta E_{1/2m}$ (meV)[2]
2	22.7	23.7±1.0
3	34.1	35.5±1.5
4	45.5	47.3±1.9
5	56.8	59.1±2.4
6	68.2	71.0±2.9

[1] Calculated using equation 2.15

[2] Values determined from figure 2.19

Table 2.2a A comparison of the calculated and measured resolutions of the monochromator as a function of the monochromating energy.

E_{oA} (eV)	$\Delta E_{1/2A}$ (meV)[3]	$\Delta E_{1/2A}$ (meV)[4]
1.50	26.9	28.0±1.8
1.75	31.3	32.6±2.1
2.00	35.8	37.3±2.4
2.25	40.3	42.0±2.7
2.50	44.7	46.6±2.7

[3] Calculated using equation 2.15

[4] Values determined from figure 2.17

Table 2.2b A comparison of the calculated and measured resolutions of the analyser as a function of the analysing energy.

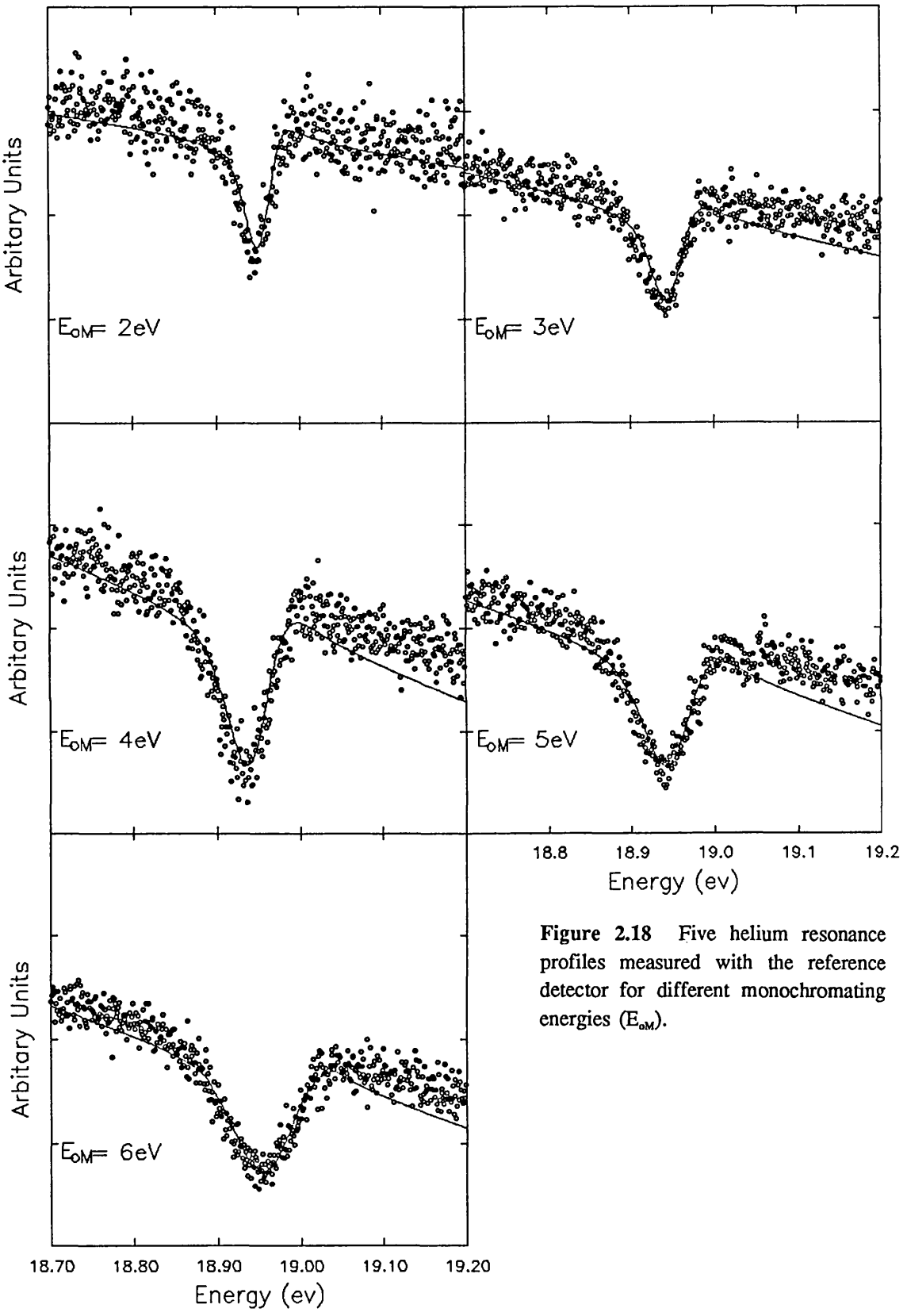

Figure 2.18 Five helium resonance profiles measured with the reference detector for different monochromating energies (E_{oM}).

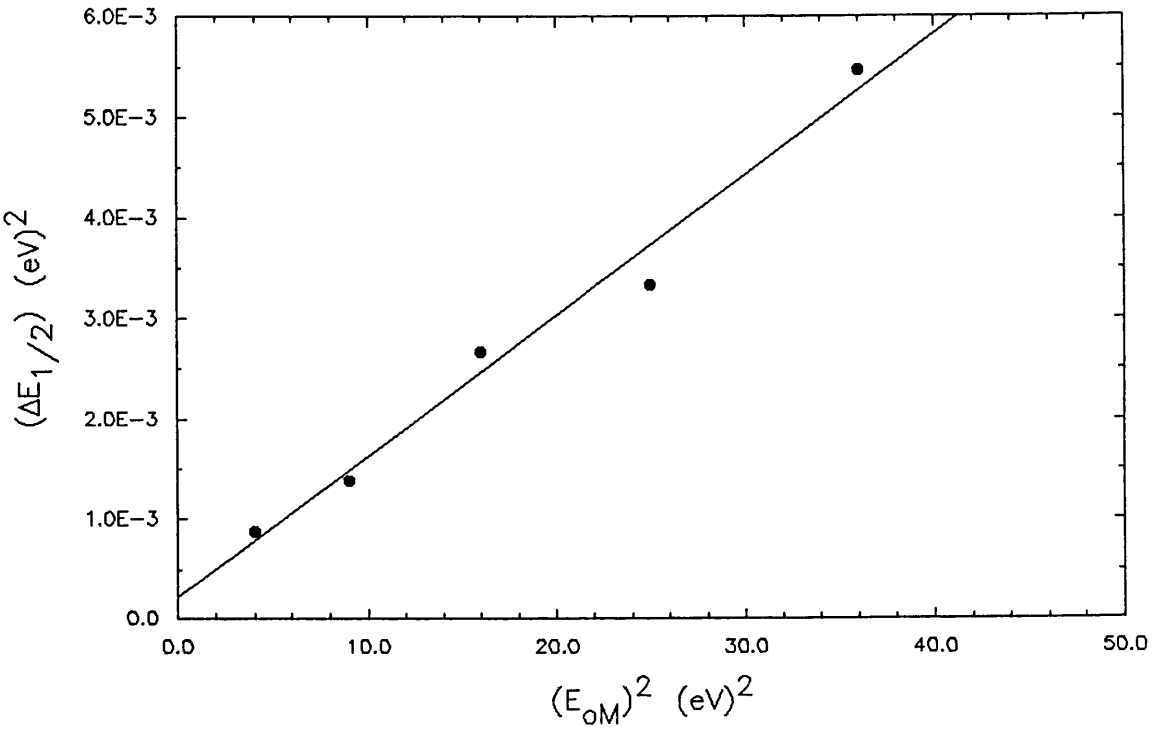

Figure 2.19 A graph of electron beam width plotted against monochromating energy. The values of $\Delta E_{1/2}$ were derived from the helium resonance profiles shown in figure 2.18.

on each hoop was varied until the best resolution was obtained. The value of $\Delta E_{1/2T}$ was also found to be dependent on the number of times that the spectrometer had been exposed to air. After two or three exposures, it was found that the value of $\Delta E_{1/2T}$ obtained for a given output current began to increase. This effect was believed to be due to "dirt" (possibly oil vapour and dust) depositing on the apertures in the gun and pre-interaction region lens stack which would charge up and reduce the amount of current transmitted around the spectrometer. This problem was reduced by heating the spectrometer with radiative heat from a projector lamp bulb placed in the vacuum chamber and with heating tapes wrapped around the outside of the vacuum chamber.

2.9 The Reference Detector

In addition to the second half of the spectrometer, a second detector was used to detect scattered electrons at θ=−90° and this was known as the reference detector. Its main purpose was to assist in the measurement of angular differential cross section measurements (see section 4.7). The detector, shown in figure 2.20, consisted of a

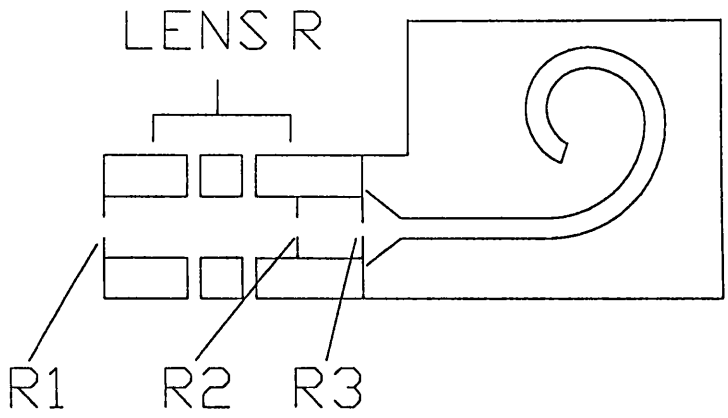

Figure 2.20 A schematic diagram of the reference detector (not to scale).

three element einzel lens followed by channeltron. A negative potential (with respect to the potential applied to E9 and E11) was applied to the centre element of the lens such that only elastically scattered electrons could pass through to the channeltron. Three apertures were placed in the detector stack, one at the entrance of the detector (R1=2mm), a second positioned between the centre element and the channeltron (R2=1.7mm) and a third in front of the channeltron (R3=2.5mm). Their purpose was to restrict the angular acceptance of the detector and to shield the lens from the channeltron mouth, which was held at +50V above the element R3. The lens and channeltron were positioned on an optical bench fixed to an arm which in turn was attached to the lower optical bench of the first half of the spectrometer. This ensured that as the first half of the spectrometer was rotated, the reference detector was maintained at an angle of -90° with respect to the incident electron beam.

Figure 2.21 shows a typical transmission profile of the detector as a function of the voltage on the centre element. The presence of the maximum point B provided a useful reference point. Once the spectrometer had been tuned to the desired collision energy, gas was admitted to the system via a capillary tube. The voltage on the centre element was then adjusted until the scattered electron count rate reached the maximum at point B. It should be noted that the value of the voltage required was dependent on the collision energy. If the energy of the beam varied, e.g. because of a contact potential shift, then the voltage required to obtain the maximum count rate would also

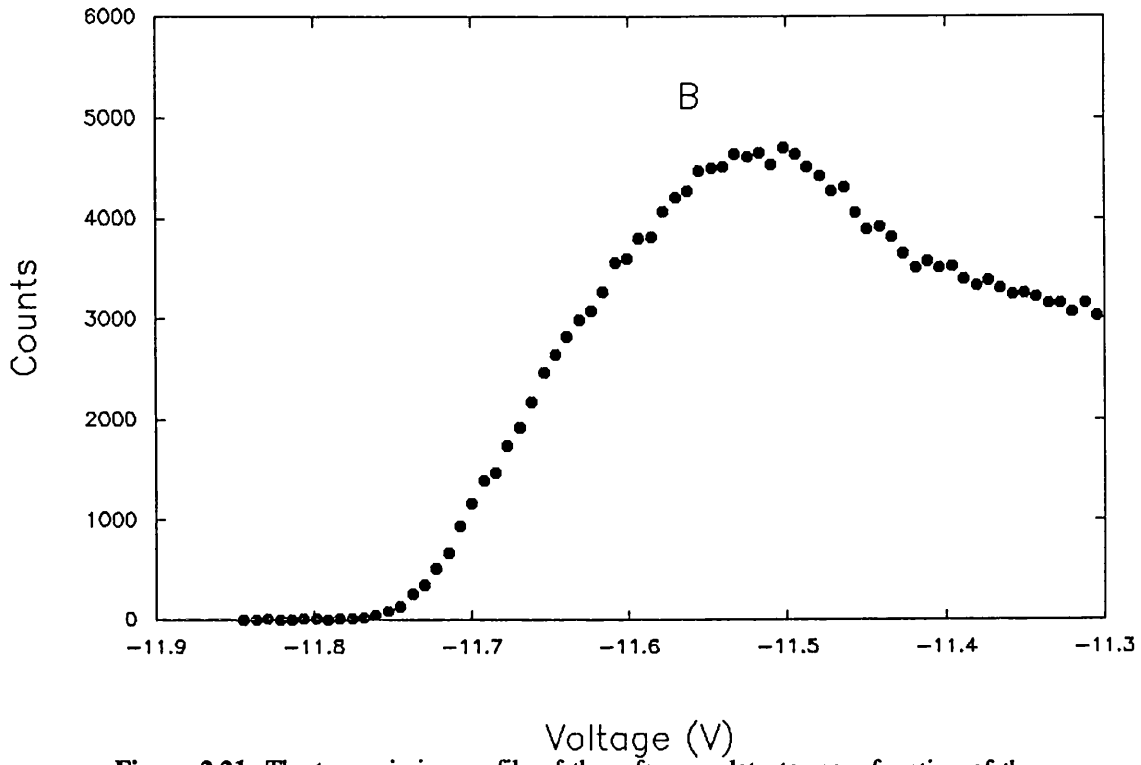

Figure 2.21 The transmission profile of the reference detector as a function of the voltage applied to the centre element of the detector. The profile was measured for electrons scattered from helium with an incident beam energy of 10eV.

change by the same amount. This effect was used to detect any drifts in the contact potential.

2.10 Summary

In this chapter the design and operating characteristics of the electron spectrometer have been described, a summary of which is given in table 2.3. In general, the electron lens systems used were found to operate in accordance with calculations except lens 1 in the electron gun. In common with several other gun designs, the anode aperture was taken as the source of electrons from the emission system and the object and image distances were chosen accordingly. This proved to be the incorrect choice as it was found that the tip of the hairpin filament was the source of electrons used in this work. This resulted in lens 1 having a large filling factor and hence the image sizes were increased due to severe aberrations. Nevertheless, the gun was still able to produce currents between 1×10^{-7}A and 6×10^{-7}A for injection into the monochromator.

Two hemispherical selectors were used in the spectrometer, one to reduce the energy spread of the electron beam from the filament and the second to analyse the energy distribution of the electrons scattered from the gas beam target. Calculations and experimental measurements of the resolution of both selectors were found to be in reasonable agreement. The differences that were observed were attributed to the inadequate cancellation of the fringing fields at the selector entrances and exits.

The intensity of the electron beam current at the interaction region was dependent on the energy spread of the electron beam. For a FWHM of 20meV, the beam current was typically $2x10^{-9}$A rising to $50x10^{-9}$A for a FWHM of 65meV. The best observed total resolution from the spectrometer was 28meV for an incident beam current of $2x10^{-9}$A. The spectrometer was usually operated with higher beam currents and a total resolution of 50-60meV to reduce the data collection time. This resolution was generally sufficient to distinguish between elastically and inelastically scattered electrons from the molecular targets used in this work.

Operational energy range:	2-100eV
Primary beam current:	1.5-70nA
Energy resolution:	28-100meV
Beam diameter in interaction region:	0.75mm
Angular resolution:	1-5°
Extraction system:	Pierce
Filament:	thoriated tungsten hair pin

LENS	
1	3 element, 3:1 decelerating, D=6mm, A/D=0.5
2	2 element, 9:1 decelerating, D=6mm, G/D=0.1
3	2 element, 9:1 accelerating, D=6mm, G/D=0.1
4	3 element, variable, D=8mm, A/D=1
5	3 element, variable, D=6mm, A/D=1
6	3 element, enizel, D=6mm, A/D=0.5
7	2 element, 10:1 decelerating, G/D=0.1
8	2 element, 20:1 accelerating, G/D=0.1

APERTURES	Diameter
A1	0.33mm
A2,A3,A4,A5	0.5mm
A6	2.0mm
A7,A8	0.7mm

MONOCHROMATOR Mean radius 37.5mm, outer radius 46.5mm, inner radius 28.5mm monochromating energy range 2-7eV, virtual apertures used.

ANALYSER Mean radius 37.5mm, outer radius 46.5mm, inner radius 28.5mm monochromating energy range 2-7eV, virtual apertures used.

Material of lenses:	titanium
Material of hemispheres:	molybdenum
Material of apertures:	molybdenum
Surface coating of apertures:	Acheson dag (508)
Surface coating of hemispheres:	soot from oxy-acetylene flame.

Table 2.3 Design summary of the electron spectrometer.

CHAPTER 3

The Experimental Chamber And The Vacuum System

3.1 Introduction

In this chapter further experimental details of the apparatus are given. The vacuum system and the gas handling procedures are described, with particular attention given to the measurement of the pressure and the flow rates in the gas line. Details of the mechanical construction of the spectrometer, the power supplies for the lens elements and the signal detection are also given.

3.2 The Vacuum System

The electron spectrometer was housed in a cylindrical vacuum chamber approximately 300mm in diameter and 160mm high, constructed from stainless steel, type EN58J and access to the spectrometer was achieved by removal of a single top flange. Nine ports, equally spaced around the side wall, were used to mount an ionisation gauge and electrical feedthroughs. The chamber was constructed and cleaned to ultra high vacuum (UHV) standards, all flanges being sealed with copper or viton gaskets. Whilst ultra high vacuum conditions were not required or attained in the present work, UHV materials and procedures were employed wherever possible to reduce the possibility of contamination. A schematic diagram of the pumping system is shown in figure 3.1.

An Edwards water cooled EO4 diffusion pump, backed by an Edwards ED250 rotary pump, was used to evacuate the chamber through an 80mm diameter port on the bottom flange. To reduce backstreaming of diffusion pump oil into the chamber, a liquid nitrogen cold trap and a Peltier cooled chevron baffle were placed between the diffusion pump and the chamber. The cold trap also aided in the evacuation of water and other condensible gases from the chamber during the initial pump down period. The diffusion pump stack (from the top of the liquid nitrogen trap) could be isolated

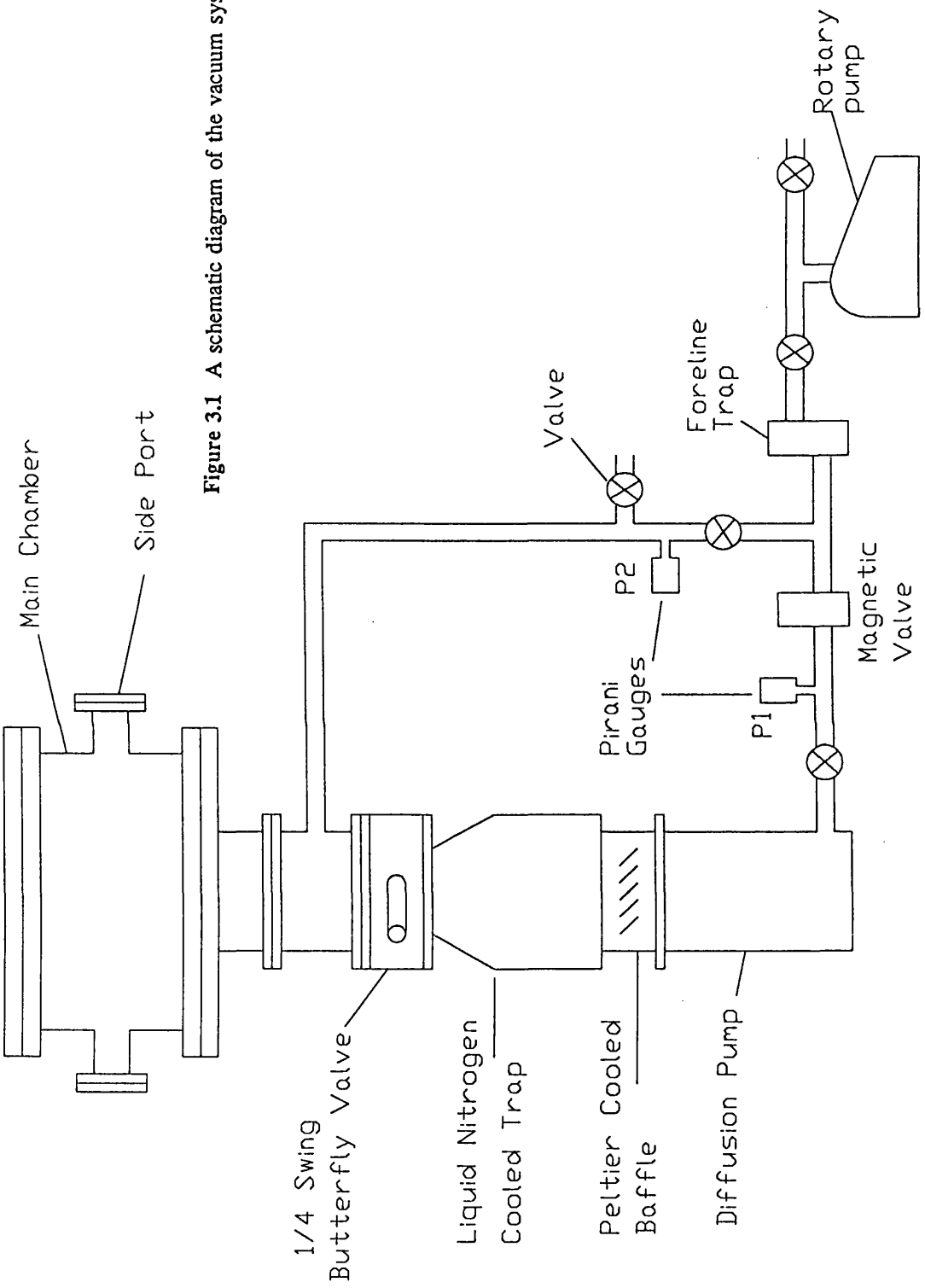

Figure 3.1 A schematic diagram of the vacuum system.

from the chamber by means of a quarter turn butterfly valve and this allowed access to the vacuum chamber while the diffusion pump was still in operation. The speed of the pumping system was calculated to be 100 ls^{-1} at the entrance to the chamber.

During the initial pump down period the spectrometer and the chamber were heated to a temperature of approximately 70°C using radiative heat from an internally fitted projector lamp bulb and heating tapes fitted to the exterior walls of the chamber. This aided the removal of any gases (particular water vapour) adsorbed on the surfaces within the chamber. In general, when the spectrometer was not in operation, it was maintained at (≈50°C) to reduce the possibility of any build up of oil on the surfaces of the electron lens elements. After several days of pumping and baking, the pressure, measured with a Vacuum Generators VIG8 ion gauge and a Kratos VC35 ion gauge control unit, was typically $5x10^{-8}$ torr.

The experiment was protected by a series of electrical trips. If the mains power supply or the flow of cooling water was interrupted then the experiment was shut down and did not restart when the supplies were resumed. If the backing line pressure, measured by the Pirani P1 (see figure 3.1), exceeded 0.1 torr then the power supplies to the diffusion pump and Peltier baffle were cut and the magnetic valve was shut. This protected the diffusion pump from contamination by rotary pump oil which might be sucked into the high vacuum region. Also, if the pressure in the vacuum chamber exceeded one and half times the full scale deflection of the ionisation gauge, the spectrometer power supplies, ionisation gauge and high voltage supplies were switched off.

3.3 Magnetic Shielding Of The Spectrometer

The direction of an electron beam can be significantly altered by the presence of a magnetic field. According to Powell (1968), the maximum magnetic flux density (in gauss) which can be tolerated at right angles to an electron beam for a maximum acceptable beam deflection d (cm) is given by

$$B_{max} = 6.74\ E^{1/2}\ d/S^2 \qquad 3.1$$

where S is the path length (cm) and E is the electron beam energy in electron volts. In the spectrometer used in the present work, there were two regions where it was vitally important to reduce the residual magnetic fields to a minimum. These were within the monochromating and analysing hemispherical selectors. In the hemispherical selector, the electron beam was deflected through 180° by the spherical potentials between the inner and outer electrodes. Since the path length was large (≈0.1m) and the electron beam energy small (1.5-6eV), it can be seen from equation 3.1 that the effect of any stray magnetic fields would have been greatest in these areas. For example, in the monochromating selector, if an acceptable deviation was taken as 0.1mm for a path length of 120mm and a mean electron beam energy of 3eV, then $B_{max}=2x10^{-3}$ gauss. This result clearly indicates the possible detrimental effects caused by the presence of stray magnetic fields. Thus it was necessary to construct the spectrometer from non-magnetic materials and provide sufficient shielding against the Earth's magnetic field (0.45 gauss).

Attenuation of the contribution from the Earth's magnetic field was achieved by lining the inside of the vacuum chamber with 1.6mm thick mu-metal. However, in order to provide sufficient pumping of the chamber and to allow for electrical connections between the spectrometer and the feedthroughs, it was necessary to have a number of openings in the mu-metal. To reduce the field penetration, all holes were fitted with additional mu-metal tubes. With the mu-metal in position, the residual field when measured with a Bell 120 gaussmeter was found to be less than $5x10^{-3}$ gauss.

3.4 Mechanical Details Of The Spectrometer

In order to provide a smooth level surface on which the components of the spectrometer could stand or slide, a stainless steel baseplate was fixed to the bottom of the vacuum chamber. As even a slight strain can impair the properties of the mu-metal shielding, small stainless steel spacers were passed through the mu-metal to separate the baseplate from the chamber bottom. The supports holding the monochromator and its associated optics were attached to a large brass gear wheel, the centre of which bared upon a carefully machined ridge on the base plate. The gear wheel was driven by a small pinion mounted on a rotary motion feedthrough (VG

model RD3) with a pitch diameter ratio of 1:7 and this allowed the first half of the spectrometer to be rotated about the central axis of the vacuum chamber. The external half of the rotary feedthrough was marked with an angular scale to allow the first half of the spectrometer to be rotated to any scattering angle in the range −10° to 120°. The second half of the spectrometer was mounted on similar supports which stood on the base plate and was held in position with machined dowels. To obtain the maximum angular range between the incident and scattered electron beams, the area occupied by the monochromating and analysing hemispheres plus their associated optics were kept to a minimum. This was achieved by designing the optics such that the electron trajectories through the monochromator and the analyser were perpendicular to the plane of rotation.

All the electrostatic lenses used in the spectrometer were cylindrical and had a common external diameter of 15mm. The individual elements making up the lenses were supported on carefully machined optical benches and were electrically isolated from the benches using ceramic rods. Each element was clamped in position using stainless steel studding insulated from the optical benches by ceramic spacers. The optical benches were designed such that they could be slotted into accurately machined supports in the vacuum chamber. A cross section of an optical bench and lens element is shown in figure 3.2. An end on view of the lens systems with the hemispheres in place is shown in figure 3.3

All the materials used in the construction of the spectrometer were chosen, where possible, to be compatible with the requirements of a baked ultra high vacuum (UHV) system. Oxygen free copper, aluminium, brass and stainless steel were used in the construction of the supports and optical benches and great care was taken to demagnetise any stainless steel studding, nuts and screws in close proximity to the electron lenses.

The materials used in the manufacture of the lens elements and the hemispheres had to conform to the following criteria: they had to be non-magnetic, have a surface which was easily cleaned and not susceptible to the formation of insulating layers. Materials typically used are gold plated OHFC copper, aluminium, molybdenum and titanium. In this work, the hemispheres and hoops were made from molybdenum, the

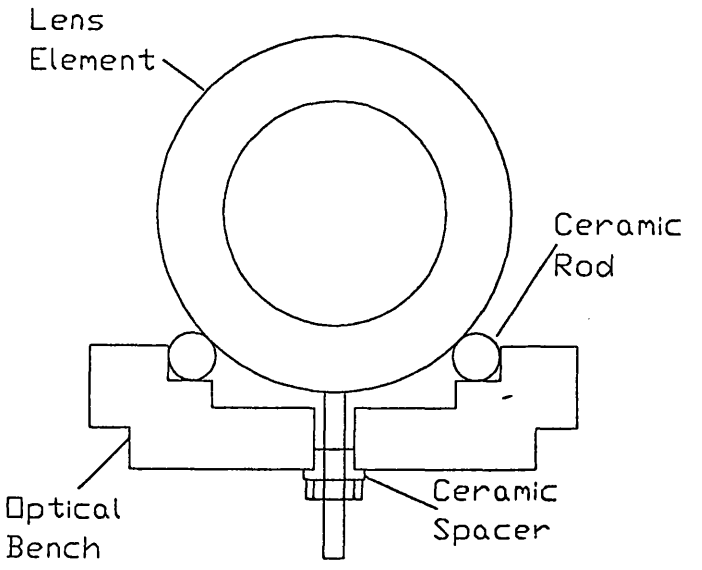

Figure 3.2 A cross sectional view of a lens element and optical bench.

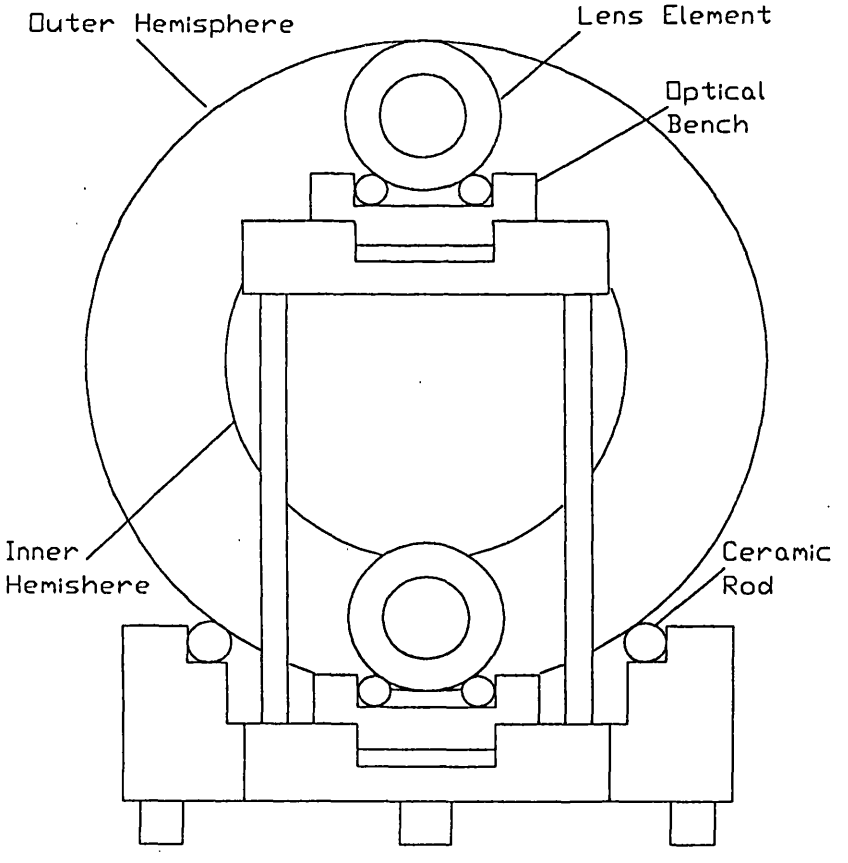

Figure 3.3 An end view lens elements and hemispherical selector.

lens elements from titanium and the beam defining apertures from 0.05mm thick molybdenum sheet. The surfaces of the hemispheres and hoops were coated with soot from an oxy-acetylene flame as it has been reported (McGowan, 1967) that this significantly reduces the electron reflection coefficient of the surface. The apertures were painted with a graphite solution (Acheson DAG 580) to reduce electron reflection.

Before assembling the spectrometer, the following cleaning procedure was employed. The lens elements were first washed with detergent and then rinsed in distilled water. The hemispheres, hoops and apertures were cleaned with acetone by hand while the lens elements were placed in an acetone bath and cleaned ultrasonically. The lens elements were then removed from the bath and after the acetone had evaporated from the surfaces, the cleaning procedure was repeated using methyl-alcohol. This process ensured that the lens element were free from grease and oil and thus reduced the possibility of static charge building up on the surfaces. Once dry, the apertures were painted with the graphite solution and the hoops and the hemispheres were coated with soot from an oxy-acetylene flame.

3.5 The Interaction Region

The purpose of the interaction region was to provide a field free region in which the electron beam could scatter from the target gas beam free from the influence of any stray fields. Magnetic fields were reduced to a minimum by lining the whole chamber with mu-metal and the use of non-magnetic materials within the chamber. Exclusion of electrostatic fields was ensured by earthing the interaction region and minimising the size of the openings to avoid field penetration.

The interaction region was manufactured from an aluminium tube suspended from the support holding the electron gun optical bench. Two holes were cut in the tube wall, the first to allow the primary beam to enter and the second to allow the electrons scattered through θ=–90° to reach the reference detector mounted outside the tube. A 10mm wide slot was also cut in the tube wall to allow electrons scattered between θ=-10°and 120° to be detected by the second half of the spectrometer. The width of the slot was reduced to 4mm using strips of stainless steel mesh to reduce the amount of solid surface from which the electrons could scatter. All the internal

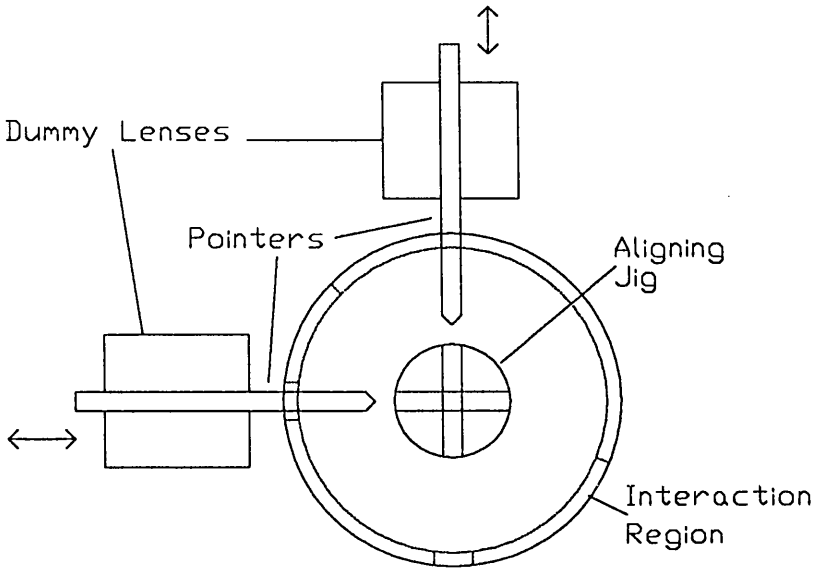

Figure 3.4 Arrangement used for aligning the gas source in the interaction region.

surfaces of the interaction region were coated in soot to further reduce the number of electrons scattered from the surfaces.

Suspended at the centre of the interaction region was a capillary tube used to form the gas beam. It was vitally important that this tube should lie on the axis of rotation of the spectrometer otherwise a significant error could be introduced into the measurement of any angular cross sections.

To ensure the correct alignment of the capillary tube the following procedure was adopted. Dummy lenses containing movable rods were attached to the upper optical benches used to mount the electron gun and post analyser optics. The capillary tube was then replaced with a specially machined jig through which two holes had been drilled perpendicular to its central vertical axis. The distance between the centres of the two holes was equal to that between the axes of the two lens systems. The first half of the spectrometer was then rotated to a scattering angle of 90° and the rods from the dummy lenses extended such they could be inserted into the machined jig (see figure 3.4). If the interaction region was not correctly positioned then either one or both of the rods would not enter the jig. The position of the interaction region was then adjusted until both rods could be smoothly inserted into the jig.

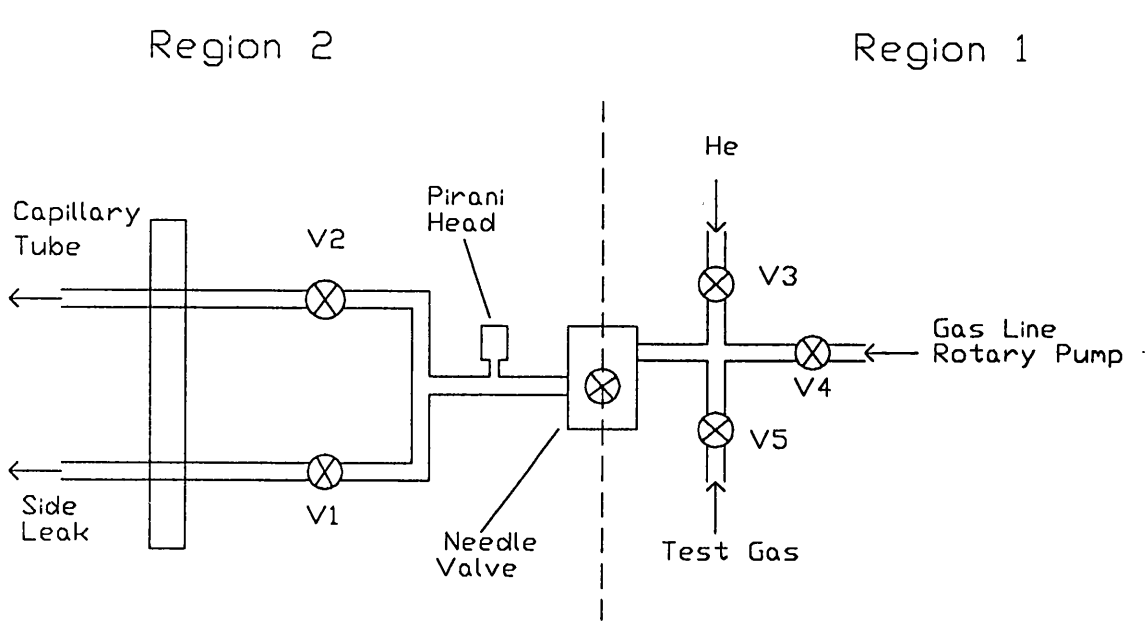

Figure 3.5 A schematic diagram of the gas line.

3.6 The Gas Line

All the molecules studied in this work, with the exception of water, were gaseous at room temperature making their preparation and handling relatively easy. Gas was admitted into the chamber via the capillary tube held at the centre of the interaction region or through a side leak in the vacuum chamber wall. Apart from water, all the gases were supplied from a lecture bottle and were of research grade purity (>99%). Water vapour was obtained from a cell containing distilled, de-ionised water connected to valve V5 in the gas line (see figure 3.5). To purge the air from the cell and to remove any gases dissolved in the water, the following procedure was employed. The cell was first evacuated to "boil" off any gases dissolved in the water, e.g. carbon dioxide and then, while continuing to evacuate the cell, the water was frozen using liquid nitrogen. The cell was then sealed and the ice allowed to melt. This procedure was repeated two or three times to reduce the amount of dissolved gases in the water to minimum.

All the gases investigated were fed to the chamber through a gas line, a schematic diagram of which is shown in figure 3.5. The gas line can be divided into two regions 1 and 2. In region 1, two gas supplies, one of which was always He, were

connected to valves V3 and V5. Either of the two gases could then be fed to the needle valve where its flow was regulated into region 2. Region 1 could be pumped down to 10^{-2} torr using a two stage rotary pump thus avoiding any mixing of the different gases. When the gas was fed into the vacuum system, the pressure in region 1 was maintained above atmospheric pressure to reduce the probability of contamination due leaks. In region 2, the gas could be directed through the capillary tube or the side leak using valves V1 and V2 and the pressure in this region was measured with a calibrated Pirani gauge. All the connections in region 2 were HV compatible as this section of the gas line was regularly opened to the main chamber. To aid the removal of any contaminants which may have been adsorbed onto the internal surfaces, region 2 of the gas line was wrapped with heating tapes and periodically heated to ≈50° when not in use. A capillary tube, 25mm in length and with an internal diameter of 0.6mm and made from copper was used to form the gas beam. Originally, a stainless steel tube had been used but demagnetisation proved to be difficult and so it was discarded.

The procedure adopted for admitting gas into the spectrometer was as follows. Region 1 of the gas line was pumped out through V4 using the gas line rotary pump. Gas was then admitted to the region via V3 (or V5). Valve V3 (or V5) was then closed and region 1 was again pumped out using the gas line rotary pump. This process was repeated several times to reduce the likelihood of any contamination from any gas initially present in the region. Valves V1 and V2 were then opened and region 2 of the gas line was pumped down to less than 10^{-3} torr. The needle valve was then slowly opened until the Pirani gauge showed a rise in the gas pressure. If the gas was to be passed into the vacuum chamber via the capillary tube, V1 was closed and the needle valve was adjusted until the desired pressure was reached in region 2. Alteratively, if the gas was to be fed directly into the chamber via the side leak, V2 was closed and the needle valve adjusted until the desired pressure in the vacuum chamber was reached.

The presence of any leaks in the gas line was determined by admitting water into the vacuum system via the capillary tube, using the procedure outlined above. Water was chosen as the pressure in region 1 of the gas line was always less than

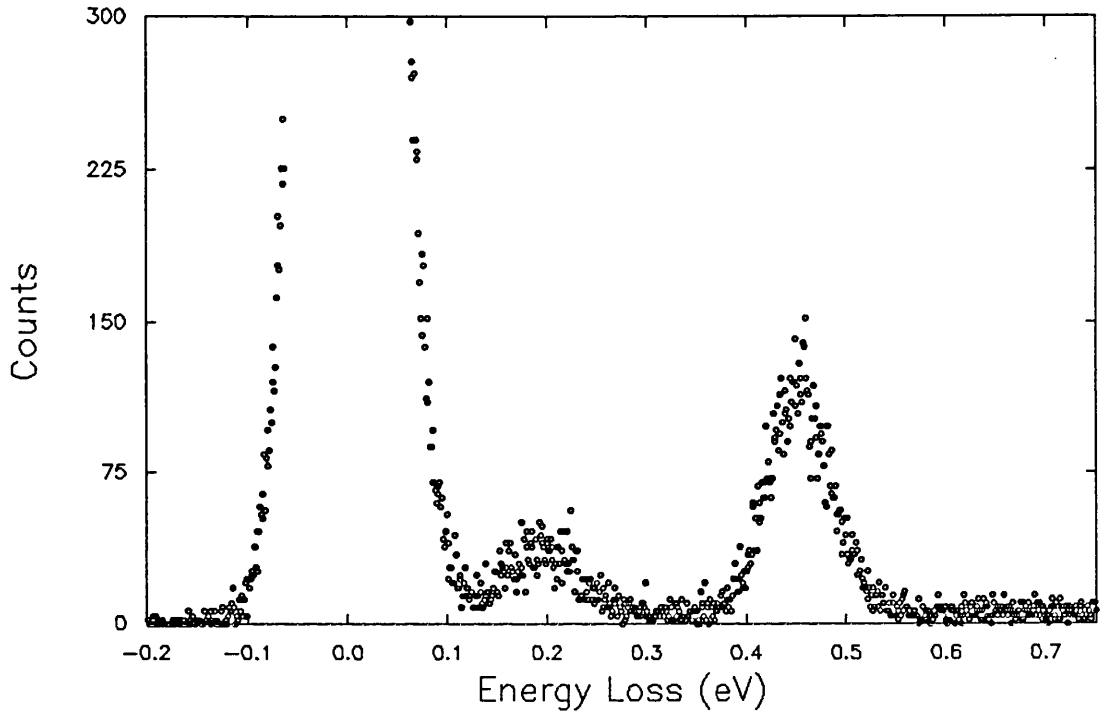

Figure 3.6a An energy loss spectrum taken for electron scattering from water with an incident energy of 2eV and a scattering angle of 90°.

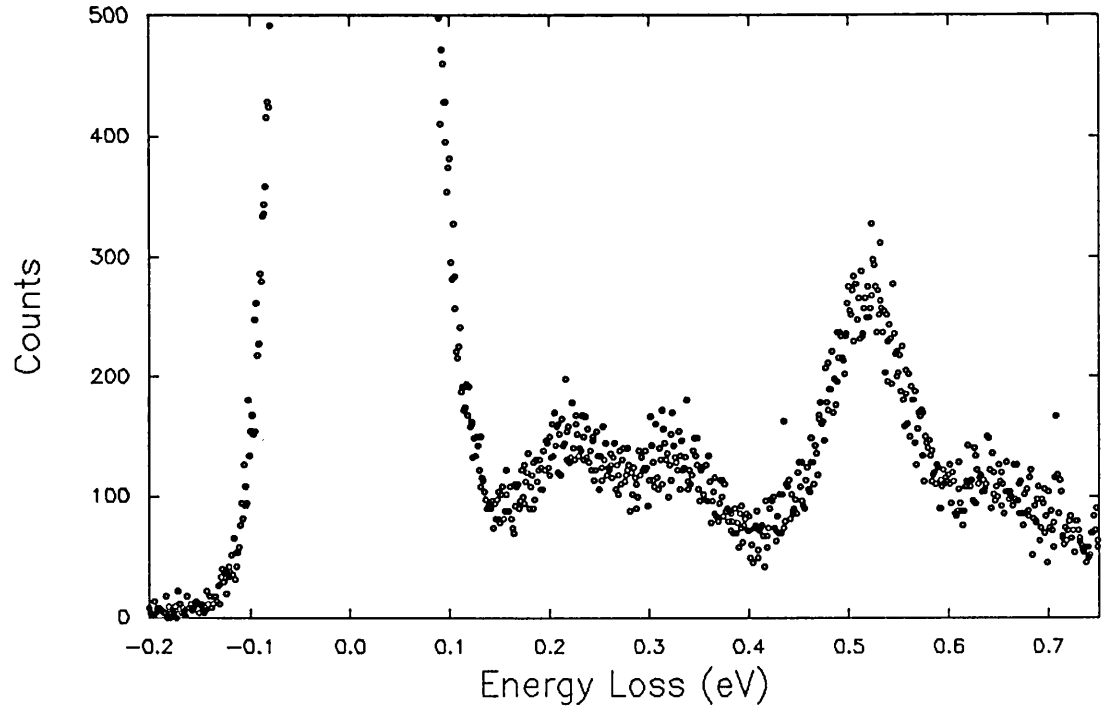

Figure 3.6b As figure 3.6a. The presence of the two extra peaks indicates a nitrogen leak.

atmospheric pressure and thus the contamination resulting from any leaks would have been greatest. The spectrometer was tuned for an incident beam energy of 2eV and the scattered electron flux was then measured as a function of electron energy at a scattering angle of 20°. Figures 3.6a and 3.6b show the results of two such measurements. Figure 3.6a is an energy loss spectrum taken with no leak present and the two peaks shown are the result of electrons exciting vibrational energy levels in the water molecules. In figure 3.6b, two extra peaks can be seen and these derive from vibrational excitation of nitrogen molecules present in the beam due to a leak in the gas line.

3.7 Pressure Measurement In The Gas Line

The pressure in region 2 of the gas line was measured with a Vacuum Generators PVG3SKF Pirani head connected to a Vacuum Generators PIR2 control box. To obtain absolute measurements of the pressure, the Pirani head was calibrated against the output from an MKS 2203A1 baratron for all the gases used in this work. In addition to indicating the pressure via a meter graduated with the usual logarithmic scale, the Pirani control box also produced a voltage output between 0-10V. The Pirani was calibrated by comparing the voltage output from the control box against the pressure recorded from the baratron. Figures 3.7 to 3.11 show calibration curves for He, H_2O, N_2O, SF_6 and Ar. From the figures it can be seen that for all the gases there was a point of inflexion corresponding to an output voltage of 2V from the Pirani. To determine the pressure from the voltage output of the Pirani, two separate curves were used to fit the calibration data, a second order polynomial for Pirani voltages less than 2V and a fourth order polynomial for voltages greater than or equal to 2V. A list of the coefficients for each gas is given in table 3.1.

3.8 Flow Rate Measurements

In chapter 4, the method used for measuring absolute differential cross sections with the relative flow technique is described and the use of this technique, as its name suggests, requires a knowledge of the relative flow rates between two gases. The procedure used in the present work for measuring the flow rate of gas through the

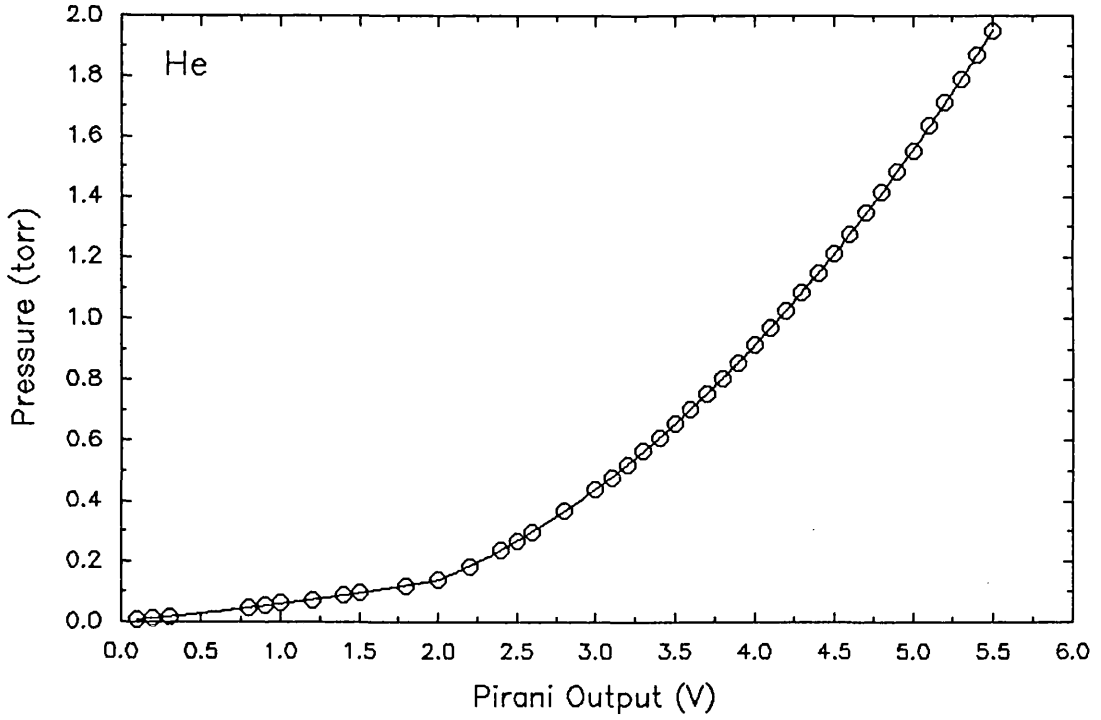

Figure 3.7 A calibration curve of absolute pressure against Pirani output voltage in the presence of helium.

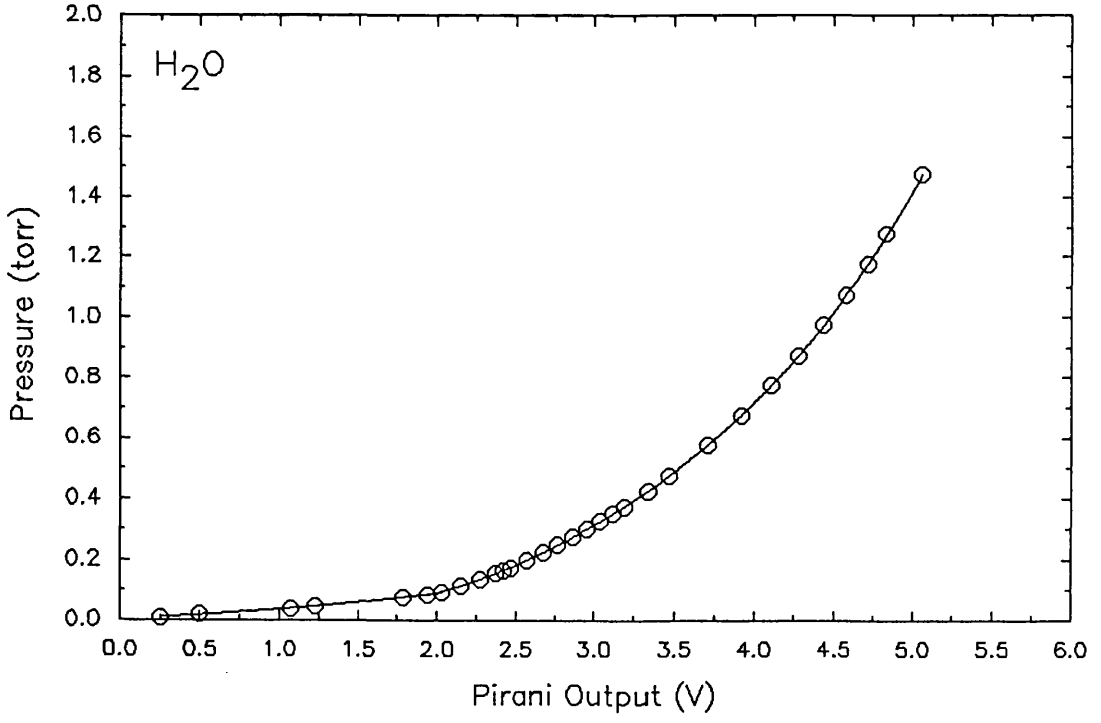

Figure 3.8 A calibration curve of absolute pressure against Pirani output voltage in the presence of water.

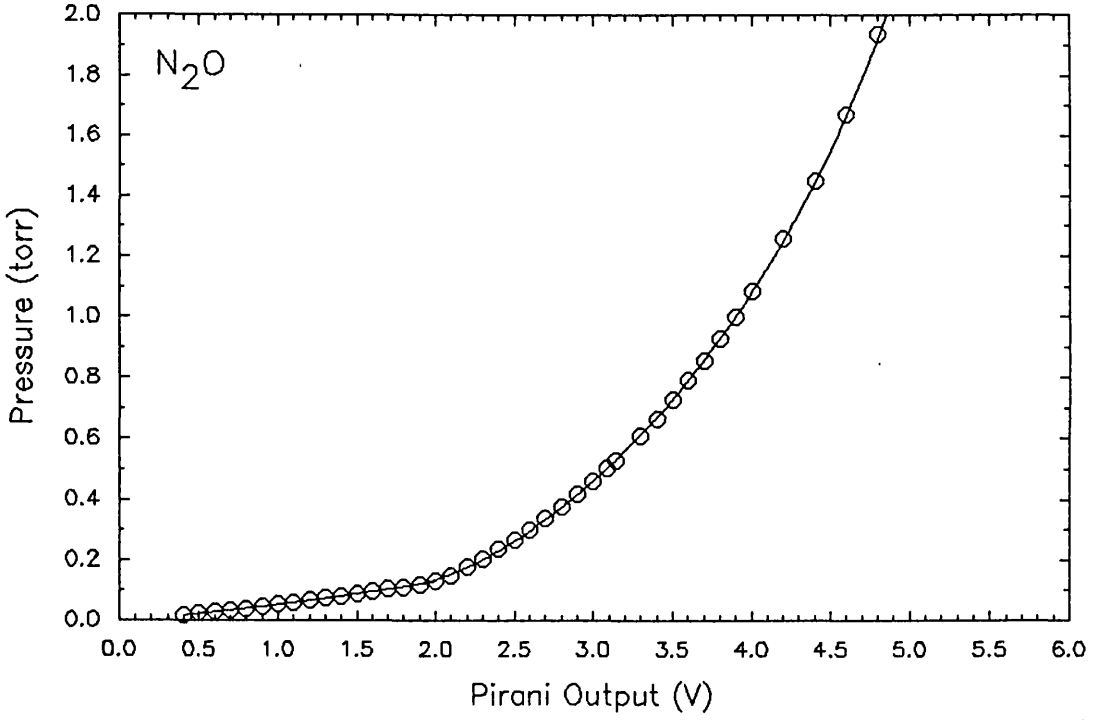

Figure 3.9 A calibration curve of absolute pressure against Pirani output voltage in the presence of nitrous oxide.

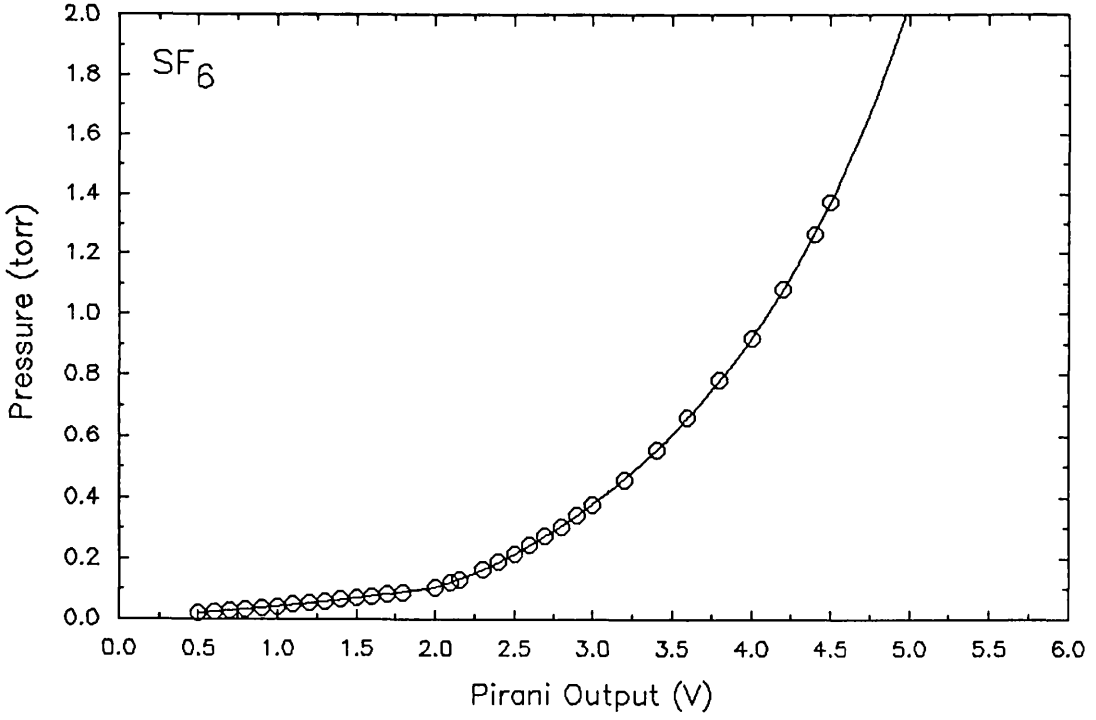

Figure 3.10 A calibration curve of absolute pressure against Pirani output voltage in the presence of sulphur hexafluoride.

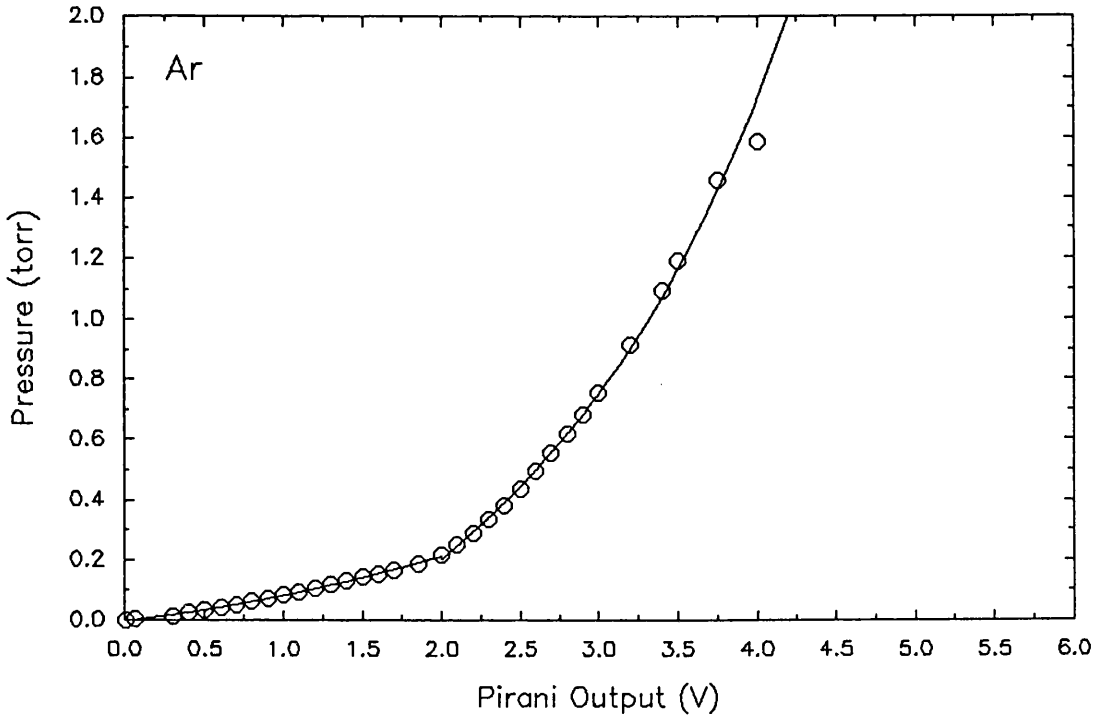

Figure 3.11 A calibration curve of absolute pressure against Pirani output voltage in the presence of argon.

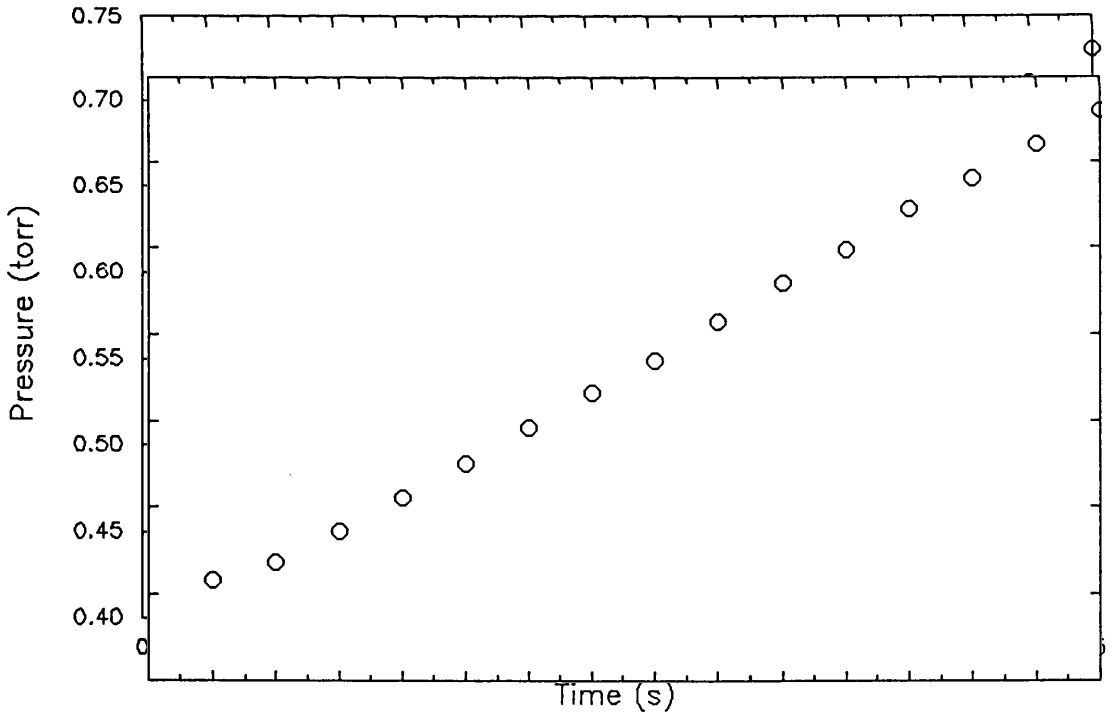

Figure 3.12 A graph of pressure rise (in region 2 of gas line) as a function of time measured with helium gas.

	a_0	a_1	a_2	a_3	a_4
He					
$V_p \leq 2V$	3.4493×10^{-3}	4.4568×10^{-2}	1.1428×10^{-2}		
$V_p > 2V$	2.0766×10^{-1}	-3.3508×10^{-1}	1.8372×10^{-1}	1.9611×10^{-2}	1.4201×10^{-3}
N_2O					
$V_p \leq 2V$	-2.3421×10^{-3}	4.4591×10^{-3}	1.0720×10^{-2}		
$V_p > 2$	1.4153	-1.9474	9.7356×10^{-1}	-1.9289×10^{-1}	1.6498×10^{-2}
H_2O					
$V_p \leq 2V$	5.3382×10^{-3}	2.0736×10^{-2}	1.0876×10^{-2}		
$V_p > 2V$	3.2536×10^{-1}	-4.9682×10^{-1}	2.7152×10^{-1}	-5.0841×10^{-2}	5.0287×10^{-3}
SF_6					
$V_p \leq 2V$	2.3917×10^{-3}	3.0385×10^{-2}	1.0615×10^{-2}		
$V_p > 2$	1.0359	-1.15073	8.0194×10^{-1}	-1.7227×10^{-1}	1.6046×10^{-2}
Ar					
$V_p \leq 2V$	-3.5464×10^{-3}	6.3231×10^{-2}	2.2168×10^{-2}		
$V_p > 2$	-3.9959×10^{-1}	1.1136×10^{-1}	1.1564×10^{-1}	-4.8952×10^{-2}	9.0419×10^{-3}

Table 3.1 Calibration coefficients to convert pirani output voltage to absolute pressure. $P = \sum a_n V_p$ where V_p is the output voltage from the pirani and P is the pressure in torr.

capillary tube was based on one described by Khakoo and Trajmar (1986). The gas under investigation, was admitted to the chamber via the capillary tube using the procedure described in section 3.6 and the pressure in region 2 of the gas line allowed to stabilise. With a constant pressure in region 2, the flow rate through the needle valve was equal to the flow rate through the capillary tube. Valve V2 was then closed and the rise in pressure in region 2 was measured at regular intervals for a time period, t. As the pressure differential between regions 1 and 2 was large, the rise in pressure in region 2 had no effect on the flow rate through the needle valve and after an initial transitionary period, the pressure was seen to rise linearly with time. This is illustrated in figure 3.12, which shows a typical plot of pressure versus time taken with helium. This process was repeated for several different initial pressures. The relationship between the flow rate and the rate of change of pressure dp/dt could then be found using the ideal gas law

$$pV = nkT \qquad 3.2$$

where V is the volume of region 2, p is the pressure in region 2, n is the number of gas molecules, k is Boltzmann's constant and T is the room temperature. Differentiation of equation 3.2 with respect to time gives

$$dn/dt = dp/dt\ (V/Tk) \qquad 3.3$$

where dn/dt is the flow rate. It was not necessary to determine the absolute value of the flow rate as only the ratio of the flow rates was required.

The rate of change of pressure in region 2 was recorded using a BBC computer. The 0-10V output from the Pirani control unit was fed into the analogue to digital convertor (ADC) of the BBC computer via a simple interface unit. The purpose of the interface was to reduce the maximum voltage to less than 1.8V, the maximum acceptance voltage of the ADC. A program was written to control the sampling time of the voltage, to convert the voltage to a pressure and finally to calculate dp/dt. The program allowed the user to set the sampling period and the total sampling time. For

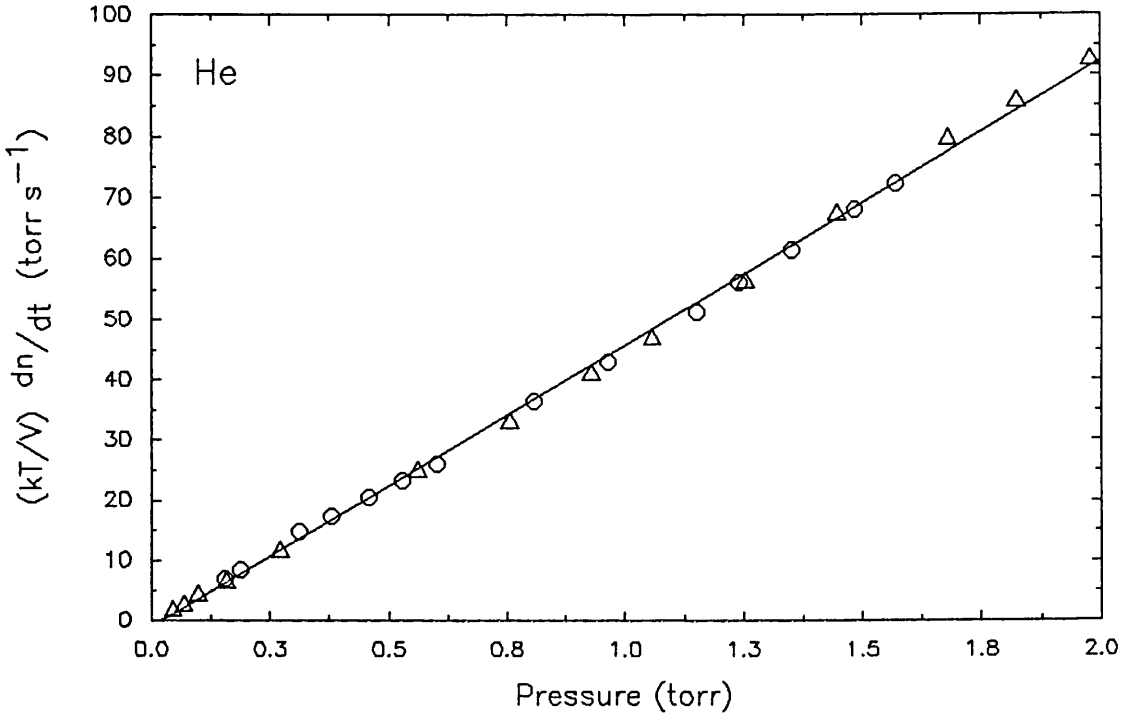

Figure 3.13 A graph of helium flow rate through the capillary tube against pressure as measured in region 2 of the gas line. Different symbols represent several sets of measurements.

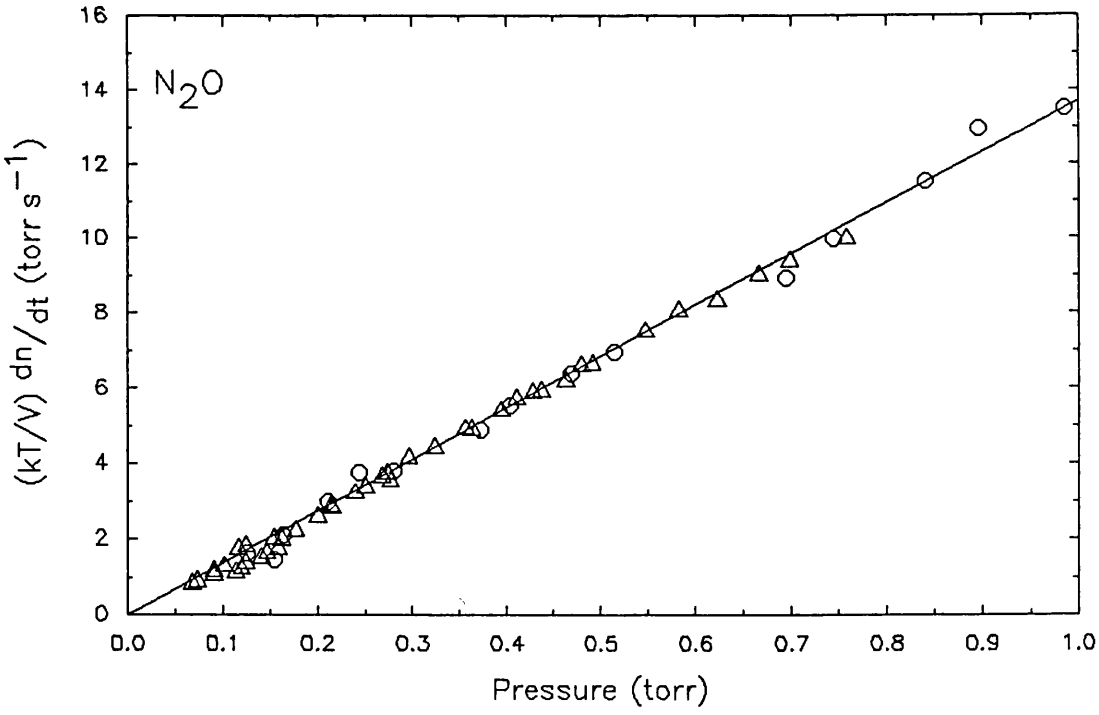

Figure 3.14 A graph of nitrous oxide flow rate through the capillary tube against pressure as measured in region 2 of the gas line. Different symbols represent several sets of measurements.

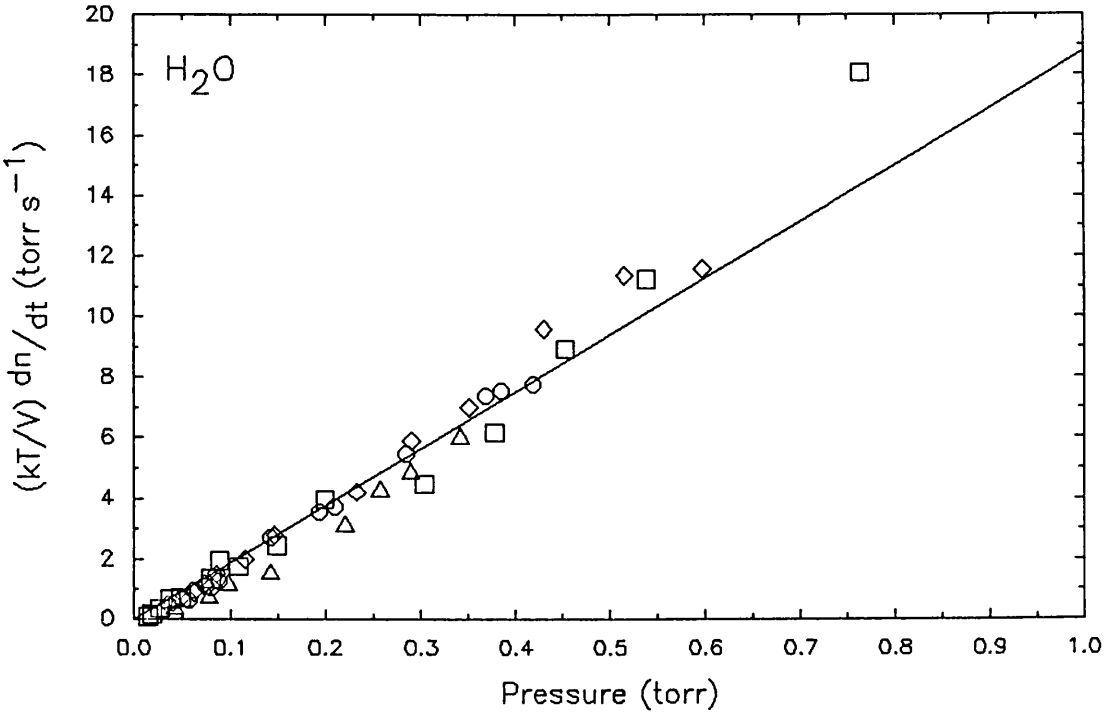

Figure 3.15 A graph of water vapour flow rate through the capillary tube against pressure as measured in region 2 of the gas line. Different symbols represent several sets of measurements.

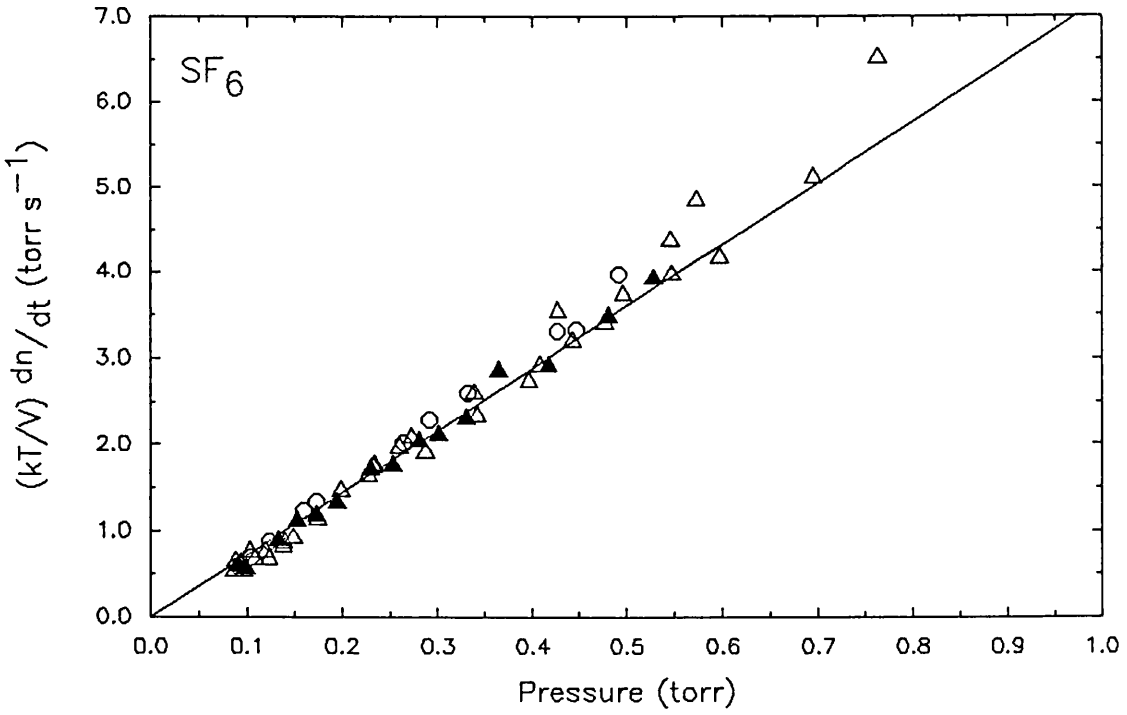

Figure 3.16 A graph of sulphur hexafluoride flow rate through the capillary tube against pressure as measured in region 2 of the gas line. Different symbols represent several sets of measurements.

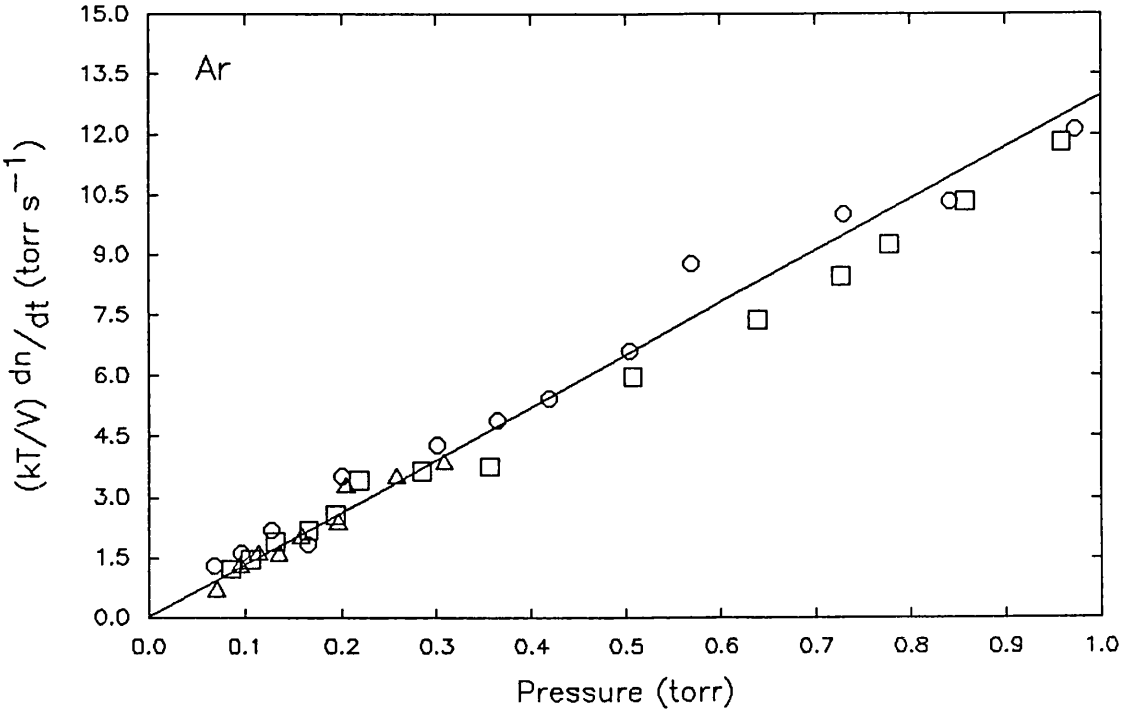

Figure 3.17 A graph of argon flow rate through the capillary tube against pressure as measured in region 2 of the gas line. Different symbols represent several sets of measurements.

each conversion, a number between 0 and 4095 was generated by the ADC and the relationship between this number and the voltage output from the Pirani determined by feeding a known voltage to the ADC before each run. At the end of each run, the voltages were converted to pressure using the data given in section 3.6. The value of dp/dt could then be calculated. If necessary all the data could be stored on disc for further analysis at a later date.

The relationship between the pressure in region 2 and the flow rate through the capillary tube was found for all the gases used in this work and the results are shown in figures 3.13 to 3.17. All the figures show that there was a linear dependence between the flow rate and the pressure.

3.9 The Spectrometer Power Supplies

The spectrometer power supplies were designed to comply with the following requirements:

a) The a.c. ripple had to be minimised to prevent modulation of the electron

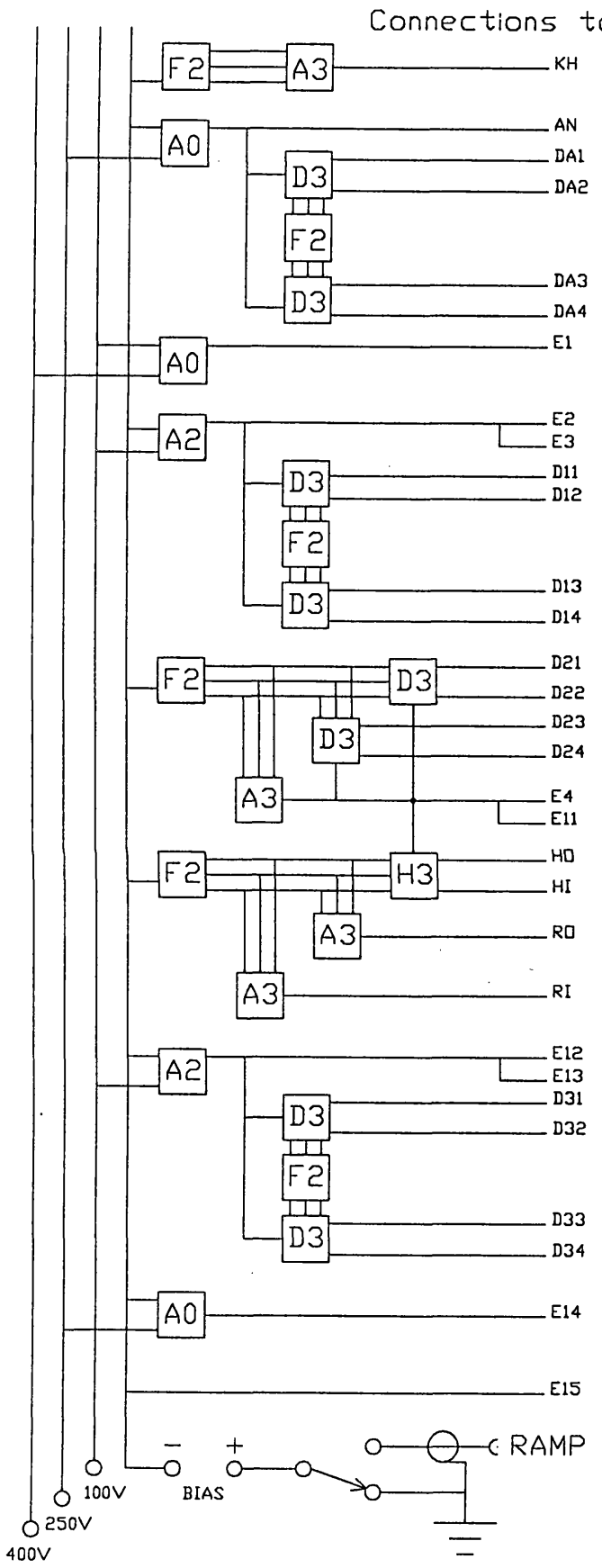

Figure 3.18 A schematic diagram of the power supplies providing the voltages to all the electrodes in the first half of the spectrometer. Details of the individual power supplies are given in figure 3.20. DA1-DA4, D11-D14, D21-D24 and D31-D34 refer to the deflectors shown in figures 2.11 and 2.12. HI and HO are the connections to the inner and outer hemispheres of the monochromator and RI and RO are the connections to the inner and outer fringing field correcting hoops. All other connections are to the lens elements shown in figures 2.11 and 2.12.

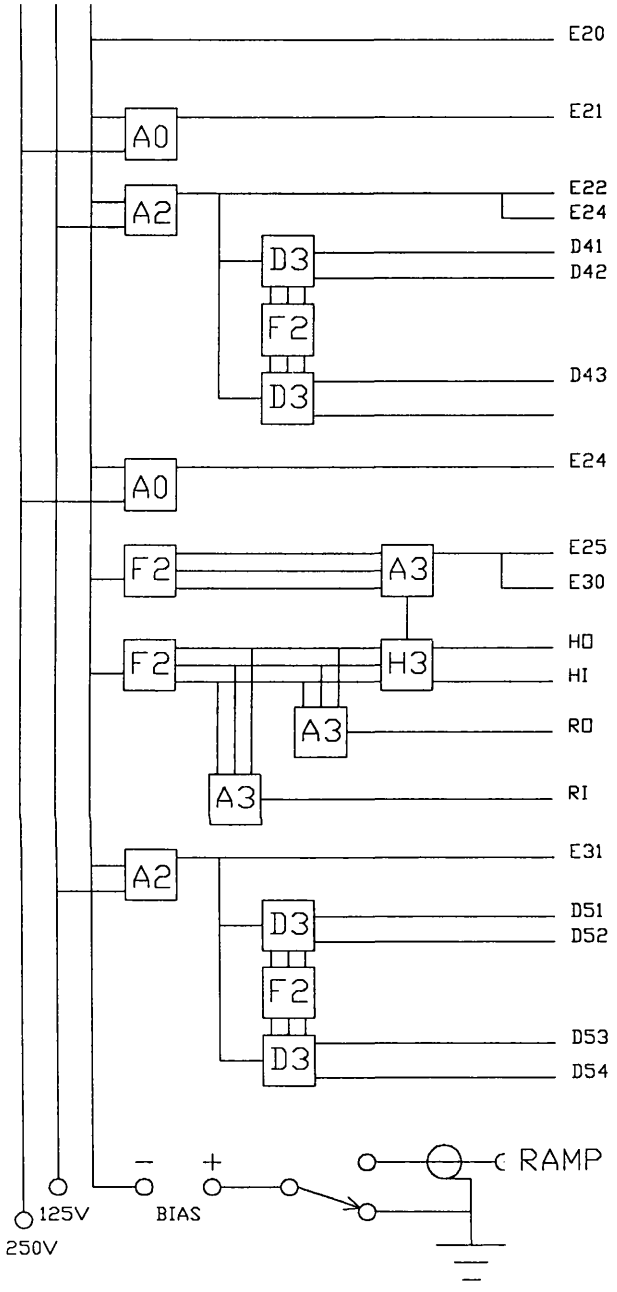

Figure 3.19 A schematic diagram of the power supplies providing the voltages to all the electrodes in the second half of the spectrometer. Details of the individual power supplies are given in figure 3.20. D41-D44 and D51-D54 refer to the deflectors shown in figures 2.13 and 2.14. HI and HO are the connections to the inner and outer hemispheres of the analyser and RI and RO are the connections to the inner and outer fringing field correcting hoops. All other connections are to the lens elements shown in figures 2.13 and 2.14.

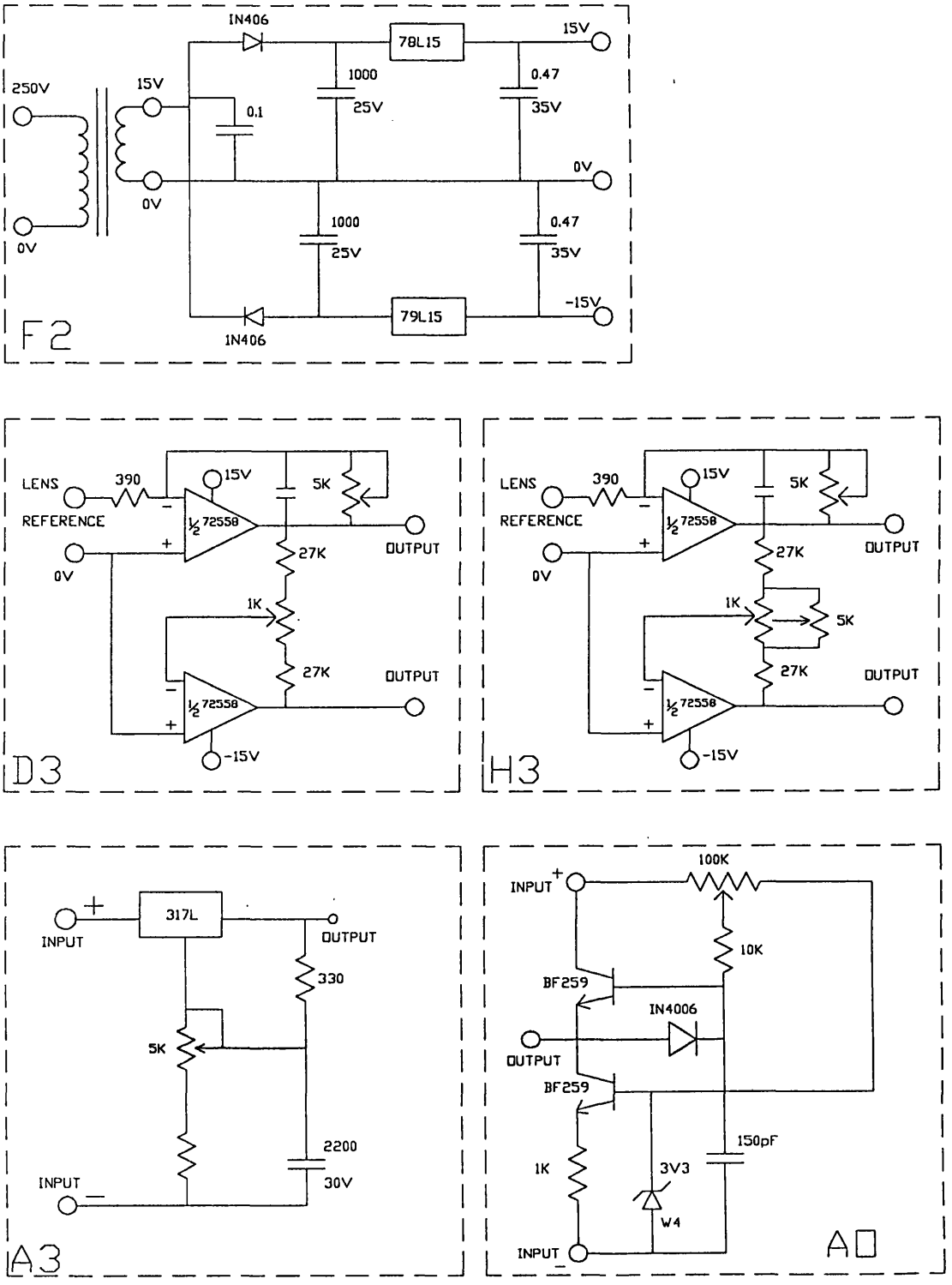

Figure 3.20 The layouts of the individual circuits used to provide the outputs shown in figures 3.18 and 3.19.

beam energy which would degrade the resolution,

b) The output from the supplies had to be smoothly varying to allow precise tuning of the lens voltages.

The power supplies used were designed and built in house and were based on a series of transistor, variable voltage regulators and operational amplifier circuits, which had a low impedance output and included ten turn potentiometers in the control circuits. The a.c. ripple on these circuits was always observed to be less than 5meV, of which the major contribution came from the supply lines. Particular care was taken in the earthing arrangements to eliminate any loops which would increase pick-up. Diagrams of the overall electrical arrangement of the power supplies are given in figures 3.18 and 3.19. Circuit diagrams of the individual power supplies are shown in figure 3.20.

The bias voltage power supplies (Kingshill 1500) were used to set the energy of the electron beam at the interaction region and were connected between the 0V line and the ground. All lens voltages were measured with respect to the 0V line. The filament was connected to the negative terminal of the bias supply of the first half of the spectrometer via a pair of identical resistors. To enable the 19.37eV He resonance profile (see figure 2.18) to be measured, a staircase voltage ramp was applied between the ground and bias supplies of the first and second halves of the spectrometer. To allow the energy distribution of the scattered electrons to be measured, the ramp voltage was only applied to the bias supplies of the second half of the spectrometer.

3.10 Signal Detection

In the analysing half of the spectrometer, electrons were detected with a channel electron multiplier (CEM) Mullard type X919BL driven by a voltage of 2.75kV applied to its back end and this gave a typical gain of $1x10^8$. The output pulses from the CEM were fed into a charge sensitive pre-amplifier, with a typical gain of ≈10 (Petley, 1971). These output from the pre-amplifier was further amplified using a spectroscopy amplifier (Ortec, model 575) and subsequently fed into a discriminator (Ortec, model 550) where the contributions from any electrical noise were eliminated. The count rate from the CEM was monitored with a ratemeter (Ortec, model 541). An identical arrangement, was used to detect the pulses from the CEM in the reference detector.

To enable the count rates from both CEMs to be measured simultaneously, pulses from both discriminators were fed into a dual counter (Ortec, model 778) and gated using a timer/counter (Ortec, model 773).

When measuring the He resonance profile or the energy spread of the scattered electrons, the output from the CEM in the second half of the spectrometer (or in the reference detector) was fed into a multichannel analyser (MCA). The channel advance was triggered by the ramp generator for each new step in the ramp voltage. When a suitable spectrum had been collected, the data was down loaded onto a BBC computer where it could be saved onto a floppy disk allowing the data to be analysed at a later date.

CHAPTER 4

Absolute Differential Cross Section Measurements

4.1 Introduction

Since the 1930s, a large amount of data for differential cross sections in electron molecule collisions has been published. A significant proportion of this data has been in the form of relative scattering intensities measured as a function of incident energy, scattering angle or electron energy loss. However, in the last ten to fifteen years there has been an increasing demand for *absolute* electron collision cross sections for use in developing models of gas lasers, plasma devices and planetary atmospheres. Theorists have also required data with which to compare the results of the numerous models used to calculate electron collision cross sections.

A number of experimental techniques have been developed to measure absolute cross sections and the method employed is dependent upon the atom or molecule chosen for study, the energy of the incident electrons and the process under investigation. In the present work, absolute elastic differential cross sections for electron scattering from three molecular targets (SF_6, N_2O and H_2O) were measured and the approach used employed a two stage process. The relative differential cross sections, normalised at 90°, were obtained using the subtraction technique. The absolute value of the differential cross section at 90° was then measured with the relative flow technique and the value obtained subsequently used to normalise the relative differential cross section values onto an absolute scale. In the following sections, a detailed description is given of the scattering geometry used and the experimental procedures required by the subtraction and relative flow techniques. For convenience, the terms monochromator and analyser have been used to denote the first and second halves of the spectrometer respectively.

4.2 The Scattering Geometry

Two types of scattering geometry are commonly used in electron scattering measurements, a gas cell geometry and a crossed beam geometry. The gas cell geometry may be employed in one of two configurations (Kuyatt, 1968). In the first, the complete vacuum system containing both the monochromator and analyser is filled with the target gas. However, to observe a significant scattered electron signal, the pressure in the chamber has to be increased to levels which may have an adverse effect on the electron source and the electron optics. This problem can be reduced by adopting a second configuration in which a small differentially pumped cell contained within the main chamber, is filled with the target gas. The incident and the scattered electrons enter and the leave the cell through small apertures or slots in the cell walls. There are a number of disadvantages in using a gas cell geometry, in particular the increased pumping requirements and the increase in the energy spread of the scattered electrons due to Doppler broadening effects. Chantry (1971) has shown that the increase in the energy spread ΔE_{dp} due to Doppler broadening can be calculated using

$$\Delta E_{dp} = (E/E_i)^{1/2}\ \Delta_T \qquad 4.1$$

where

$$\Delta_T = 4(\ln 2)^{1/2}\ (kTmE_i/M)^{1/2} \qquad 4.2$$

and

$$E = (m/2)\Delta v^2 = (m/2)(v_i^2+v_f^2-2v_iv_f\cos\theta) \qquad 4.3$$

where m and M are the electron and target mass, T is the target temperature, v_i and v_f are the incident and final electron velocities, θ is the scattering angle and Δv is the change in electron velocity. Clearly the value of ΔE_{dp} is dependent on the scattering angle, incident energy and target mass. For example, for electrons with an incident energy of 20eV elastically scattered through 90° from an helium gas cell at 293K, ΔE_{dp} will be 29meV. This value will add in quadrature to the initial energy spread of the electron beam and the resolution of the analysing half of the spectrometer (Read, 1975), increasing the observed FWHM of the energy distribution of the scattered electrons.

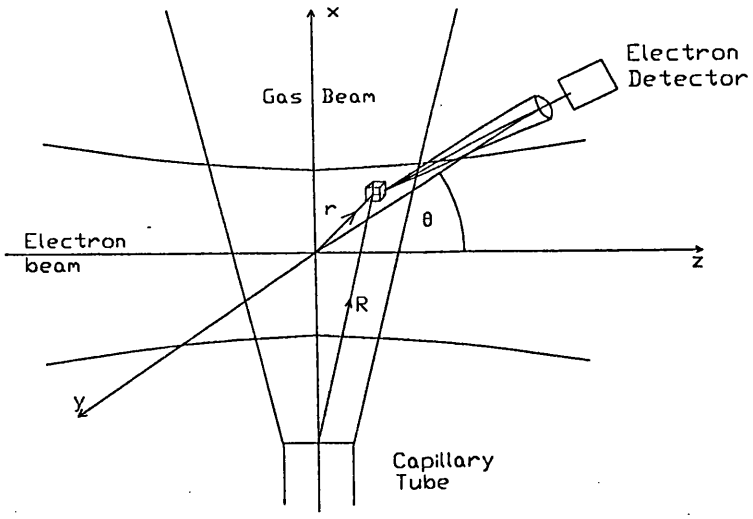

Figure 4.1 The scattering geometry used in a typical crossed beam experiment (Nickel *et al*, 1989).

The crossed beam geometry employed in the present work is now used in virtually all differential scattering experiments. In this configuration, the incident electron beam intersects a gas beam produced from any variety of sources such as an orifice, capillary tube, an array of capillary tubes (capillary array) or a supersonic nozzle. Densities in these gas beams corresponding to pressures of 10^{-3} torr are easily obtained, with the size and intensity of the beam dependent upon the type of source. Capillary tubes and arrays are the most commonly used sources as they provide high intensity, low divergence beams yet do not require high pumping speeds. If the gas and electron beams intersect at 90° (which is the usual configuration) the effects of Doppler broadening will be significantly reduced. When the gas beam has an intensity distribution with a full angular width at half-maximum equal to Δ_B radians, the value of ΔE_{dp} is reduced by factor $\approx 1/2\Delta_B$ (Read, 1975). One problem encountered with the crossed beam geometry is the determination of the size of the gas beam and hence the overlap volume with the electron beam.

4.3 The Relationship Between The Scattered Electron Flux And The Cross Section In The Crossed Beam Configuration

The geometry used in a typical crossed beam configuration is shown in figure 4.1. The observed scattered electron count rate, $N^e(E_o,\theta_o)$, for electrons elastically

scattered through an angle θ° from an electron beam of incident energy E_o is (Nickel *et al*, 1989)

$$N^e(E_o,\theta_o) = \int_{V,E} \sigma(E,\theta(\mathbf{r}))\eta(E,\mathbf{r})N(\mathbf{r})F^e(E,\mathbf{r})\Delta\Omega^e(\mathbf{r})dEdV \qquad 4.5$$

where $\sigma(E,\theta(\mathbf{r}))$ is the elastic differential cross section (DCS) at an incident energy E and angle $\theta(\mathbf{r})$. The distance from the centre of the overlap of the electron and gas beams to a scattering point within the overlap volume is defined as **r**. $F(E,\mathbf{r})$ and $N(\mathbf{r})$ are the electron and gas beam distributions, respectively. The solid angle subtended by the electron detector at the scattering point **r** is $\Delta\Omega^e(\mathbf{r})$ and $\eta(E,\mathbf{r})$ is the probability of detecting the scattered electrons once they had entered the analyser. The integration extends over the energy spread of the beam E and the surface of the scattering volume V defined by the overlap of the two beams.

A number of approximations can be made to reduce the complexity of equation 4.5. First, if the cross section is slowly varying in energy and angle with respect to the detector resolution then the DCS can be averaged over the instrumental resolution. Thus $\sigma(E_o,\theta_o)=\sigma(E,\theta(\mathbf{r}))$ and the cross section term can be removed from the integral. Secondly, η can be assumed constant over the range of scattering angles and incident energies defined by the energy and angular resolution of the detector and so this term can also be removed from the integral. Finally, it can be assumed that the function $F^e(E,\mathbf{r})$ can be separated into two parts $F^e(E)F^e(\mathbf{r})$. Thus equation 4.5 reduces to

$$N^e(E_o,\theta) = \eta(E_o)\sigma(E_o,\theta)V_{eff}(\theta)C(E) \qquad 4.6$$

where

$$V_{eff}(\theta) = \int_V F^e(\mathbf{r})N(\mathbf{r})\Delta\Omega^e(\mathbf{r})dV \qquad 4.7$$

and

$$C(E) = \int_E F^e(E)dE_o \qquad 4.8$$

The quantity C(E) is the integral over the energy spread of the incident electron beam and $V_{eff}(\theta)$ is known as the effective scattering volume or path length correction.

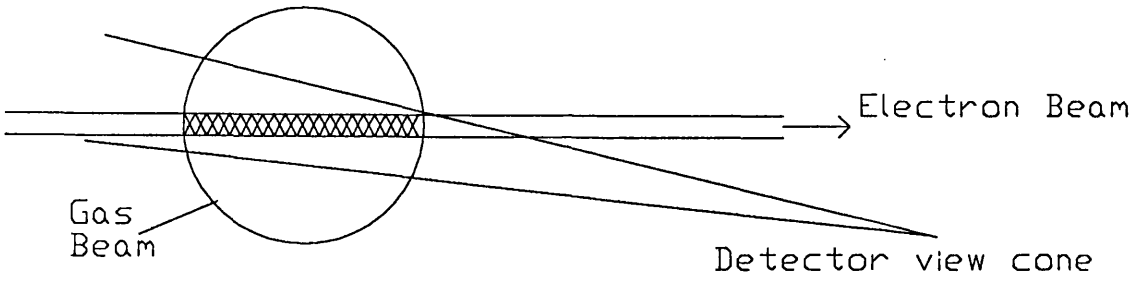

Figure 4.2a Overlap of the electron and gas beams seen by the detector for a scattering angle $\theta \approx 10°$.

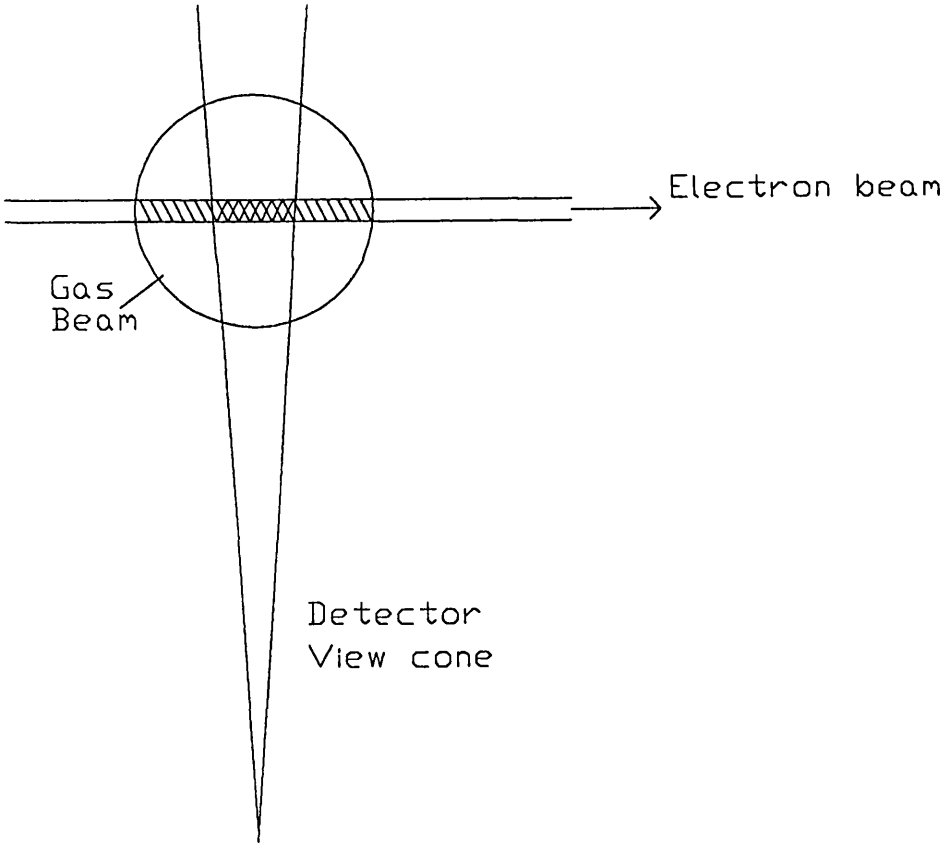

Figure 4.2b As figure 4.2b except $\theta = 90°$.

$V_{eff}(\theta)$ will have an angular dependence if the total overlap volume does not lie within the view cone of the detector. If this is the case, then as the analyser is rotated to different scattering angles, the amount of the overlap volume seen by the detector will change. This is illustrated in figures 4.2a and 4.2b. From figure 4.2a it can be seen that for a small scattering angle, the complete overlap volume lies within the detector view cone but for a scattering angle of 90° (figure 4.2b) only 50% of the scattering volume is within the view cone. Thus the scattered electron count rate will be artificially reduced as the scattering angle increases. If the gas and electron beam sizes ($F(\mathbf{r})$ and $N(\mathbf{r})$) and the solid angle of the detector are known, $V_{eff}(\theta)$ can be calculated. Brinkman and Trajmar (1981) have performed such calculations for a number of commonly used gas beam sources (capillary tubes and arrays and orifices) and expressed their results in terms of an "effective path length" correction factor defined as

$$F_{eff}(\theta) = V_{eff}(90°)/V_{eff}(\theta) \qquad 4.9$$

The value of $F_{eff}(\theta)$ can also be inferred from measurements made on an atomic or molecular target for which the cross section is already well known, for example the elastic scattering cross section from helium. This method will be described in more detail in section 4.8.

4.4 Absolute Measurements

In the previous section the relationship between the scattered electron count rate, the cross section and the various experimental parameters for a crossed beam configuration was given. In principle, if $\eta(E_o)$, $V_{eff}(\theta)$ and $C(E)$ are known and the scattered electron flux is measured it is possible to calculate $\sigma(E_o,\theta)$. For high energy electron beams (>100eV) and a gas cell configuration, $C(E)$ and $V_{eff}(\theta)$ can be accurately calculated or measured and $\sigma(E_o,\theta)$ determined from the scattered electron count rate measurements (Chamberlain *et al*, 1970). At low or intermediate energies,

a calculation of $V_{eff}(\theta)$ becomes less reliable due to uncertainties in the electron beam size resulting from lens aberrations and the influence of stray magnetic and electric fields. Further complications arise when using a crossed beam geometry due to the difficulty in calculating the gas beam density distribution. Therefore, absolute differential cross sections at low and intermediate energies are usually obtained using one of two other methods.

In the first method, relative differential cross sections ($\sigma_{rel}(E_o,\theta)$ are measured and these values related to the absolute integral cross ($\sigma_t(E_o)$) section using

$$\sigma_t(E_o) = 2\pi\ A(E_0)\int_o^{\pi}\ \sigma_{rel}(E_o,\theta)\sin\theta d\theta \qquad 4.10$$

where $A(E_0)$ is a normalisation constant. Thus the absolute value of the differential cross section, $\sigma_{ab}(E_0,\theta)$, is

$$\sigma_{ab}(E_0,\theta) = A(E_0)\sigma_{rel}(E_0,\theta) \qquad 4.11$$

The absolute integral cross section, σ_t, is usually obtained from the total cross section σ_T, the ionisation cross section σ_{ion} and the total excitation cross section σ_{exc} using

$$\sigma_t = \sigma_T-\sigma_{ion}-\sigma_{exc} \qquad 4.12$$

There are two problems associated with this method. In general, experimental difficulties only allow the DCS to be measured over a limited angular range, usually between 10° and 140°, requiring the relative DCS values to be extrapolated in the low and high angular regions. If the DCS is changing rapidly at the angles where it cannot be measured, then significant errors may occur in the extrapolation process. The second problem arises in obtaining a value of σ_t. Values of σ_T are now available for a large

number of molecules with accuracies better than 5% (Trajmar *et al*, 1983). Values of σ_{ion} are also available for a wide range of molecules but there is a greater uncertainty in the absolute magnitude and the shape of the cross sections (Märk, 1983). In comparison, the values of σ_{exc} are known for only a small number of molecules over a limited energy range. At high energies, σ_{exc} may become comparable to σ_{ion} and this may lead to significant errors in the calculation of σ_t.

A second method frequently used is the relative flow technique. In this procedure, the unknown elastic differential cross section is determined by comparing the intensity of the scattered electron flux from the molecule under investigation with that from an atom or molecule whose cross section is already well known. If the electron beam density, the detection efficiency and the flux distributions of the two gas beams remain the same in both measurements, then the ratio of the cross sections can be determined from the relative scattering intensities and the relative target densities of the two gas beams.

In this work, normalisation to the integral cross section was not used for two reasons. First, the largest angle at which the scattered electron flux could be measured was 120°, requiring the differential cross section to extrapolated from 130° to 180° with the attendant possibility of large errors. Secondly, for the molecules studied in this work, little or no data existed to enable an accurate value of σ_{exc} to be used. Therefore, absolute differential cross sections were obtained using the relative flow technique which will now be described in detail.

4.5 The Relative Flow Technique

The relative flow technique for measuring absolute elastic differential cross sections from gaseous targets was first used by Srivastava *et al* (1975). Since then, the technique has been refined by a number of authors and has recently been reviewed by Nickel *et al* (1989). Using the relative flow technique, the elastic differential cross

section is determined by a measurement of the relative scattering intensities between the molecule under investigation and an atom or molecule whose cross section is already well established. The ratio of the scattering intensities from the two gases is given by

$$\frac{N^e_1(E_o,\theta)}{N^e_2(E_o,\theta)} = \frac{\eta_1(E_o,\theta)\ \sigma_1(E_o,\theta)\ \int F^e_1(\mathbf{r})N_1(\mathbf{r})\Delta\Omega^e_1(\mathbf{r})dV \int F^e_1(E)dE}{\eta_2(E_o,\theta)\ \sigma_2(E_o,\theta)\ \int F^e_2(\mathbf{r})N_2(\mathbf{r})\Delta\Omega_{e2}(\mathbf{r})dV \int F^e_2(E)dE} \qquad 4.13$$

where the subscript 1 refers to the molecule whose cross section is to be determined and the subscript 2 refers to the gaseous species used as the reference standard. If the electron beam profile, the detector efficiency and the solid angle of the detector remain the same in both measurements then equation 4.13 can be simplified to

$$\frac{N^e_1(E_o,\theta)}{N^e_2(E_o,\theta)} = \frac{\sigma_1(E_o,\theta) \int N_1(\mathbf{r})\ dV}{\sigma_2(E_o,\theta) \int N_2(\mathbf{r})\ dV} \qquad 4.14$$

reducing the problem to a determination of the relative target densities of the two gas beams.

Olander and Kruger (1970) and Giordmaine and Wang (1960) have studied the flow of gases through a capillary tube under a variety of flow rate conditions and have obtained expressions from which N(**r**) can be calculated. Before continuing, a few terms will be introduced which are commonly used when discussing the flow of a gas through a capillary tube. The capillary tube (of length l and diameter d) used to produce a gas beam is attached to a source reservoir containing a gas of density N_s at a temperature T_s. The kinetic molecular diameter of the gas is δ and λ_s $(=1/(2)^{1/2}N_s\pi\delta^2)$ is the mean free path of the gas in the source reservoir. Two other terms commonly used are the Knudsen number, K_{nl} $(=\lambda_s/l)$, which relates the mean free path in the source reservoir based to the length of the capillary and the aspect ratio, γ $(=d/l)$, of the tube.

From Olander and Kruger (1970), the intensity (in molecules s^{-1} sr^{-1}) at a polar angle θ (with respect to the central axis of the tube) is

$$J(\theta) = (\upsilon_s/\pi)(\pi d^2/4)\ j(\theta) \qquad 4.15$$

where υ_s is the rate at which gas molecules enter the tube and $j(\theta)$ is the normalised flux distribution function. The flow rate of gas, N', through the tube is

$$N' = K\upsilon_s\ (\pi d^2/4) \qquad 4.16$$

where K (=4d/3l) is the Clausing factor. From equation 4.15 and 4.16 it can be seen that

$$J(\theta) = (j(\theta)\ N')/(\pi K) \qquad 4.17$$

The spatial density distribution $N(\mathbf{r})$ is related to $J(\theta)$ by

$$N(\mathbf{r}) = J(\theta)/(R^2 v) \qquad 4.18$$

where R is the distance from the end of the capillary tube exit to the point $\mathbf{r}$ (see figure 4.1) and v is the mean velocity of molecules in the gas beam. Substituting equation 4.17 into equation 4.18 yields

$$N(\mathbf{r}) = [N'j(\theta)]/(\pi K R^2 v) \qquad 4.19$$

and equation 4.14 can be rewritten as

$$\frac{N^{e}_{1}(E_o,\theta)}{N^{e}_{2}(E_o,\theta)} = \frac{\sigma_1(E_o,\theta)\ N_1'\ v_2 \int j(\theta)\ d\theta}{\sigma_2(E_o,\theta)\ N_2'\ v_1 \int j(\theta)\ d\theta} \qquad 4.20$$

The expressions used to describe $j(\theta)$ depend on the density in the source reservoir. If the density is such that the mean free path of the gas in the source region is greater than the length of the capillary tube then $j(\theta)$ is dependent upon the collisions between the gas and the walls of the capillary tube and this is known as the molecular flow regime. Using a computational method described by Clausing (1930), Olander and Kruger (1970) derived an expression for $j(\theta)$ in the molecular flow regime which predicted the shape and density of the gas beam. However, in this regime the resultant gas beam density is low which results in large data collection times due to the low scattered electron count rate. Thus, the gas beam density is usually increased by raising the pressure in the source reservoir. As the pressure in the source is increased, the mean free path falls and the effects of inter-molecular collisions become important. Olander and Kruger (1970) also derived expressions for $j(\theta)$ in which these effects were included. They found that although $j(\theta)$ was affected by the presence of inter-molecular collisions, the flow rate could still be calculated using equation 4.19 if the Knudsen numbers in the source region were in the range

$$\gamma < K_{nl} < 10 \qquad 4.21$$

They also found that $j(\theta)$ was dependent only on the dimensions of the tube and the Knudsen number in the source reservoir. This result implies that the angular distribution of two gas beams formed by two different species flowing through the

same tube will be the same provided the Knudsen numbers in the source region are the same. Thus equation 4.20 can be simplified to

$$\frac{N^e_1}{N^e_2} = \frac{\sigma_1(E_0,\theta)\ N'_1\ m_1^{1/2}}{\sigma_2(E_0,\theta)\ N'_2\ m_2^{1/2}} \qquad 4.22$$

where the ratio of the gas beam velocities has been replaced with the ratio of the atomic or molecular masses. Equal Knudsen numbers in the source reservoir for the two gases implies that the mean free paths for the two gases should be the same. Hence, with an accurate knowledge of the relative flow rates, relative scattering intensities and a known cross section $\sigma_2(E_0,\theta)$, the absolute value of $\sigma_1(E_0,\theta)$ can be determined.

4.6 The Experimental Procedure Used To Determine An Absolute Cross Section

Subject to the experimental conditions outlined above, the relative flow technique can be used, in principle, to measure the absolute differential cross section at any scattering angle and incident energy for which it is possible to detect scattered electrons. The stability of the incident electron beam current is usually monitored with a Faraday cup. In the present experiment it was not possible to incorporate such an arrangement due to space limitations, therefore the electron beam current could not be monitored when using the analysing half of the spectrometer to measure the scattered electron flux. To overcome this problem, the reference detector (see section 2.9) was used to measure the scattered electron flux enabling the incident electron beam to be collected and monitored in the post-interaction lens stack (lenses 5, 6 and 7). Adopting this approach meant that an absolute measurement of the differential cross section could only be made at one angle, −90°. To obtain absolute values at the remaining angles, the relative

differential cross section was measured from 10° to 120° using the subtraction technique (see section 4.7) and normalised to an absolute scale with the value determined at 90°.

In obtaining an absolute value of the differential cross section at 90°, the following procedure was adopted. The calibration gas, helium, was admitted to the vacuum chamber through the capillary tube and the contact potential determined by measuring the position of the 19.37eV helium resonance. The energy of the electron beam was then set to the desired value, suitably corrected for the contact potential and the spectrometer tuned to give the maximum electron beam current with the desired FWHM at the interaction region. The unscattered electron beam was collected in the post-interaction region optics and deflected onto the aperture A7 (see figure 2.13) where its magnitude could be measured. The voltage applied to the centre element of the lens in the reference detector was then adjusted so as to allow only those electrons elastically scattered from the gas beam to reach the channeltron.

The pressure in the source reservoir was then adjusted such that the mean free path of the helium atoms was the same as the capillary tube diameter (0.6mm), the scattered electron count rate at the reference detector, N^e_{Heb}, was measured with the data collection time chosen to give a statistical accuracy better than 2%. The pressure P_{He} in the source reservoir, the current I_{He} reaching A7, and the background pressure in the vacuum chamber were also monitored. To ascertain the contribution from electrons scattered from the background gas in the chamber and other possible sources, the procedure was repeated without the gas beam present but with the same background pressure. The scattered electron count rate N^e_{Hec} was measured and the data collection time again chosen to obtain a statistical accuracy better than 2%. The flow of helium was then replaced by the molecular species X under investigation, with the flow of the second gas directed through the capillary tube and the pressure in the source reservoir chosen to give the same Knudsen number as that used for the helium measurements. The scattered electron count rate, N^e_{Xb}, the pressure, P_X, the current, I_X reaching A7 and

the background pressure were again measured. The second gas was then diverted from the capillary tube to the side leak and the background count rate, N^{e}_{Xc}, was measured. From equation 4.22, the ratio of the two cross sections is given by

$$\frac{\sigma_X(E,\theta)}{\sigma_{He}(E,\theta)} = \frac{(N^{e}_{Xb}-N^{e}_{Xc})\ N_{He}{}'\ (m_{He})^{1/2}}{(N^{e}_{Heb}-N^{e}_{Hec})\ N_X{}'\ (m_X)^{1/2}} \qquad 4.23$$

When changing between the two gases, it was not uncommon for the incident electron beam current to change. To account for this Kanik *et al* (1989) have suggested adding two current terms to equation 4.23 giving

$$\frac{\sigma_X(E,\theta)}{\sigma_{He}(E,\theta)} = \frac{(N^{e}_{Xb}-N^{e}_{Xc})\ N_{He}{}'\ (m_{He})^{1/2}\ I_{He}}{(N^{e}_{Heb}-N^{e}_{Heb})\ N_X{}'\ (m_X)^{1/2}\ I_X} \qquad 4.24$$

The flow rates ($N_{He}{}'$ and $N_X{}'$) were determined in a separate experiment (see section 2.8) where the relationship between the reservoir pressure, P, and the flow rate, N′, was found. The value of the helium cross sections were taken from two sources. For incident energies below 20eV, the data of Nesbet (1979) were used, while for energies of 20eV and above the data of Register *et al* (1980a) were used. Nesbet (1979) calculated the first three phases shifts for incident energies between 0.58eV and 19eV using a variational calculation. Using these phase shifts, the absolute helium differential cross section could be calculated for any angle and at any energy between 0.58eV and 19eV. The data of Register *et al* (1980a) was obtained by measuring the relative differential cross section, extrapolating it to 0° and 180° and then normalising to the integral cross section using the procedure outlined in section 4.4. For energies where the two works overlapped, the cross sections were found to be in good agreement (within 5%).

In order to test the validity of the procedure described above, a measurement was made of the absolute elastic differential cross section for electron scattering from

Energy	Present	Furst et	al (1989)	Williams	Srivastava	*et al*	Fon *et al*
(eV)	Work			(1979)	(1981)		(1983)
	RFT	PSA	RFT	PSA	PSA	RFT	Theory
5	1.11±0.09	0.87±0.08	0.91±0.1		0.97	0.82±0.16	0.88
10	1.07±0.09	0.97±0.06	1.02±0.12	1.12	1.1	0.78±0.16	0.92
15	0.54±0.05	0.54±0.05	0.49±0.06	0.58	0.57	0.62±0.12	0.54

Table 4.1 Absolute elastic differential cross sections for electron scattering at 90° from argon ($x10^{-16}cm^2sr^{-1}$). RFT denotes values obtained using the relative flow technique and PSA denotes values obtained using a phase shift analysis.

argon at 5eV, 10eV and 15eV. Several measurements of these cross sections have been reported using a variety of techniques and it therefore provided a good target with which to test the experimental technique. Table 4.1 shows the results of the present work together with those of previously published reports. All of the results shown, except those of Fon *et al* (1983), were obtained experimentally. The results of Fon *et al* (1983) were derived theoretically using an R-matrix calculation described by Fon *et al* (1981) and Fon and Berrington (1981). The experimentally derived results were obtained using the relative flow technique (RFT) or from a phase shift analysis (PSA) of relative differential cross section data. From table 4.1, it can be seen that there is good agreement between the present results and those of the previous studies. This confirmed that the procedure adopted for measuring absolute differential cross sections using the relative flow technique was essentially correct and that accurate values could be obtained.

4.7 Relative Differential Cross Section Measurements

In the previous section, the procedure used to make an absolute measurement of the differential cross section at 90° was described. To obtain absolute cross sections at the remaining angles, the relative differential cross section was measured and then normalised to an absolute scale using the value measured at 90°. In this

section, a description is given of the technique used to measure relative differential cross sections (normalised to 90°) at scattering angles between 10° and 120°.

A major problem associated with any electron scattering experiment is ensuring the long term stability of both the electron and target gas beams. This is particularly important when making comparisons between measurements made at different scattering angles, as it must be established whether any variations observed are due to a change in the cross section or a change in intensity of either the gas or electron beam. The stability of the target gas beam can be easily monitored by observing the pressure in the source reservoir and it is usual for the electron beam current to be measured by collection in a Faraday cup. However, for the reason given in the previous section, it was not possible to employ one in the present spectrometer. Therefore, a slightly different approach was adopted.

The observed scattered count rate is directly proportional to the electron beam current and the gas beam density. Therefore, if a detector were to be placed at a fixed scattering angle, any fluctuations in the gas or electron beam intensities would produce a similar change in the observed count rate. In the present work, this was achieved with the use of the reference detector positioned at a fixed scattering angle of θ=–90°. Each time a count rate was recorded by the analyser at an angle θ, it was normalised to the simultaneously measured count rate from the reference detector. Thus, if $D(\theta)$ was the count rate recorded from the analyser and $R(\theta)$ was the count rate simultaneously recorded from the reference detector, then the ratio of the cross sections, $\sigma(\theta)/\sigma(90°)$, was given by

$$\frac{\sigma(\theta)}{\sigma(90°)} = \frac{D(\theta)R(90°)\ F_{eff}(\theta)}{D(90°)R(\theta)} \qquad 4.25$$

Any change in $D(\theta)$ due to a change in gas pressure or electron beam current was compensated for in the ratio $R(90°)/R(\theta)$. The term $F_{eff}(\theta)$ is the volume correction factor introduced in section 4.3 and its presence is necessary to correct for the

varying amount of the overlap volume seen by the analyser at different scattering angles.

Equation 4.25 assumes that the only source of scattered electrons is the target gas beam. If there are significant contributions to the count rates measured by either detector from sources other than the gas beam then equation 4.25 must be modified to account for these extra contributions. In the present work there were three additional sources to the detected signals: electrons scattered from the background gas, electrons scattered from the surfaces in and around the interaction region and electrons from the primary beam. The contribution from the background gas was dependent on the pressure in the chamber, the incident beam current and the scattering angle. The angular dependence was a result of the angular behaviour of the differential cross section and the changes in the overlap volume of the electron beam and the background gas seen by the analyser at different scattering angles. The contribution from surface scattering was also found to be dependent on the scattering angle as well as the incident beam current. Finally, electrons from the edge of the primary beam were detected by the analyser at small scattering angles (10° and 15°) and low incident beam energies (≤10eV), where the angular divergence of the beam was large (≈5°).

Hence the count rates measured by the analyser (D_{bc}) and the reference detector (R_{bc}) in the "beam plus cell" configuration may be given by

$$D_{bc} \propto I_o[(V_{beff}(\theta)\rho_b + V_{ceff}(\theta)\rho_c)\sigma(\theta) + S_D(\theta) + B_D(\theta)] \qquad 4.26$$

$$R_{bc}(\theta) \propto I_o[(\rho_b + \rho_c)\sigma(90°) + S_R(\theta)] \qquad 4.27$$

where ρ_b represents the gas beam density, ρ_c is the density of the background gas in the cell, $S_D(\theta)$ and $S_R(\theta)$ are the contributions from electrons scattered from surfaces and $B_D(\theta)$ is the contribution from the primary beam. In the case of a "cell only"

configuration the measured count rates are given by

$$D_c(\theta) \propto I_o'[V_{ceff}(\theta)\rho_c\sigma(\theta) + S_D(\theta) + B_D(\theta)] \quad 4.28$$

$$R_c(\theta) \propto I_o'[\rho_c\sigma(\theta) + S_R(\theta)] \quad 4.29$$

where due allowance has been made for any possible change in the electron beam current in the two measurements. Combining equations 4.26 and 4.27 with 4.28 and 4.29 yields the following expressions

$$D_b = D_{bc}(\theta)-(I_o/I_o')D_c \propto I_o[V_{beff}(\theta)\rho_b\sigma(\theta)] \quad 4.30$$

$$R_b = R_{bc}(\theta)-(I_o/I_o')R_c(\theta) \propto I_o[\rho_b\sigma(\theta)] \quad 4.31$$

Thus equation 4.25 can be rewritten as

$$\frac{\sigma(\theta)}{\sigma(90)} = \frac{[D_{bc}(\theta)-(I_o/I_o')D_c(\theta)][R_{bc}(90°)-(I_o/I_o')R_c(90°)]F_{eff}(\theta)}{[D_{bc}(90°)-(I_o/I_o')D_c(90°)][R_{bc}(\theta)-(I_o/I_o')R_c(\theta)]} \quad 4.32$$

To obtain the true value of $\sigma(\theta)/\sigma(90°)$, $F_{eff}(\theta)$ must be determined. The principles underlying the derivation of equation 4.32 were first introduced by Andrick and Bitsch (1975). The derivation of equations 4.25 to 4.32 are based on a refinement of the subtraction technique used by Newell *et al* (1981).

4.8 The Determination Of $F_{eff}(\theta)$

The quantity $F_{eff}(\theta)$ represents the changing overlap volume of the gas and the electron beams seen by the analyser as a function of scattering angle relative to that

seen at 90°. For example, if the view cone of the analyser were to encompass the entire overlap volume at any scattering angle, then $F_{eff}(\theta)$ would be equal to 1. However, if the gas beam was large and the view cone of the analyser narrow, then the fraction of the total overlap volume seen by the analyser would change with the scattering angle and $F_{eff}(\theta)$ would show a $\sin\theta$ dependence (Kuyatt, 1968). Ideally, the analyser should be designed such that the view cone always encompasses the total overlap volume but this can result in the analyser having a large angular resolution making it insensitive to abrupt changes in the differential cross section occurring over a small angular range. In most experiments, the form of $F_{eff}(\theta)$ lies somewhere between these two cases.

Two methods can be employed to determine $F_{eff}(\theta)$. If the overlap volume of the electron and gas beams can be calculated and the solid angle of the analyser is known, then $F_{eff}(\theta)$ can be computed. Brinkman and Trajmar (1981) have performed such a calculation for a variety of gas beam sources and detector solid angles. Alternatively, $F_{eff}(\theta)$ can be found by measuring the relative differential cross section, normalised to 90°, for an atom or molecule where the differential cross section is already well known. $F_{eff}(\theta)$ is then the value needed to match the measured values with the true values.

In the present work, differential cross section measurements were made over a large range of incident energies (5eV to 80eV) and therefore the electron beam did not have a fixed spatial profile. Thus, it was expected that the value of $F_{eff}(\theta)$ would be dependent on the electron beam energy and the focusing of the beam. Therefore, the second method described above was used to determine $F_{eff}(\theta)$. Due to the availability of accurate differential cross section over a wide range of energies helium was chosen as the gas with which to determine $F_{eff}(\theta)$.

4.9 The Experimental Procedure Used To Determine The Relative Differential Cross Section

Helium was admitted to the system via the capillary tube and the source reservoir pressure allowed to rise to ≈1 torr. The contact potential was determined from an observation of the position of the 19.37eV helium resonance and the incident electron beam energy set to the desired value corrected for the effects of the contact potential. The spectrometer was then tuned to maximise the current, I_o, reaching the outer hemisphere in the analyser. The voltage applied to the centre element of the lens in the reference detector was then adjusted to achieve a peak count rate, as described in section 3.9. The monochromator was then rotated to a scattering angle of 10° and the potentials applied to the analysing hemispheres adjusted until the peak elastic scattering count rate was observed. The count rates from both the analyser and the reference detector were then recorded as a function of scattering angle for angles between 10° and 120° with the timing period chosen to give a statistical accuracy better than 2%.

The helium gas flow to the capillary tube was then stopped and redirected through the side leak into the main chamber. The background pressure was then allowed to rise until it reached the same level observed with the gas beam present. The current, I_o', reaching the outer hemisphere of the analyser was measured and the scattered electron count rates recorded at the same scattering angles with the gas beam present. Using equation 4.32, the value of $F_{eff}(\theta)$ was then calculated using the count rates measured from both detectors and the value of $\sigma(\theta)/\sigma(90°)$ calculated from the helium differential cross section data of Nesbet (1979) or the results of Register *et al* (1980).

The helium flow was then stopped and replaced by the molecule under investigation. Again the gas flow was directed through the capillary tube but the pressure in the source reservoir was chosen so that the Knudsen numbers for the

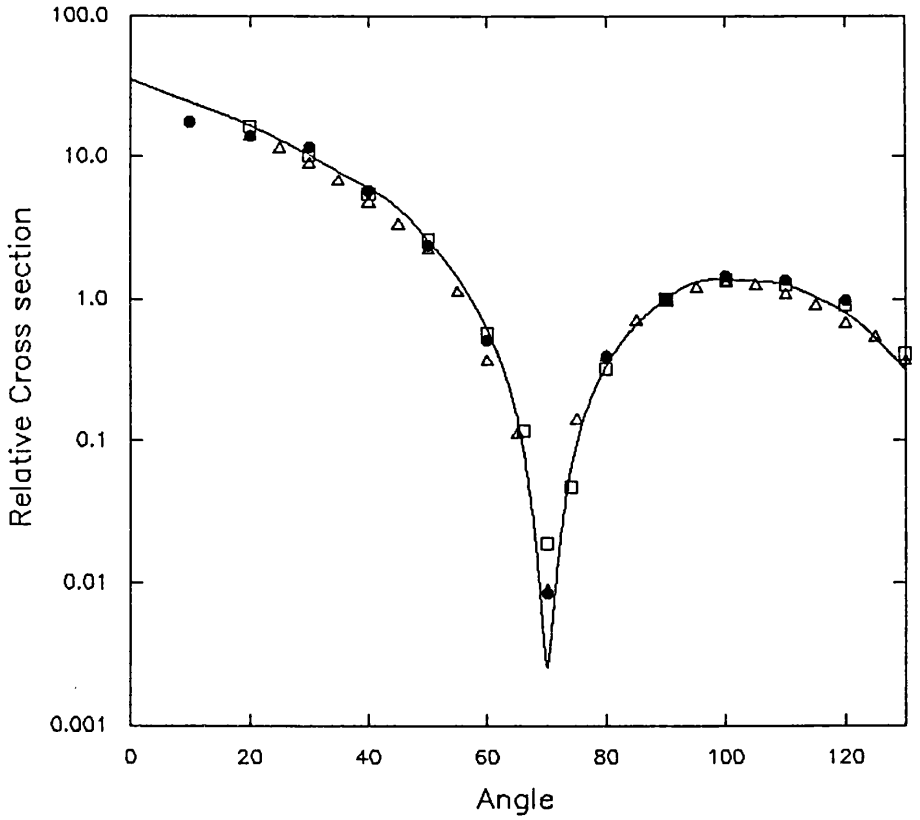

Figure 4.3 Relative elastic differential cross section for electron scattering from argon for an incident energy of 30eV. Experimental data: ● Present work; □ Williams and Willis (1976); △ Srivastava *et al* (1981). Theory: —— Fon *et al* (1983). All data has been normalised to their respective values at 90°.

molecule and helium were the same. This ensured that the two gas beams were the same size and therefore the overlap volume remained unchanged (see section 4.5). The count rates from both detectors were then measured for scattering angles between 10° and 120° using the same procedure employed to make measurements from helium. Great care was taken not to alter any lens voltages or deflector settings in the spectrometer. The relative differential cross section from the molecule was then calculated from the measured count rates and the values of $F_{eff}(\theta)$ calculated from the helium measurements.

To determine the accuracy of this technique, relative differential cross section measurements were made on argon and the results with an incident electron beam energy of 30eV are shown in figure 4.3. The experimental results of Srivastava *et al* (1981) and Williams and Willis (1975) and the theoretical calculations of Fon *et*

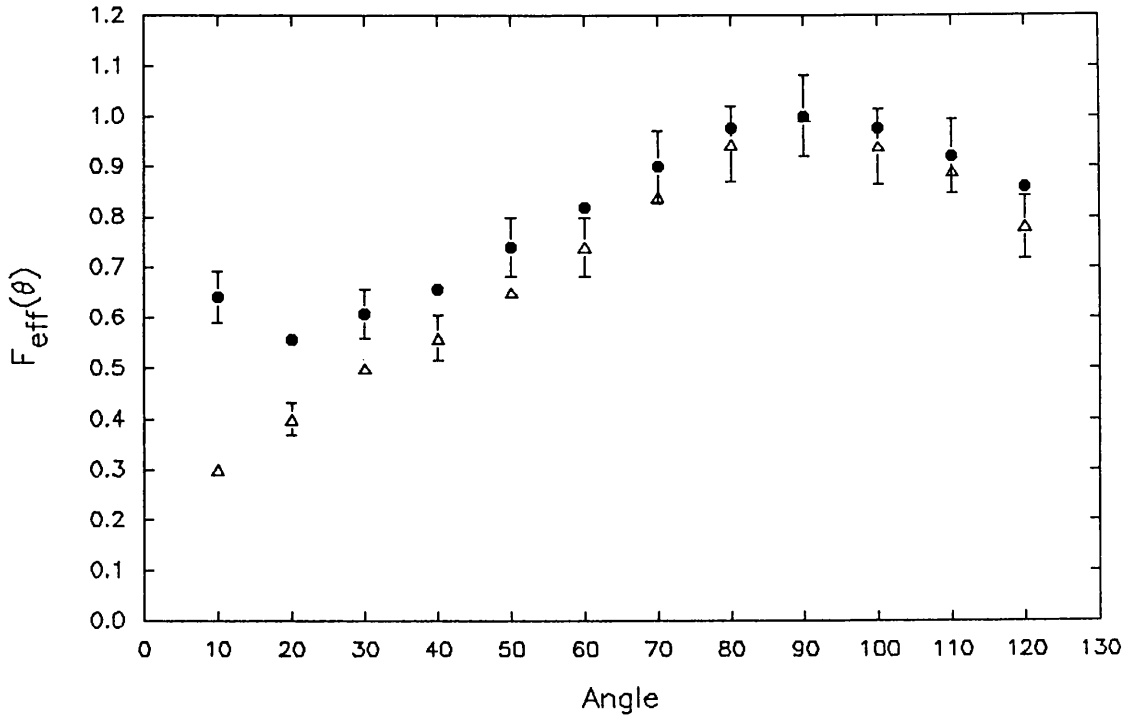

Figure 4.4 Two volume corrections determined for an incident electron beam energy of 30eV but recorded on different days.

al (1983) are also shown. These results were originally given as absolute cross sections but have been normalised to their respective values at 90° to enable a comparison with the present work. There is excellent agreement between the present results and those of the previous studies, confirming the validity of the technique described above. It should also be noted that the position of the minimum is in good agreement with the previous works, verifying the correct angular calibration of the rotation mechanism.

Finally, it was found that shape of the volume correction changed for different electron beam energies and for measurements made at the same energy but taken on different days and this is illustrated in figure 4.4. Therefore, each time an unknown differential cross section was measured the necessary volume correction was also measured.

4.10 Errors

The errors associated with the absolute differential cross section measurements arose from several sources and can be divided into two groups: those from the

measurement of the relative differential cross section and those from the determination of the absolute differential cross section value at 90°. For the relative differential cross section measurements, the first source of uncertainty arose from the measurement of $F_{eff}(\theta)$. The value of $F_{eff}(\theta)$ was determined by comparing the values obtained from a measurement of a relative differential cross section with the correct values. Therefore the uncertainty in $F_{eff}(\theta)$ was the result of the statistical errors in the measured count rates, errors in measuring the electron beam current, the error in the pressure measurement in the vacuum chamber plus the error in the published helium data. The magnitude of the error associated with the measured parameters was calculated to be ≈5%. For the helium cross section data, it was the error in the shape of the differential cross section that was required rather than the error in the absolute values. In the data of Nesbet (1979), the error in the calculated cross section was given as 1.5%. Register *et al* (1980a) quote errors of between 3.5% and 5% on the shapes of their differential cross section data. Therefore, a value of 5% was chosen as the error in the relative differential cross sections used to determine $F_{eff}(\theta)$. Thus, the final error ascribed to the values of $F_{eff}(\theta)$ was 7%. The errors in measuring the unknown differential cross section were the same as those for the helium differential cross section measurement (≈5%). Therefore, the error in the final values of the relative differential cross section for the molecule being studied was 9%.

For the absolute cross section measurements made at 90°, the sources of experimental uncertainties arose from the measurement of the flow rate, 5%, and errors in the current measurement, 2%. The error in the scattered electron signal contained two contributions, statistical counting errors, 3% and a contribution from inelastically scattered electron. As a result of the low resolution of the reference detector, a small proportion of the measured electron count rate may have been due to the detection of inelastically scattered electrons which had excited vibrational energy levels in the molecules under investigation. The three molecules studied, SF_6 H_2O and N_2O, were found to have vibrational excitation cross sections which were at most 2% of the elastic cross section at 90° for the non-resonant energies studied in this work (SF_6, Trajmar and Chutjain (1977); H_2O, Shyn *et al* (1988); N_2O, Andric and Hall (1984) and Tronc *et al* (1981)). However, for electron scattering from SF_6 at incident electron energies

of 12eV the ratio of vibrational excitation and elastic cross sections was seen to rise to 5% (Trajmar and Chutjian (1977). A similar behaviour was seen in N_2O at 8eV where the ratio was found to rise to 3.5% (Andric and Hall (1984) and Tronc *et al* (1981)).

Therefore, the total error in the relative intensities measured by the reference detector was found to vary between 6% and 8% depending on the incident energy and the target. The error on the absolute helium cross section at 90° used varied between 5% and 7%. Thus, the errors in the absolute measurements were calculated to be between 8% and 11%. Therefore, the final error in any absolute differential cross section measured in this work was found to be between 12% and 14%.

CHAPTER 5

Absolute Elastic Cross Sections For Electron Scattering From SF_6

5.1 Introduction

In this chapter, measurements are reported for the absolute elastic differential, integral and momentum transfer cross sections for electron scattering from sulphur hexafluoride (SF_6). In addition to providing a useful comparison with theory, there are several practical applications where electron scattering cross sections from SF_6 are of considerable interest. For example, as the feature sizes of very large scale integrated circuits are reduced to the sub-micron level, dry plasma etching techniques are gradually replacing wet chemical etching methods (Endo and Kurogi, 1980, Pinto *et al*, 1987). This is due to the ability of the dry etching process to give anisotropic and highly directional vertical etch profiles with good selectivity. In this respect halogen bearing gas discharges (e.g. SF_6) have proved effective as they provide large quantities of fluorine atoms and other active species capable of selectively etching a silicon surface.

SF_6 is also widely used as a gaseous dielectric to prevent high voltage breakdown, for example in high voltage ($\geq$ 300kV) power supplies, high voltage switch gear and transmission lines, where extensive damage can occur due to arcing between electrodes (Christophorou *et al*, 1982). Since SF_6 has a very large cross section ($5.2 \times 10^{-14} cm^2$ Chutjian, 1981) for the formation of SF_6^- at near zero electron energies, many of the low energy electrons are "mopped up" before they can be accelerated to energies high enough to initiate an avalanche breakdown.

In order to obtain a better understanding of the important physical processes involved in plasma etching and gaseous dielectrics, plasma models are constructed using electron transport equations which require an accurate set of electron-impact cross section data.

SF_6 has an octahedral structure with a sulphur atom at the centre and the fluorine atoms occupying each of the six corners of the octahedron and it is a large polyatomic molecule containing 70 electrons. Therefore, it is not surprising that very little theoretical work has been performed on this system. A validated set of electron scattering cross sections are necessary to provide a benchmark for any further theoretical and experimental investigations.

5.2 Differential Measurements

A number of differential cross section measurements have been reported for electron scattering from SF_6, covering a wide range of incident energies from 0.05eV to 700eV and there are significant disagreements where these measurements overlap. Absolute elastic measurements have been reported by Rohr (1979) for incident electron energies between 0.05eV to 10eV and for scattering angles between θ=20° and 120°, by Srivastava *et al* (1976) for energies between 5eV to 75eV for θ=20° to 135° and by Sakae *et al* (1989) between 75eV to 700eV for θ=5° to 135°. Trajmar and Chutjian (1977) have reported relative measurements between 9eV and 17eV for θ=20°, 60°, 90° and 135°. Absolute inelastic measurements have been reported by Rohr (1977) in a study of vibrational excitation for impact energies between 0.05 and 3eV. Trajmar and Chutjian (1977) have also studied vibrational excitation for incident energies between 9 and 17ev and made absolute measurements of electronic excitation for an incident energy of 20eV.

The results of the present work are shown in figures 5.1 to 5.16 and are tabulated in table 5.1. Figures 5.1 to 5.10 show absolute elastic differential cross sections as a function of scattering angle for incident electron beam energies between 5eV and 75eV and the cross sections were determined using the experimental procedures outlined in chapter 4. The data of Srivastava *et al* (1976), Rohr (1979) and Sakae *et al* (1989) are shown for comparison. The data of Srivastava *et al* (1976) have been recalculated by Trajmar *et al* (1983) using the improved helium cross sections of Register *et al* (1980a). In this and the following sections, comparisons between the present work and that of Srivastava *et al* (1976) were made using these renormalised cross sections.

Figure 5.1 shows the results obtained at an incident electron energy of 5eV. The trend of the present cross section data is in qualitative agreement with those of Rohr (1979) and Srivastava *et al* (1976) for scattering angles greater than or equal to 40°. For $\theta<40°$, the data of Srivastava *et al* (1976) shows a minimum, whereas both the present work and the data of Rohr (1979) show a maximum. For incident energies between 10eV and 20eV, there is good agreement between the present work and that of Srivastava *et al* (1976). At 7.2eV, the agreement with the data of Rohr (1979) is also good but at 10eV Rohr's data, as at 5eV, is consistently higher at the smaller scattering angles. At 12eV, there is no previous work with which to compare the present results.

At 30eV (figure 5.7), the present data has the same general shape as that of Srivastava *et al* (1976) but, as at 5eV, the magnitude of the present cross section is consistently lower at scattering angles greater than 40°. At 40eV and 50eV, the major differences between the present work and that of Srivastava *et al* (1976) occur for $\theta\geq100°$ and $\theta\leq40°$. For scattering angles less than 40° a minimum or inflexion is observed in the present work prior to the cross section rising steeply as θ approaches 0°. A similar structure has been seen by Sakae *et al* (1989) at 75eV (figure 5.10), whose data concurs with the present work. The absence of this feature in the data of Srivastava *et al* (1976) may be due to the lower angular resolution of their apparatus compared to that used in either the present work or by Sakae *et al* (1989).

All the differential cross sections shown in figures 5.1 to 5.10 exhibit considerable structure indicating the contribution from a significant number of partial waves in the scattering process. At 5eV (figure 5.1), the present data shows a relatively flat shape and the absence of any forward peaking in the behaviour of the cross section at the small scattering angles suggests that there is a large contribution from the l=0 partial wave. Between 7.2eV and 20eV, the maximum at $\theta=35°$, present in the cross section at 5eV disappears and the cross section becomes forward peaked. The position of a minimum, initially located at $\theta=80°$, moves to $\theta\approx60°$ and a second minimum appears at $\approx120°$. This can be attributed to an increasing contribution from the l=2 (d-wave) partial wave and the size of the second minimum at 12eV would seem to indicate that d-wave scattering dominates at this energy. As the incident energy is

	Incident Energy									
θ	5.0eV	7.2eV	10eV	12eV	15eV	20eV	30eV	40eV	50eV	75eV
0										
10			5.00	20.05	7.75		12.62	16.22	15.62	16.90
15		8.19	4.80	15.30	6.55	9.56	9.95	10.21	9.61	8.70
20	2.26	7.02	4.46	12.32	5.44	5.92	7.23	6.23	4.35	2.94
25	2.35	6.54	3.93	9.20	4.83	4.29	4.00	2.61	1.77	1.18
30	2.44	5.64	3.56	7.17	3.86	2.85	1.94	1.18	1.12	1.26
35	2.43	4.76	3.03	4.68	2.90	1.72	1.04	0.81	1.05	1.30
40	2.29	3.82	2.30	3.12	1.87	1.00	0.90	0.83	1.04	1.11
45	2.13	2.98	1.63	1.95	1.14	0.60	1.01	1.00	0.95	0.84
50	2.00	2.20	1.20	1.36	0.77	0.60	1.20	1.03	0.88	0.56
55	1.74	1.58	0.86	0.80	0.67	0.77	1.35	0.96	0.73	0.44
60	1.44	1.15	0.73	0.62	0.81	1.04	1.28	0.79	0.53	0.29
65	1.15	0.87	0.75	0.80	0.96	1.21	1.15	0.58	0.36	0.28
70	0.95	0.78	0.88	0.96	1.09	1.28	0.96	0.41	0.24	0.23
75	0.79	0.79	1.01	1.26	1.19	1.31	0.74	0.26	0.16	0.21
80	0.69	0.91	1.11	1.35	1.15	1.20	0.55	0.17	0.15	0.20
85	0.71	1.06	1.19	1.42	1.16	1.03	0.42	0.17	0.21	0.20
90	0.74	1.32	1.17	1.44	0.99	0.81	0.35	0.20	0.23	0.17
95	0.81	1.41	1.04	1.44	0.89	0.68	0.35	0.27	0.26	0.15
100	0.91	1.37	0.90	1.37	0.76	0.59	0.44	0.34	0.29	0.15
105	1.00	1.27	0.78	1.25	0.69	0.55	0.52	0.42	0.30	0.14
110	1.04	1.14	0.64	1.28	0.65	0.55	0.59	0.46	0.34	0.16
115	1.06	1.05	0.61	1.31	0.64	0.61	0.62	0.48	0.38	0.23
120	1.04	0.93	0.61	1.51	0.64	0.72	0.66	0.52	0.43	0.27
error	12.0%	12.0%	12.0%	13.0%	12.0%	12.0%	13.0%	12.5%	12.5%	13.0%

Table 5.1 Absolute elastic differential cross sections for electron scattering from SF_6 ($x10^{-16}cm^2sr^{-1}$).

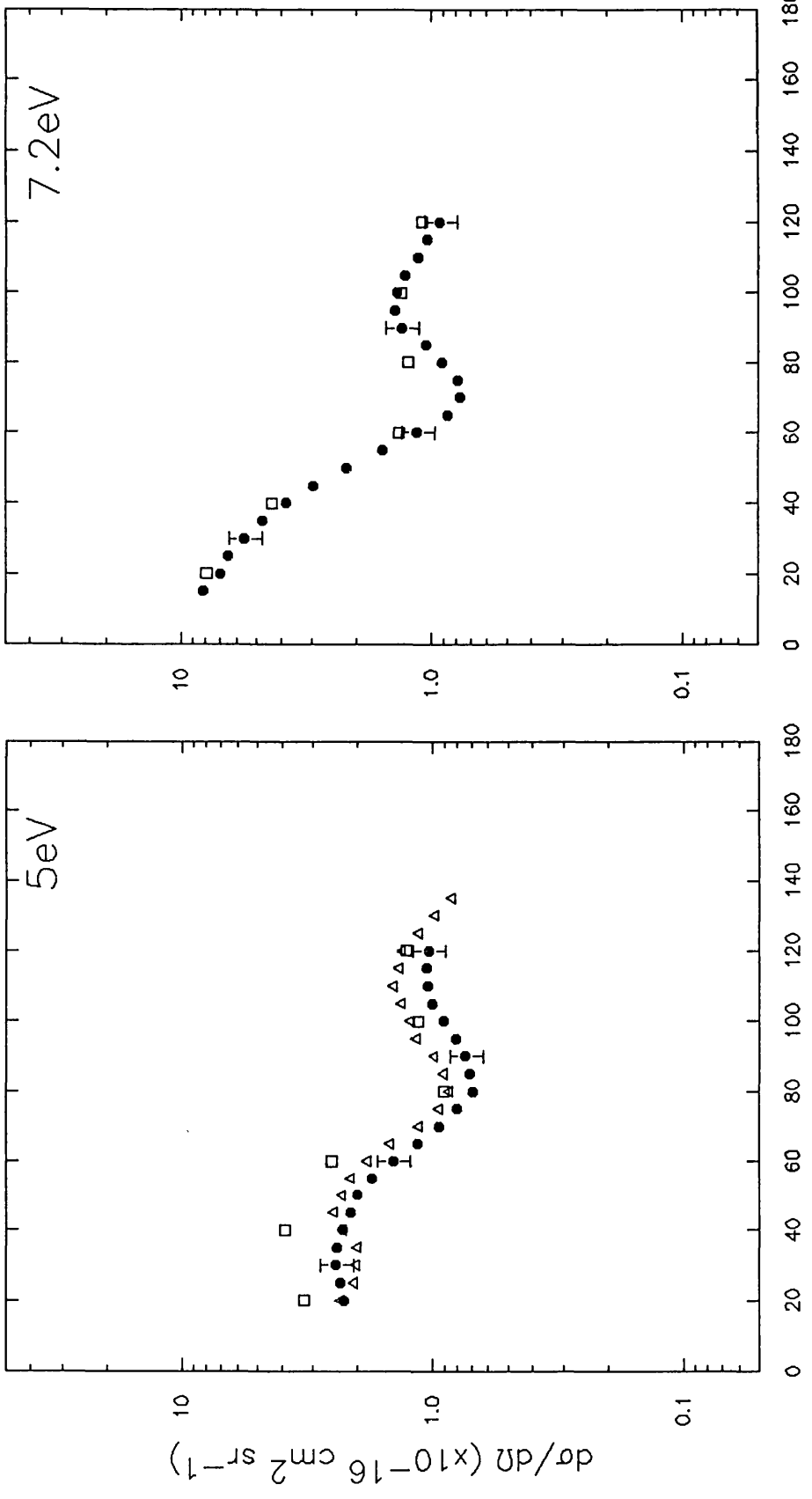

Figure 5.1 Absolute elastic differential cross sections for electron scattering from SF_6 for an incident energy of 5eV (x10^{-16} cm^2 sr^{-1}). ● Present work; △ Srivastava *et al* (1976); □ Rohr (1979).

Figure 5.2 Absolute elastic differential cross sections for electron scattering from SF_6 for an incident energy of 7.2eV (x10^{-16} cm^2 sr^{-1}). ● Present work; □ Rohr (1979).

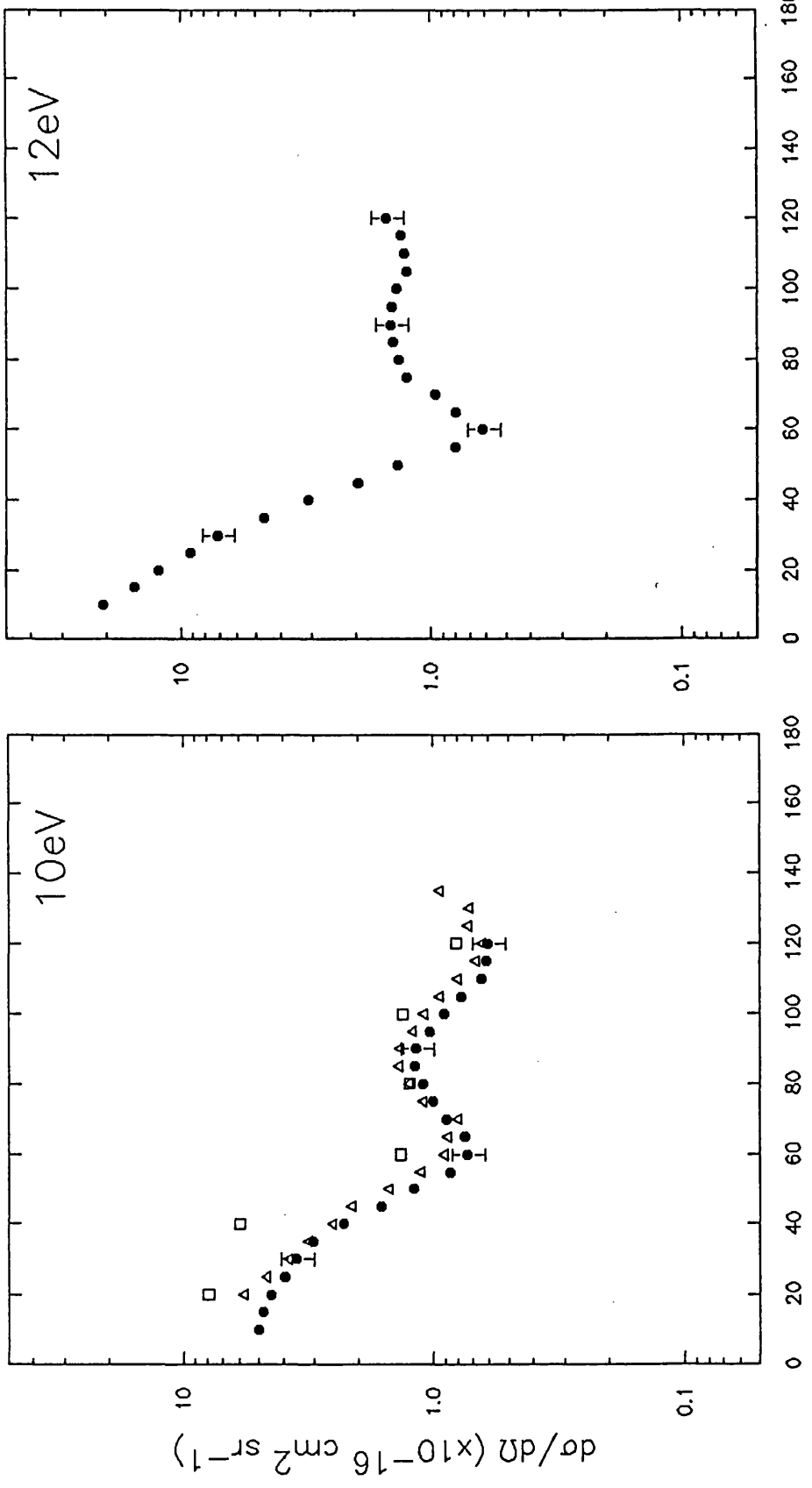

Figure 5.3 Absolute elastic differential cross sections for electron scattering from SF_6 for an incident energy of 10eV (x10^{-16} cm^2 sr^{-1}). ● Present work; △ Srivastava *et al* (1976); □ Rohr (1979).

Figure 5.4 Absolute elastic differential cross sections for electron scattering from SF_6 for an incident energy of 12eV (x10^{-16} cm^2 sr^{-1}). ● Present work.

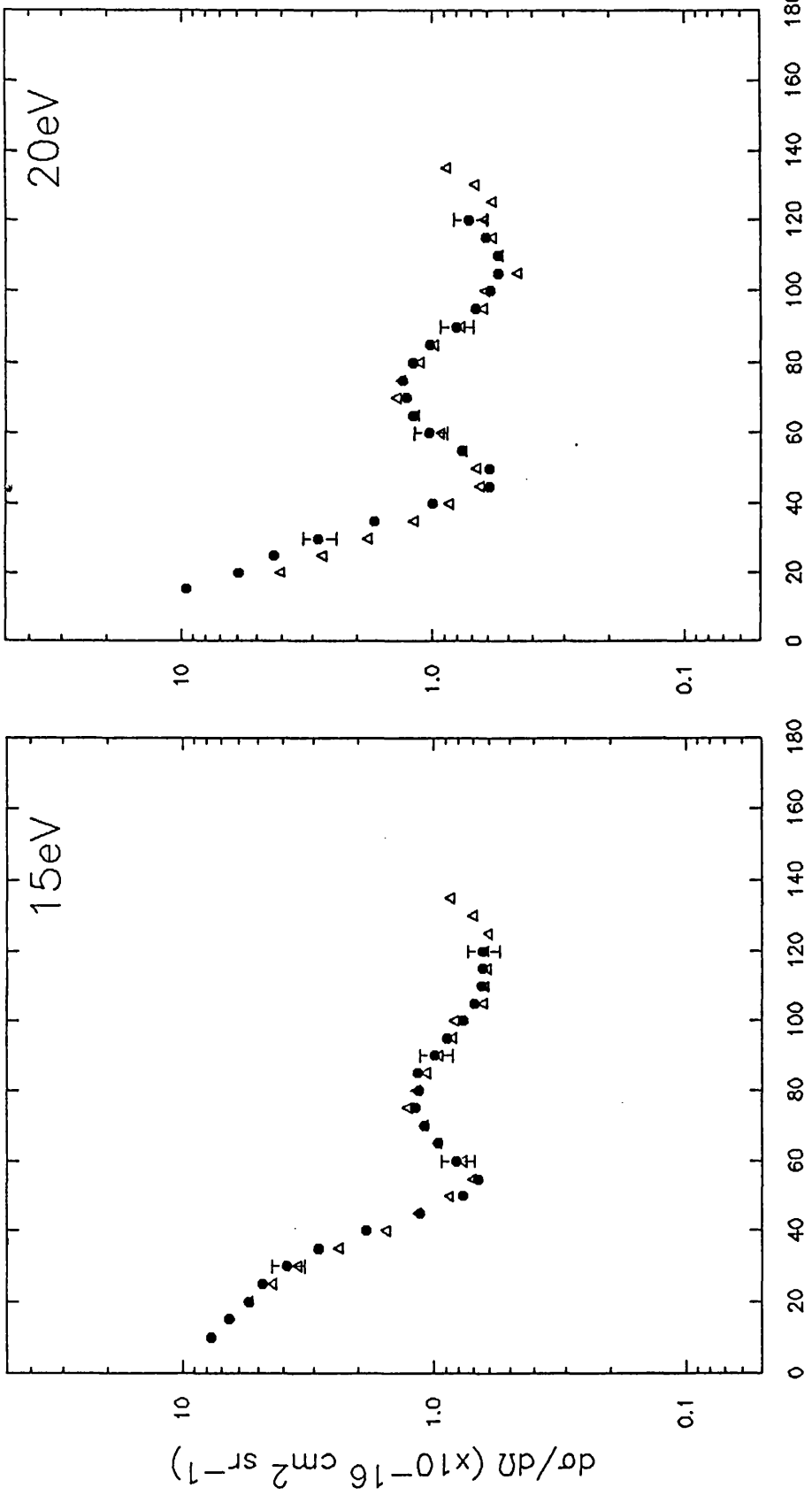

Figure 5.5 Absolute elastic differential cross sections for electron scattering from SF_6 for an incident energy of 15eV (x10^{-16} cm^2 sr^{-1}). ∂ Present work; Δ Srivastava *et al* (1976).

Figure 5.6 Absolute elastic differential cross sections for electron scattering from SF_6 for an incident energy of 20eV (x10^{-16} cm^2 sr^{-1}). ● Present work; Δ Srivastava *et al* (1976).

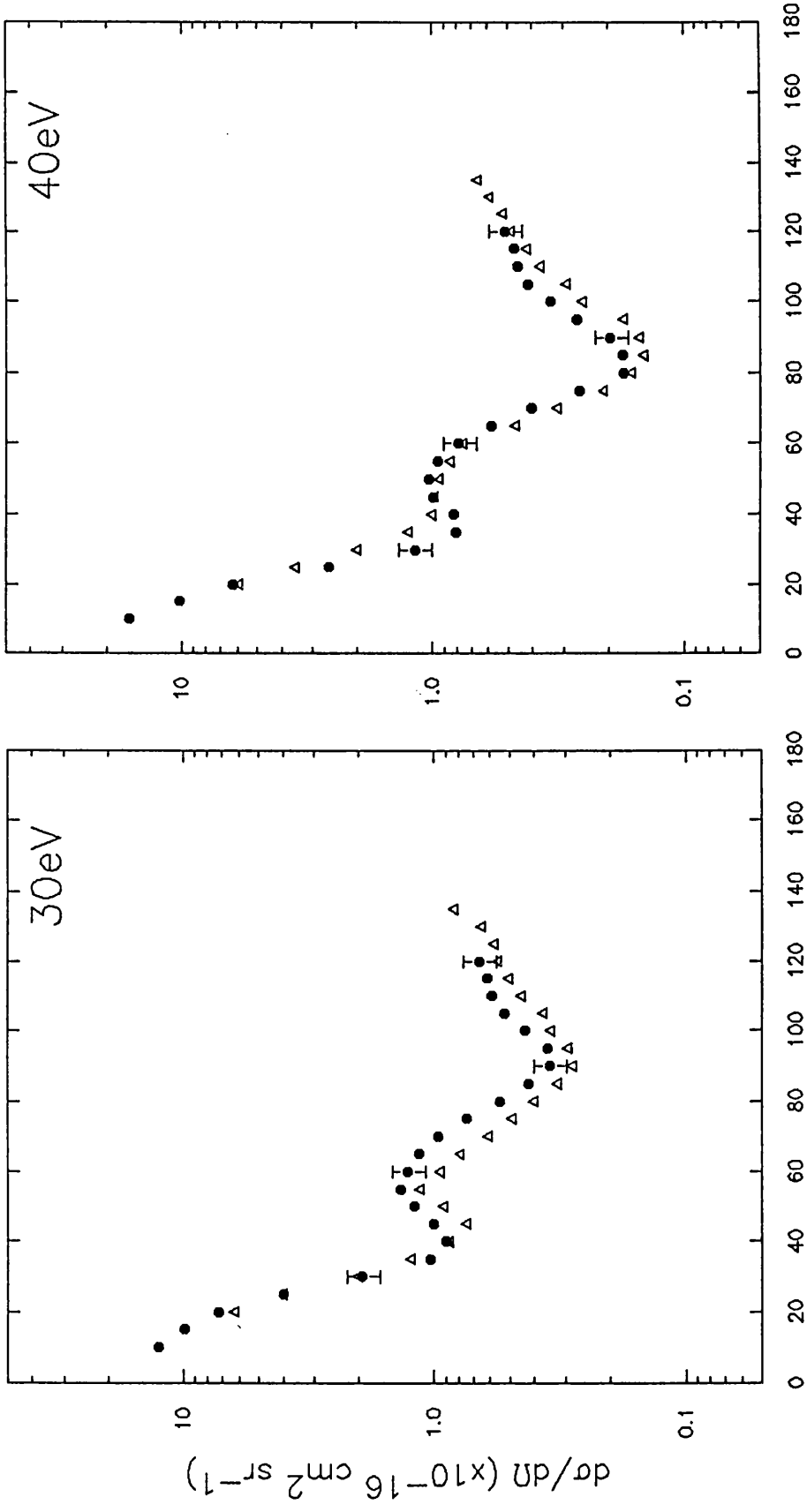

Figure 5.7 Absolute elastic differential cross sections for electron scattering from SF_6 for an incident energy of 30eV ($x10^{-16}$ cm^2 sr^{-1}). ● Present work; Δ Srivastava *et al* (1976).

Figure 5.8 Absolute elastic differential cross sections for electron scattering from SF_6 for an incident energy of 40eV ($x10^{-16}$ cm^2 sr^{-1}). ● Present work; Δ Srivastava *et al* (1976).

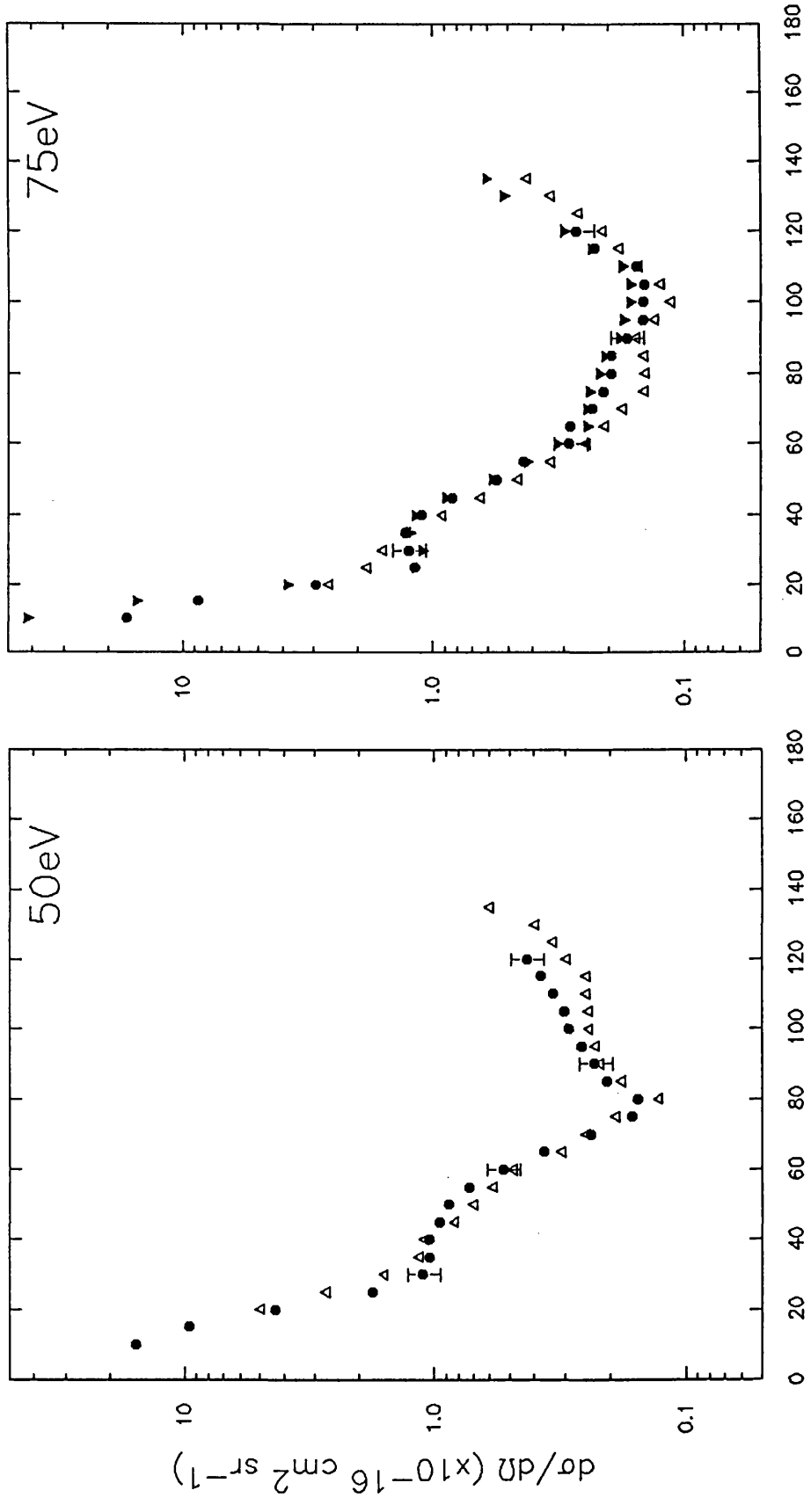

Figure 5.9 Absolute elastic differential cross sections for electron scattering from SF_6 for an incident energy of 50eV ($x10^{-16}$ cm^2 sr^{-1}). ● Present work; Δ Srivastava *et al* (1976).

Figure 5.10 Absolute elastic differential cross sections for electron scattering from SF_6 for an incident energy of 75eV ($x10^{-16}$ cm^2 sr^{-1}). ● Present work; Δ Srivastava (1976); ▼ Sakae *et al* (1989).

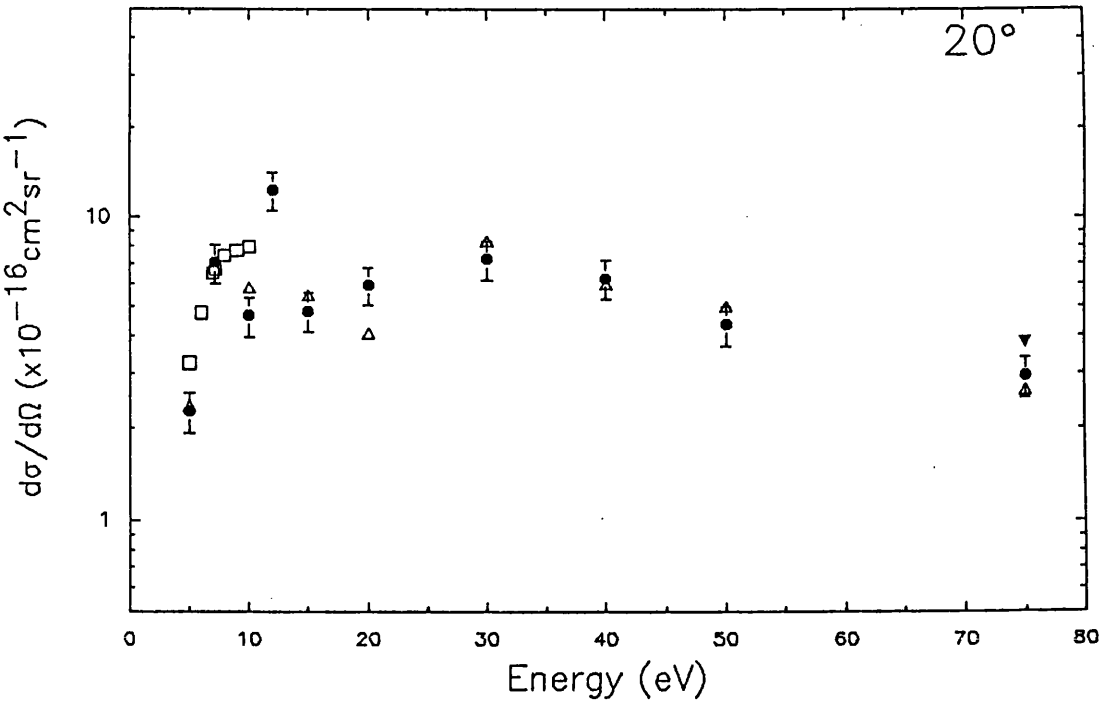

Figure 5.11 Absolute elastic differential cross sections for electron scattering from SF_6 at 20° ($x10^{-16}$ cm^2 sr^{-1}). ● Present work; △ Srivastava *et al* (1976); □ Rohr (1977); ▼ Sakae *et al* (1989).

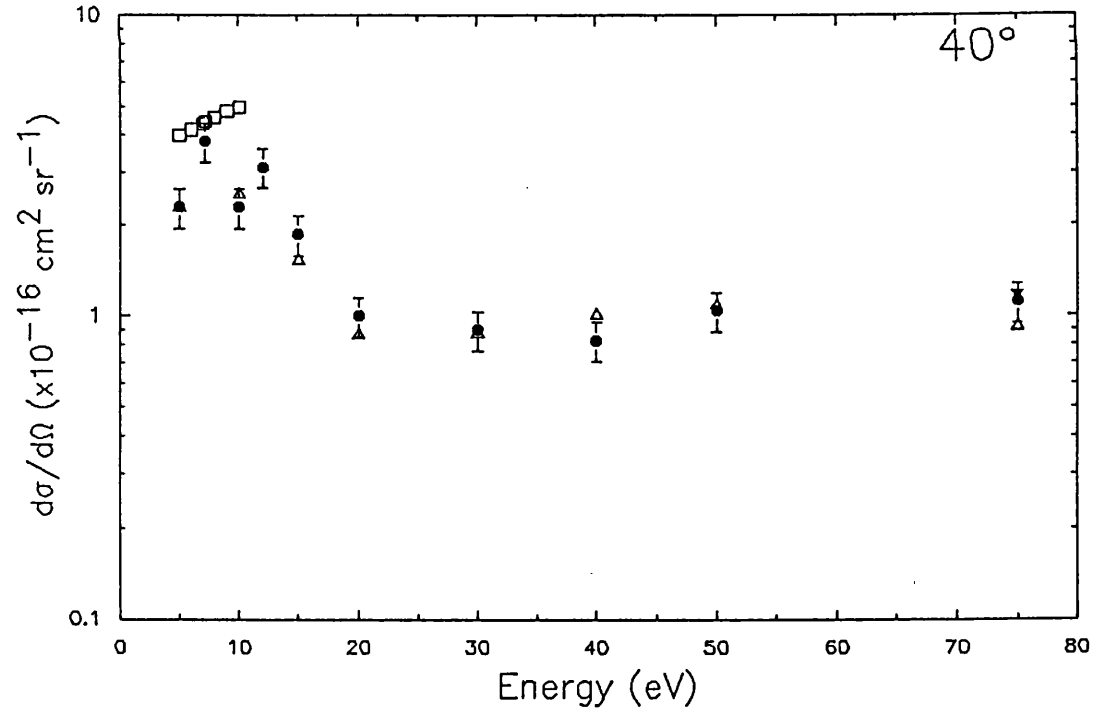

Figure 5.12 Absolute elastic differential cross sections for electron scattering from SF_6 at 40° ($x10^{-16}$ cm^2 sr^{-1}). ● Present work; △ Srivastava *et al* (1976); □ Rohr (1977); ▼ Sakae *et al* (1989).

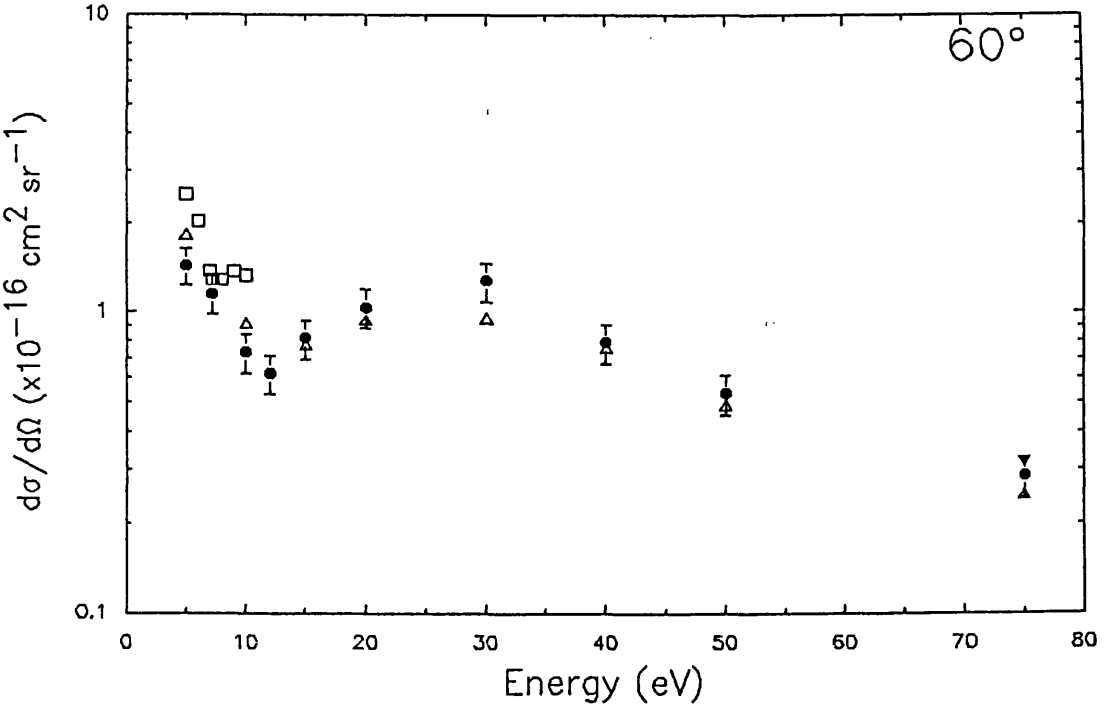

Figure 5.13 Absolute elastic differential cross sections for electron scattering from SF_6 at 60° ($x10^{-16}$ cm^2 sr^{-1}). ● Present work; △ Srivastava *et al* (1976); □ Rohr (1977); ▼ Sakae *et al* (1989).

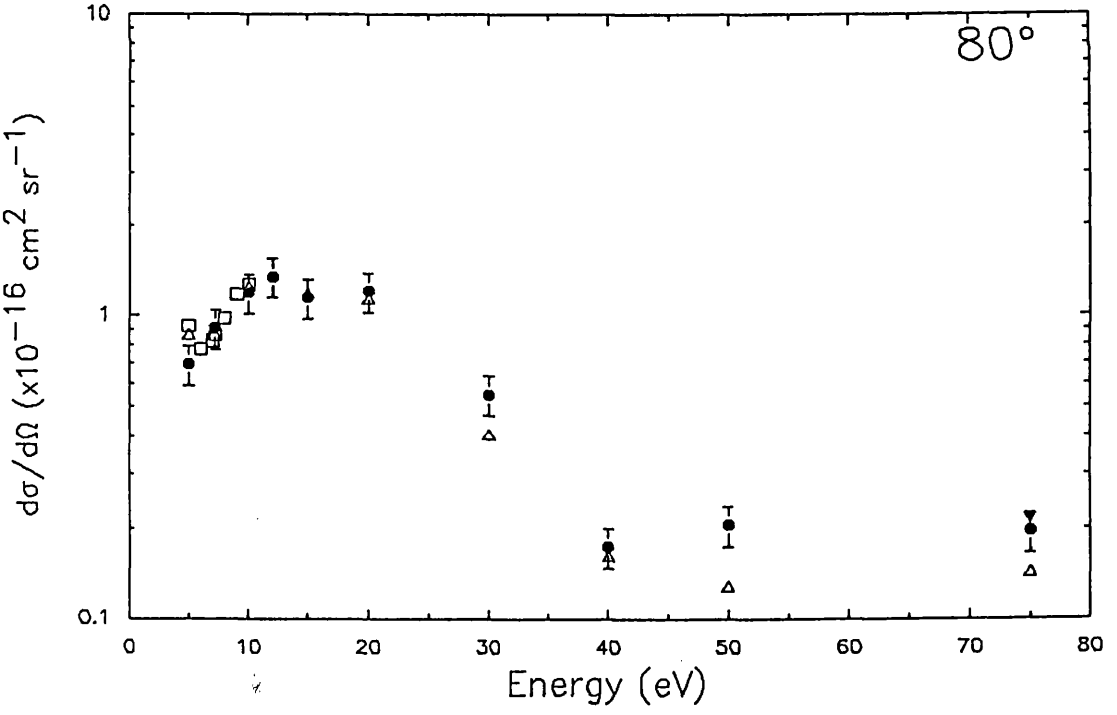

Figure 5.14 Absolute elastic differential cross sections for electron scattering from SF_6 at 80° ($x10^{-16}$ cm^2 sr^{-1}). ● Present work; △ Srivastava *et al* (1976); □ Rohr (1977); ▼ Sakae *et al* (1989).

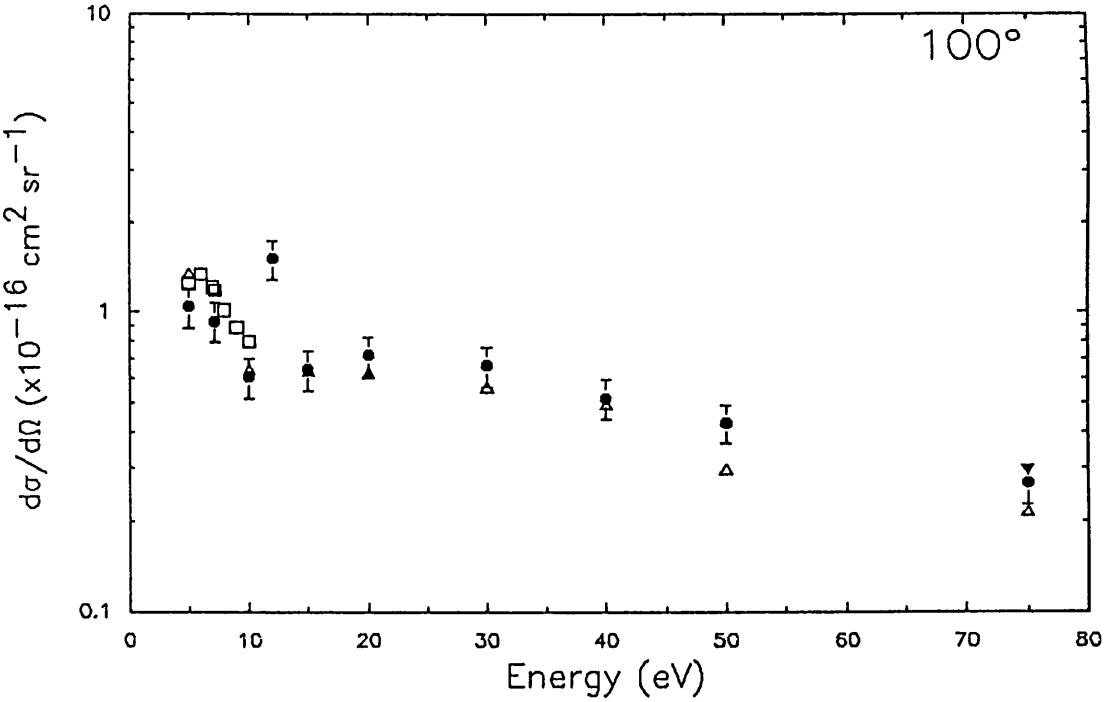

Figure 5.15 Absolute elastic differential cross sections for electron scattering from SF_6 at 100° ($x10^{-16}$ cm^2 sr^{-1}). ● Present work; △ Srivastava *et al* (1976); □ Rohr (1977); ▼ Sakae *et al* (1989).

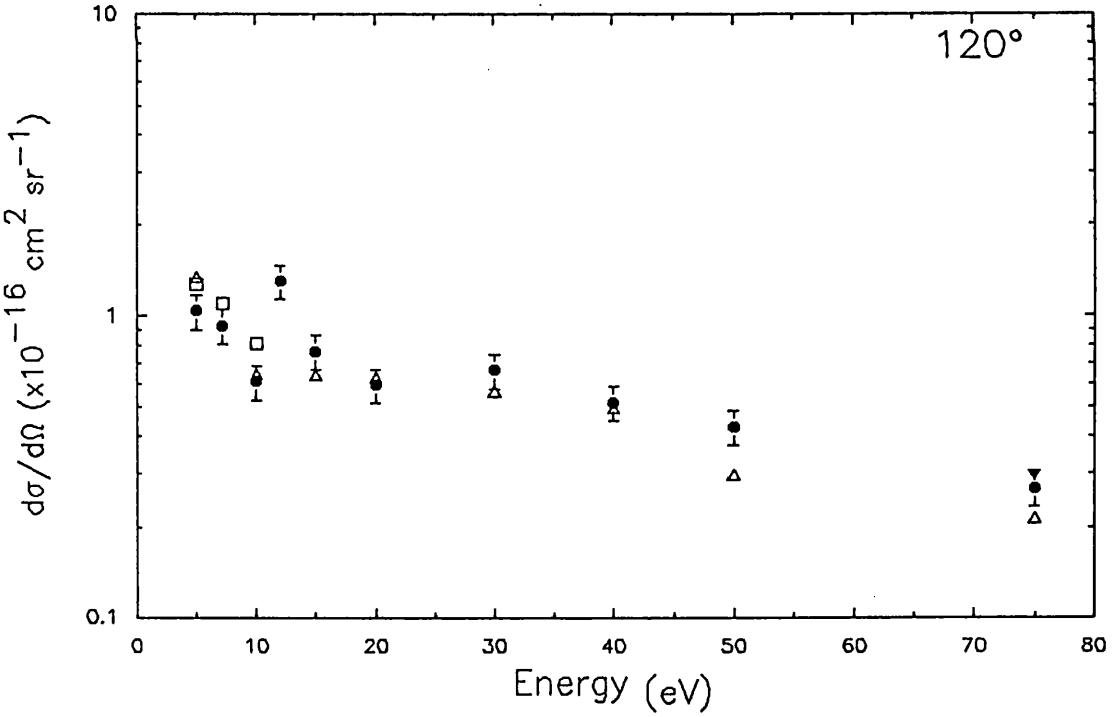

Figure 5.16 Absolute elastic differential cross sections for electron scattering from SF_6 at 120° ($x10^{-16}$ cm^2 sr^{-1}). ● Present work; △ Srivastava *et al* (1976); □ Rohr (1977); ▼ Sakae *et al* (1989).

increased further, the positions of all the maxima and minima migrate to smaller angles until at 75eV a "U" shape feature appears with the lowest point between 60° and 100° indicating the contribution from a large number of partial waves.

Figures 5.11 to 5.16 show absolute elastic cross sections as a function of incident energy for scattering angles θ=20°, 40°, 60°, 80°, 100° and 120°. From these figures it can be seen that the cross section shows a considerable increase at an incident energy of 7.2 at 20° and 40° and for an incident energy of 12eV at θ=20°, 40°, 100° and 120°. Chutjian and Trajmar (1977) have observed similar behaviour in the elastic cross section in the 12eV region for θ=20°, 60°, 90° and 135°. Rohr (1979) made measurements of the elastic cross section in the 7eV region but his results do not show the same increase at or around 7.2eV. This may be due to a normalisation error in his data as at the lower scattering angles, where the largest enhancement is seen, the data of Rohr (1979) is considerably higher than the present work and that of Srivastava *et al* (1976). Peaks in the total cross sections have also been seen at similar energies and have been attributed to the formation of negative ion resonances and this will be discussed in more detail in section 5.4.

5.3 Integral And Momentum Transfer Cross Section Measurements

In the present work the integral and momentum transfer cross sections have been determined from the measured angular differential cross sections using equations 1.3 and 1.4 defined in section 1.2. The determination of σ_t and σ_m requires a knowledge of $\sigma(\theta)$ from 0° to 180°. Experimentally, it is very difficult to measure $\sigma(\theta)$ over this entire range and results often have to be extrapolated to θ=0° and to θ=180°. In this work, this was done using a least squares fitting program based on a partial wave fitting procedure described by Tanaka *et al* (1983). As the largest scattering angle for which $\sigma(\theta)$ could be measured in the present apparatus was θ=120°, there was a possibility of large errors occurring in the calculation of σ_t and σ_m due to an uncertainty in the estimation of extrapolated values of $\sigma(\theta)$ between θ=125° and θ=180°. Table 5.2 gives the values for σ_t and σ_m generated using this method and the numbers shown below each value represents the percentage contribution to the cross section from the extrapolated values determined from the fitting procedure. The errors in σ_t and σ_m were estimated to be 20% and 25% respectively and arose from two sources, the

	Incident Energy									
	5eV	7.2eV	10eV	12eV	15eV	20eV	30eV	40eV	50eV	75eV
σ_t	15.08	22.72	19.41	28.26	17.07	18.10	16.41	12.38	11.23	9.37
	17%	23%	24%	13%	17%	35%	21%	15%	16%	21%
σ_m	12.11	16.11	12.68	17.62	12.26	14.73	11.40	6.94	6.01	5.13
	33%	40%	42%	36%	42%	55%	53%	50%	51%	66%

Table 5.2 Absolute integral and momentum transfer cross sections for electron scattering from SF_6 ($x10^{-16}cm^2$). The numbers given as percentages are the contributions from the extrapolated differential cross sections values.

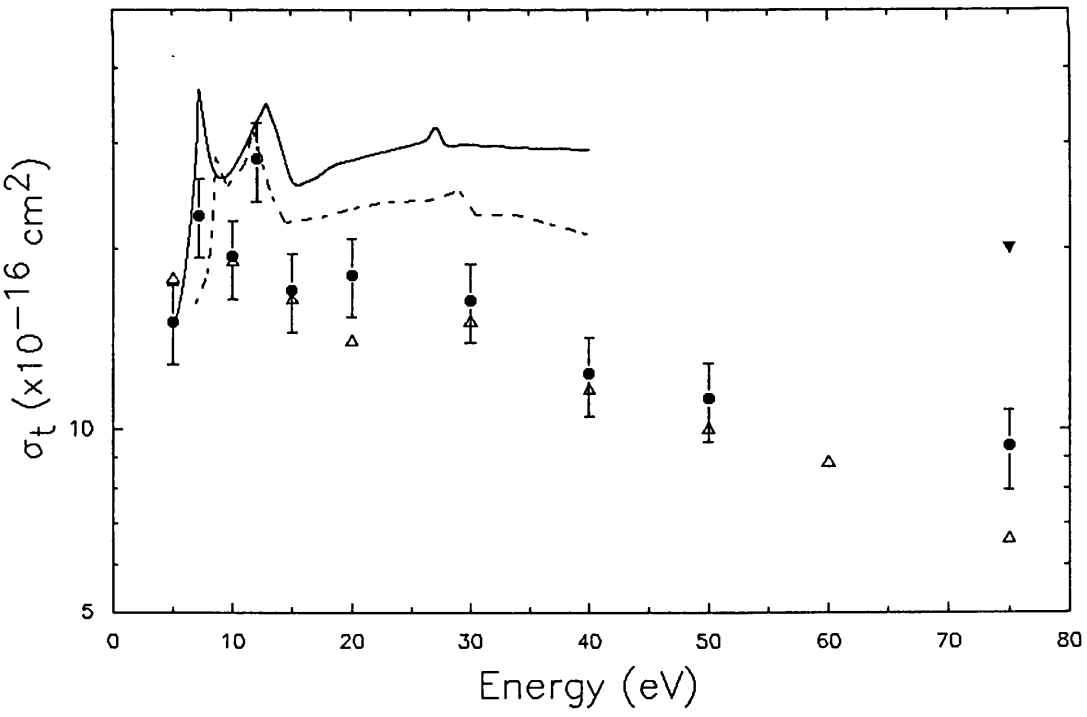

Figure 5.17 Absolute elastic integral cross sections for electron scattering from SF_6 ($x10^{-16}$ cm^2 sr^{-1}). Experiment: ● Present work; △ Srivastava *et al* (1976); ▼ Sakae *et al* (1989). Theory: ——— Dehmer *et al* (1978);——Gyemant *et al* (1980).

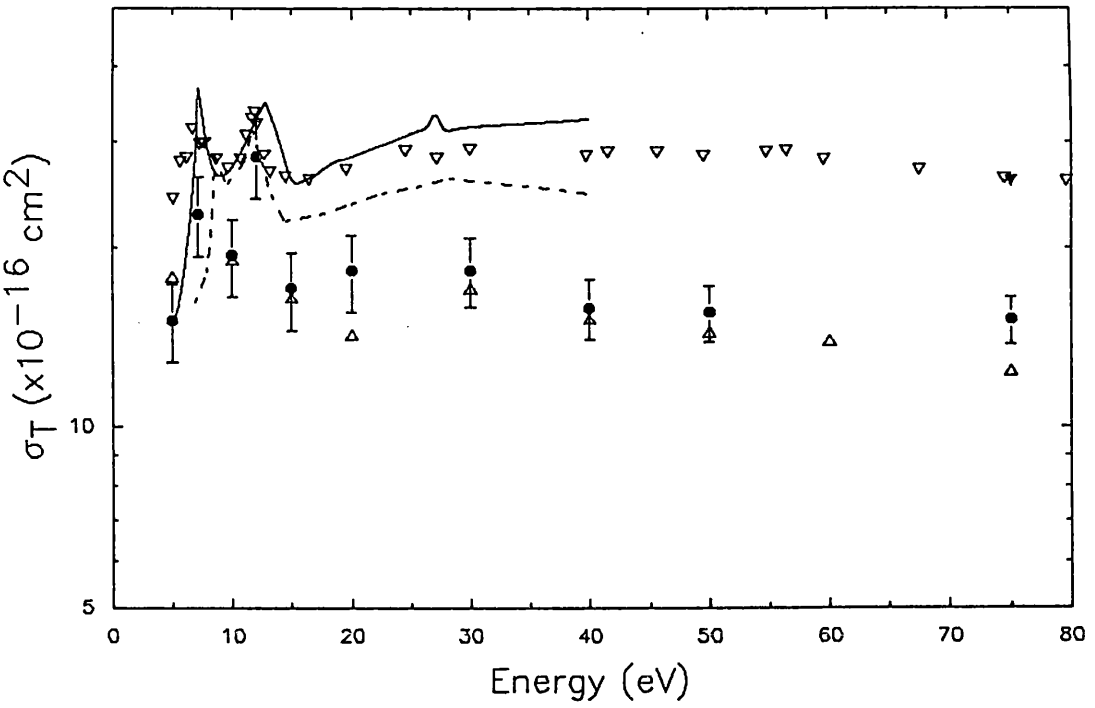

Figure 5.18 Absolute total cross sections for electron scattering from SF_6 ($x10^{-16}$ cm^2 sr^{-1}). Experiment: ● Present work; △ Srivastava *et al* (1976); ▽ Dababneh *et al* (1988); ▼ Sakae *et al* (1989). Theory: ——— Dehmer *et al* (1978);——Gyemant *et al* (1980).

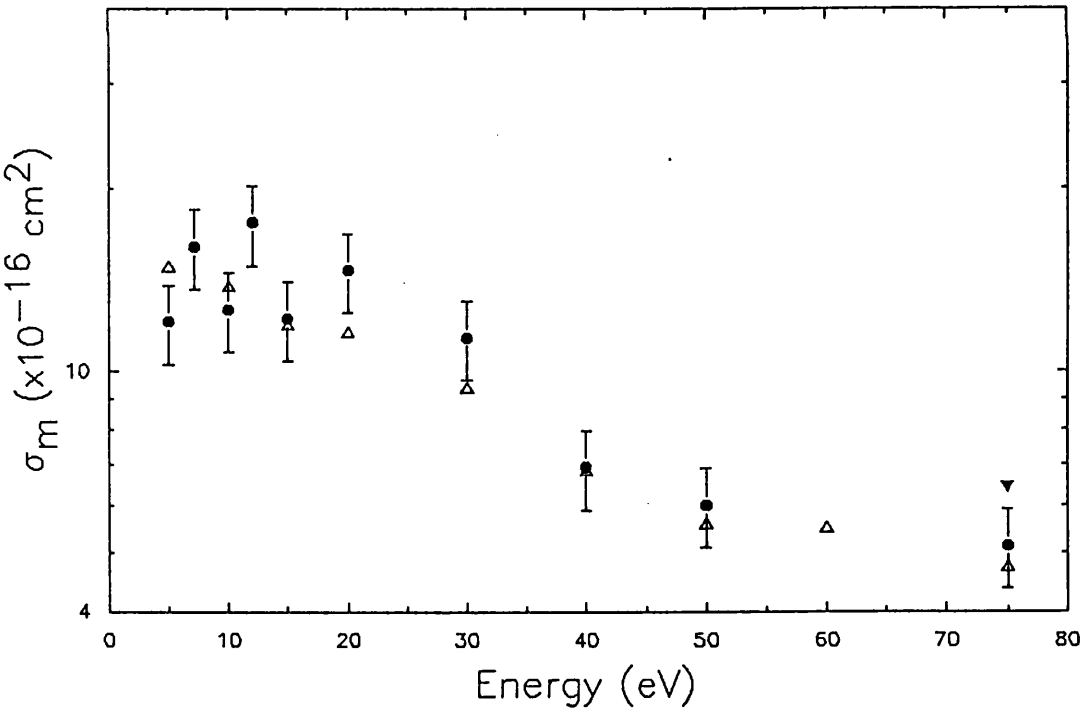

Figure 5.19 Absolute momentum transfer cross sections for electron scattering from SF_6 ($x10^{-16}$ cm^2 sr^{-1}). Experiment: ● Present work; △ Srivastava *et al* (1976); ▼ Sakae *et al* (1989).

differential cross section measurements (≈13%) and the extrapolated differential cross section values (20%). The greater error associated with the values of σ_m was a direct result of the larger contribution to the final value of σ_m from the extrapolated cross sections (see table 5.2).

Integral cross sections for electron impact on SF_6 have been reported by several authors. Srivastava *et al* (1976) and Sakae *et al* (1989) have reported integral and momentum transfer cross sections from an extrapolation of their angular differential cross sections while Dehmer *et al* (1978) and Gyemant *et al* (1980) have derived the integral cross sections using a continuum multiple scattering calculation. These results are shown in figure 5.17 together with the results derived from the present work. Again, the values of Srivastava *et al* (1976) have been recalculated by Trajmar *et al* (1983) using the renormalised differential cross sections (see section 5.2).

Two measurements have been made of the total cross section for electron impact on SF_6 by Kennerly *et al* (1979) and Dababneh *et al* (1988). It is possible to derive the total cross section from the integral cross section by addition of the total ionisation and excitation cross sections (see section 4.4). Figure 5.18 shows a plot of σ_T against incident electron energy. The ionisation cross sections of Rapp and Englander–Golden (1965) have been added to the integral sections derived in the present work and to the results of Srivastava *et al* (1976), Sakae *et al* (1989), Dehmer *et al* (1978) and Gyemant *et al* (1980). No data is available with which to calculate σ_{exc} but it is probable that its contribution is no larger than 5% of the total. The results of Kennerly *et al* (1979) are very similar to those of Dababneh *et al* (1988) and so have not been included for the sake of clarity. In figure 5.18, the agreement of the present work with that of Srivastava *et al* (1976) is good and at 7.2eV and 12eV the present work shows a significant rise in the cross section. At 75eV, the work of Sakae *et al* (1989) is notably higher than either the present work or that of Srivastava *et al* (1976) but is in good agreement with the direct σ_T measurements. The results of Kennerly *et al* (1979) and Dababneh *et al* (1988) and the calculations of Dehmer *et al* (1978) and Gyemant *et al* (1980) are also in reasonable agreement. Both calculations predict the presence of the two peaks seen near 7eV and 12eV, although at slightly different energies and intensities. In comparison with the values of σ_T determined from the present work and by Srivastava *et al* (1976), the measurements and calculation of Kennerly *et al* (1979), Dababneh *et al* (1988), Dehmer *et al* (1978) and Gyemant *et al* (1980) are consistently higher but are similar in shape.

The disagreement seen at the higher energies between the total cross section measurements and the theory with the values of σ_T derived from the present work and

that of Srivastava *et al* (1976) can be explained by an examination of the differential cross section data, particularly at 75eV. From figure 5.10, it can be seen that the data of Sakae *et al* (1989) is much higher at the smaller scattering angles than the present work or that of Srivastava *et al* (1976). There is a similar difference between the present work and that of Srivastava *et al* (1976) at 40eV and 50eV. Thus at the higher energies, the discrepancy in the values of σ_T appears to be due to a difficulty in accurately measuring the steeply rising differential cross section at the small scattering angles.

There have only been two reported measurements of the momentum transfer cross section for incident energies in the range 5eV to 75eV; that of Srivastava *et al* (1976) and the single measurement of Sakae *et al* (1989). The momentum transfer cross sections of these authors together with those calculated from the present work are shown in figure 5.19. Despite the large contribution to σ_m from the extrapolated values used to extend the differential cross section to 0° and 180°, the agreement between the present data and that of Srivastava *et al* (1976) is good. The trend in σ_m is similar to that of σ_t with two peaks in the cross section at 7.2eV and 12eV and a subsequent decrease as the incident beam energy is increased towards 75eV. As the calculation of σ_m is heavily weighted in favour of angles greater than 90°, the errors encountered in measuring $\sigma(\theta)$ at small angles were expected to have a smaller effect on the final value of σ_m than for σ_t.

5.4 Resonance Structure In e^-–SF_6 Scattering Cross Sections

It has already been noted that the differential, integral and momentum transfer cross section measurements showed significant enhancement at 7.2eV and 12eV (figures 5.11 to 5.19) and it was suggested that this behaviour was due to the formation of negative ion resonances. Dehmer *et al* (1978) and Gyemant *et al* (1980) have produced theoretical calculations for integral electron scattering cross sections in which a similar resonant behaviour was observed (figure 5.18). Dehmer *et al* (1978) have found evidence of four negative ion states, a_{1g}, t_{1u}, t_{2g} and e_g which have been classified according to the irreducible representations of the O_h symmetry group of the SF_6 molecule. The energy positions and orbital assignments of the observed resonances reported by several authors are shown in table 5.3. The calculations of Dehmer *et al* (1978) and Gyemant *et al* (1980) were both based on the multiple scattering method described in section 1.5.1 in which the molecular field is partitioned into three regions. Both Dehmer *et al* (1978) and Gyemant *et al* (1980) performed their calculations within the fixed nuclei model and determined the ground state charge distributions in the

orbital	Kennerly *et al* (1978)	Dababneh *et al* (1988)	Trajmar and Chutjian (1977)	Dehmer *et al* (1978)	Gyemant *et al* (1980)
a_{1g}	2.56	2.30		2.10	
t_{1u}	7.05	6.70		7.20	8.70
t_{2u}	11.87	11.90	12.00	12.70	11.80
e_g				27.00	28.60

Table 5.3 Positions (peak maxima) and orbital assignments of the resonances observed in electron scattering from SF_6 obtained by experiment and theory.

manner of Connolly and Johnson (1971). The fundamental differences between these two calculations lay in the construction of the electron molecule interaction potential and the number of partial waves used. Dehmer *et al* (1978) used up to twelve partial waves, employed a Hara free electron gas exchange (HFEGE) potential and included a polarisation potential $-\alpha/r^4$ in region III, adding its value at the II/III boundary to the potential in region II. Gyemant *et al* (1980) used a maximum of seven partial waves and experimented with three combinations (A, B and C) of exchange and polarisation potentials. Combination A used an asymptotically adjusted free electron gas exchange (AAFEGE) potential, whilst in combination B a HFEGE potential was used in region II and an AAFEGE potential in region III. In combination C, a polarisation potential was added to combination B in the same manner as described by Dehmer *et al* (1978). The results of Gyemant *et al* (1980) shown in figure 5.17 and 5.19 are those obtained using combination C.

Dehmer *et al* (1978) have predicted the existence of four resonances and have found that the partial waves which contribute to the resonance formation are (0,**4**), (1,**3**), (2,**4**,6) and (2,**4**,**6**) for a_{1g}, t_{1u}, t_{2g} and e_g, respectively, where the bold numbers denote the partial waves exhibiting an increase in phase at the resonance energies. These calculations also indicated that the two lowest lying resonances, a_{1g} and t_{1u}, were molecular in origin, whereas the t_{2g} and e_g resonances arose from an atomic d-type resonance associated with the sulphur atom. Comparison with the experimental results of Kennerly *et al* (1978) and Dababneh *et al* (1988), indicates that the theory of Dehmer *et al* (1978) predicts accurately the position of the resonance at 7eV (t_{1u}) but overestimates its magnitude and underestimates its width. The position of the second resonance is placed at a higher energy than that seen in both experiments. In the work

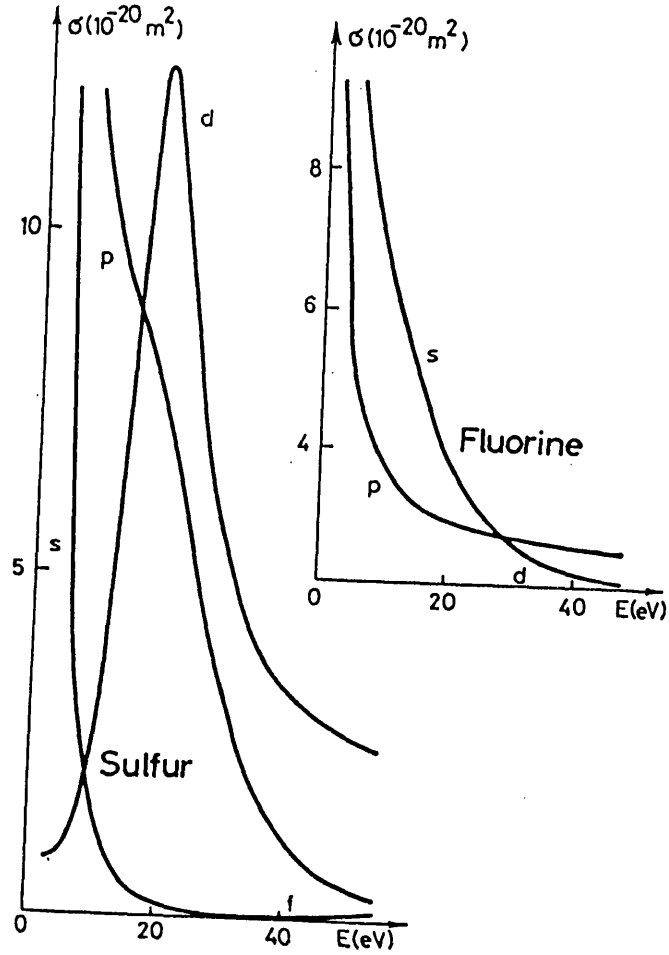

Figure 5.20 Scattering cross sections from fluorine and sulphur atomic regions in the SF_6 molecule (Gyemant *et al*, 1980).

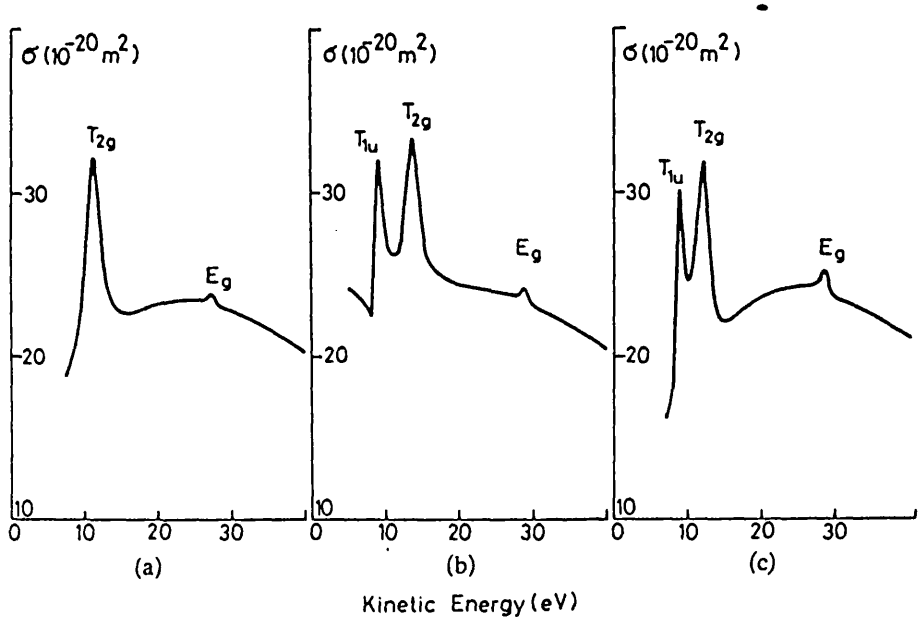

Figure 5.21 Calculated total elastic cross sections of the SF_6 molecule for potentials A, B and C, see text (Gyemant *et al* (1980).

of Gyemant *et al* (1980), the lowest energy to which they could extended their calculation was 5eV and so were only able to provide data for the three highest lying resonances. Gyemant *et al* (1980) were able to calculate the contribution to the total integral cross section for electron scattering from the individual sulphur and fluorine regions in the molecule and these are shown in figure 5.20. It can be seen that the s– and p–wave partial cross sections for the sulphur and fluorine regions decrease as a function of energy but the partial cross section associated with d-wave scattering from the sulphur shows a sharp rise and peaks around 20eV. The rise in the d-wave partial cross section is in accordance with the work of Dehmer *et al* (1978) who reported that the two highest lying resonances (t_{2g} and e_g) originated from the sulphur region of the molecule. In comparison with the σ_T measurements of Kennerly *et al* (1979) and Dababneh *et al* (1988), Gyemant *et al* (1980) underestimate the size of the t_{1u} resonance and places it at a much higher energy than either the experimental results or the theory of Dehmer *et al* (1978). The location and magnitude of the second resonance (t_{2u}) are however in good agreement with the experimental results.

There are a number of points that should be noted concerning the theoretical calculations. The first is the lack of any experimental evidence for the e_g resonance in the experimental data. The second is that, apart from the of the e_g resonance, there is good agreement between the direct measurements and the theory. It is surprising that a complete disregard of the nuclear dynamics should work so well for such a complex molecule (Gianturco and Jain, 1986). Indeed, Dehmer *et al* (1978) have noted that inclusion of nuclear motion into the calculation may significantly change the shape and the position of the resonance structures. Finally, Gyemant *et al* (1980) have noted that the presence, position and width of the resonances are highly dependent on the construction of the scattering potential. Figure 5.21 shows the cross sections obtained by Gyemant *et al* (1980) with the three combinations of exchange and polarisation potentials they employed.

From an analysis of the angular behaviour of the differential cross section data it may be possible to estimate which are the dominant partial waves at the resonance energies. For the first resonance, a_{1g}, Dehmer *et al* (1978) have indicated that the dominant partial wave is l=4. The differential cross section data of Rohr (1979) at 2.7eV and the present data at 5eV (figure 5.1) would seem to support this. It is surprising that the l=4 partial wave should have such a significant contribution at such a low energy and its importance may be due to exchange and polarisation effects. At the second resonance, t_{1u}, Dehmer *et al* (1978) suggest that the dominant partial wave is l=3. An inspection of the differential cross section at 7.2eV (figure 5.2) would

appear to contradict this as the behaviour indicates the presence of both l=2 and 4. Finally, the l=2, 4 and 6 are calculated to be the principle partial waves for the t_{2g} resonance. The differential cross section shown in figure 5.4 does show such a behaviour but the dominant partial wave would appear to be l=2. This is in agreement with Gyemant *et al* (1980) who show a rapidly rising contribution from the l=2 partial wave at this energy.

5.5 Summary

In this chapter, absolute elastic cross section measurements for electron scattering from SF_6 have been presented. By extrapolating, the differential cross section measurements to 0° and 180°, integral and momentum transfer cross sections have been derived. In general, agreement between the present work and the previously reported measurements is good. At the lower incident energies, the present work was found to be in better agreement with the renormalised data of Srivastava *et al* (1976) than that of Rohr (1979), whereas at 75eV, there was a better agreement with the data of Sakae *et al* (1989). The differential, integral, momentum transfer and total cross sections were all found to show significant resonant enhancement at 7.2eV and 12eV, in accord with the total cross section measurements of both Kennerly *et al* (1978) and Dababneh *et al* (1988) and the theoretical calculations of Dehmer *et al* (1978) and Gyemant *et al* (1980).

CHAPTER 6

Absolute Elastic Cross Sections For Electron Scattering From H_2O

6.1 Introduction

The interaction of electrons with water molecules is of fundamental importance in a wide variety of naturally occurring phenomena and in many practical applications. One area of particular relevance is the study of the effects of ionising radiation on the human body. Any radiation that penetrates the body may produce secondary electrons with appreciable kinetic energy and since the water content of the body is approximately 60%, interactions between electrons and water molecules will be of major importance in the study of the biological effects of radiation on tissue-like material. Even though there is clearly a difference between the cross sections for electrons scattered from water in a gaseous and liquid phase, cross sections determined from electron scattering from water vapour are still useful (Turner *et al*, 1982). Water has also been found to be a major constituent in the plasmas produced in magnetohydynamic power generators (Norcross, 1982). To enable the conductivity of the plasma to be determined, accurate absolute cross sections are required, particularly momentum transfer cross sections.

The water molecule has a bent configuration in the ground state where the bond angle H-O-H, is 105.5°. As a result of this bent configuration the water molecule has a large dipole moment, d=0.724au. In this chapter absolute elastic differential, integral, and momentum transfer are presented are compared with previously published data where ever possible.

6.2 Differential Electron Scattering Cross Sections

Unlike SF_6, several theoretical calculations have been reported for electron scattering from H_2O. Therefore, this section will be divided into two parts. In the

first part the results from the present work will be presented and compared with previously reported experimental data. In the second section, a brief outline of the approaches used in obtaining the theoretically derived cross sections will be given and the results will then be compared with the experimental results.

6.2.1 Experimentally Determined Differential Cross Sections

The first comprehensive set of absolute elastic differential cross sections were reported by Danjo and Nishimura (1985) at incident energies between 4eV and 200eV and for scattering angles from 15° to 120°. These were followed by the measurements reported by Katase *et al* (1986) at incident energies between 100eV and 2000eV for scattering angles between 5° and 130° and the results of Shyn and Cho (1987) at energies between 2.2eV and 20eV and scattering angles between 15° and 150°. Jung *et al* (1982) also reported absolute elastic differential cross sections as part of their observation on the rotational excitations of water at incident energies of 2.2 and 6eV.

Results obtained in the present work for absolute elastic differential cross sections for electron scattering from water at incident energies between 6eV and 50eV are shown in figures 6.1 to 6.10 and these have also been tabulated in table 6.1. Figures 6.1 to 6.6 show the differential cross sections as a function of scattering angle while figures 6.7 to 6.10 display the same cross sections as a function of incident energy. The experimental data of Jung *et al* (1982), Danjo and Nishimura (1985) and Shyn and Cho (1987) and the relevant theoretical data (see the following section 6.2.2) are shown for comparison. The experimental results of Shyn and Cho (1987) were obtained using a similar two step procedure to that used in the present work. The relative differential cross sections were measured before normalisation to the absolute value at 90° found in a second experiment. The value of the absolute cross section at 90° was determined from the relative intensities of the scattered signal from water and He measured in a gas cell experiment and the absolute helium cross sections of Shyn (1980) were used as the normalisation standard. The measurements of Danjo and Nishimura (1985) were made using the relative flow technique with the helium elastic scattering data of Register *et al* (1980a) used as the normalisation standard. The helium data of Register *et al* (1980a) has also been used as a normalisation standard in the

	Incident Energy					
θ	6eV	10eV	15eV	20eV	30eV	50eV
0						
10	7.63	9.62	9.45	11.02	11.44	10.76
15	5.86	6.69	7.10	8.15	7.80	6.55
20	4.46	4.89	5.17	5.91	5.66	4.30
25	3.31	3.52	3.85	4.38	4.04	2.92
30	2.40	2.75	2.91	3.12	2.88	1.84
35	1.80	2.13	2.34	2.48	2.17	1.17
40	1.45	1.67	1.95	1.94	1.67	
45	1.25	1.46	1.50	1.48	1.17	0.49
50	1.14	1.25	1.23	1.17	0.87	0.41
55	0.98	1.08	1.07	0.97	0.66	
60	0.96	1.02	0.91	0.73	0.49	0.25
65	0.87	0.93	0.82	0.65	0.37	
70	0.85	0.83	0.70	0.52	0.33	0.16
75	0.76	0.79	0.64	0.46	0.27	
80	0.74	0.71	0.59	0.42	0.24	0.11
85	0.70	0.68	0.53	0.39	0.21	
90	0.63	0.60	0.45	0.32	0.19	0.073
95	0.55	0.52	0.40	0.30	0.18	
100	0.45	0.47	0.36	0.30	0.17	0.062
105	0.42	0.44	0.30	0.29	0.18	
110	0.36	0.42	0.31	0.30	0.19	0.074
115	0.31	0.39	0.32	0.37	0.21	
120	0.32	0.40	0.34	0.37	0.23	0.14
error	12.0%	12.0%	12.0%	12.0%	12.0%	12.0%

Table 6.1 Absolute elastic differential cross sections for electron scattering from H_2O ($x10^{-16}cm^2sr^{-1}$).

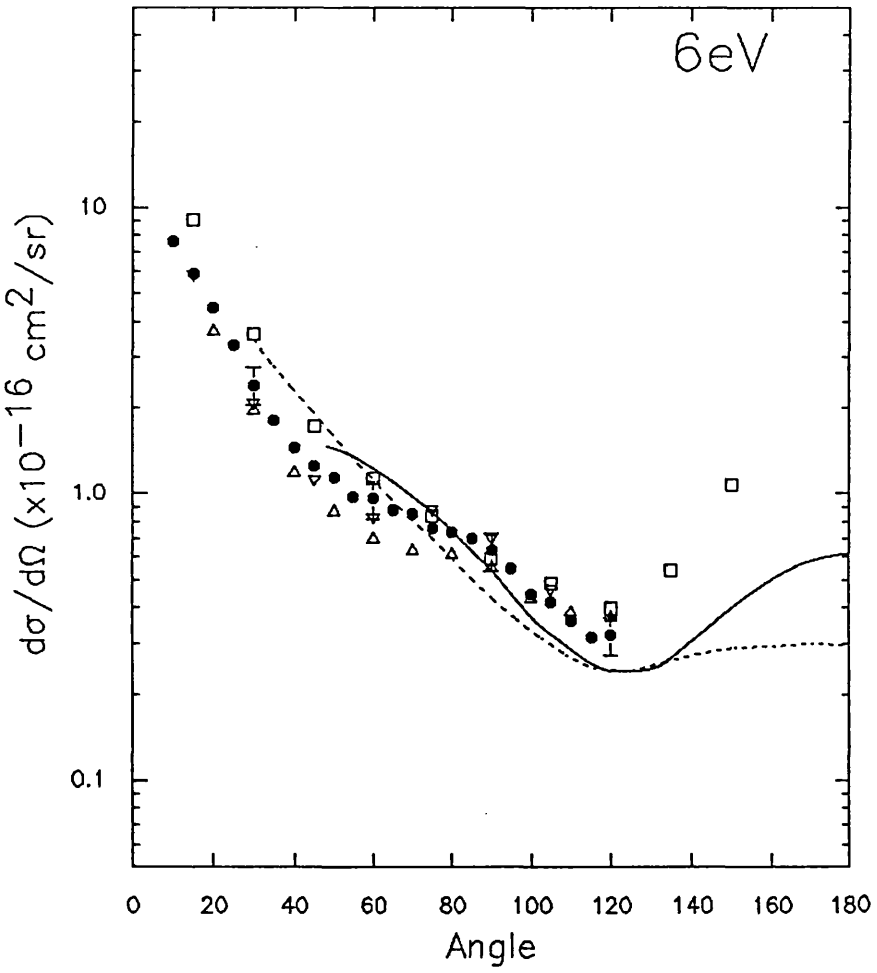

Figure 6.1 Absolute elastic differential cross section for electron scattering from H_2O for an incident energy of 6eV (x10^{-16} cm^2 sr^{-1}). Experimental data: ● Present work; ▼ Jung *et al* (1982); △ Danjo and Nishimura (1985); □ Shyn and Cho (1988). Theory: ——— Brescansin *et al* (1986);---- Gianturco and Scailla (1987b).

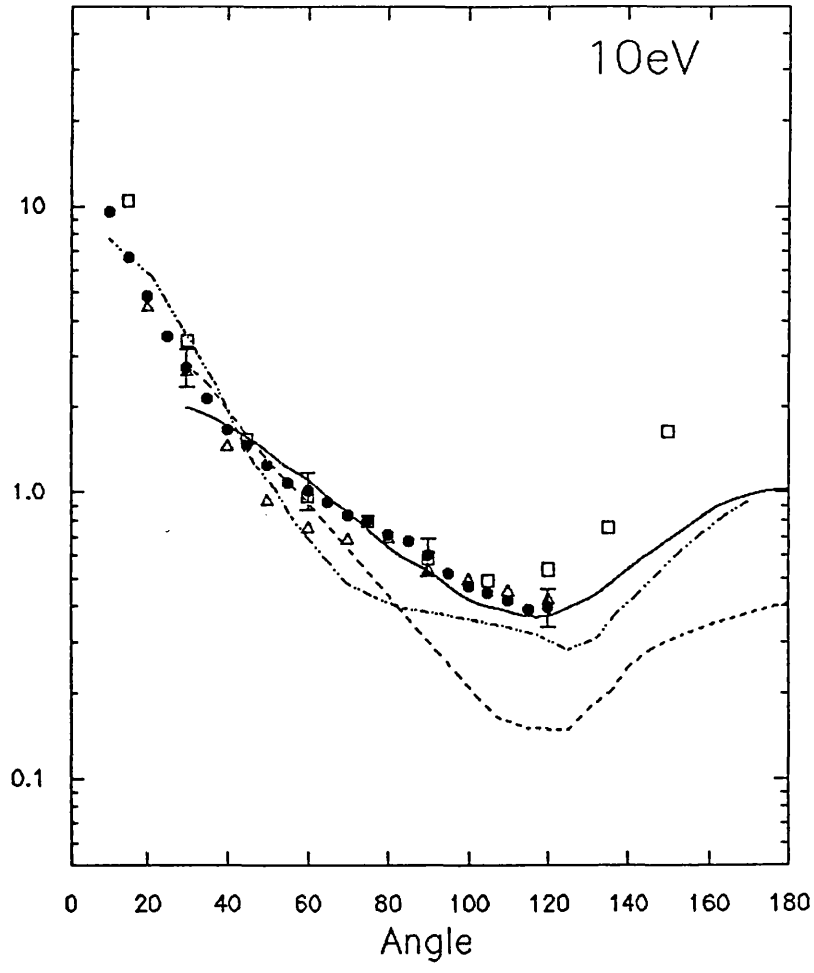

Figure 6.2 Absolute elastic differential cross section for electron scattering from H_2O for an incident energy of 10eV (x10^{-16} cm^2 sr^{-1}). Experimental data: ● Present work; △ Danjo and Nishimura (1985); □ Shyn and Cho (1987). Theory: ——— Brescansin *et al* (1986); ---- Gianturco and Scailla (1987b); ---- Sato *et al* (1988).

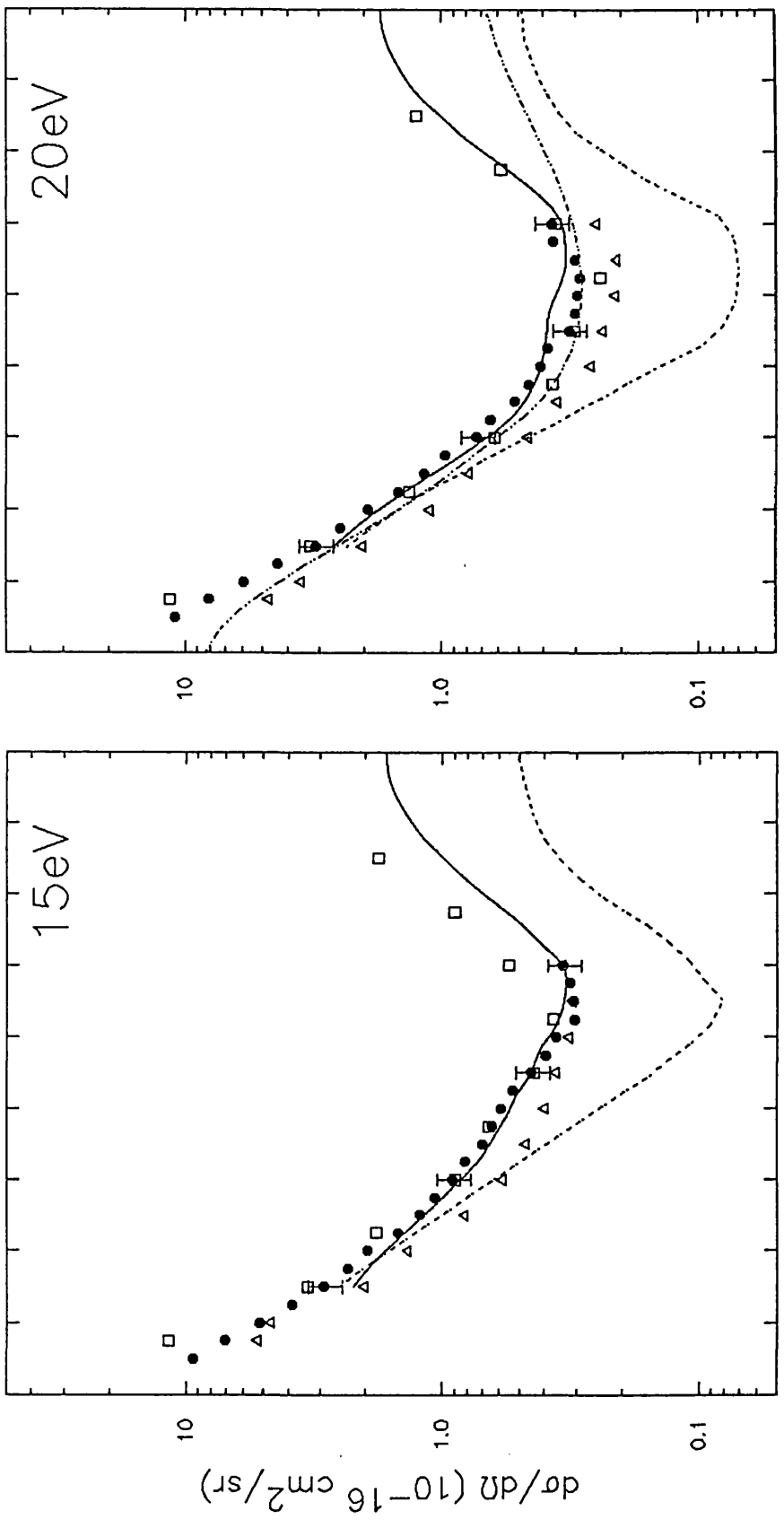

Figure 6.3 Absolute elastic differential cross section for electron scattering from H_2O for an incident energy of 15eV ($x10^{-16}$ cm^2 sr^{-1}). Experimental data: ● Present work; △ Danjo and Nishimura (1985); □ Shyn and Cho(1988). Theory: ——— Brescansin *et al* (1986);----- Gianturco and Scailla (1987b).

Figure 6.4 Absolute elastic differential cross section for electron scattering from H_2O for an incident energy of 20eV ($x10^{-16}$ cm^2 sr^{-1}). Experimental data: ● Present work; △ Danjo and Nishimura (1985); □ Shyn and Cho (1987). Theory: ——— Brescansin *et al* (1985);----- Gianturco and Scailla (1987b); ····· Sato *et al* (1988).

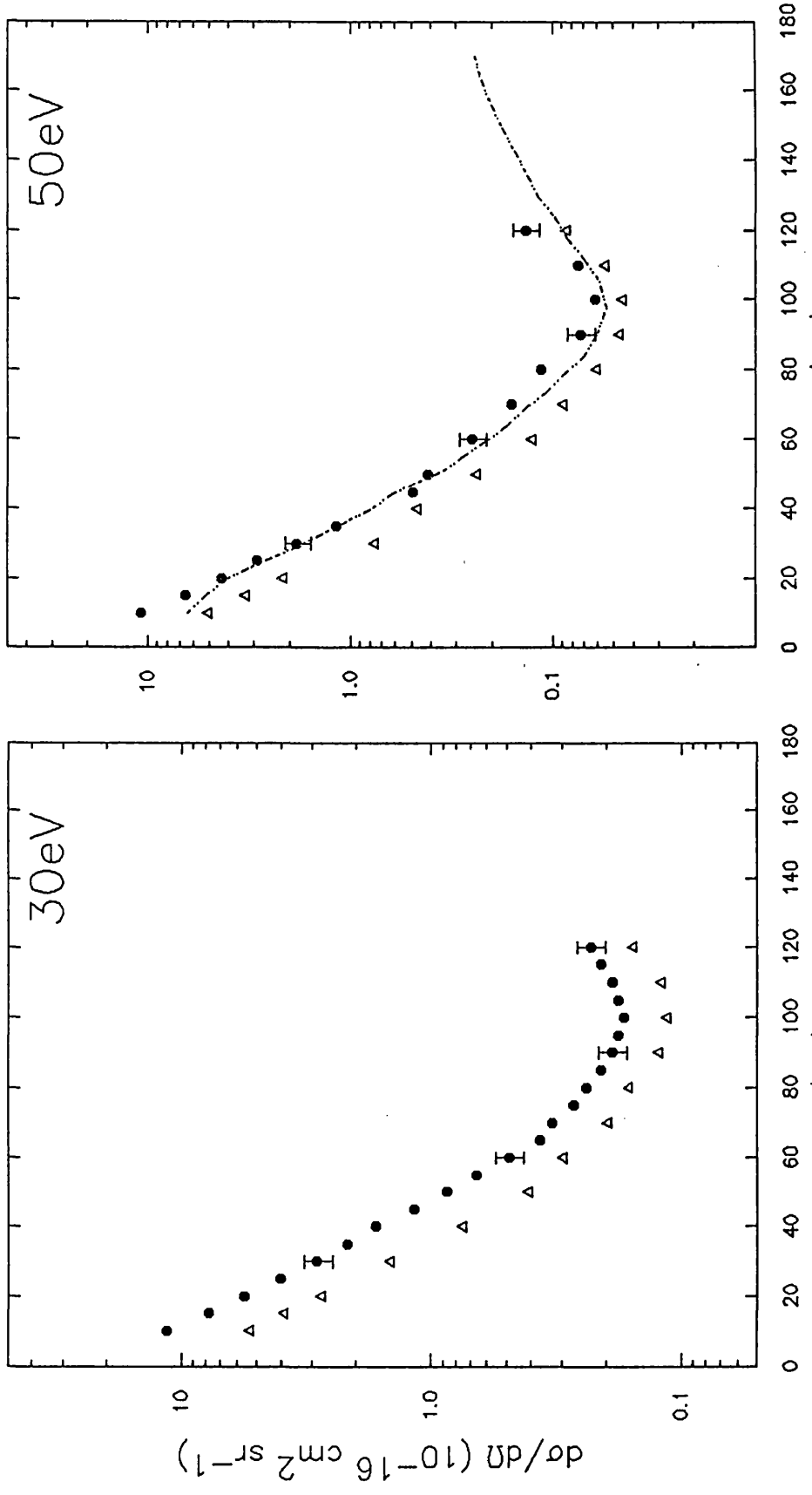

Figure 6.5 Absolute elastic differential cross section for electron scattering from H_2O for an incident energy of 30eV (x10^{-16} cm^2 sr^{-1}). Experimental data:
● Present work; Δ Danjo and Nishimura (1985).

Figure 6.6 Absolute elastic differential cross section for electron scattering from H_2O for an incident energy of 50eV (x10^{-16} cm^2 sr^{-1}). Experimental data:
● Present work; Δ Danjo and Nishimura (1985). Theory:---- Sato *et al* (1988).

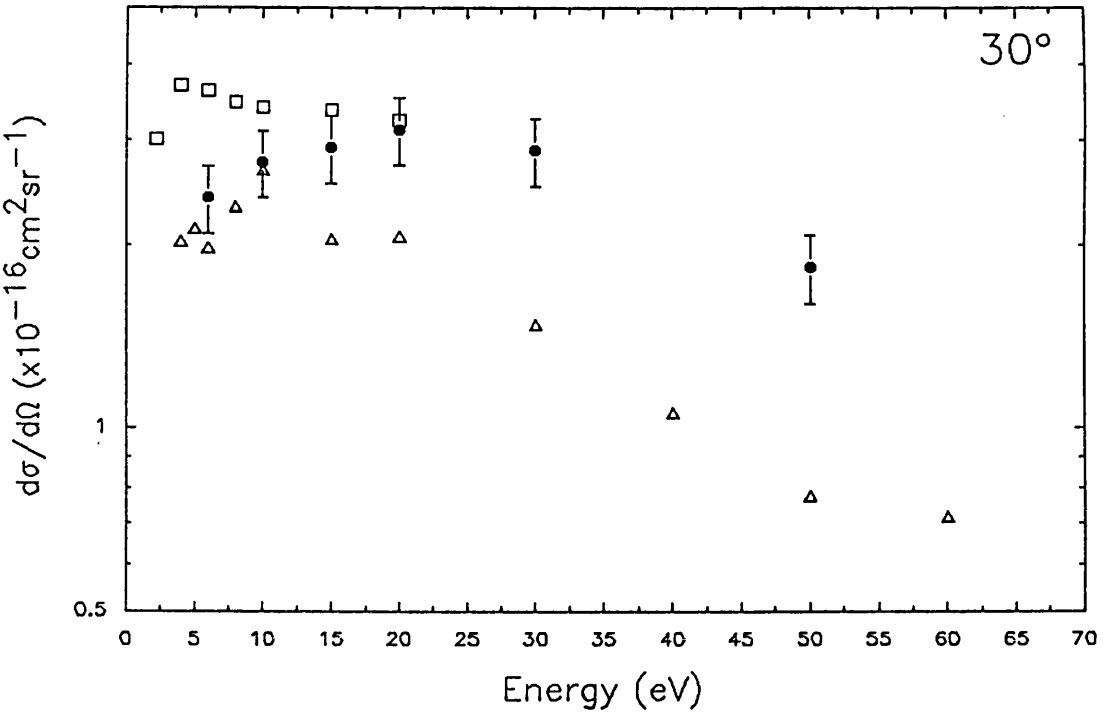

Figure 6.7 Absolute elastic differential cross sections for electron scattering from H_2O at 30° ($x10^{-16}$ cm^2 sr^{-1}). ● Present work; △ Danjo and Nishimura (1985); □ Shyn and Cho (1988).

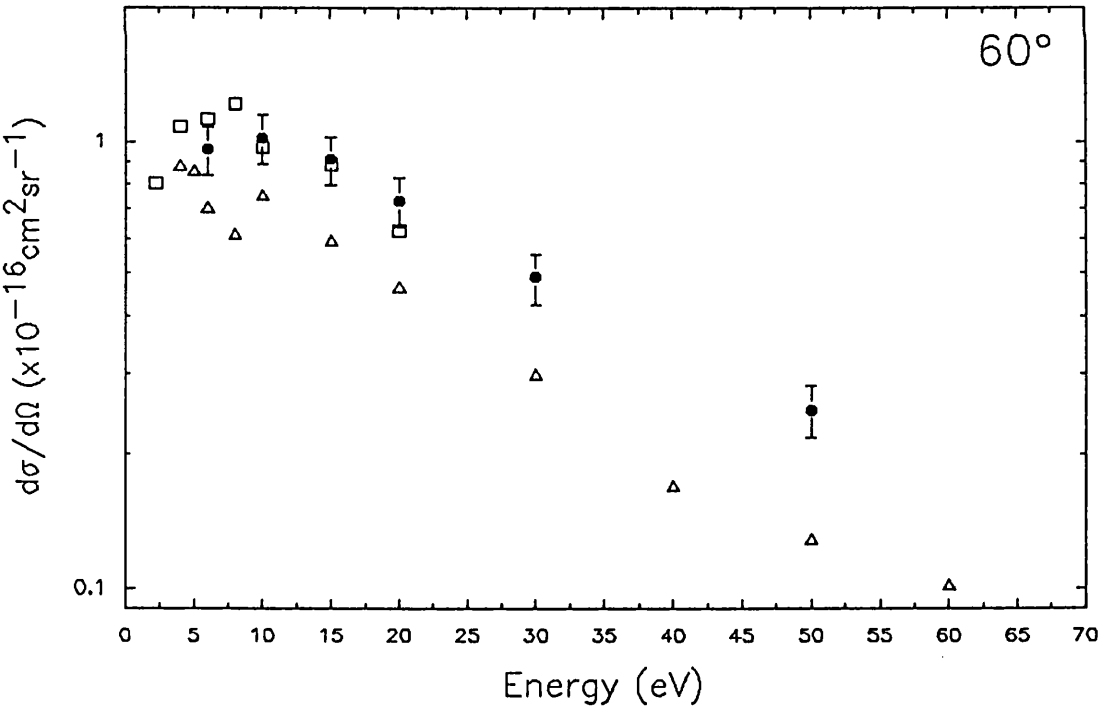

Figure 6.8 Absolute elastic differential cross sections for electron scattering from H_2O at 60°($x10^{-16}$ cm^2 sr^{-1}). ● Present work; △ Danjo and Nishimura (1985); □ Shyn and Cho (1988).

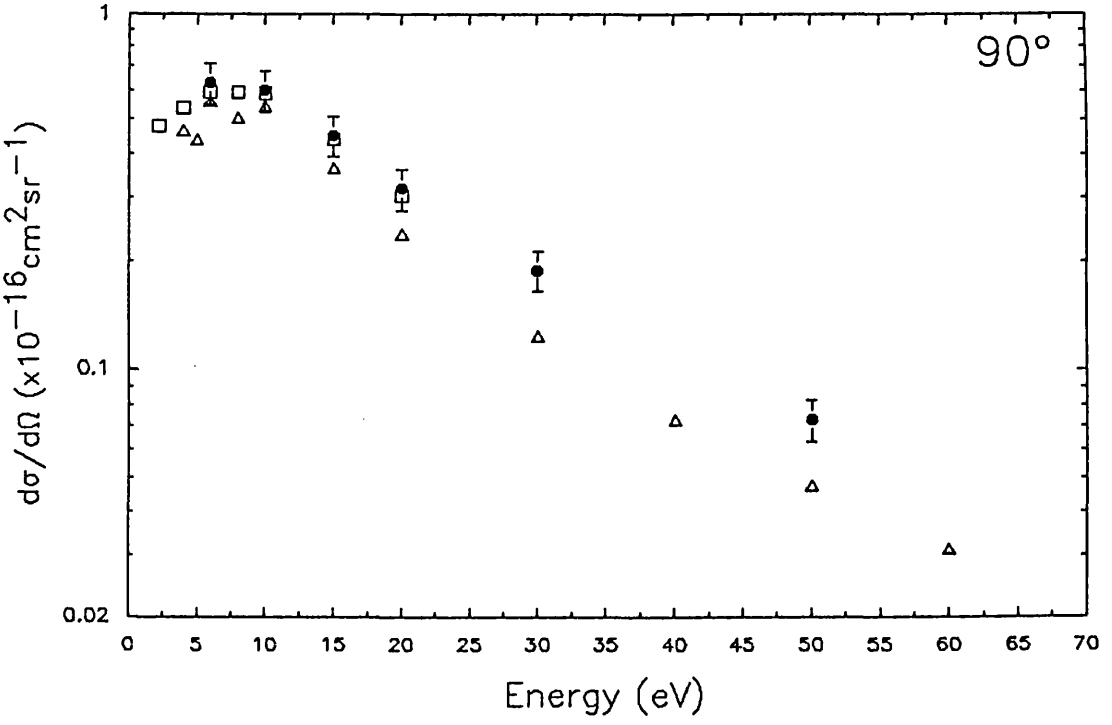

Figure 6.9 Absolute elastic differential cross sections for electron scattering from H_2O at 90°($x10^{-16}$ cm^2 sr^{-1}). ● Present work; △ Danjo and Nishimura (1985); □ Shyn and Cho (1988).

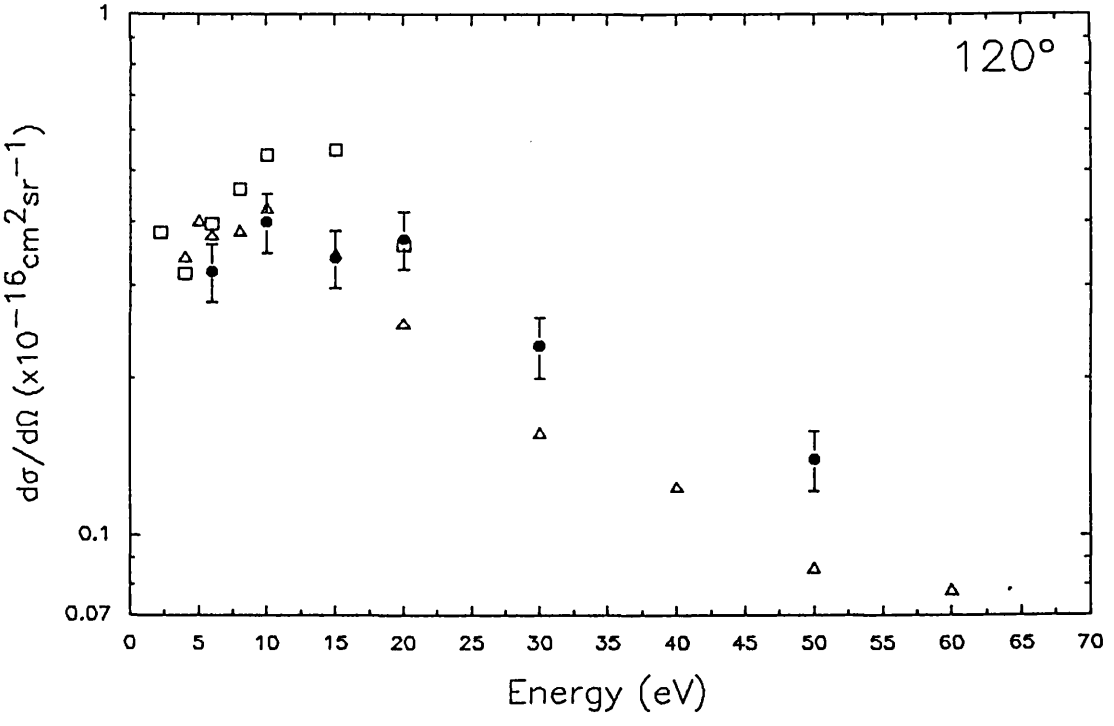

Figure 6.10 Absolute elastic differential cross sections for electron scattering from H_2O at 120° ($x10^{-16}$ cm^2 sr^{-1}). ● Present work; △ Danjo and NIshimura (1985); □ Shyn and Cho (1988).

present work, therefore the data of Shyn and Cho (1987) has been renormalised to that of Register *et al* (1980a) to eliminate any discrepancies arising from the use of different normalisation standards. This has resulted in an increase of approximately 10% in the published values of Shyn and Cho (1987).

Examination of the experimental data presented in figures 6.1 to 6.6 reveal two features. At an incident energy of 6eV, a minimum is observed at 120° which can be seen to migrate to an angle of 95° as the incident energy is increased to 50eV. Secondly, an inflexion is observed between 50° and 80° at 6eV and, less distinctly, at 10eV between 40° and 70°. In general, agreement between the present work and that of Shyn and Cho (1987) is good, except at the smaller scattering angles ($\theta<40°$) and scattering angles larger than 110°, where their data is consistently higher (see figures 6.7 and 6.10). There is also reasonable agreement between the present work and that of Danjo and Nishimura (1985), but as the incident energy is increased, their data is seen to be consistently lower than the present work and that of Shyn and Cho (1987). This is particularly noticeable for incident energies of 20eV and above where the data of Danjo and Nishimura (1985) is lower at all scattering angles. A comparison between the measurements of Katase *et al* (1986) and Danjo and Nishimura (1985) for an incident energy of 100eV also reveals a similar behaviour. In figure 6.1 the data of Jung *et al* (1982) is shown and this is the sum of the pure elastic and rotational excitation cross section sections. The excellent agreement between these results and the present work indicates that the cross sections measured in this work (and also by Danjo and Nishimura (1985) and Shyn and Cho (1987)) contain a significant contribution from rotational excitation and de–excitation cross sections. Finally, it should be noted that the differential cross sections of Shyn and Cho (1987) show a sharp rise for scattering angles greater than 120°. As these points lie outside the angular range of both the present work and that of Danjo and Nishimura (1985), it is not possible to say whether this is a true feature of the cross section or a result of an experimental error in the data of Shyn and Cho (1987).

6.2.2 A Review Of The Theoretically Calculated Differential Cross Sections

A large number of theoretical studies have been reported for electron scattering from H_2O. Several Born or Born-like calculations have been performed (e.g. Itikawa, 1972 and Fujita *et al*, 1983), but have only had limited success at high energies (>100eV) and low scattering angles ($\theta<30°$) and so will not be discussed here.

Gianturco and Thompson (1980) were the first to attempt an *ab initio* calculation of the cross sections for electron scattering from water using the single centre expansion method outlined in section 1.5.2. These calculations were later improved by Jain and Thompson (1982) who included a superior treatment of exchange and a parameter free polarisation potential. Gianturco and Scialla (1987b) made further improvements by increasing the number wavefunctions used to calculate the static potential. They also utilised a modified semiclassical exchange potential (MSCE) in preference to the usual Hara exchange potential and employed the polarisation-correlation potential described in section 1.4.5. To overcome the problems of divergence (a result of the large dipole moment, see section 1.4.3), Gianturco and Scailla (1987b) used the Born approximation to account for rotational excitation via a pure dipole interaction. The results of these calculations have been shown in figures 6.1 to 6.4. Interestingly, the authors calculated these cross sections without the inclusion of the polarisation potential as they claimed it played only a minor role due to the large dipole moment of the molecule.

Jain (1988) also used a single centre expansion method but employed a semi-empirical optical potential (SCOP) (see Jain, 1986 and Jain, 1987) to model the electron molecule interaction and obtained total (elastic plus inelastic) cross sections over the energy range 10-3000eV. The real part of the SCOP term was composed of the sum of three isotropic interactions, namely static, polarisation and exchange potentials and were determined as a function of the target charge density evaluated from single centre molecular functions. The contribution from the non-spherical interactions (such as the permanent dipole etc.) were included via the first Born approximation. The imaginary part of the SCOP (i.e. the absorption potential) was determined as a function of the charge density of the molecule, static-exchange force of the electron-molecule system, incident energy and the mean excitation energy of the target. He observed that the best agreement between the theoretical and experimental differential cross sections was found when absorption effects were not included. Only the differential cross section at 100eV was given, but momentum transfer and total cross sections were reported for incident electron energies between 10eV and 3000eV and these are shown in figures 6.12 and 6.13 (see the following section).

Sato *et al* (1988) have published electron scattering cross section using the continuum multiple scattering (CMS) method described in section 1.5.1. They employed a "modified" version of the CMS method which had the advantage of no constant potential in region II, thus giving a more physically realistic potential. No details of this modification were given, except a reference to a forthcoming paper to be published by the authors. To overcome the divergence problems in calculating the differential

cross sections, they used the Born approximation to calculate the contributions from partial waves larger than l=7. Using this approach they were able to calculate differential (see figures 6.2, 6.3 and 6.5) and momentum transfer cross sections (see figure 6.13) between 2eV and 200eV.

Finally, the cross sections obtained with perhaps the most sophisticated calculations, have been reported by Brescansin *et al* (1986). They were obtained within the fixed-nuclei model using the Schwinger variational principle at incident energies between 2eV and 20eV. An exact static-exchange potential was employed to account for short range aspects of the collision governed by the low partial waves. As a result of the divergence problems encountered when calculating the differential cross sections for a polar molecule within the fixed nuclei model, Brescansin *et al* (1986) were only able to calculate differential cross sections for angles greater than 30°. The results of their differential cross section calculations are shown figures 6.1 to 6.4.

The theoretical calculations are only partly successful in predicting the shape and magnitude of the differential cross sections. For incident electron energies between 6eV and 20eV the results of Brescansin *et al* (1986) are found to be in good agreement with the experimental results. Their differential cross sections show the minimum around 120° and also a rising cross section for angles greater than 120°, however, it is only at 20eV that their results approach the magnitude of the large angle cross sections of Shyn and Cho (1987). At all other energies the values of Brescansin *et al* (1986) are significantly lower. The results of Sato *et al* (1988) are also found to be in good agreement with the experimental data, particularly at 20eV and 50eV. At the large scattering angles ($\theta \geq 120°$), the work of Sato *et al* (1988) also shows a rising cross section but not to the same degree as Brescansin *et al* (1986) or Shyn and Cho (1987). Finally, the work of Gianturco and Scialla (1987) compares poorly with the two other theoretical studies. Although, their work agrees well with the experimental results at the smaller scattering angles, the cross sections for angles greater than 70° are significantly lower.

Due to the considerable differences in the computational methods used in the theoretical treatments discussed above, it is difficult to evaluate their relative merits except for their ability to match the experimental data. The results of Brescansin *et al* (1986) and Sato *et al* (1988) are seen to be in reasonable agreement with the experiments but the results of Gianturco and Scialla (1987b) are significantly lower for scattering angles in excess of 70°. Sato *et al* (1988) report that the shape and magnitude of their differential cross sections in this angular region were sensitive to the strength of the exchange interaction in their model. Therefore, the discrepancy in the

data of Gianturco and Scialla (1987b) may be a result of the exchange potential they employed. In addition, no polarisation potential was included in their calculation of the differential cross sections and this may also explain the poor quality of their results. The inclusion of the Born approximation in the works of Gianturco and Scialla (1987b) and Sato *et al* (1988) can be seen to result in a better agreement with the experimental data at the smaller angles.

6.3 Integral and Momentum Transfer Cross Sections

Integral (σ_t) and momentum transfer (σ_m) cross sections have been derived in the present work by an extrapolation of the measured differential cross section data to the scattering angles 0° and 180°. The errors associated with the values of σ_t and σ_m may be large due to the large angular range over which the differential cross section has to be extrapolated (see section 4.4). The values of σ_t and σ_m are given in table 6.2 and the percentages represent the contribution to the final values from extrapolated regions of the differential cross sections. The errors in σ_t and σ_m were 20% and 25% respectively (see section 5.3).

The integral cross sections derived from the differential cross sections in the present work are shown in figure 6.11 together with the results of Danjo and Nishimura (1985) and Shyn and Cho (1987), who also derived values of σ_t from an extrapolation of their differential cross section data. The data of Danjo and Nishimura (1985) is lower at all energies and this is particularly noticeable above 15eV. In their differential cross section measurements, it is observed that for incident energies of 15eV and above, their results are consistently lower than the present work and this explains their smaller values of σ_t. The total cross sections (σ_T) has also been derived from the present work, Danjo and Nishimura (1985) and Shyn and Cho (1987) with the addition of the total ionisation cross sections of Orient and Srivastava (1987) to the integral cross sections and the results are shown in figure 6.12. A direct measurement of the total cross section has been reported by Sueoka *et al* (1986), Szmytkowski (1987) and Nishimura and Yano (1988) and their results are also shown in figure 6.12. In addition to these measurements, Jain (1988) has calculated the total cross section from 10eV to 1000eV using a semi-classical complex optical potential (see previous section). There is qualitative agreement between the total cross section measurements, all indicating a maximum around 10eV. However, the magnitude of the cross section remains uncertain, particularly below 20eV. It is interesting to note the good agreement between the theoretical cross sections of Jain (1988) and the experimental values.

Incident Energy

	6eV	10eV	15eV	20eV	30eV	50eV
σ_t	13.76	13.89	13.31	13.66	11.29	7.76
	22%	16%	16%	20%	20%	20%
σ_m	10.63	9.36	8.44	8.90	6.83	5.09
	52%	43%	45%	55%	60%	73%

Table 6.2 Absolute integral and momentum transfer cross sections for electron scattering from H_2O ($x10^{-16}cm^2$). The numbers given as percentages are the contributions from the extrapolated differential cross sections values.

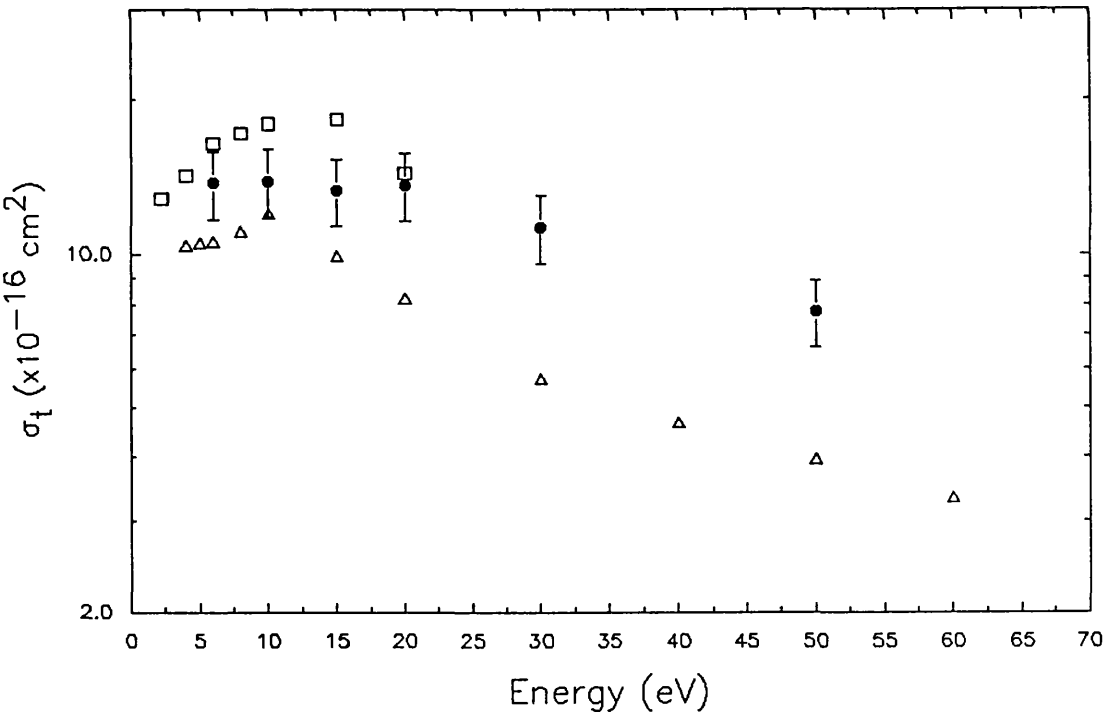

Figure 6.11 Absolute elastic integral cross sections for electron scattering from H_2O ($x10^{-16}$ cm^2 sr^{-1}). ● Present work; △ Danjo and Nishimura (1985);□ Shyn and Cho (1988).

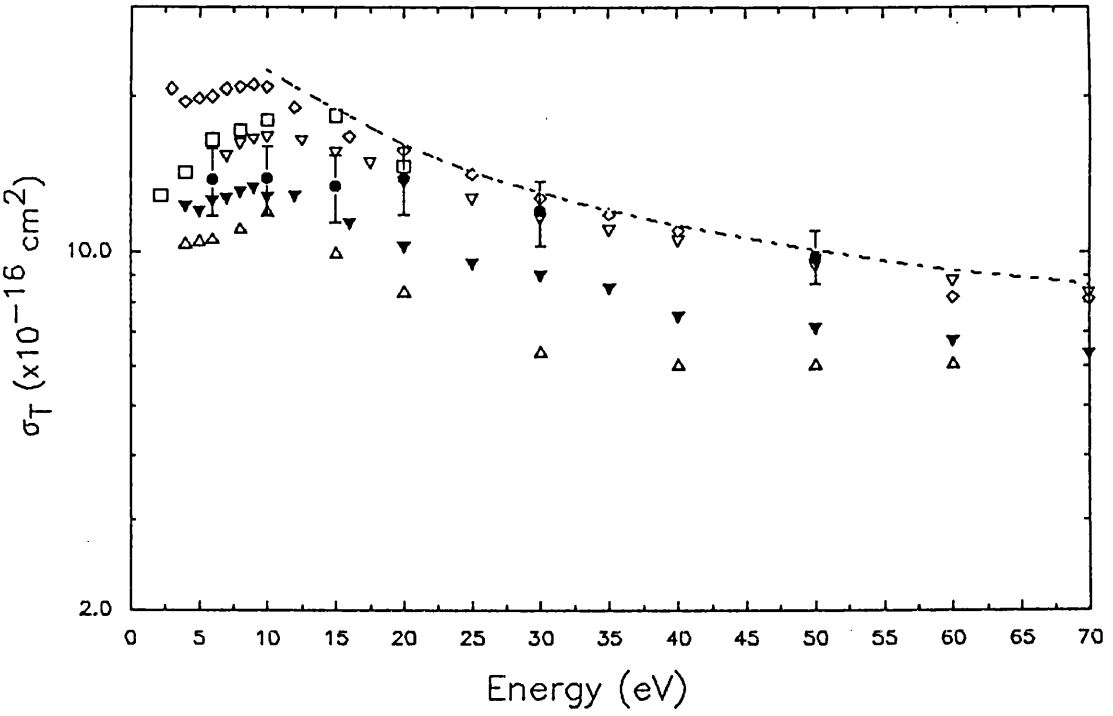

Figure 6.12 Absolute total cross sections for electron scattering from H_2O (x10^{-16} cm^2 sr^{-1}). Experiment: ● Present work; △ Danjo and Nishimura (1985); □ Shyn and Cho (1988); ▼ Sueoka *et al* (1986); ◇ Szmytkowski *et al* (1987); ▽ Nishimura and Yano (1988). Theory:- - - Jain (1988).

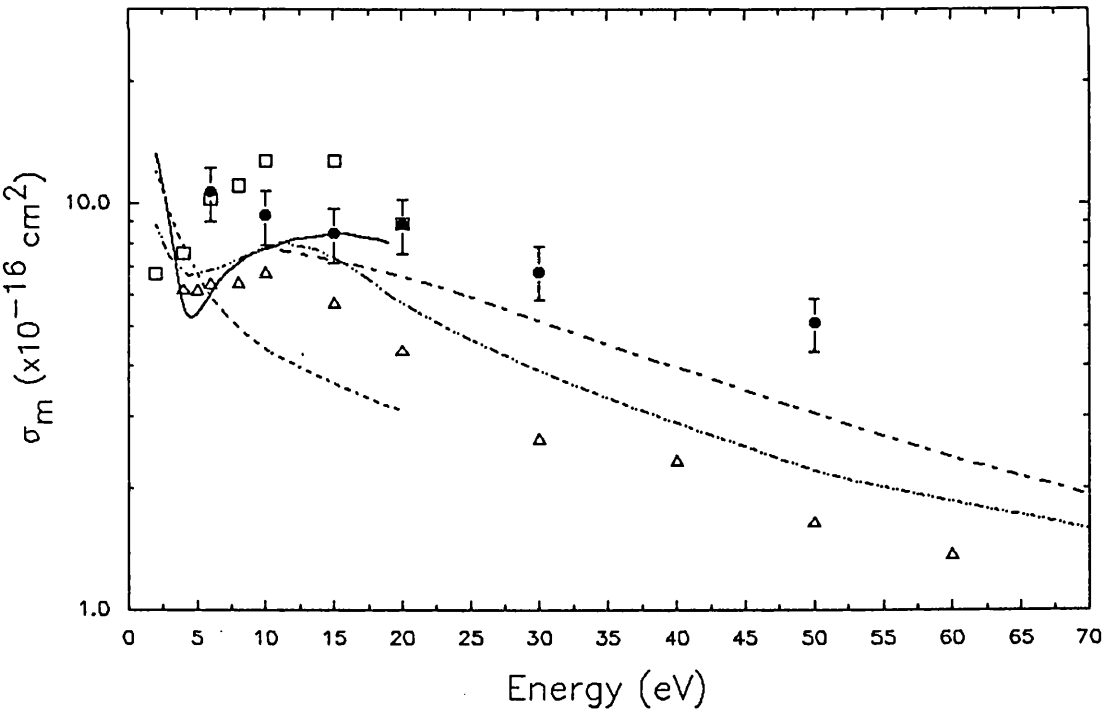

Figure 6.13 Absolute momentum transfer cross sections for electron scattering from H_2O (x10^{-16} cm^2 sr^{-1}). Experiment: ● Present work; △ Danjo and Nishimura (1985); □ Shyn and Cho (1988). Theory: ——— Brescansin *et al* (1985); ..... Gianturco and Scailla (1987b); ------ Sato *et al* (1988); – – · Jain (1988).

The momentum transfer cross sections calculated from the present data are shown in figure 6.13 together with the experimental results of Danjo and Nishimura (1985) and Shyn and Cho (1987) and the theoretical results of Brescansin *et al* (1986), Gianturco and Scialla (1987b), Sato *et al* (1988) and Jain (1988). The data of Shyn and Cho (1987) are generally larger than the other works and this is a result of the increased size of the differential cross sections at large scattering angles ($\theta \geq 120°$). Conversely, the data of Danjo and Nishimura (1985) are notably lower and is a consequence of their generally lower differential cross section values. At the low energies (E<20eV), the theoretical results of Brescansin *et al* (1986) and Sato *et al* (1988) are in general agreement, showing a minimum at 4eV and a broad maximum around 15eV. At the higher energies, the results of Sato *et al* (1988) and Jain (1988) show the same trend, lying between the data from the present work and that of Danjo and Nishimura (1985).

6.4 Summary

In this chapter absolute elastic differential, integral, and momentum transfer cross sections have been presented. Using the total ionisation cross sections of Orient and Srivastava (1987), total cross sections have also been derived. Agreement between the present differential cross sections and the two previous works is reasonable. At the higher energies (≥15eV), the results of Danjo and Nishimura (1985) are consistently lower than the present work and the theoretical results of Sato *et al* (1988). The integral, momentum transfer and total cross sections of Danjo and Nishimura (1985) are therefore also significantly lower than the published data of several other authors and this would seem to indicate the possibility of a systematic error in their measurements. The present work was unable to confirm the sharp rise in the differential cross sections at large scattering angles (≥120°) as reported by Shyn and Cho (1987) but from the evidence of the theoretical data, it would appear that these cross sections may have been overestimated, especially at the lower energies (E<20eV).

The total cross section data derived from the present data is in good agreement with the previously reported direct measurements. All total cross section measurements indicate a small maximum at an incident energy of 10eV and this may be due negative ion formation. The presence of resonance effects in this energy region has been reported by a number of authors in a variety of channels. Mathur and Hasted (1974) reported resonance structure in their transmission experiments at 8eV. Melton and Neece (1971), Jungen *et al* (1979) and Belić *et al* (1981) have all observed significant increases in the production of H^- at 6.5eV, 8.6eV and 11.8eV and this has been

attributed to the formation of three resonances with $^2B_1$, $^2A_1$ and $^2B_2$ symmetries which decay via dissociative attachment. Seng and Linder (1976) have observed an enhancement in the vibration excitation cross section around 8eV and attributed this to the formation of the $^2A_1$ resonance indicating that the autoionisation cross section of this state may be significant.

Chapter 7

Absolute Elastic Cross Sections For Electron Scattering From N_2O

7.1 Introduction

In recent years, nitrous oxide (N_2O) has attracted increasing scientific interest due to its role in a number of processes. N_2O lasers have been used as a secondary frequency standard and in areas of spectroscopy within the 10μm region where the frequency range of the CO_2 laser is inadequate (Fox and Reid, 1985). N_2O has also been found to be increasingly important within the chemistry of the upper atmosphere where it plays an important role in the destruction of the ozone layer (Hahn and Junge, 1977; Wang and Sze, 1980). It has been noted that electron scattering cross sections for molecules with a similar structure show similar characteristics. For example, Jain (1982) has reported that for incident electron energies between 40eV and 800eV, the elastic differential, integral and momentum transfer cross sections for electron scattering from N_2 and CO are similar. As N_2O and CO_2 are isoelectronic and linear in their ground states, they may also be expected to follow this trend.

7.2 Differential Cross Sections

Two measurements of the absolute elastic differential cross sections for elastic scattering from N_2O have been reported. Kubo *et al* (1981) measured the differential cross section at incident energies of 5eV, 10eV, 20eV and 30eV for scattering angles between 30° and 140° using the relative flow technique described in section 4.5. Marinković *et al* (1986) measured relative differential cross sections at incident energies between 10eV and 80eV, for scattering angles between 10° and 148°. They obtained absolute cross sections by normalising their relative integral cross sections to the total cross sections of Szmytkowski *et al* (1984), corrected for the effects of ionisation using the cross sections of Rapp and Englander-Golden (1965). Azria *et al* (1975), Tronc *et al* (1981) and Andrić and Hall (1984) have reported vibrational excitation differential

cross sections for incident energies in the 2eV and 8eV region. Several theoretical calculations and assignments of the electronic states of N_2O have been performed (Chutjian and Segal, 1972; Fridh *et al*, 1978; Nakatsuji, 1983) but only one attempt has been made to calculate electron scattering cross sections. Dubé and Herzenberg (1975) have used the adiabatic nuclei approximation to calculate vibrational excitation cross sections at low incident energies (E<4eV) but no elastic scattering cross sections were given.

The absolute elastic differential cross sections measured in the present work are shown in figures 7.1 to 7.17 and tabulated in tables 7.1 and 7.2. The data of Kubo *et al* (1981) and Marinković *et al* (1986) are also shown for comparison. Figures 7.1 to 7.11 show the differential cross sections as a function of scattering angle for incident energies between 5eV and 80eV. Figures 7.1 to 7.4 show that as the energy increases from 5eV to 10eV the shape of the differential cross section undergoes a significant change. At 5eV, the cross section has a broad maximum around 60° and a minimum at 130°. As the energy increases, the maximum disappears and the cross section becomes forward peaked, with the minimum moving to 100°. For incident energies greater than 10eV, this trend continues with the small angle cross sections increasing while the minimum deepens and continues to move to smaller scattering angles. Between 10eV and 20eV, there appears to be a slight shoulder in the 30° to 90° region and this is particularly noticeable in the data of Marinković *et al* (1986) at 12eV. While a similar feature is seen in the present data, it is not as pronounced.

The agreement between the present results and those reported by Kubo *et al* (1981) and Marinković *et al* (1986) is good. The largest discrepancies are found at the higher scattering angles, where the cross sections in the present work are generally larger. It should also be noted that the minimum seen in the data of Marinković *et al* (1986) is generally deeper than that seen in the present work or that of Kubo *et al* (1981). As the data of Marinković *et al* (1986) is also slightly higher at the smaller scattering angles, this suggests that the angular resolution of their apparatus may have been superior to that used in the present work or by Kubo *et al* (1981).

Figures 7.12 to 7.17 show the differential cross section as a function of energy at scattering angles of 20°, 40°, 60°, 80°, 100° and 120°. The general trend in the

	Incident Energy					
θ	5eV	7.5eV	8.0eV	8.5eV	10eV	12eV
0						
10	0.80	1.89	2.71	2.73	4.43	8.19
15	0.60	1.4	1.91	2.12	3.77	5.44
20	0.8	0.99	1.37	1.52	2.95	4.58
25	0.82	0.82	1.18	1.38	2.45	
30	0.91	0.82	1.10	1.30	2.22	3.08
35	1.02	0.83	1.06	1.19	1.93	
40	1.06	0.86	1.07	1.16	1.59	2.00
45	1.16	0.86	1.05	1.09	1.45	
50	1.21	0.84	1.04	1.05	1.31	1.50
55	1.17	0.81	0.99	1.04	1.19	
60	1.16	0.76	0.97	0.99	1.09	1.20
65	1.12	0.66	0.92	0.93	0.95	
70	0.98	0.60	0.88	0.88	0.84	0.98
75	0.67	0.66	0.81	0.81	0.80	
80	0.95	0.70	0.76	0.71	0.72	0.73
85	0.87	0.65	0.68	0.65	0.64	0.63
90	0.80	0.61	0.60	0.53	0.56	0.55
95	0.72	0.52	0.51	0.51	0.47	
100	0.60	0.45	0.48	0.44	0.44	0.41
105	0.54	0.38	0.42	0.44	0.41	0.40
110	0.46	0.36	0.42	0.46	0.44	0.41
115	0.40	0.36	0.41	0.44	0.50	0.47
120	0.36	0.38	0.46	0.59	0.61	0.60
error	12%	12%	13%	12%	12%	12%

Table 7.1 Absolute elastic differential cross sections for electron scattering from N_2O for incident energies between 5ev and 12eV ($x10^{-16}cm^2sr^{-1}$).

	Incident Energy				
	15eV	20eV	30eV	50eV	80eV
θ					
0					
10	8.26	33.79	29.97	23.17	18.29
15	6.43	8.89	12.88	13.27	8.73
20	5.40	4.50	5.54	4.88	1.78
25	4.12				
30	3.28	2.83	2.50	1.96	0.65
35	2.68				
40	2.10	1.65	1.21	0.85	0.28
45	1.72				
50	1.45	1.13	0.73	0.46	0.14
55	1.27				
60	1.12	0.82	0.44	0.24	0.084
65	0.96				
70	0.85	0.57	0.24	0.15	0.070
75	0.74	0.47	0.17	0.14	0.068
80	0.64	0.37	0.16	0.13	0.063
85	0.54	0.28	0.17	0.12	0.062
90	0.43	0.26	0.18	0.10	0.054
95	0.36	0.26	0.21	0.11	0.050
100	0.34	0.24	0.24	0.10	0.051
105	0.34	0.31	0.27	0.13	0.057
110	0.41	0.37	0.30	0.15	0.070
115	0.50				0.076
120	0.64	0.46	0.34	0.27	0.10
error	12%	12%	12%	12%	13%

Table 7.2 Absolute elastic differential cross sections for electron scattering from N_2O for incident energies between 15ev and 80eV ($x10^{-16}cm^2sr^{-1}$).

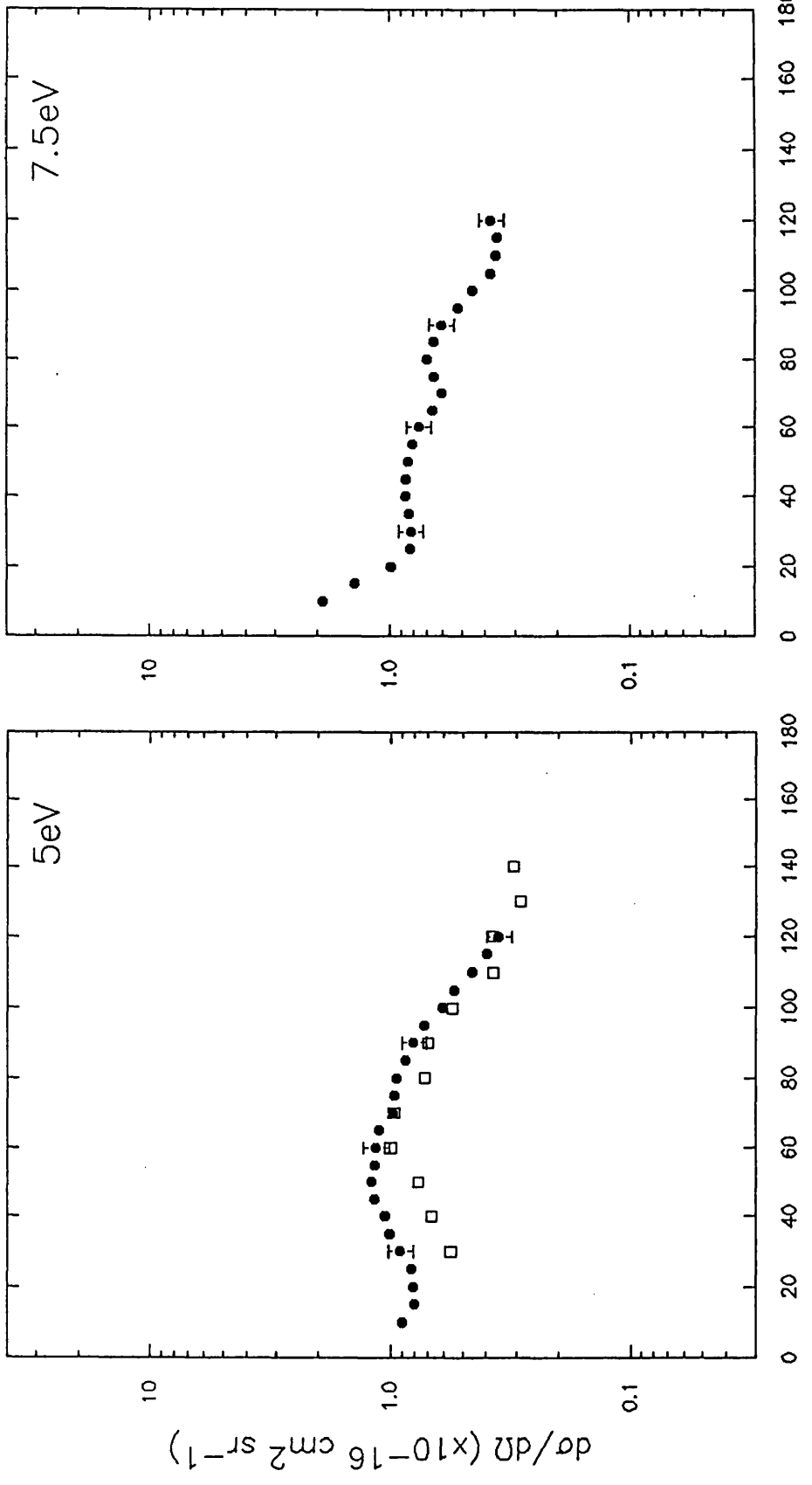

Figure 7.1 Absolute elastic differential cross sections for electron scattering from N_2O for an incident energy of 5eV ($x10^{-16}$ cm^2 sr^{-1}). ● Present work; □ Kubo *et al* (1981).

Figure 7.2 Absolute elastic differential cross sections for electron scattering from N_2O for an incident energy of 7.5eV ($x10^{-16}$ cm^2 sr^{-1}). ● Present work.

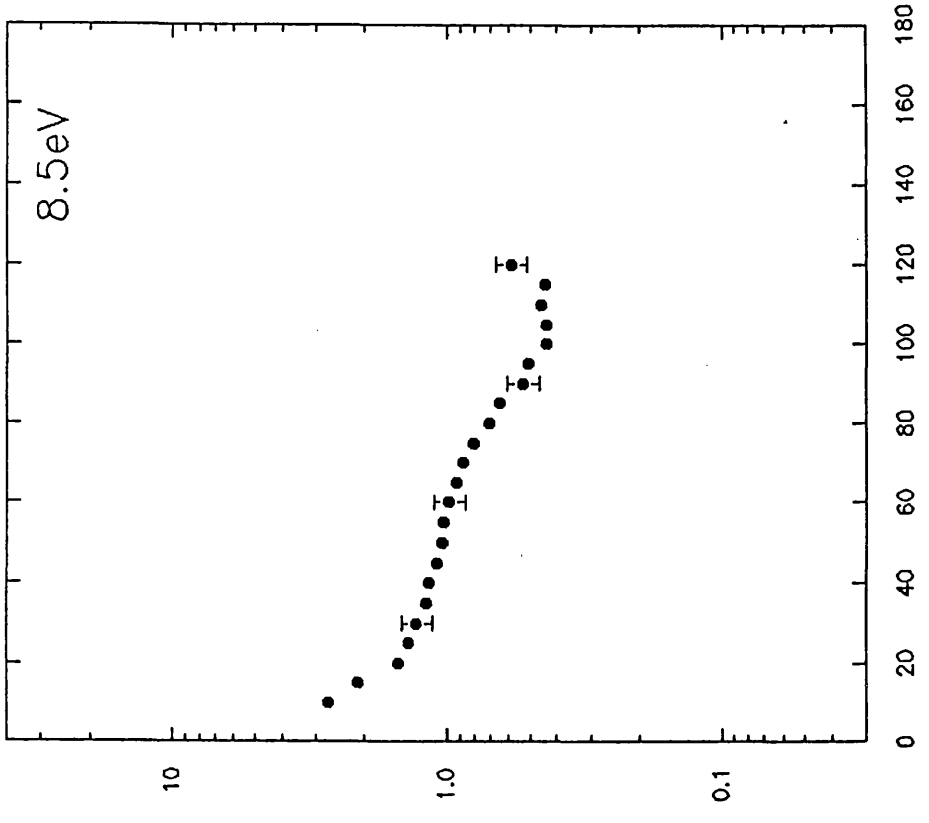

Figure 7.4 Absolute elastic differential cross sections for electron scattering from N_2O for an incident energy of 8.5eV ($x10^{-16}$ cm^2 sr^{-1}). ● Present work.

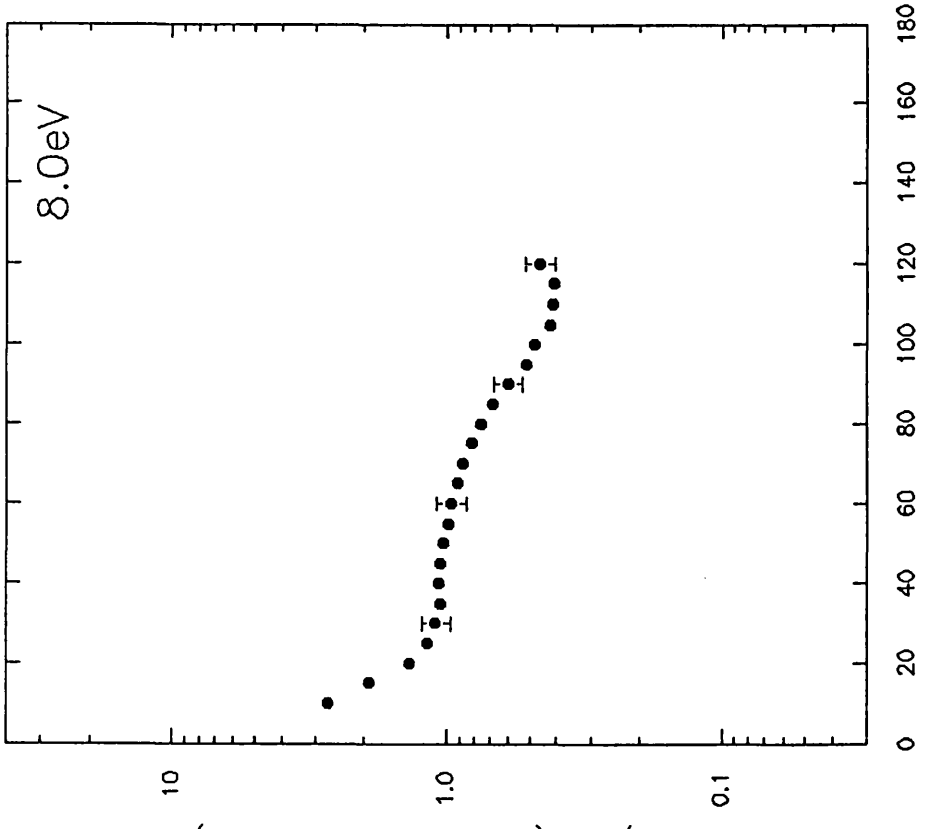

Figure 7.3 Absolute elastic differential cross sections for electron scattering from N_2O for an incident energy of 8.0eV ($x10^{-16}$ cm^2 sr^{-1}). ● Present work.

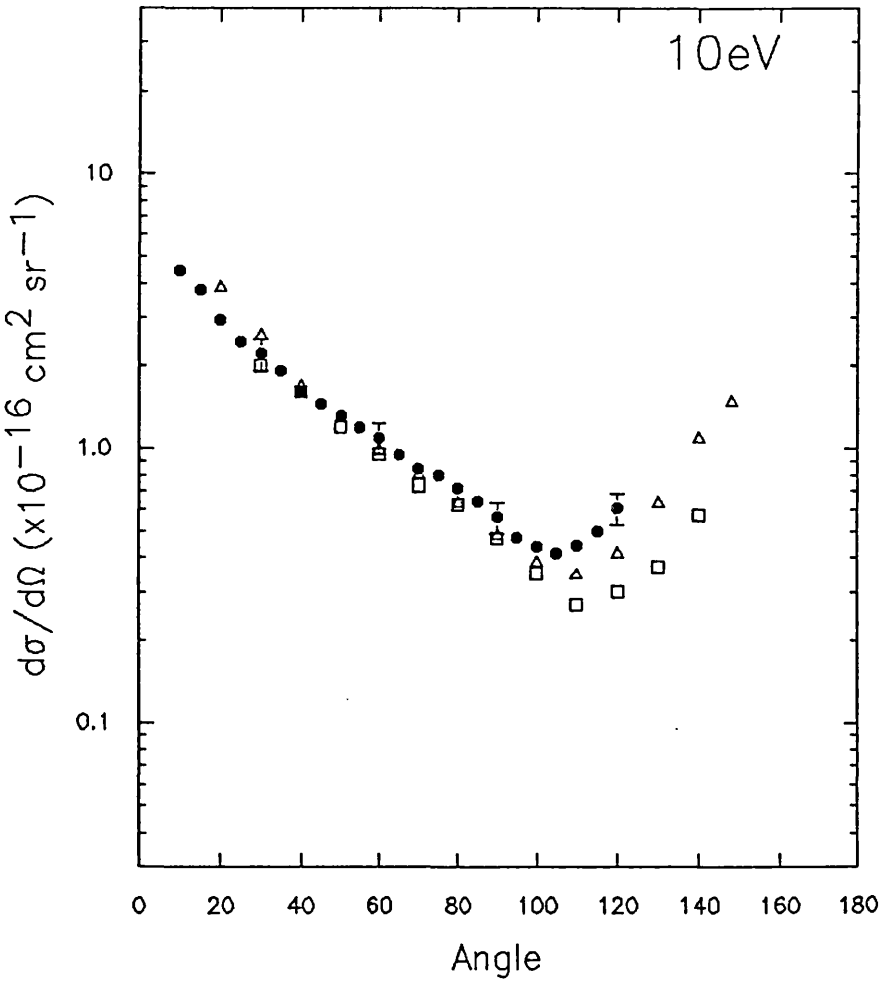

Figure 7.5 Absolute elastic differential cross sections for electron scattering from N_2O for an incident energy of 10eV ($x10^{-16}$ cm^2 sr^{-1}). ● Present work; □ Kubo *et al* (1981); △ Marinković *et al* (1986).

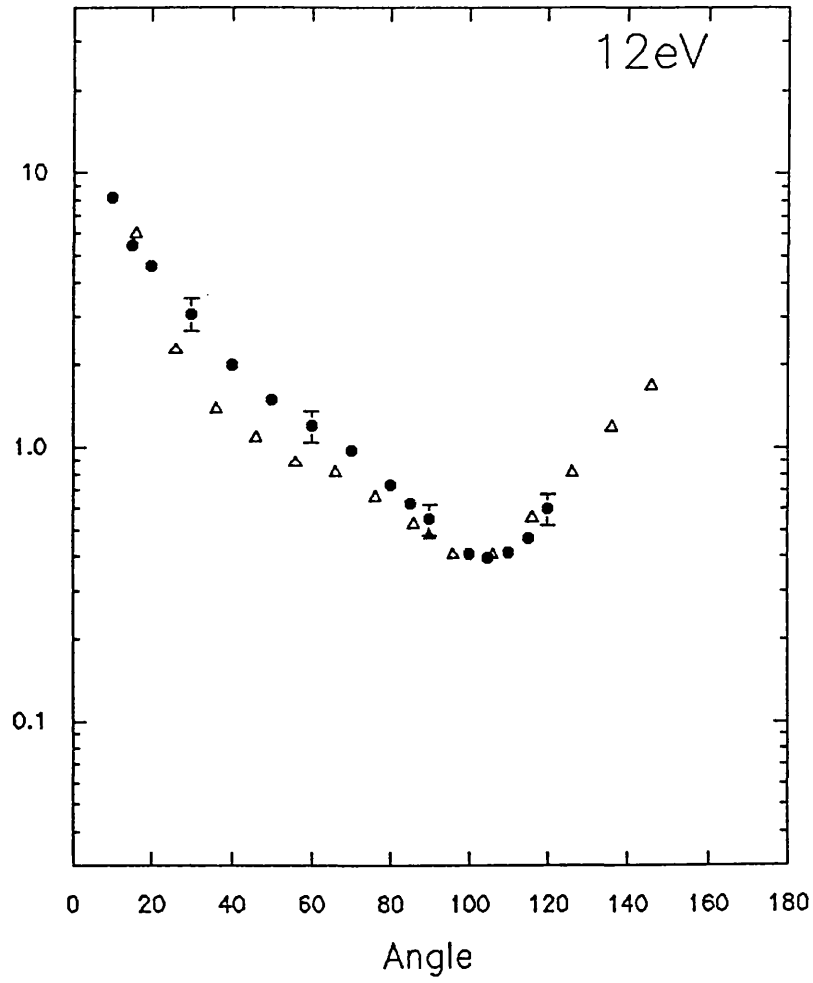

Figure 7.6 Absolute elastic differential cross sections for electron scattering from N_2O for an incident energy of 12eV ($x10^{-16}$ cm^2 sr^{-1}). ● Present work; △ Marinković *et al* (1986).

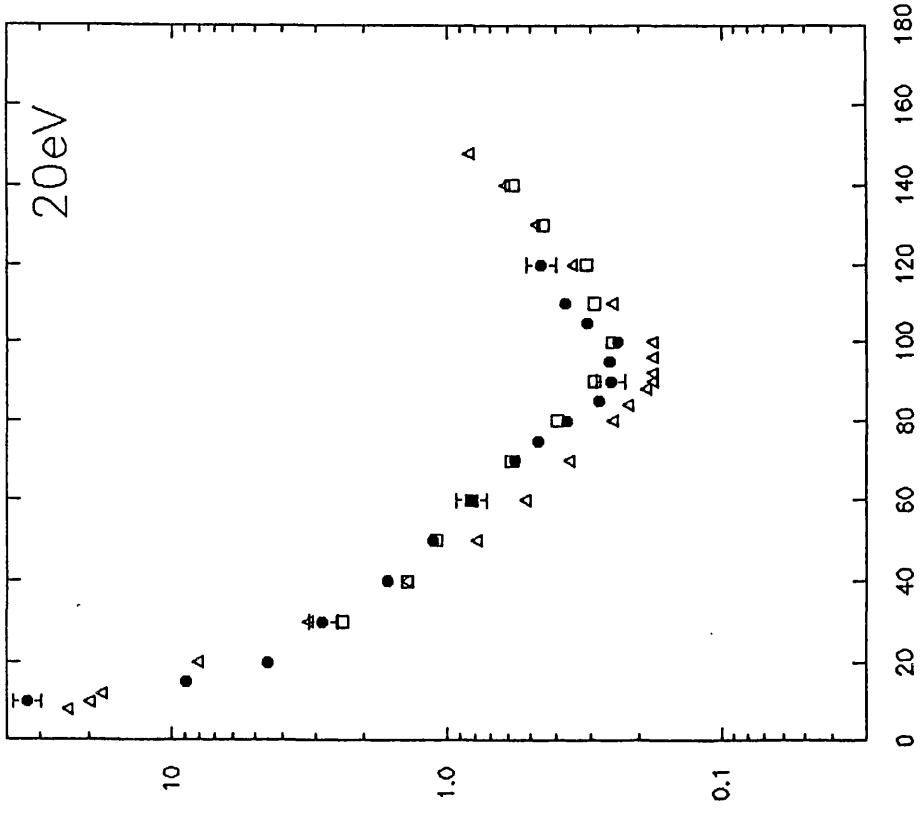

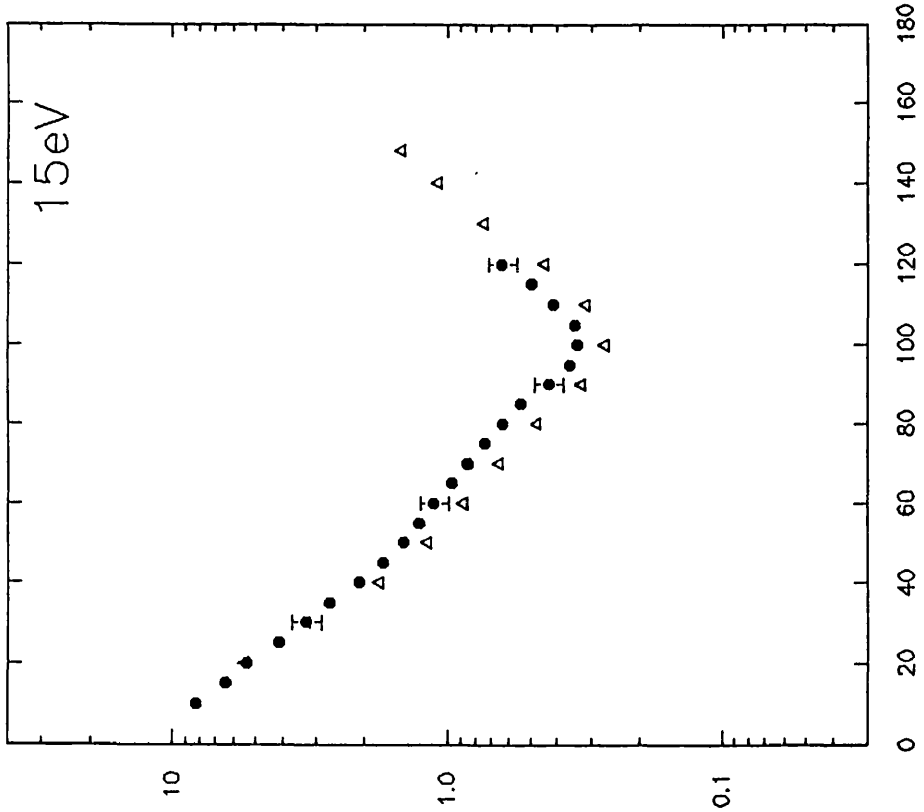

Figure 7.8 Absolute elastic differential cross sections for electron scattering from N_2O for an incident energy of 20eV ($x10^{-16}$ cm^2 sr^{-1}). ● Present work;□ Kubo *et al* (1981); △ Marinković *et al* (1986).

Figure 7.7 Absolute elastic differential cross sections for electron scattering from N_2O for an incident energy of 15eV ($x10^{-16}$ cm^2 sr^{-1}). ● Present work; △ Marinković *et al* (1986).

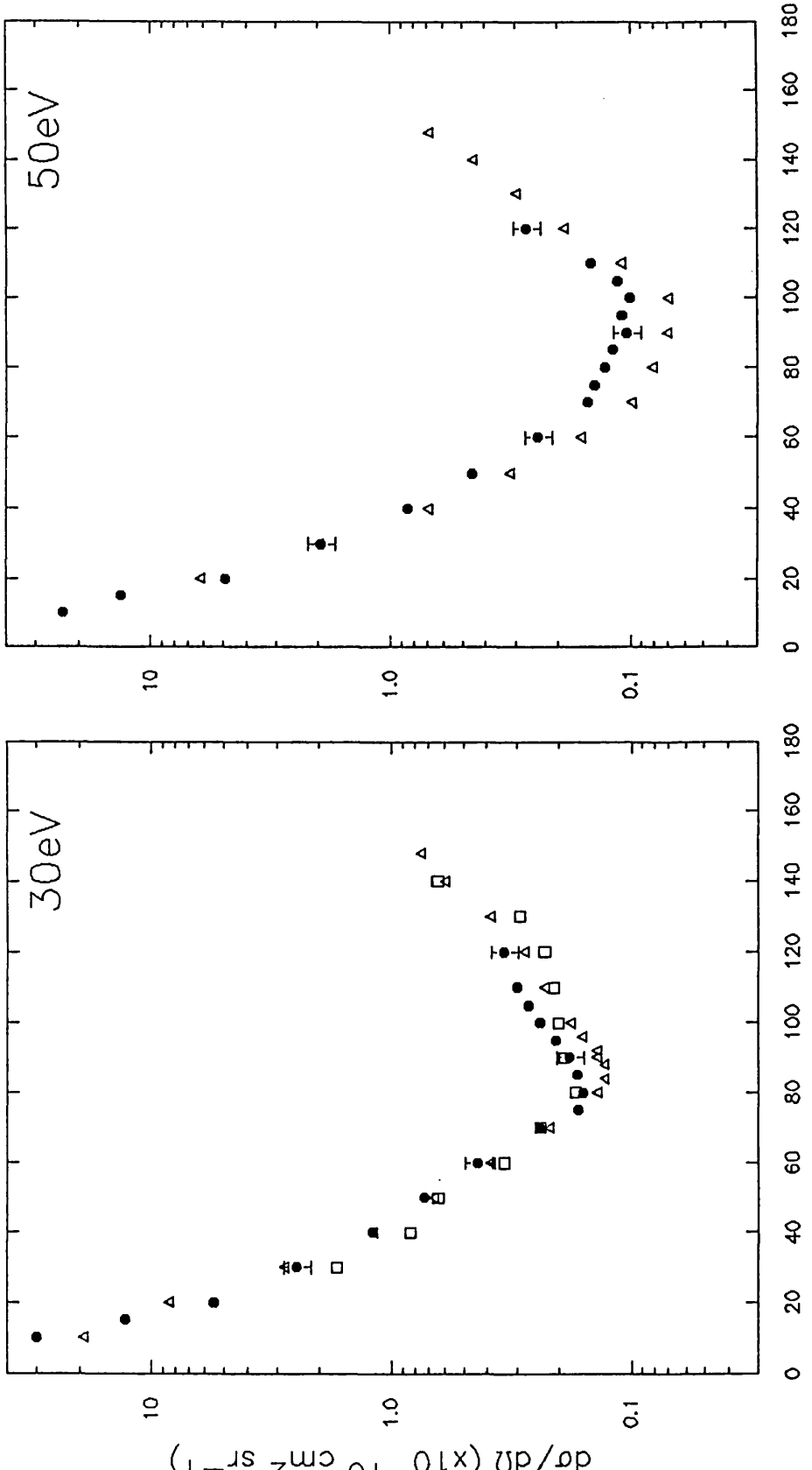

Figure 7.9 Absolute elastic differential cross sections for electron scattering from N_2O for an incident energy of 30eV (x10^{-16} cm^2 sr^{-1}). ● Present work; □ Kubo *et al* (1981); △ Marinković *et al* (1986).

Figure 7.10 Absolute elastic differential cross sections for electron scattering from N_2O for an incident energy of 50eV (x10^{-16} cm^2 sr^{-1}). ● Present work; △ Marinković *et al* (1986).

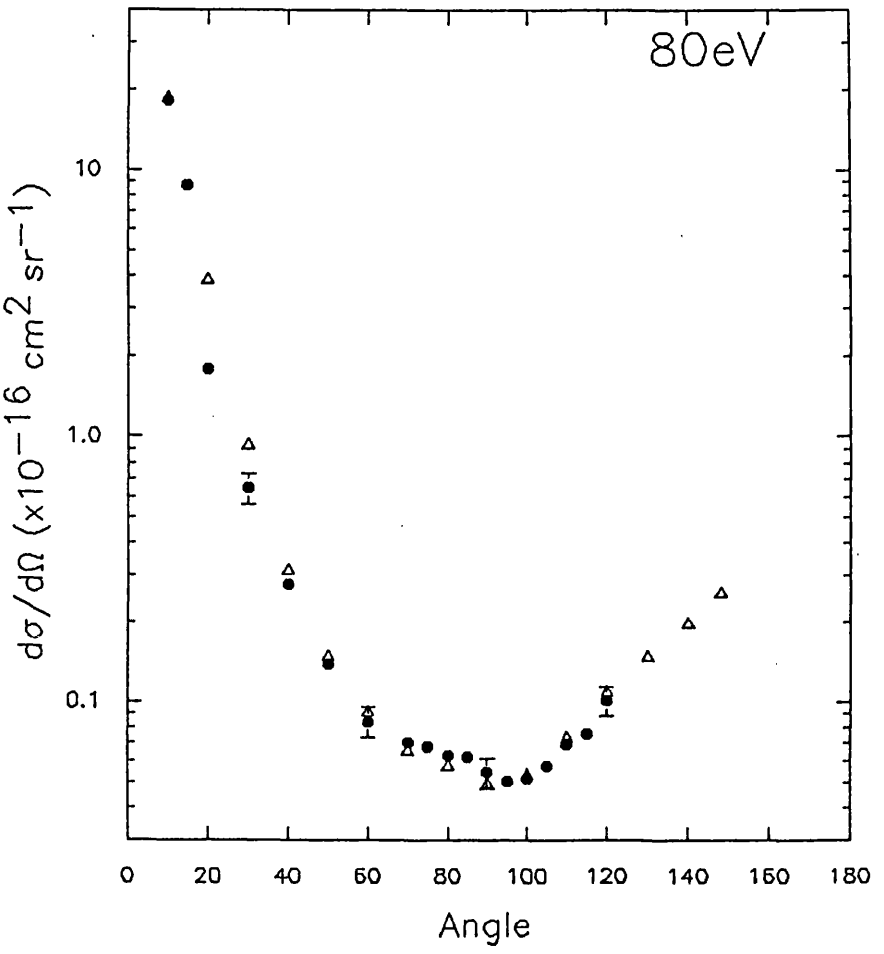

Figure 7.11 Absolute elastic differential cross sections for electron scattering from N_2O for an incident energy of 80eV ($x10^{-16}$ cm^2 sr^{-1}). ● Present work; △ Marinković *et al* (1986).

cross section shows a maximum in the 10eV region before falling away as the incident energy increases. Two resonances have been detected in low energy electron scattering experiments at 2eV and 8eV. At 2eV a shape resonance has been observed and its effects have been seen in a variety scattering processes. For example, Kwan *et al* (1984) and Szmytkowski *et al* (1984) have observed an enhancement in the total cross section, Azria *et al* (1975), Tronc *et al* (1981) and Andrić and Hall (1984) have all measured increased vibrational excitation and Tronc *et al* (1977) have reported a rise in O^- production formed by dissociative attachment. The second higher lying resonance at 8eV has only been seen by Tronc *et al* (1981) and Andrić and Hall (1984) in their work on vibrational excitation. From their measurements of the angular behaviour of

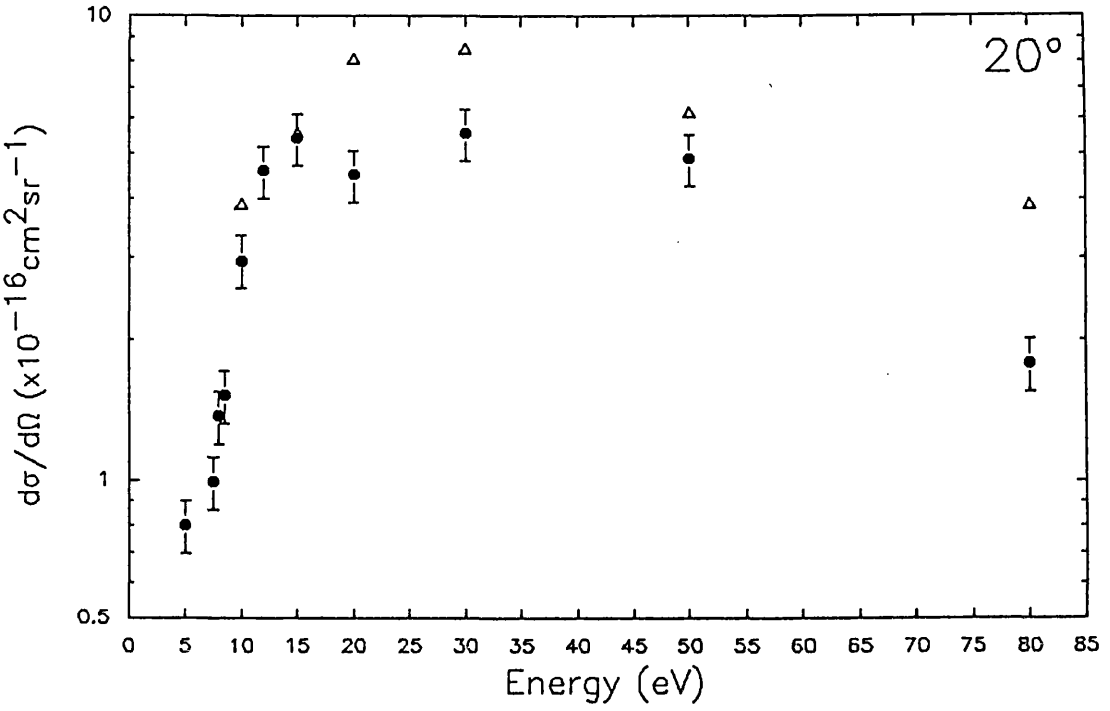

Figure 7.12 Absolute elastic differential cross sections for electron scattering from N_2O at 20° ($x10^{-16}$ cm^2 sr^{-1}). ● Present work; □ Kubo *et al* (1981); △ Marinković *et al* (1986).

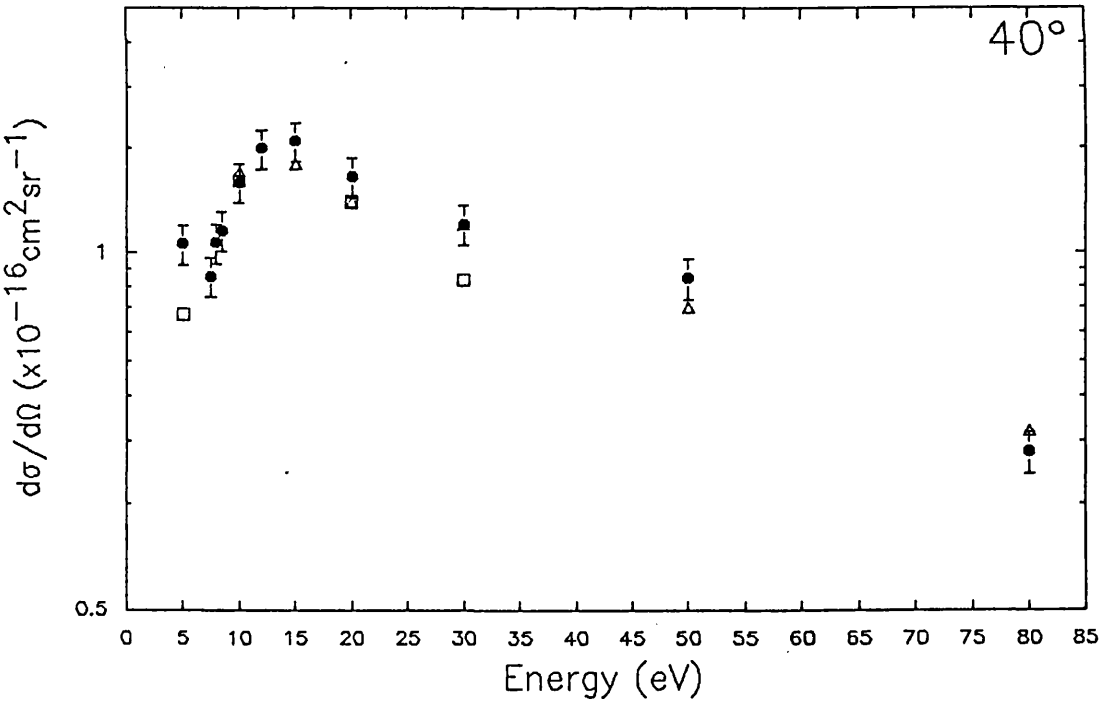

Figure 7.13 Absolute elastic differential cross sections for electron scattering from N_2O at 40° ($x10^{-16}$ cm^2 sr^{-1}). ● Present work; □ Kubo *et al* (1981); △ Marinković *et al* (1986).

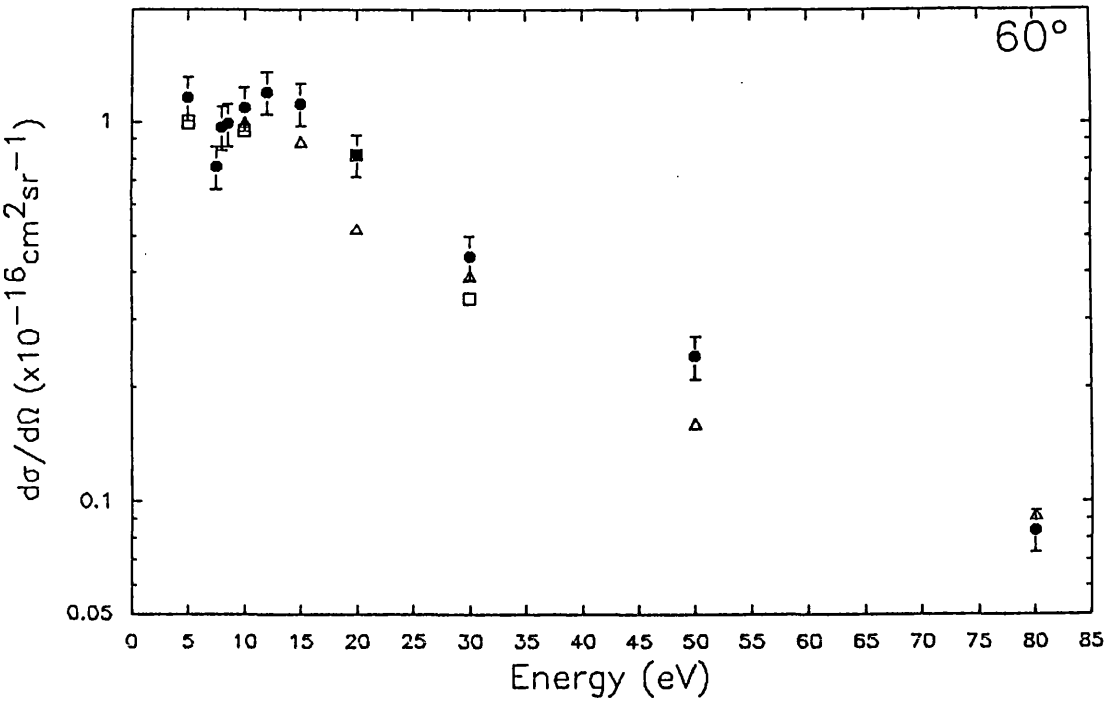

Figure 7.14 Absolute elastic differential cross sections for electron scattering from N_2O at 60° ($x10^{-16}$ cm^2 sr^{-1}). ● Present work; □ Kubo *et al* (1981); △ Marinković *et al* (1986).

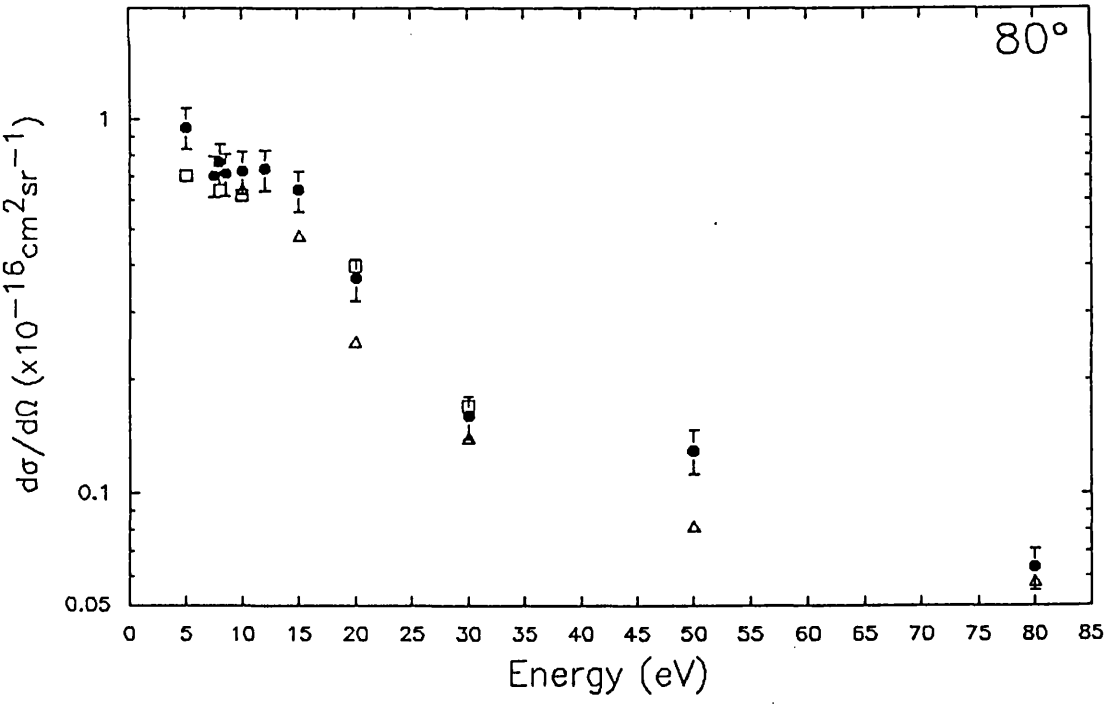

Figure 7.15 Absolute elastic differential cross sections for electron scattering from N_2O at 80° ($x10^{-16}$ cm^2 sr^{-1}). ● Present work; □ Kubo *et al* (1981); △ Marinković *et al* (1986).

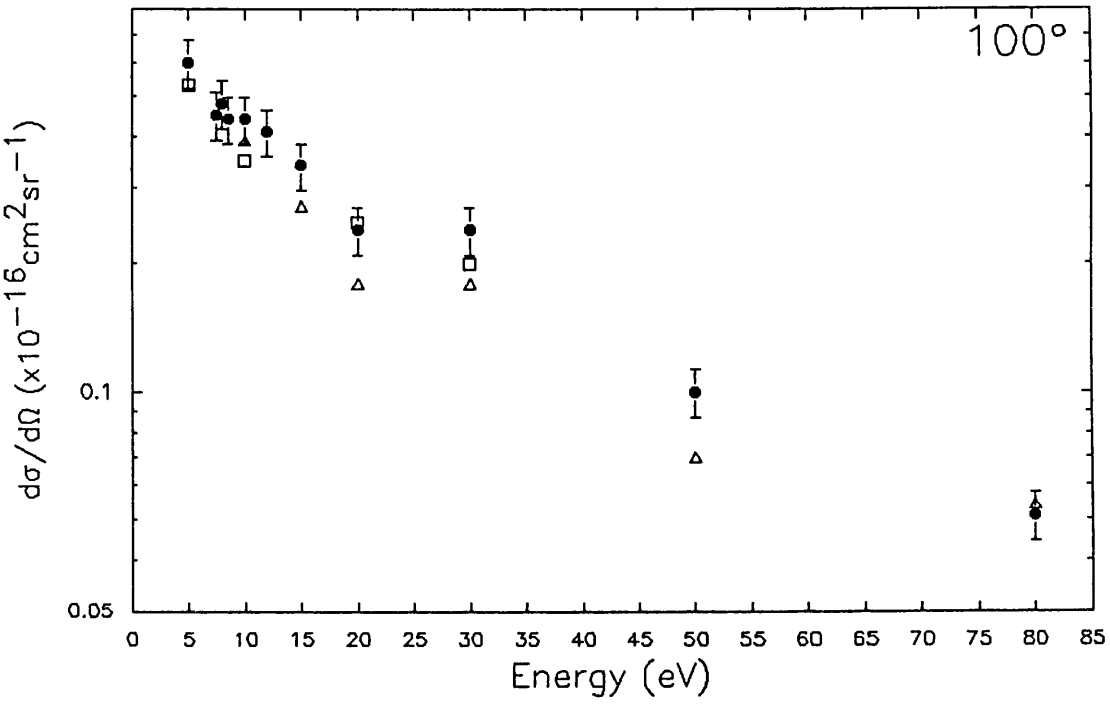

Figure 7.16 Absolute elastic differential cross sections for electron scattering from N_2O at 100° ($x10^{-16}$ cm^2 sr^{-1}). ● Present work; □ Kubo *et al* (1981); △ Marinković *et al* (1986).

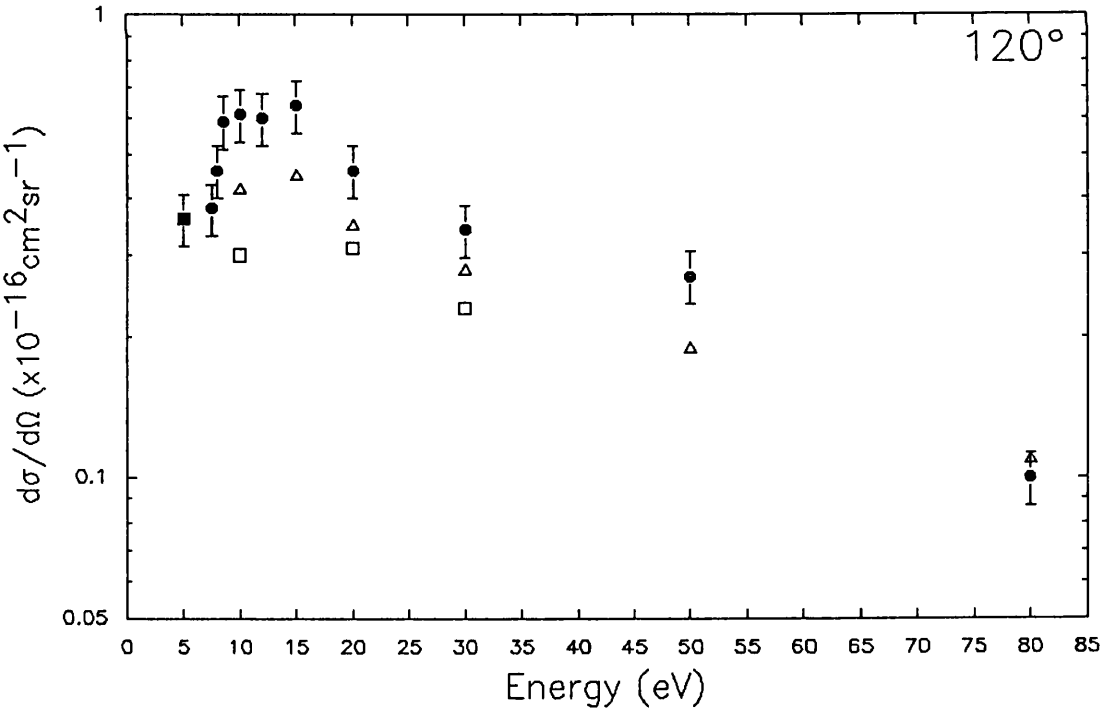

Figure 7.17 Absolute elastic differential cross sections for electron scattering from N_2O at 120° ($x10^{-16}$ cm^2 sr^{-1}). ● Present work; □ Kubo *et al* (1981); △ Marinković *et al* (1986).

the vibrational excitation cross sections, Andrić and Hall (1984) postulated the formation of a resonance at 8eV, where the l=1 partial wave was dominant. However, unlike the example of SF_6 where significant resonant enhancement of the cross section was seen (see figures 5.11 to 5.16), none is seen in figures 7.12 to 7.17. It is therefore probable that the elastic cross sections are dominated by non-resonant scattering.

7.3 Integral and Momentum Transfer Cross Sections

Integral and momentum transfer cross sections have been obtained, as in chapters 5 and 6, from an extrapolation of the differential cross section data to 0° and 180°. As discussed in chapter 5, the errors associated with this process were large due to the large angular range over which the differential cross section had to be extrapolated ($\Delta\sigma_t \approx 20\%$, $\Delta\sigma_m \approx 25\%$). The values of σ_t and σ_m obtained are shown in table 7.3. The values of σ_t obtained from the present work are shown in figure 7.18 together with the results of Marinković *et al* (1986). Total cross sections (σ_T) were also derived by addition of the ionisation cross sections of Rapp and Englander-Golden (1965) to values of σ_t shown in figure 7.18 and these are displayed in figure 7.19. Also presented are the direct measurements of the total cross section from Kwan *et al* (1984), Szmytkowski *et al* (1984) and Szmytkowski *et al* (1989). It is observed that there is good agreement between the total cross sections derived from the present work and those obtained from a direct measurement. The integral and total cross sections have a similar shape, with a minimum at 8eV and maximum at 15eV, but the total cross section shows a much slower decrease as a function of increasing energy which is the result of the increasing contribution of the ionisation cross section. The momentum transfer cross sections are shown in figure 7.20. The general trend of the cross section is similar to that seen in σ_t, with the cross section rising to a peak at 12eV and then falling away as the incident energy is increases.

7.4 Comparison Between N_2O and CO_2 Cross Sections

Investigations of the electron scattering cross sections from CO and N_2 have revealed several similarities between the shape and magnitude of the cross sections. Kwan *et al* (1984) have shown that the total cross section for N_2 and CO agree to within 5% for energies greater than 20eV, while Jain (1982) has noted that the elastic differential cross sections are similar in magnitude and shape for energies ≥40eV. These striking similarities have been attributed to the similar structure and geometries of these two molecules. The reason for these similarities may be explained by considering the time spent by the electron within the "field of influence" of the

	Incident Energy					
	5eV	7.5eV	8.0eV	8.5eV	10eV	12eV
σ_t	9.7	9.1	10.8	11.6	13.7	17.0
	12%	27%	25%	27%	12%	26%
σ_m	7.8	8.9	10.0	11.1	11.7	14.2
	27%	50%	49%	53%	53%	58%
	15eV	20eV	30eV	50eV	80eV	
σ_t	16.2	14.8	12.3	9.3	4.5	
	23%	17%	16%	17%	16%	
σ_m	12.3	8.6	6.4	4.8	2.1	
	55%	53%	56%	62%	64%	

Table 7.3 Absolute integral and momentum transfer cross sections for electron scattering from N_2O ($x10^{-16}cm^2$).

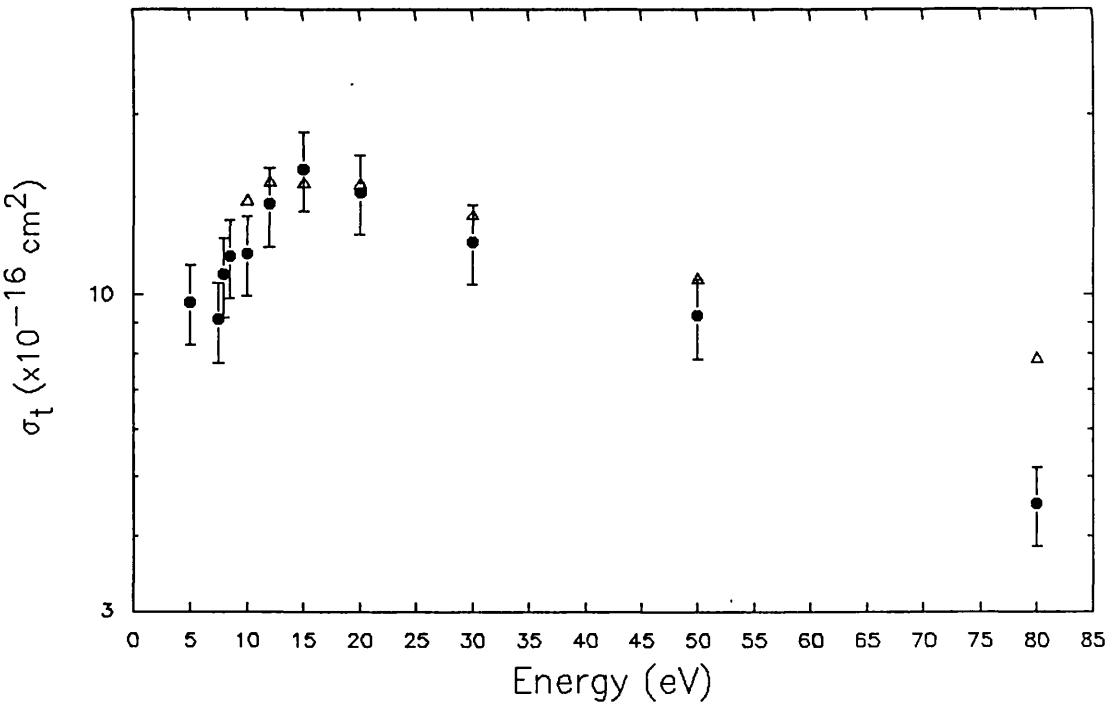

Figure 7.18 Absolute elastic integral cross sections for electron scattering from N_2O ($x10^{-16}$ cm^2). Experiment: ● Present work; △ Marinković *et al* (1986).

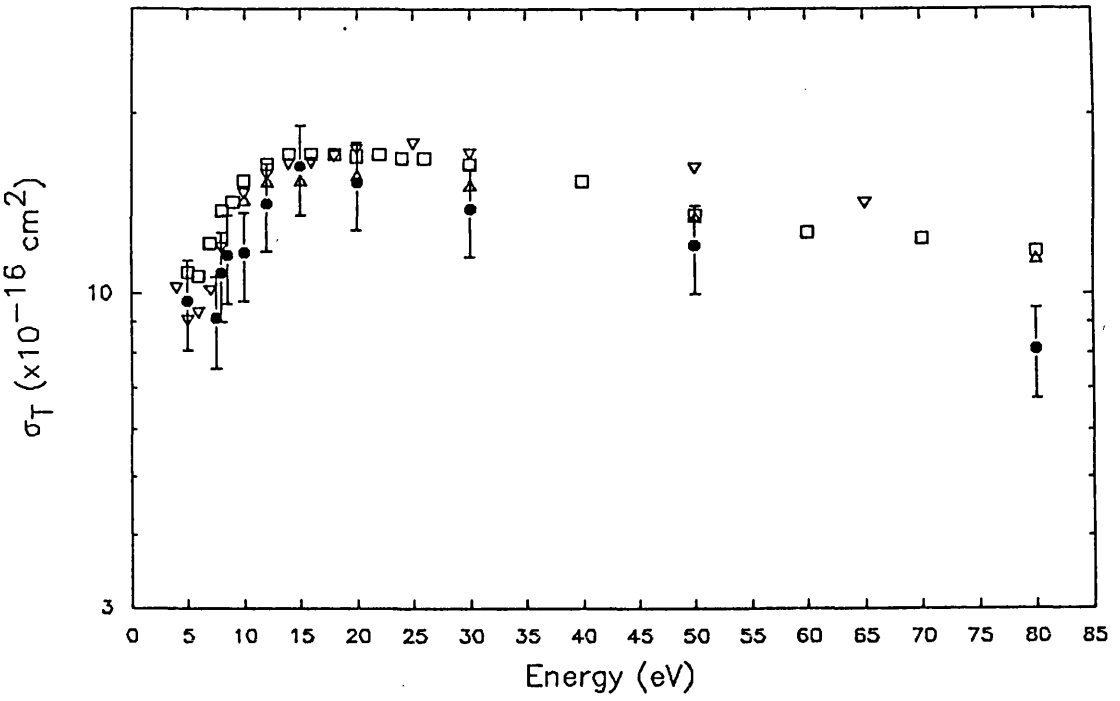

Figure 7.19 Absolute total cross sections for electron scattering from N_2O (x10^{-16} cm2). ● Present work; △ Marinković *et al* (1986); ▽ Kwan *et al* (1984); □ Szmytkowski *et al* (1984) and (1989).

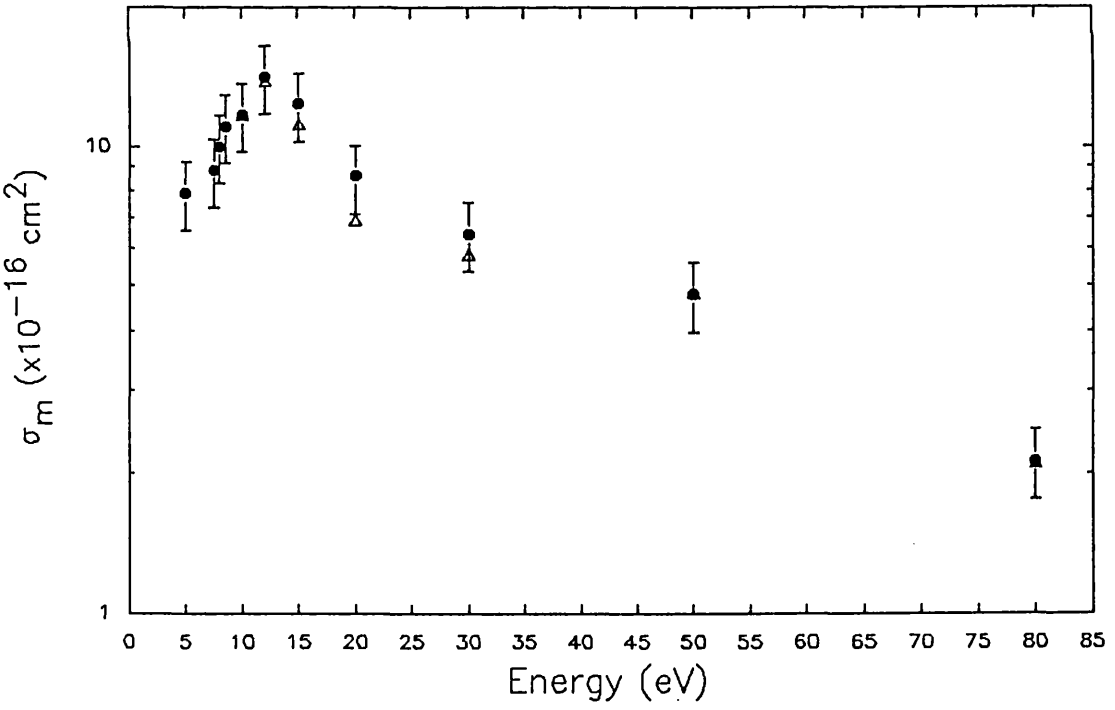

Figure 7.20 Absolute momentum transfer cross sections for electron scattering from N_2O (x10^{-16} cm2). ● Present work; △ Marinković *et al* (1986).

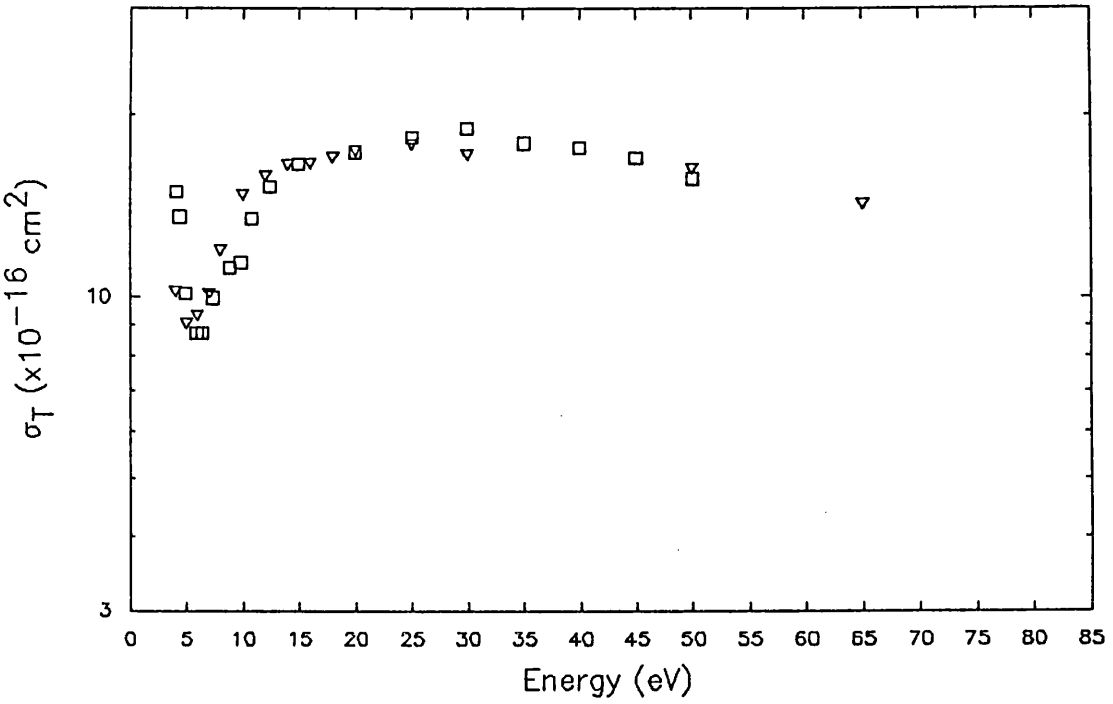

Figure 7.21 Comparison of the total cross sections for electron scattering from N_2O and CO_2 (x10^{-16} cm^2). N_2O: ▽ Kwan *et al* (1984). CO_2: □ Hoffman *et al* (1982) and Kwan *et al* (1983).

molecule. At low energies (≤10eV), the electron will remain within the field of the molecule for a relatively long time and its behaviour will be heavily influenced by the short range static and exchange effects. As the forces associated with these effects are very sensitive to the structure of the molecule, it is probable that even small differences in configuration of "similar" molecules will result in significant differences in the cross sections. As CO has a small dipole moment, this may also result in differences at low energies. Also the presence of resonances will complicate the situation further. At higher energies, the electron will remain within the field of the molecule for much shorter times and therefore the electron-molecule interaction will be insensitive to small differences in the structure of the target.

N_2O and CO_2 are isoelectronic (containing the same number of bound electrons) and linear in their ground states. Therefore, as with N_2 and CO, the electron scattering cross sections might be expected to show similar characteristics. Kwan *et al* (1984) were the first to investigate this possibility when they compared their own total cross section measurements for N_2O and with the CO_2 total cross sections of Hoffman *et al* (1982) and Kwan *et al* (1983) and these are shown in figure 7.21. There is good agreement between the σ_T measurements of the two molecules for incident energies of

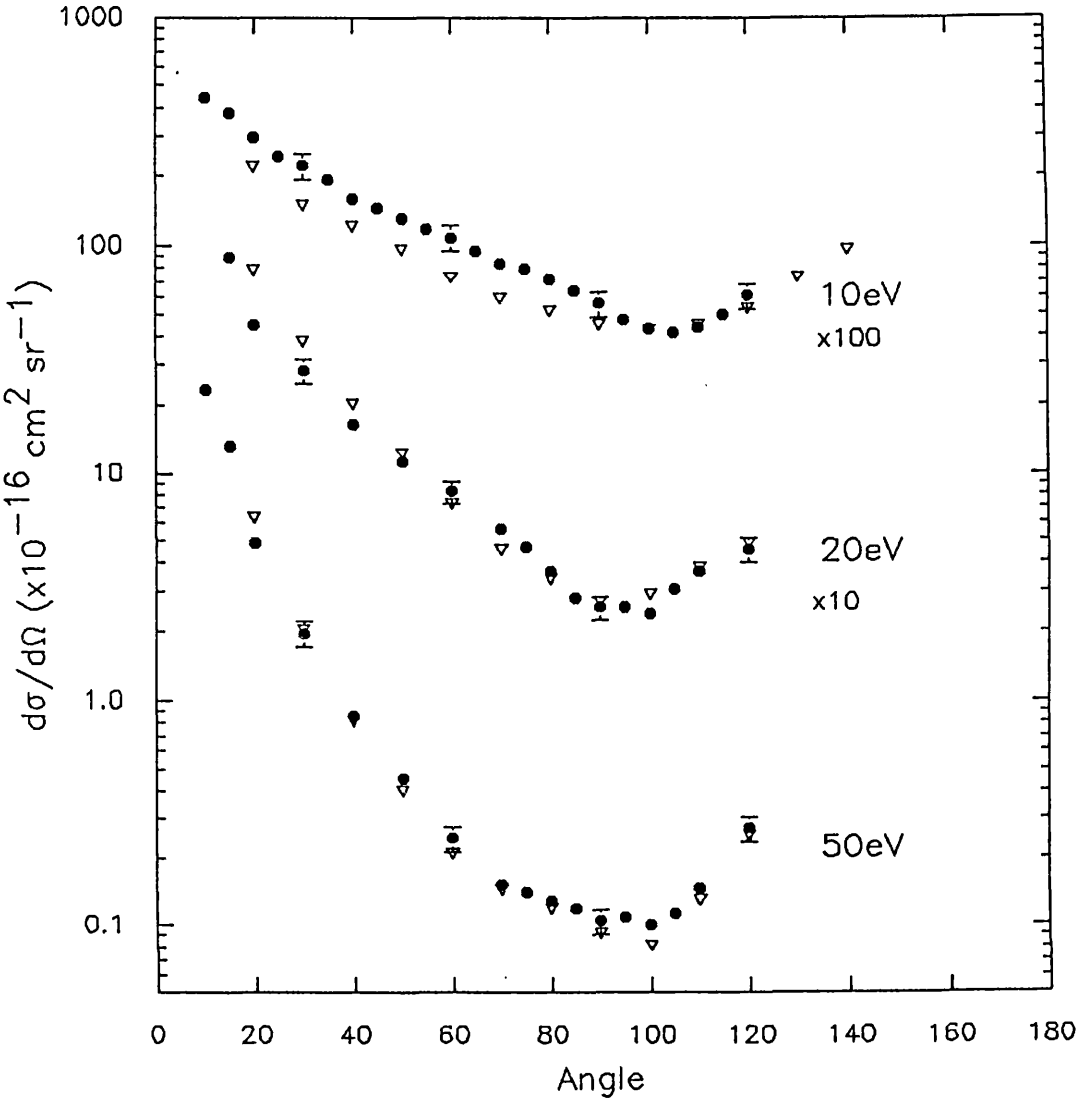

Figure 7.22 Comparison of the differential cross sections for electron scattering from N_2O and CO_2 ($x10^{-16}$ cm^2 sr^{-1}). 10eV: ● N_2O, Present work; ▽ CO_2, Register *et al* (1980). 20eV; ● N_2O, Present work; ▽ CO_2, Kanik *et al* (1989). 50eV: ● N_2O, Present work; ▽ CO_2, Kanik *et al* (1989).

15eV and above. Figure 7.22 compares the N_2O elastic differential cross sections measured in the present work and the CO_2 cross sections of Register *et al* (1980) at 10eV and those of Kanik *et al* (1989) for 20eV and 50eV. At 10eV, the CO_2 cross sections are lower for all angles below 90°, in agreement with the CO_2 σ_T measurements which are also lower than the N_2O cross sections at this energy. This may be a result of the permanent dipole moment of the N_2O molecule which may increase the differential cross sections at the smaller scattering angles. At 20eV and 50eV the agreement between the N_2O and CO_2 differential cross sections is good. Not

only do the shapes of the cross sections agree well but the magnitudes are also in good agreement.

7.5 Summary

In this chapter, the elastic differential, integral and momentum transfer cross sections have been presented. In general, there was good agreement between the present work and the previously published works of Kubo *et al* (1981) and Marinković *et al* (1986). The largest disagreements between all three works were found around the minimum in the angular differential cross sections where the data of Marinković *et al* (1986) was generally found to be lower than the present work or that of Kubo *et al* (1981). The angular differential cross sections were also compared with those of CO_2 and found to be in good agreement for energies above 15eV; this is believed to be a result of the similar electronic structure of the N_2O and CO_2 molecules.

Chapter 8

Conclusion And Suggestions For Future Work

In this thesis, the design of a high resolution electron spectrometer and its subsequent use in obtaining absolute elastic differential cross sections from three polyatomic molecules has been described. The spectrometer, detailed in chapter 2, had an operational energy range from 2eV to 100eV and reasonable resolutions (28meV to 100meV) were obtained with incident beam currents from 2nA to 60nA. The electrostatic lens system used to guide the electron beam around the spectrometer was found to operate as designed except for the first lens in the electron gun. In common with several other electron gun designs, the initial source of electrons from the emission system was taken as the anode aperture but it was subsequently found that the hairpin tip of the filament should have been used.

The resolutions of the monochromator and analyser were observed to be sensitive to the fringing fields at the entrance and exit, but in general, found to agree with the calculated values. A second detector, known as the reference detector, was incorporated into the spectrometer to measure the scattered electron flux at a fixed angle of 90°. It served two purposes: to enable an absolute measurement of the differential cross section to be made at 90°, and to assist in the determination of the relative differential cross section.

Absolute elastic differential, integral and momentum transfer cross sections were measured for three molecules, SF_6, H_2O and N_2O, for incident beam energies between 5eV and 80eV. The maximum error on the differential cross section measurements was 14%, which was comparable to or better than previous measurements made on these molecules. The errors associated with the integral and momentum transfer cross sections were significantly larger (20% and 25%, respectively) as a result of the limited angular range of the spectrometer (10° to 120°), which necessitated an extrapolation of the differential cross section values over a large angular range (0° to 10° and 130° to 180°).

A number of details were noted from the results. For electron scattering from SF_6, strong resonant enhancement was seen in the differential, integral and momentum transfer cross sections for incident energies around 7eV and 12eV. This was in agreement with similar behaviour seen in the total cross section measurements of Kennerly *et al* (1978) and Dababneh *et al* (1988). Interestingly, the theoretical calculations of Dehmer *et al* (1978) and Gyement *et al* (1980) for the integral cross section of this large complex molecule were also seen to produce a similar resonant structure.

The differential cross sections obtained for electron scattering from H_2O were found to be large in the forward direction and this is a common characteristic of electron scattering from polar molecules. As a result of the limited angular range of the present spectrometer, it was not possible to confirm the high differential cross sections reported at large scattering angles ($\theta \geq 120°$) by Shyn and Cho (1987) and to a lesser extent by the theoretical calculations of Brescansin *et al* (1986). Three theoretical calculations of the differential cross sections have been reported and the results of Brescansin *et al* (1986) and Sato *et al* (1988) were found to be in good agreement with the experimental data. It is interesting to note that both these works employed completely different methods to obtain the cross sections. Sato *et al* (1988) used a variation of the relatively simple continuum multiple scattering method whereas Brescansin *et al* (1986) implemented a complex exact static-exchange calculation using the Schwinger variational principle.

The differential cross sections measured for electron scattering from N_2O were seen to undergo a significant change for incident electron energies between 5eV and 10eV. At 5eV the cross section was seen to have a maximum around 50°, but as the incident energy was increased, the differential become forward peaked with a minimum at ≈100°. It had been previously reported that the cross sections for electron scattering from isoelectronic molecules were similar in size and shape. As N_2O is isoelectronic with CO_2, the N_2O differential cross sections were compared with the absolute CO_2 differential cross sections of Register *et al* (1980b) and Kanik *et al* (1989). For incident energies of 20eV and above cross sections were found to have the same

magnitude and shape. Similar results had also been reported by Kwan *et al* (1984) in measurements of the total cross section.

In the future, there are two areas of the spectrometer where further improvements could be made and these are lens 1 in the electron gun and the interaction region. Lens 1 was the only part of the electron optics which did not perform as originally designed (see section 2.6.1). It may be possible to increase the current entering the monochromator by redesigning the lens to reduce the amount of current lost to aperture A2 (see figure 2.11). The lens would be required to operate at a similar voltage ratio (3:1) in order to maintain the same anode voltage, also the sum of the maximum object and image distances would have to be no greater than the present value due to the limitations of space.

The interaction region used in the spectrometer was constructed from an aluminium tube with holes and slots cut in the walls to allow the entry of the incident beam and the escape of the scattered electrons to the analyser and reference detector. A significant electron count rate was detected in both detectors from electrons scattered from the internal surfaces of the interaction region. While it did not prove to be an obstacle in the current work, this problem must be rectified if energy loss measurements are to be made. One possible solution would be to replace the solid metal tube with one constructed from wire mesh.

There are several areas where the spectrometer could be used to make further measurements. The resonant structure observed in the cross sections for electron scattering from SF_6 could be examined in more detail. This would involve the measurement of the elastically scattered electron flux at a fixed scattering angle as a function of incident energy. To avoid defocusing effects in lenses 4 and 5, two separate compensating voltages could be applied to the centre elements of these lenses. This technique has been used extensively to investigate the behaviour of the cross section as a function of incident beam energy and more details can be found in Seng and Linder (1976). Using this method, it would be possible to locate the centres of the resonances and obtain estimates of their widths.

In addition to the polyatomic molecules studied in this work, there are several other molecules which could be studied. For example, only two studies have been made of

scattering from CO_2 and the coverage below 20eV is particularly poor. Cross sections for electron scattering from CO_2 are useful for modelling high powered CO_2 lasers and in the understanding of the upper atmospheric processes of planets such as Mars and Venus, in addition to comparison with theoretical calculations. NH_3 is another molecule suitable for investigation. In plasma chemistry, it is an important source of nitrogen atoms for the fabrication of the nitride films and other nitride compounds. Recently, theoretical cross sections have been reported by Jain (1988) but with the exception of one measurement made at high energies, no experimental differential cross sections measurements have been reported for this system.

In addition to elastic cross sections, it would also be possible to measure inelastic (or excitation) cross sections with the present spectrometer. In order to carry out these measurements the background signal from electrons scattered from the walls of the interaction region would need to be eliminated. Also the transmission of the post-interaction region optics would have to be determined as a function of scattered energy. Techniques for determining the transmission of the optics and measuring absolute excitation cross sections have been given by Nickel *et al* (1989). Absolute excitation cross sections measurements for electron scattering from molecules remain limited, particularly for electronic excitation. Therefore, further investigation of these cross sections would not only provide a benchmark with which to compare theoretical results but also data for use in a number of practical applications such as atmospheric processes and gas discharges. Finally, with the availability of tunable lasers covering a wide range of wavelengths it may now be possible to study electron scattering from excited molecular species. For example, the excitation energy of the infra red active υ_3 fundamental vibrational mode of SF_6 is coincident with 10.4μm line from the CO_2 laser. Therefore, using a CO_2 laser it may be possible to produce of a beam of SF_6 where a significant proportion of the molecules are in an excited molecular state. It would then be possible to compare superelastic scattering with the analogous vibrational excitation. It would also be interesting to see whether the position and shape of the resonances seen in the elastic scattering of electrons from SF_6 were altered by scattering from the molecule in an excited vibrational state.

Publication List

1. Nogueira J.C., Newell W.R. and Johnstone W.M., 15th. ICPEAC Brighton, 1987. abstracts p.143
2. Nogueira J.C., Newell W.R. and Johnstone W.M., J. Phys. B **20** L537 (1987)
3. Johnstone W.M. and Newell W.R., 3rd. ECAMP Bordeaux, 1989. abstracts p.631
4. Johnstone W.M. and Newell W.R., 16th. ICPEAC (1989) abstracts p.280
5. Johnstone W.M. and Newell W.R., 1st. ATMOP Belfast, 1990. abstracts W17
6. "Absolute Elastic Differential Cross Sections For Electron Scattering From SF_6", Johnstone W.M. and Newell W.R., J. Phys. B (1990) accepted for publication.
7. "Absolute Elastic Cross Sections For Electron Scattering From H_2O", Johnstone W.M. and Newell W.R. in preparation.
8. "Absolute Elastic Cross Sections For Electron Scattering From N_2O", Johnstone W.M. and Newell W.R. in preparation

References

Altshuler S., Phys. Rev. **107** 114 (1957)

Andrick D. and Bitsch A., J. Phys. B., **8** 393 (1975)

Andrić L. and Hall R.I., J. Phys. B **17** 2713 (1984)

Azia R., Wong S.F. and Schulz G.J., Phys. Rev. A **11** 1309 (1975)

Ballu, Y. "Advances in Electronics and Electron Physics",
supplement 13B, (Academic Press, 1980)

Barton R.A. and Allison W., J. Phys. E **21** 292 (1988)

Bederson B. and Kieffer L.J., Rev. Mod. Phys. **43** 601 (1971)

Belić D.S., Landau M. and Hall R.I., J. Phys. B **14** 175 (1981)

Boersch H., Z. Phys. **139** 115 (1954)

Born M., Z. Phys. **38** 803 (1926)

Brescansin L.M., Lima M.A.P., Gibson T.L., McKoy V. and Huo W.M.
J. Chem. Phys. **85** 1854 (1986)

Brinkman R.T. and Trajmar S. J. Phys. E. **14** 245 (1981)

Brüche E., Ann. Phys. **1** 93 (1929)

Brunt J.N.H. and Read F.H., J. Phys. E **8** 1015 (1975)

Brunt J.N.H., King G.C. and Read F.H., J. Phys. B. **10** 1289 (1977a)

Brunt J.N.H., Read F.H. and King G.C., J. Phys. E **10** 134 (1977b)

Bullard E.C. and Massey H.S.W., Proc. R. Soc. London **A133** 637 (1931)

Buckley B.D., Burke P.G. and Nobel C.J., in "Electron-Molecule",
(eds. I. Shimamura and K.Takayanagi, Plenum, New York 1984) chapter 7

Burke P.G., Adv. At. Molec. Phys. **15** 471 (1979)

Burke P.G. and Chandra N., J. Phys. B **5** 1696 (1972)

Burke P.G. and Noble C.J., Comments At. Mol. Phys. **12** 301 (1983)

Castillejo L., Percival I.C. and Seaton M.J.,
Proc. R. Soc. London A **254** 259 (1960)

Chamberlain G.E., Mielczarek S.R. and Kuyatt C.E., Phys. Rev. A **2** 1905 (1970)

Chandra N., Phys. Rev. A **16** 80 (1977)

Chang E.S. and Fano U., Phys. Rev. A **6** 173 (1972)

Chantry P.J., J. Chem. Phys. **55** 2746 (1971)

Chase D.M., Phys. Rev. **104** 838 (1956)

Chutjian A., Rev. Sci. Instrum. **50** 347 (1979)

Chutjian A. and Segal G. J. Chem. Phys. **57** 3069 (1972)

Christophorou L.G., James D.R. and Pai R.Y
in "Applied Atomic Collision Physics" (eds: H.S.W. Massey,
E.W. McDaniel and B.Bederson Academic Press, New York, 1982) p.87

Chutjian A., Phys. Rev. Lett. **46** 1511 (1981)

Clausing P., Z. Physik **66** 471 (1930)

Collins L.A. and Norcross D.W., Phys. Rev. A **18** 467 (1978)

Collins L.A., Henry R.J.W. and Norcross D.W., J. Phys. B **13** 2229 (1980)

Comer J. and Read F.H., J. Phys. E **4** 368 (1971)

Connolly J.W.D. and Johnson K.H., Chem. Phys. Lett. **10** 616 (1971)

Csanak G., Cartwright D.C., Srvastava S.K. and Trajmar S.,
in "Electron Molecule Interactions and Their Applications",
(ed. L.G. Christophorou, Academic Press, London 1984) chapter 1

Dababneh M.S., Hseih Y.-F., Kauppila W.E., Kwan C.K.,
Smith S.J., Stein T.S. and Uddin M.N., Phys. Rev. A **38** 1207 (1988)

Danjo A. and Nishimura H., J. Phys. Soc. Jpn. **54** 1224 (1985)

Dehmer J.L., Siegel J. and Dill D., J. Chem. Phys. **69** 5205 (1978)

Dehmer J.L. and Dill D., in "Electron Molecule and Photon Molecule Collisions"
(Eds; Rescigno T.N., Mckoy V. and Schneider B.I.,
Plenum, New York 1979) p.225

Dehmer J.L., Siegel J. and Dill D, J. Chem. Phys. **69** 5205 (1978)

Dill D. and Dehmer J.L., J. Chem. Phys. **61** 692 (1974)

Dubé L. and Herzenberg A., Phys. Rev. A **11** 1314 (1975)

Endo N. and Kurogi Y., IEEE Trans. Electron Devices, **ED-27**, 1346 (1980)

Fano U., Comments At. Mol. Phys. **2** 47 (1970)

Ferch J., Granitza B., Masche C. and Raith W., J. Phys. B **18** 967 (1985)

Field D., Mrotzek G., Knight D.W., Lunt S. and Ziesel J.P.,
J. Phys. B **21** 171 (1988)

Fon W.C., Berrington K.A. and Hibbert A., J. Phys. B. **14** 307 (1981)

Fon W.C. and Berrington K.A., J. Phys. B. **14** 323 (1981)

Fon W.C., Berrington K.A., Burke P.G. and Hibbert A.,
J. Phys. B. **16** 307 (1983)

Fox. K.E. and Reid J., J. Opt. Soc. Am. B **2** 807 (1985)

Fridh C., Asbrink L. and Lindholm E., Chem. Phys. **27** 169 (1978)

Fujita T., Ogura K. and Watanabe Y., J. Phys. Soc. Japan **52** 811 (1983)

Furst J.E., Golden D.E., Mahgerefteh M., Zhou J. and Mueller D.,
Phys. Rev. A **40** 5592 (1989)

Garrett W.R., Phys. Rev. A **4** 2229 (1971)

Gianturco F.A. and Jain A., Phys. Rep. **143** 347 (1986)

Gianturco F.A., Jain A. and Pantano L.C., J. Phys B **20** 571 (1987)

Gianturco F.A. and Scialla S., J. Phys. B **20** 3171 (1987a)

Gianturco F.A. and Scialla S., J. Chem. Phys. **87** 6468 (1987b)

Gianturco F.A. and Thompson D.G., Chem. Phys. **14** 111 (1976)

Gianturco F.A. and Thompson D.G., J. Phys. B **13** 613 (1980)

Giordmaine J.A. and Wang T.C., J. App. Phys. **31** 463 (1960)

Gibson T.L., Lima M.A.P., Takatsuka K. and Mckoy V.,
Phys. Rev. A **30** 3005 (1984)

Golden D.E., Bandel H.W. and Salerno J.A., Phys. Rev. **146** 40 (1966)

Guo X.Q., Crowe D.M., Lubell M.S., Tang F.C., Vasilakis A., Eminyan M.
and Slevin J., Rev. Sci. Instrum. **61** 1858 (1990)

Gyemant I., Varga ZS. and Benedict M.G., Int. J. Quantum Chem. **17** 255 (1980)

Gyement I., Varga ZS. and Benedict M.G., Int. J. Quant. Chem. **18** 255 (1980)

Hahn J. and Junge C., Z. Naturorsch. **32a** 190 (1977)

Haine M.E. and Einstein P.A., Brit. J. Appl. Phys. **3** 40 (1952)

Hara S., J. Phys. Soc. Japan **22** 710 (1967)

Hara S., J. Phys. Soc. Japan **27** 1009 (1969)

Harting E. and Read F.H., "Electrostatic Lenses", (Elsevier, Amsterdam 1976)

Henry R.J.W. and Lane N.F., Phys. Rev. **183** 221 (1969)

Herzog R., Z.Phys., **97** 596 (1935)

Hoffman K.R., Dababneh M.S., Hsieh Y.-F. Kauppila W.E., Pol V., Smart J.H. and Stein T.S., Phys. Rev. A **25** 1393 (1982)

Huxley L.G.H. and Crompton R.W., "The Diffusion and Drift of Electrons in Gases", (John Wiley and Sons, New York 1974)

Itikawa Y., J. Phys. Soc. Japan **32** 217 (1972)

Jansen G.H., Groves T.R. and Stickel W., J. Vac. Sci. Technol **B3(1)** 190 (1984)

Jain A., J. Phys. B **15** 1533 (1982)

Jain A., Phys. Rev. A **34** 3707 (1986)

Jain A., J. Chem. Phys. **86** 1289 (1987)

Jain A., J. Phys. B **21** 905 (1988)

Jain A. and Thompson D.G., J. Phys. B **15** L631 (1982)

Jost K., J. Phys. E **12** 1001 (1979)

Jung K., Antoni T., Mueller R., Kochem K.H. and Ehrhardt H., J. Phys. B **15** 3535 (1982)

Jungen M., Vogt J. and Staemmler V., Chem. Phys. **37** 49 (1979)

Kanik I., McCollum D.C. and Nikel J.C., J. Phys. B **22** 1225 (1989)

Kennerly R.E. and Bonham R.A., Phys. Rev. A **17** 1844 (1978)

Kennerly R.E., Van Brunt R.J. and Gallagher A.C., Phys. Rev. A **23** 2430 (1981)

Klemperer O. and Barnett M.E., "Electron Optics", (Cambridge University Press, 3rd. Edition, London, 1971)

Klemperer O. and Klinger Y. Proc. Phys. Soc. B **64** 231 (1951)

Kwan Ch. K., Hsieh Y.-F., Kauppila W.E., Smith S.J., Stein T.S., Uddin M.N. and Dababneh M.S., Phys. Rev. A **27** 1328 (1983)

Kwan Ch. K., Hsieh Y.-F., Kauppila W.E., Smith S.J., Stein T.S., Uddin M.N. and Dababneh M.S., Phys. Rev. A **52** 1417 (1984)

Katase A., Ishibashi K., Matsumoto Y., Sakae T., Maezono S., Murakami E., J. Phys. B **19** 2715 (1986)

Kennerly R.E., Bonham R.A. and McMillian M., J. Chem. Phys. **70** 2039 (1979)

Khakoo M.A. and Trajmar S., Phys. Rev. **34** 138 (1986)

Kubo M., Matsunaga D., Suzuki T. and Tanaka H., XIIth. ICPEAC abstacts p. 360, 1981

Kuyatt C.E. and Simpson, J.A., Rev. Sci. Instrum. **38** 103 (1967)

Kuyatt C.E. in "Methods of Experimental Physics"
(Bederson B. and Fite W.L., eds.) Academic Press, New York 1968, p.1

Lane N.F., Rev. Mod. Phys. **52** 29 (1980)

van Leeuwen J.M.J and Jansen G.H., Optik **65** 179 (1983)

Lima M.A.P., Gibson T.L., Huo W.M., and McKoy V.,
Phys. Rev. A **32** 2696 (1985)

Linder F. and Schmidt H., Z. Naturforsch **26a** 1603 (1971)

Marinković B., Szmytkowski Cz., Pejčev V., Filipović D. and Vuškković I.,
J. Phys. B **19** 2365 (1986)

Märk T.D. in "Electron Molecule Interactions and their Applications Vol. 1"
ed L.G. Christophorou (Academic Press, London 1984) chapter 3

Mathur D. and Hasted J.B., Chem. Phys. Let. **34** 90 (1975)

Mason N.J. and Newell W.R., J. Phys. E **19** 722 (1986)

Massey H.S.W., Proc. R. Soc. London **A129** 616 (1930)

Massey H.S.W. in "Electronic and Ionic Imapct Phenomena Vol. II",
(Clarendon Oxford, 1969)

Massey H.S.W. and Burhop E.H.S. in
"Electronic and Ionic Imapct Phenomena Vol. I", (Clarendon Oxford, 1969)

Massey H.S.W. and Mohr C.B.O., Proc. R. Soc. London **A135** 258 (1932)

McGowan J.W., Rev. Sci. Instrum. **38** 285 (1967)

Melton C.E. and Neece G.A., J. Chem. Phys. **55** 4665 (1971)

Morrison M.A., Austr. J. Phys. **36** 239 (1983)

Morrison M.A. and Collins L.A., Phys. Rev. A **23** 127 (1981)

Nakatsuji H., Chem. Phys. **75** 425 (1983)

Nesbet R.K., Phys. Rev. A. **20** 58 (1979)

Newell W.R., Brewer D.F.C. and Smith A.C.H., J. Phys. B., **14** 3209 (1981)

Nickel J.C., Zetner P.W., Shen G. and Trajmar S., J. Phys. E. **22** 730 (1989)

Nishimura H. and Yano K., J. Phys. Soc. Jpn. **57** 1951 (1988)

Norcross D.W., in "Applied Atomic Collision Physics"
(eds: H.S.W. Massey, E.W. McDaniel and B.Bederson Academic Press, New York, 1982) p.69

Norcross D.W. and Collins, L.A., Adv. At. Mol. Phys. **18** 341 (1982)

Olander D.R. and Kruger V., J. App. Phys. **41** 2769 (1970)

Olivero J.J., Stagat R.W. and Green A.E.S., J. Geophys. Res. **77** (1972)

Oppenheimer J.R., Phys. Rev. **32** 361 (1928)

Orient O.J. and Srivastava S.K., J. Phys. B **20** 3923 (1987)

Petley C.H., Mullard Tech. Rev. **24** 130 (1971)

Pierce J.R., J. Appl. Phys. **11** 548 (1940)

Pierce D.T., Celotta R.J., Wang G.L., Galejs A., Kuyatt C.E. and Mielczarek S.R. Rev.Sci.Instrum. **51** 478 (1980)

Pinto R., Ramanthan K.V. and Babau R.S., J. Electrochem. Soc. **134** 165 (1987)

Powell C.J., "Methods of Experimental Physics Vol. 7B"
(ed. L. Morton, Academic Press, New York, 1968)

Purcell E.M., Physical Review, **54** 818 (1938)

Ramsauer C., Ann. Phys. **64** 513 (1921)

Ramsauer C. and Kollath R., Ann. Phys. **12** 529 (1932)

Rapp D. and Englander-Golder P., J. Chem. Phys. **43** 1464 (1965)

Read F.H., J. Phys. B. **8** 1034 (1975)

Read F.H., Commer J., Imhof R.E., Brunt J.N.H. and Harting E., J. Elect. Spec. Rel. Phenom. **4** 293 (1974)

Register D.F., Trajmar S. and Srivastava S.K., Phys. Rev. A., **21** 1134 (1980a)

Register D.F., Nishimura H. and Trajmar S., J. Phys. B **13** 1651 (1980b)

Rohr K., J. Phys. B **10** 1175 (1977)

Rohr K., J. Phys. B **12** L185 (1979)

Sakae T., Sumiyoshi S., Murakami E., Matsumoto Y., Ishibashi K. and Katase, J. Phys. B **22** 1385 (1989)

Sato H., Kimura M. and Fujima K., Chem. Phys. Let. **145** 21 (1988)

Seng G. and Linder F., J. Phys. B **9** 2539 (1976)

Sevier K.D., "Low Energy Electron Spectroscopy", (New York: Wiley, 1972)

Shyn T.W., Phys. Rev. A **22** 916 (1980)

Shyn T.W. and Cho S.Y., Phys. Rev. A **36** 5138 (1987)

Shyn T.W., Cho S.Y. and Cravens T.E., Phys. Rev. A **38** 678 (1988)

Siegel J., Dehmer J.L. and Dill D., Phys. Rev. A **23** 632 (1981)

Srivastava S.K., Chutjian A and Trajmar S., J. Chem. Phys. **63** 2659 (1975)

Srivastava S.K., Trajmar S., Chutjian A, and Williams W.,
J. Chem. Phys. **64** 2767 (1976)

Srivastava S.K., Tanaka H., Chujain A. and Trajmar S.,
Phys. Rev. A **23** 2156 (1981)

Sueoka O., Mori S. and Katayama Y., J. Phys. B **19** L373 (1986)

Szmytkowski Cz., Maciag K., Karwasz G., Chem. Phys. Lett. **107** 481 (1984)

Szmytkowski C., Chem. Phys. Let. **136** 363 (1987)

Szmytkowski Cz., Maciag K., Karwasz G. and Filipović D.,
J. Phys. B **22** 525 (1989)

Takatsuka K. and Mckoy V., Phys. Rev. A **24** 2473 (1981)

Takatsuka K. and Mckoy V., Phys. Rev. A **30** 1734 (1984)

Tanaka H., Kubo M., Onodera N., and Suzuki A., J. Phys. B **16** 2861 (1983)

Trajmar S. and Chutjian A., J. Phys. B **10** 2943 (1977)

Trajmar S., Register D.F. and Chutjian A., Phys. Reports **97** 219 (1983)

Trajmar S. and Register D.F., in "Electron-Molecule Collisions"
(eds: K. Takayanagi and I. Shimamura, Plenum, New York 1984) chapter 6

Tronc M., Fiquet-Fayard F., Schermann C. and Hall R.I., J. Phys. B **10** L459 (1977)

Tronc M., Malegat L., Azria R. and LeCoat Y XIIth ICPEAC, Gatlinberg,
abstracts p.372 (1981)

Turner J.E., Paretzke H.G., Hamm R.N., Wright H.A. and Ritchie R.H.,
Radiat. Res. **92** 47 (1982)

Wang W., and Sze N.D., Nature **286** 589 (1980)

Watanabe K. and Maki H., J. Phys. B **19** 2715 (1986)

Williams J.F., J. Phys. B **12** 265 (1979)

Williams J.F. and Willis B.A., J. Phys. B **8** 1670 (1975)

Wong S.F. and Shulz G.J., Phys. Rev. Let. **32** 1089 (1974)

Zecca A., Karwasz G., Oss S., Grisenti R. and Brusa R.S.,
J. Phys. B **20** L133 (1987)

Zhou J.X., Furst J.E., Golden D.E. and Mueller D.W., XVIth I.C.P.E.A.C.
New York, Abstract of Contributed Papers, p.799 (1989)